# Modelling of Displacement Ventilation and Chilled Ceiling Systems Using Nodal Models

by

Simon J. Rees

A Doctoral Thesis

Submitted in partial fulfilment of the requirements
for the award of

Doctor of Philosophy of Loughborough University
March 1998

# Abstract

Cooling and ventilation of office spaces by displacement ventilation and chilled ceiling panel systems is potentially more energy efficient than conventional air conditioning systems. Heat transfer in this type of system is characterised by the presence of vertical temperature gradients and significant radiant asymmetry. The room heat transfer models used in current building simulation methods do not allow adequate representation of this type of system due to their reliance on a single node to define the internal air temperature. The overall aim of the work described in the thesis has been to develop a model of this type of system that is suitable for use in annual building energy simulation. The model presented, is intermediate in complexity between a CFD numerical model and the current single air node models, having ten air nodes.

The operating characteristics of displacement ventilation systems, used both with and without chilled ceiling panels, have been studied by making experimental measurements in a test chamber and by reference to published experimental data. Numerical calculations of the flow and temperature fields have been made with a coupled flow and radiant exchange CFD code. Steady state calculations have been made of displacement ventilation using a conjugate heat transfer method. Interesting oscillations in the flow and temperature field of displacement ventilation operating with a chilled ceiling have been found through adopting a fully transient calculation procedure.

The thesis describes how the experimental and numerical data has been used to develop the structure and define the parameters of a simplified nodal model. The logical development of the model structure, from the most elementary model to one which is able to capture *the effects of the temperature gradients and incomplete* mixing of the air in the room is described. A method is also presented whereby the parameters of the model are found directly from the experimental data by solving the heat and mass balance equations of the nodal model. The parameters of the model have been generalised by analysing these calculations and by making use of established convection coefficient correlations.

The performance of the model is demonstrated by firstly making comparisons of the experimental and numerical data under steady state conditions, and also by demonstrating that the model is able to reproduce the characteristics of displacement ventilation and chilled ceiling systems under different operating conditions.

## Acknowledgements

I would firstly like to thank my supervisors, Dr. Philip Haves and Prof. Jim McGuirk, for their support, encouragement and guidance during this work. I am grateful to them for the insight they have given me into the subjects of building system modelling and simulation, and computational fluid dynamics. I would also like to thank my Director of Research, Prof. Vic Hanby for his support through out my time working in the department. Thanks is also due to my student colleagues for the help and stimulation they have given, and in particular Dr. Bernardo Vazquez for his help during the experimental stage of the project.

I am also grateful to the organisations that have given there financial support to the project, namely, Ove Arup and Partners, EA Technology Ltd. and British Gas plc. I would like to thank Mike Holmes of Ove Arup and Partners for his interest in the project and the technical input he has given. Thanks must also go to Ed Sowell for his support in the use of the LIGHTS program and to Yuguo Li for provision of experimental data and helpful discussions during the model development. I would particularly like to thank my family for support me through this work and for putting up with me being distracted more than usual. I also give thanks to God for his grace that I have experienced in the period that has been taken up with completing this work.

To
Alastair
and
Oliver.

# Contents

# List of Figures

# List of Tables

# Nomenclature

| Symbol | Meaning | Units |
|---|---|---|
| A | Area | $m^2$ |
| Ar | Archimedes number | - |
| b | Plume radius | m |
| C | Capacity Rate/Specific heat | $W.K^{-1}$, $J.kg.^{-1}.K^{-1}$ |
| d | depth | m |
| E | Heat Load | W |
| Fr | Froude number | - |
| g | Gravitational acceleration | $m.s^{-2}$ |
| G | Water mass flow rate/Irradiation | $kg.s^{-1}$, $W.m^{-2}$ |
| h | Convection coefficient/static enthalpy | $W.m^{-2}.K^{-1}$, $J.kg.^{-1}$ |
| H | Height | m |
| I | Radiant intensity | $J.rad^{-1}$ |
| J | Radiosity | $W.m^{-2}$ |
| k | Turbulent kinetic energy | $m^2.s^{-2}$ |
| m | Plume constant | - |
| p | Plume constant | - |
| P | Pressure | Pa |
| Pe | Peclet number | - |
| q | Heat flux | $W.m^{-2}$ |
| Q | Heat load | W |
| r | Radius | m |
| s | Distance along radiation beam | m |
| S | Capacity rate ratio | - |
| t | Time | s |
| T | Temperature | K |
| U | Overall thermal conductance | $W.m^{-2}.K^{-1}$ |
| u,v,w | Fluctuating velocity components | $m.s^{-1}$ |
| U,V,W | Mean velocity in cartesian directions | $m.s^{-1}$ |
| x,y,z | Cartesian coordinate positions | m |

| Greek Symbol | Meaning | Units |
|---|---|---|
| $\alpha$ | Entrainment constant/relaxation factor | - |
| $\beta$ | Thermal expansion coefficient | $K^{-1}$ |
| $\Gamma$ | Diffusion coefficient | - |
| $\varepsilon$ | Turbulent dissipation rate | $m^2.s^{-3}$ |
| $\epsilon$ | Emissivity | - |
| $\lambda$ | Thermal conductivity | $W.m^{-1}.K^{-1}$ |
| $\kappa$ | Temperature ratio | - |
| $\mu$ | Viscosity | $Kg.m^{-1}.s^{-1}$ |
| $\rho$ | Density | $kg.m^{-3}$ |
| $\phi$ | Transported scalar | - |
| $\sigma$ | Prantl number | - |

| Subscript | Meaning |
|---|---|
| a | air |
| c | convective |
| e | extract |
| e1-3 | entrainment |
| E | East |
| f,F | Floor |
| fl | floor surface |
| fla | air adajacent floor |
| i,j,k | Tensor/direction indexes |
| nb | neighbouring |
| N | North |
| P | Pressure |
| P1-4 | Plume |
| R | Roof |
| R1-4 | Room air |
| s | Supply (air) |
| S | South |
| sw | Supply (chilled water) |
| w | wall |
| wl | lower wall |
| W | West |

# Chapter 1

# Introduction

## 1.1 Background

International concern over the issues of global warming and ozone layer depletion in recent years has focused attention within the building services industry on low energy cooling systems. Governments have made commitments both to stabilise carbon dioxide emission levels and to outlaw the use of ozone depleting refrigerants within the next few years. Energy usage within buildings is known to be a significant proportion of total energy usage and of associated $CO_2$ emissions. Reduction of energy use in building cooling systems can therefore be an important contribution to the effort to reduce $CO_2$ emissions and associated global warming. Buildings incorporating vapour compression refrigeration equipment also represent both a large capital holding and a large annual consumption of CFC/HCFCs. Whilst there is a considerable research effort into development of alternative refrigerants which is resulting in competitive replacements for existing refrigerants (Takla 1992), low energy cooling technologies also offer some potential for avoidance of the use of such refrigerants.

This century has seen a dramatic rise in the demand for office space. Whilst business practice is evolving and may result in a reversal of this trend (Brown 1992) there is a continued demand for both office space and improved comfort and air quality conditions. Demand is increasing for office buildings that offer lower energy consumption from certain building owners and tenants who want to be 'environmentally friendly', and may also come from government legislation. The

exact nature of any legislation is unclear at the moment, but may take the form of a 'carbon tax' and probably the introduction of 'energy targets' set within the building regulations. This situation will increasingly favour cooling systems that offer both lower energy consumption. A number of low energy cooling technologies and systems—including displacement ventilation and chilled ceiling systems—are currently being researched within Annex 28 of the International Energy Agency.

Displacement ventilation is a system of air distribution which offers the potential for both lower energy consumption for cooling applications and improved indoor air quality. It does this by introducing air at low level and at temperatures close to the operating temperature of the room, and by seeking to avoid the recirculation of heat and contaminants within the room. However, the demands of thermal comfort place limitations on the temperature gradients that can be permitted in office rooms, and therefore on the size of cooling loads that can be dealt with by this type of system. It is for this reason that building designers have proposed combining displacement ventilation with both chilled ceiling panel and chilled beam systems.

Chilled ceiling systems encompass a range of systems that use various forms of room cooling elements, with either water or air as the heat transfer fluid, which cool the occupied space directly by some combination of both radiant and natural convection effects. Both chilled ceiling and displacement ventilation systems have been used for a number of years with conventional central chilling plant making use of vapour compression refrigeration technology. Chilled ceiling and displacement ventilation systems are complementary in the sense that they use similar primary water temperatures of the order of 14–16°C.

The fact that this primary water temperature is of the order of ten degrees higher than that of conventional systems, means that there is much greater potential for making use of ambient energy. This can be realised, for example, by taking advantage of depressed air wet-bulb temperatures for indirect evaporative cooling of the ventilation air, and using cooling towers to provide water for the static cooling elements. A number of low energy cooling techniques such as evaporative cooling and desiccant cooling which which have been studied within IEA Annex 28, may also prove to give beneficial performance in conjunction with chilled ceilings and displacement ventilation. It is clearly desirable that the potential advantages of displacement ventilation and chilled ceilings, and the benefits of combining this method of cooling and ventilation with other low energy cooling technologies, be evaluated through simulation before construction. It is with this long term aim in

mind that the work described here has been undertaken.

## 1.2 Objectives and Approach

A significant body of research has developed over the last decade concerned with the characterisation of air flow and air quality in displacement ventilation systems. There is also a considerable amount of data available (mainly from manufacturers) on the performance of components of displacement ventilation and chilled ceiling systems—although not all measured to the same standards. There is little published data concerning displacement ventilation combined with chilled ceiling systems. Whilst there are also some obvious energy saving advantages of such systems, there has been little reported in the way of field energy measurements in real offices, or analysis of such systems from computer simulation results.

The simulation of annual energy usage in conventional cooling systems using mechanical ventilation or vapour compression refrigeration and fully mixed air in the occupied space, is treated by a number of building energy analysis programs, e.g. (DOE-2 1982, BLAST 1986, TAS n.d., FACET 1991). Low energy central plant systems are now being incorporated into many of these programs. Whilst the building heat transfer processes may be modelled in different ways within such programs they generally have the common feature that the thermal conditions within each room or zone are modelled on the basis of the air being fully mixed. It is this drawback principally, that needs to be overcome to enable systems like displacement ventilation to be modelled realistically.

The overall objective of the work described here has been to develop a simplified model of rooms with displacement ventilation and chilled ceiling systems that can be used to predict thermal conditions. The ultimate goal in developing the model is that it could be used in annual energy simulations. It is therefore important that the model is also computationally efficient. The model presented here is, accordingly, of intermediate complexity between that of a single air node model, and that of a CFD model, and has the order of ten air nodes. The model is of the type that has been called a 'zonal model' or 'nodal model'. In this type of model the room heat transfer is determined by a network of nodes, at which heat balances are calculated, that are interconnected by conductances representing bulk air movement or convective heat transfer paths. In this type of model the parameters that determine the bulk air flow movement have to be pre-determined

in some way.

In order to develop a model of this type it is necessary to have reasonably comprehensive temperature and heat flux data for a number of operating conditions. The test chamber data of Li, Sandberg and Fuchs (1995) has been used to deal with some displacement ventilation conditions. The primary source of experimental temperature and heat flux data however, has been a series of test chamber experiments conducted in the Civil and Building Engineering Department's test chamber equipped with a commercial displacement ventilation and chilled ceiling system.

In parallel to the experimental work, numerical studies of the flow and heat transfer in rooms with displacement ventilation and chilled ceilings, and in conditions identical to that of the test chamber experiments, have been made. The objective of carrying out these calculations of the test chamber experiments has been to gain further insight into the room flow conditions and in particular the degree of recirculation and mixing present under typical operating conditions. In view of the importance of the radiant coupling in rooms with displacement ventilation and chilled ceiling systems a coupled flow and radiation solver has been used. In order to also take account of the conducted fluxes at the room surfaces a conjugate heat transfer calculation method has been used in the calculation of displacement ventilation cases. In making calculations of the cases with chilled ceilings, where the heat loads were greater, fully transient calculations have been made.

The structure of the nodal model has been developed through a number of stages. The distribution of nodes has been largely determined by the output requirements of the model and the desire to resolve vertical temperature gradients. The air flow network has been developed by reference to *both experimentally observed and* numerically predicted air flow paths. The approach taken to find values for the convection and bulk air flow (capacity rate) parameters of the nodal model has been to try and solve the heat and mass balance equations of the air nodes using experimentally measured air and surface temperature data as inputs to the equations, and solving for the parameters. This has been done for each experimental test case and the resulting sets of parameters have been analysed to enable rules to be established to generalise the parameters. The convection coefficient parameters of the model have been found in this way, and by reference to established correlations.

## 1.3 Overview of the Thesis

Besides the introduction and conclusions, the main part of the thesis is divided between six chapters. These are concerned with the literature review, the experimental and numerical methods and results and the nodal model itself. The first chapter after the introduction is concerned with a review of the literature associated with displacement ventilation and chilled ceiling systems. Literature concerned with the fundamental fluid dynamic phenomena associated with, and numerical and nodal modelling of, this type of system are discussed. Chapters three and four are concerned with the experimental method and results respectively. Some additional details concerned with calibration of the measurement systems are given in a separate appendix. Chapters five and six are concerned with the numerical methods adopted here, and the numerical results respectively. Details of the development of the nodal model structure, finding values for the air flow and convection coefficient parameters, and testing of the model, are all given in chapter seven.

# Chapter 2

# Literature Review

## 2.1 Introduction

This chapter is concerned with a review of the literature concerned with displacement ventilation and chilled ceiling technology and the numerical and nodal modeling of such systems. Displacement ventilation technology has been developed for office applications since the late 1980's. The body of literature concerned with this technology has steadily grown since. This body of literature is concerned with a number of aspects, including the benefits of this type of system in terms of air quality and thermal comfort. The work here is not concerned directly with these areas and so the literature review of displacement ventilation is confined to that relating to the fluid dynamics and thermal performance. Chilled ceilings technology, although pre-dating the development of displacement ventilation, has more recently seen a growth of interest, both commercially and in the research literature. Accordingly, the body of literature concerned with chilled ceiling systems, and in particular their use in combination with displacement ventilation, is modest. The first sections of this chapter are concerned with an overview of these technologies.

The principal fluid dynamic phenomena associated with displacement ventilation are the development of plumes in the upper part of the room, and a buoyancy dominated supply flow in the lower part of the room. Literature concerned with the fluid dynamics of displacement ventilation is generally concerned with only one of these aspects. Separate sections are accordingly given to the discussion of

the literature concerned with either flow in plumes, or flow from the diffuser and in the lower part of the room.

Interest in numerical modeling of room air flow and heat transfer (CFD) has grown steadily since the 1980's. Use of these techniques in studying room flows has, however, lagged behind application to other areas (e.g. aerospace). There is a large body of literature concerned with the modeling of fluid flows, turbulence and numerical methods in general. The aim of the literature review given here, however, has been to focus on that literature that is of particular relevance to displacement ventilation. A further section of the literature review is given to literature concerned with nodal models, and other simplified modeling, that has been applied to various building services systems.

## 2.2 Displacement Ventilation

Conventional air conditioning systems using cooled air as the medium for removing excess heat from rooms do so by introducing air at temperatures of the order of eight to ten degrees Celsius below the desired mean room air temperature. Air is introduced into the room—either at the ceiling or at sill level—with sufficient momentum to form a jet outside the occupied zone which quickly mixes with the rest of the air in the room. The temperature is intended to be uniform throughout the room at the design condition and is therefore close to the extract temperature. Contaminants from coverings, furniture, people etc. will also be evenly distributed about the room due to the mixing of the air.

Displacement ventilation systems (or heat-source ventilation as it is known as in Germany) seek to avoid any mixing of the air within the room and to rely on buoyancy forces to establish a movement of air from low to high level within the room. Rather than maintaining uniform air temperature and contaminant concentrations throughout most of the room, vertical gradients of both temperature and contaminant concentration are allowed to develop. The aim is that people in the occupied space are exposed to temperature and air quality conditions that are close to the supply air conditions (Skåret 1987, Jackman 1991, Jackman 1990).

Displacement ventilation systems seek to achieve this by introducing the supply air at very low velocity near the floor at temperatures only a few degrees below the 'operating temperature' of the room (see figure 2.1. The cool supply air descends

towards the floor on entering the room and spreads across the floor to establish a 'lake' of cool air. The air is slightly warmed as it passes over the floor surface and begins to rise through the room. Buoyant plumes are developed around any warm objects in the room such as people and electrical equipment. Air is drawn by the plumes from the 'lake' of air near the floor and entrained into the plume from the surrounding air in the lower part of the room. Each plume increases in size and flow rate with height until it reaches an upper zone bounded by the ceiling where there is some mixing of the fluid. Skåret (1987) describes how the plumes decelerate in this upper zone as they reach an equilibrium temperature with the surrounding stratified air.

A so-called 'stationary front' exists at the boundary between the upper mixed zone and the lower part of the room. The position of this stationary front is dependent on the flow from the plumes entering the upper mixed zone being in equilibrium with the extract flow. The height of the front is therefore a function of how the flow in the plumes vary with height, which in turn is dependent on a number of factors. In designing such systems it is desirable to maintain the upper mixed zone above head height in order to give improved air quality in the occupied zone.

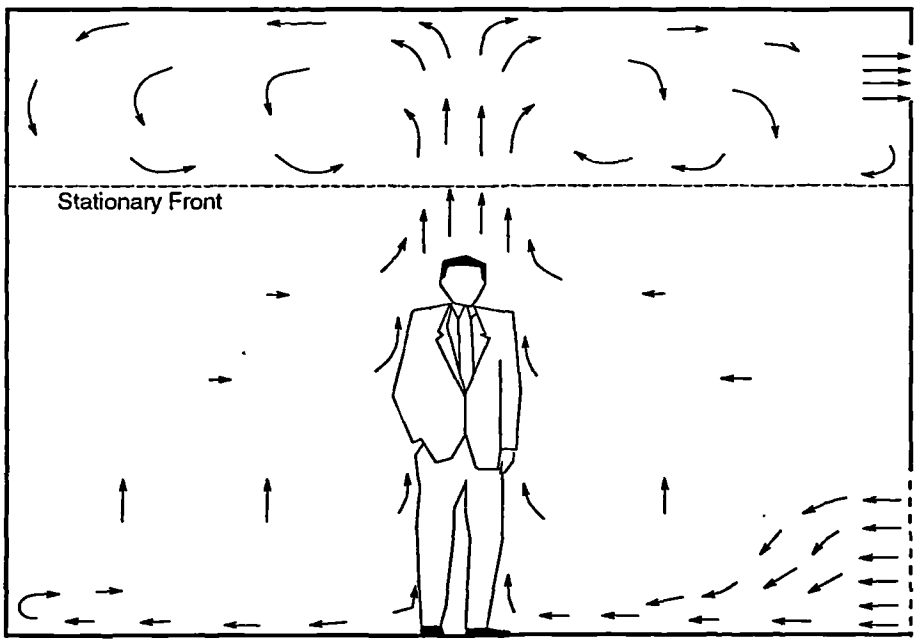


**Figure 2.1:** A Simplified view of Displacement Ventilation Flow.

Displacement ventilation systems are thought therefore, to work well under the following conditions (Jackman 1991):–

- Where the supply air is cooler than the room air
- Where contaminants are warm and/or lighter than the surrounding air and associated with a heat source
- Where the surface temperatures of heat sources are high
- Where there is sufficient height for the upper mixed zone to be above the occupied space
- Where disturbances to room air flows are weak

The need for the supply air to be cooler than the room air precludes such systems being used for heating purposes. Spaces at the perimeter of buildings using displacement ventilation therefore usually have separate heat emitter systems. Displacement ventilation systems were first developed for industrial applications in Scandinavia during the 1970s. Many industrial applications satisfy the above criteria in that spaces are high; strong plumes may develop from hot machinery; contaminants are likely to be warm and disturbances to the flow from general movement will be less significant in large spaces (Christoffersen and Modsen 1992, Bream and Slatte 1992). Svensson writing in 1989 states that displacement ventilation systems have approximately 50 % of the market for industrial applications in Scandinavia (Svensson 1989). Displacement ventilation has also been applied to public spaces and auditoria—where spaces are tall and plumes above audiences are very strong—with some success (Palonen, Ukkonen, Helenius and Majanen 1990, Mathisen 1989). Displacement ventilation was first applied to office spaces in Scandinavia during the mid 1980s—during which time there was increasing interest in systems which offered improved thermal comfort and indoor air quality—and has now become popular in Germany (Sandberg and Blomqvist 1989). Svensson suggests that such systems account for 25 % of the Scandinavian office system market.

There has been a growing body of research during the past five years—mainly in the Scandinavian countries and Germany—into the characteristics of displacement ventilation air flow in office rooms. Researchers have often studied the air flow from diffusers and the spread of air in the lower part of the room, separately from the characteristics of the plumes etc. in the upper part of the room. This is apparently because the characteristics of the plumes are not affected by the flow pattern of the diffuser, providing the plume is out of the initial discharge zone of the diffuser. The discussion of these flows have been similarly separated below. Nearly all the

research has been on the basis of two-person size offices (approx. 20 $m^2$ floor area) although displacement ventilation is also applied to larger open plan office spaces in practice. Experiments have usually used environmental chambers set up as two-person offices—for example the work of Kegel *et al.* (Kegel and Schulz 1989)—but some work has also been in the field using a selection of sites (Melikov, Langkilde and Derbiszewski 1990, Milkov and Nielson 1989).

## 2.3 Chilled Ceiling Panel Systems

The term 'Static Cooling' has been used to encompass a variety of cooling systems which can provide sensible cooling by a combination of radiant and natural convection effects. Due to the absence of forced convection and air jets with this class of cooling systems they have also been called 'Silent Cooling' systems. Static cooling systems could be subdivided into chilled ceiling panel type systems and chilled beam type systems. The former panel systems have been in use for some time and seek to maximise the radiant cooling effect. Chilled beam systems are a more recent development and rely on the down flow of cooled air induced by convection from finned tube elements. There are a number of variations on these types, but none are entirely radiant or entirely convective in effect.

Chilled beams achieve their cooling effect in the space by inducing line source plumes of cool air to flow downwards from ceiling level. The construction of chilled beams consists typically of a double row finned tube element (similar to the copper tube/aluminium fin construction found in natural convection heaters) in a metal casing with an open top and two discharge slots running along the bottom edges. The beams can either be incorporated into a false ceiling or exposed by suspending them directly from the structure. Where they are incorporated into a false ceiling the bottom of the beam usually must protrude slightly below the ceiling level and there must be a clear path through the ceiling for there to be a circulation of air from the room, through the ceiling void, and down through the chilled beam. Outputs up to 500 $W.m^{-1}$ are possible (200-300 $W.m^{-1}$ is probably more typical) with chilled water temperatures of 14–16°C. Beams are usually arranged in parallel rows in larger spaces and have the advantage over panel systems in requiring less ceiling space. Approximately 85% of the cooling capacity is delivered by natural convection, the rest by radiation from the casing (Laine 1993). A typical chilled beam construction is illustrated in figure 2.2.

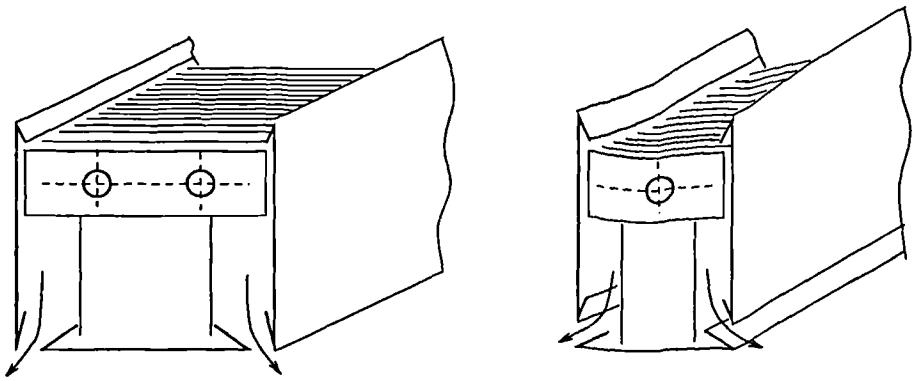


**Figure 2.2:** Typical passive chilled beams.

A variation on the basic chilled beam described above has been developed known as an active chilled beam. In such a chilled beam a supply air duct runs within the beam construction to supply air to a number of swirl outlets along the bottom of the beam. Such a construction eliminates the need for a separate supply air system and can give significantly higher outputs by inducing greater flow of air across the cooling element. Laine (1993) discusses chilled beams of this type and states that heating elements can also be built into such beams—although special low U-value window construction is necessary to avoid down-draughts when heating by this method. Active chilled beams are not included in the present study and will not be discussed further.

Panel type chilled ceiling systems have been developed in a variety of forms and include systems using air as the cooling source as well as hydronic systems. Earlier systems, such as those described by Appleby (1988) and Skåret (1987) employ a ceiling construction of metal planks (extruded aluminium) with copper chilled water pipes clipped to the back. Such planks are arranged in parallel with small gaps left deliberately between each plank to form a false ceiling. The chilled water pipework on adjacent planks is interconnected to form panels, and inactive portions of the ceiling can be created with similar planks but without any pipework attached. The gaps between each plank are left to encourage air flow into the area above the false ceiling and increase the area available for heat transfer—both convectively and by radiant cooling of the structural soffit. Systems are now available that use pressed steel ceiling planks designed to fit closely together and more easily integrate with other types of commercial false ceiling constructions. Such systems do not seek to make use of the upper side of the panel for cooling and incorporate an insulating mat to reduce any heat transfer with the ceiling

void.

Chilled ceiling constructions have also been developed which make use of the thermal mass of structural concrete slab by building rows of plastic chilled water pipework into the surface layer of the slab. The basic technology is very similar to that used for under-floor heating systems that have been in use for many years. Systems with this type of construction have been modeled by Udagawa (1993) and Kilkis (1993) . The main advantage of this type of system is that the structural slab can be used to store energy over a daily cycle and reduce peak loads. A building in Zurich using this type of chilled ceiling is described by Meierhans (1993) where use is made of cool night air to cool water circulated through the chilled ceiling and pre-cool the slab (in the canton of Zurich, day time use of refrigeration compressors is currently forbidden).

One of the disadvantages of earlier chilled ceiling panel systems was their inability to integrate with other types of architectural ceiling. This has partly been overcome by the introduction of metal chilled ceiling panels based on standard ceiling tile sizes, and metal panels that are provided with a metal backing that can receive a finishing plaster layer on-site. A system is also available that uses a mat of small diameter plastic pipes connected into plastic header pipes that can either be laid on the back of a metal ceiling panel with an insulation mat, or can be fixed to a concrete or gypsum board backing and plastered over (Stahl and Keller 1992) (Busweiler 1993). A number of the chilled water based systems described above are illustrated in figure 2.3.

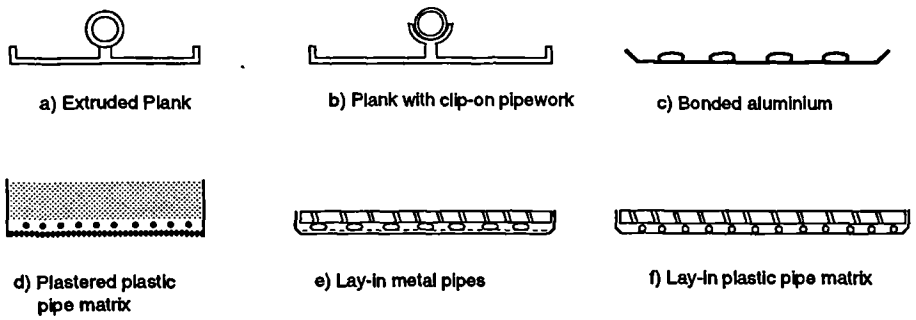


**Figure 2.3:** Some examples of chilled ceiling types.

Cooled air has also been proposed as a cooling medium for chilled ceilings. In the commercial system known as 'Termodeck' a hollow rib type precast concrete slab is used, the hollow passage ways been used to duct the air supply. In this system use is made of the thermal mass of the slab by pre- cooling or pre-heating during

night periods, depending on the season. The air passing through the slab is not recirculated but is also used as the ventilation air during occupied periods and is distributed into each room by a diffuser fixed into an opening in one of the slab airways. Niu (1994) and Niu and van der Kooi (1992, 1993) have studied an air based chilled ceiling system that uses air passages in a metal suspended ceiling connected into a plenum of a supply diffuser. Air based chilled ceiling systems have the advantage of being able to achieve some latent cooling.

A direct limitation on all types of static cooling system using chilled water is the need to avoid condensation at pipework surfaces. This imposes a limitation on the chilled water flow temperature and hence on the panel load capacity. The possibility of condensation is mainly dependent on the pipe surface temperature and the expected humidity level in the room with the greatest risk probably where the flow pipework enters each room. Humidity levels in the room are obviously dependent on supply air conditions, local latent loads and infiltration of outside air. Laine (1993) comments on this problem and states that with a chilled water flow temperature of 14°C the pipe surface is about 16°C, and so condensation was formed at conditions of 70% RH, 23°C in the room.

It is therefore usually necessary to ensure that dehumidification is provided in the ventilation system to control the room humidity under normal design conditions. This requirement imposes an energy consumption overhead—its magnitude dependent mainly on climate. This measure does not however deal with the problem of localised high humidity conditions which may occur for a number of reasons. In the system reported by Appleby (1988) in a building with opening windows, this problem is tackled by provision of two-port cut-off valves in the chilled water circuit to groups of panels and operated via local humidistats at a pre-set humidity level.

Panel type chilled ceilings systems offer the highest proportion of heat absorption by radiant effect of static cooling systems. The high proportion of radiant cooling has implications for both thermal comfort and the dynamic thermal behaviour of the room. All-air cooling systems (including displacement ventilation) are, by definition, unable to directly absorb any radiant loads such as long wave solar radiation and the radiant component of occupant and lighting loads. Such loads in all-air systems will tend to be absorbed by the room fabric and furnishings, causing an eventual rise in their temperature and a release of heat by convection to the room air. This has a dynamic effect on the overall thermal load on such systems, as there is a general lag between absorption of radiation and release by

convection from a surface depending on the thermal mass. This effect can be seen to be beneficial in some circumstances.

Chilled ceiling panel systems, by directly absorbing thermal radiation, will therefore alter the usual dynamic thermal behaviour of the room fabric and system loads—loads with a radiant component will impose an instantaneous load on the cooling system rather than lagging. Any energy simulation program used in the study of such systems must be able to deal with the radiant energy interchange in a sufficiently accurate way to reflect these effects. Chilled ceiling panel systems also therefore tend to give room surface temperatures (and thus mean radiant temperatures) closer to the mean air temperature. All-air cooling systems invariably give mean radiant temperatures a few degrees above the mean air temperature. This effect is clearly shown in the simulation results of Udagawa (1993) and the measurements of Külpmann (1993). They suggest that it is a good approximation to equate the mean air temperature and mean radiant temperature in chilled ceiling systems. If one considers the PMV comfort equation (ISO7730) this implies a higher operating air temperature for an equivalent level of thermal comfort with chilled ceiling panel systems. If advantage is taken of operating at a higher air temperature then the available cooling capacity from the ceiling panels is nominally increased in proportion to the greater temperature difference between the chilled water and the room air. Operating at slightly higher air temperatures will also reduce the effective load on the system from the infiltration of warm outside air into the room.

The overall heat transfer performance of chilled ceiling panels depends on their ability to promote natural convection in addition to acting as a plane radiant collector. In principle the specific heat transfer from a cooled surface by radiation is limited by its emissivity. For a high emissivity surface at typical room temperatures the effective radiant heat transfer coefficient is of the order of $5.7\,\mathrm{W.m^{-2}.K^{-1}}$. Any cooled plane surface exposed to the room air must also transfer heat by natural convection. The heat transfer coefficient for a cool downward facing surface is typically defined by a empirical power law relationships such as—see (Dascalaki, Santamouris, Balaras and Asimokopoulos 1994) for a recent review of such relationships:

$$h_c = 1.52(\Delta T)^{0.33}, \tag{2.1}$$

and

$$h_c = 0.6(\Delta T/d)^{0.2}, \tag{2.2}$$

for cooled surfaces facing upwards. These relationships give values of convective

heat transfer coefficient in the range 1.0–3.0 $W.m^{-2}.K^{-1}$ for the upper side, and 2.0–3.5 $W.m^{-2}.K^{-1}$ for the underside of the panel with temperature difference in the range 2–12°C. This would suggest an overall heat transfer coefficient for a plane chilled ceiling panel of 7.7–9.2 $W.m^{-2}.K^{-1}$ and radiant/convective capacity in the approximate ratio 65/35%. Niu (1994) measured the overall heat transfer coefficient for a chilled water ceiling panel system by using a heat balance on the chilled water so that the overall coefficient $h_o$, could be calculated from the formula

$$h_o = \frac{GC_p\Delta T_W}{A_P(T_R - T_P)}, \tag{2.3}$$

where G is the water mass flow rate, $\Delta T_W$ is the water temperature difference and $T_R$ and $T_P$ are the average room and panel surface temperatures. He found that the value of $h_o$ varied little around 8.0 $W.m^{-2}.K^{-1}$ over an operating temperature difference $T_R - T_P$ of 2–12°C. This demonstrates the constancy of the radiant heat transfer component (since this depends on the fourth power of the absolute temperature this hardly varies for small temperature differences at room temperatures).

Niu also defined an overall heat transfer coefficient $U$ for a chilled water ceiling panel defined by

$$U = \frac{GC_p\Delta T_W}{A_P(T_R - T_W)}, \tag{2.4}$$

where the temperature difference in the denominator is between the average room air temperature and the average chilled water temperature. Using this overall temperature difference takes into account the thermal resistance of the panel itself and the fin effectiveness. He found that the values of $U$ were also of the order of 8.0 $W.m^{-2}.K^{-1}$ over the operating temperature range—indicating a low thermal resistance for the panel type tested. Stahl and Keller (Stahl and Keller 1992) suggest values in the range 9–12 $W.m^{-2}.K^{-1}$ for approximate calculations of capacity.

The thermal resistance of the ceiling panel is a significant factor in system design and varies with the panel construction. Lower resistance means that the panel surface temperature is closer to the mean chilled water temperature. The chilled water temperature may be limited in practice by the need to avoid condensation

problems or the desire to maximise the use of free cooling in the chilled water system. A lower panel thermal resistance will therefore maximise the available cooling capacity. Brunk (1993) states that with a construction consisting of an integrated aluminium water passage and plaster covering it is possible to achieve a temperature drop of only 1.4°C between the water and the panel surface. He also suggests that temperature drops of 4–5°C would be more typical of a construction of metal panels with copper pipes clipped to the rear. Udagawa (1993) and Kilkis (1993) have used the idea of fin effectiveness to express the thermal resistance of panels consisting of pipes built into the structural slab. In this type of construction the thermal resistance seems to be significant and there is a noticeable variation in panel surface temperature between the rows of pipes.

One possible limitation to the cooling capacity of chilled ceiling panel systems is suggested by the sensitivity of occupants to asymmetric thermal radiation—a possible sensation of having a cold head. Comfort limits for asymmetric thermal radiation have been proposed by Fanger *et al.* (Fanger, Ipsen, Langkilde, Olesen and Christensen 1985) for different combinations of hot and cold room surfaces. Using this method the room can be divided into two half spaces and the so- called 'half space radiation temperature' be defined for each, so that the thermal comfort limits are defined with reference to the temperature difference:

$$\begin{aligned} \Delta T_U &= |T_{U1} - T_{U2}|, \\ T_{U1} &= \sum \varphi_i T_i, \qquad (2.5) \\ T_{U2} &= \sum \varphi_j T_j, \end{aligned}$$

(2.6)

where $T_{U1}$ and $T_{U2}$ are the room half space radiation temperatures, and $\varphi_i$ and $\varphi_j$ are the radiation values between a surface element and the surface $i$ or $j$. For a room with a cool ceiling the half space radiant temperature difference was found to be of the order of 14K for 10% dissatisfied persons. Külpmann (Külpmann 1993) carried out a number of tests in rooms with chilled ceiling panels under different load conditions and found the half space radiation temperature difference to be close to 5K. The limits of thermal comfort under asymmetrical thermal radiation would not therefore seem to be a stringent limitation on the chilled ceiling design.

Feustel and Stetiu (1995) have discussed the current state of what they term 'hydronic radiant cooling', and have suggested potential energy savings that could come from the take up of such technology. They suggest that one of the most significant energy savings, compared to conventional all-air systems, could come

from the fact that the primary energy distribution is hydronic. They suggest that the peak electrical energy of a hydronic radiant cooling system may be only 55% of that of a conventional air based system. They assume that displacement ventilation will be used in combination with the radiant cooling system. They also point out the current inability of programs like DOE-2 (1982) to deal with radiant cooling, and the need for performance standards for panel type radiant cooling systems.

## 2.4 Displacement Ventilation Combined With Chilled Ceiling Panels

Static cooling systems have not been developed with particular air distribution systems in mind, but have historically seen application with conventional varieties of mixing air distribution system. The ventilation system in static cooling systems is normally designed primarily on the basis of ventilation requirements with additional cooling capacity provided as a secondary benefit. Attention has more recently been focused on the potential benefits of using static cooling systems with displacement ventilation. The potential advantages of displacement ventilation could be described as:—

- Improved indoor air quality in the breathing zone as a result of the upward transport of contaminants
- Reduced risk of discomfort due to draught as a result of the generally low velocity and turbulence levels in the occupied zone (outside the 'near zone' of the diffuser).
- Higher supply air temperatures allow the greater use of free cooling either by direct use of outside air or indirect evaporative cooling. (Higher supply temperatures are possibly disadvantageous where much dehumidification and reheat is necessary).
- Higher return air temperatures resulting in improved heat recovery efficiencies at air handling plant.

The potential advantages of chilled ceiling panel cooling systems could be described as:—

- Lower infiltration heat gains resulting from the use of higher operating air temperatures for a given comfort level
- Greater advantage can be taken of free cooling as a result of the higher chilled water temperatures and vapour compression refrigeration may be avoided in some circumstances
- Reduced risk of discomfort due to draught can result from the lower air change rates required, as the bulk of the sensible loads can be dealt with by the ceiling panels, rather than the ventilation air.

It can be seen that displacement ventilation and chilled ceilings have a number of features and potential advantages in common. Where combined in a single system the following advantages may result:—

- The acknowledged limited load capacity of displacement ventilation can be extended by use with static cooling (giving total capacities of the order of $80\,W.m^{-2}$).
- The potential improved indoor air quality benefits of displacement ventilation may be realised.
- Improved thermal comfort may result from the lower air velocities and turbulence levels inherent in using displacement ventilation and from reduced vertical temperature gradients.
- Improved energy performance may result from taking advantage of the higher chilled water temperatures of both these systems, by maximising the amount of free cooling, and the possibilities of using alternative central plant designs. This advantage may need to be offset against additional energy required for dehumidification in some circumstances.

There is a current debate as to whether or not chilled beam static cooling systems are suitable for use with displacement ventilation. This centres around the issue of whether the down-flowing line plumes of cool air from the chilled beams are strong enough to disrupt the general up-flow of air from the lower part of the room and therefore induce a degree of mixing of air—thereby decreasing the indoor air quality and changing the temperature distribution. Wyatt using results from CFD modeling, and Dickson (1994) have suggested that the plumes from the beams only interact with the upper air layer in the room. Davis (1994) however, has used the

plume modeling work of Morton *et al.* (Morton, Taylor and Turner 1956), Cooper and Linden (1992) to suggest that the plumes from the chilled beams could impinge on the floor and result in the forming of a number of mixed layers.

There is only a small body of research at the present time reporting experiments with displacement ventilation and chilled ceiling panel type static cooling systems. Only general air flow patterns, temperature and concentration distributions have been studied. It has already been noted that with a displacement ventilation regime a positive air temperature gradient is developed in the room, and there is fairly strong radiation from the warm ceiling down to the floor. Since a chilled ceiling panel is able to both convectively cool the air near the ceiling and radiantly cool the floor, it could be expected that temperature gradients would be reduced in the case of a combination of these systems.

Vertical room temperature distributions for systems of chilled ceiling panels and displacement ventilation are reported by Skåret (1987) , Behne (1993), Krühne (1993) and Külpmann (1993). All the results reported show much reduced temperature gradients, and in some cases only small deviations from the average room temperature. Külpmann carried out a series of tests in a test chamber with different proportions of the load split between the chilled ceiling and the displacement ventilation system and reports the effect on temperature distribution—see figure 2.4. Külpmann's results suggest that with the chilled ceiling meeting all the load, the temperature is virtually constant throughout the height of the room. As the proportion of the load carried by the displacement ventilation system is increased, some positive temperature gradient is developed in the lower part of the room with a near vertical temperature profile in the upper part of the room.

There have been no detailed studies of the air flow in the plumes and surrounding environment in systems combining displacement ventilation and static cooling reported to date, and so it is unclear which flow and heat transfer mechanisms are dominant. Since the room internal loads are of the order 50–70 $W.m^{-2}$ in such systems this implies that the plumes from internal loads are stronger than is usual in displacement ventilation flows and that the 'stationary front' is correspondingly lower (ventilation flow rates would still be of the order 2/3 air changes per hour). This in itself may explain why a temperature gradient appears only near the floor—the rest of the room possibly being a well mixed zone above the stationary front. This would also imply poorer air quality due to the 'stationary front' being lower in the room. However, it may be that the radiant cooling of the room alters the surface temperatures sufficiently to set up quite different convective flows and

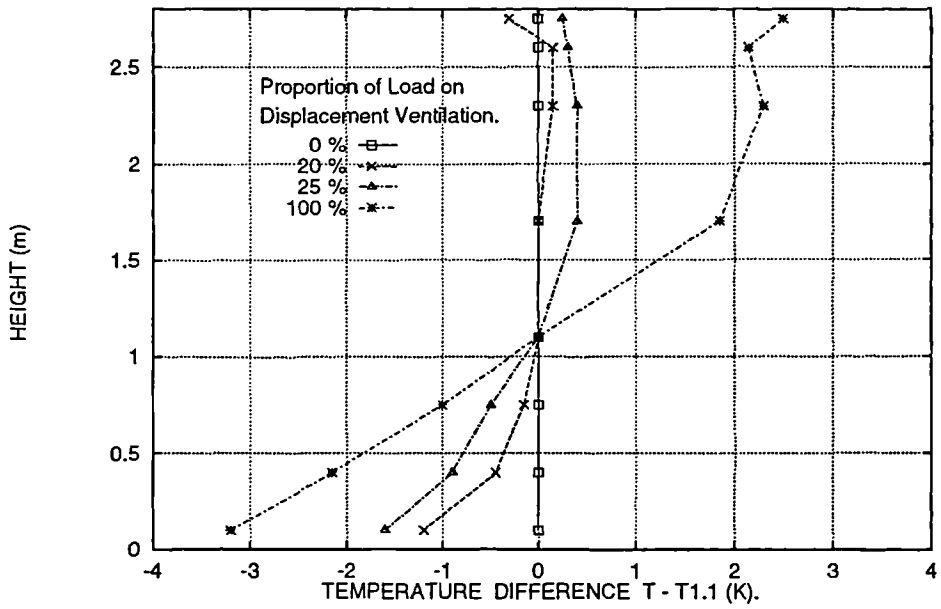


**Figure 2.4:** Temperature profiles in a room with Displacement Ventilation and Chilled Ceiling panels .

heat transfer than usually occur in displacement ventilation. One would expect that from the known behaviour of plumes that where there is no stratification, any rising plumes would be free to impinge directly on the chilled ceiling surface. This may promote both cooling and mixing in the zone near the ceiling and possibly enhance the convective heat transfer from the chilled ceiling.

Behne (1993) and Krühne (1993) have studied the indoor air quality and thermal comfort in test rooms with displacement ventilation and chilled ceiling panel systems. Behne considered the effects on thermal comfort of different positions of the active portion of the chilled ceiling (about 50% of the ceiling area in this case) relative to the internal loads. While the alternative positions did not alter the temperature distributions sufficiently to cause problems with thermal comfort, it is interesting to note that definite recirculatory air flow patterns were observed in each case. Down flowing air currents were observed generally at walls and below the active part of the ceiling — especially when the loads were below the inactive part of the ceiling.

Krühne (1993) has studied indoor air quality resulting from a chilled ceiling panel and displacement ventilation system in a test room of twenty square metres floor area. The main phenomena observed were down- flowing boundary layers along

the walls—the wall temperatures being lower than the air temperature at all levels in this case. This was seen to have an obvious effect on the indoor air quality measured by a tracer gas technique. The degree of mixing was seen to increase with increasing temperature difference between the panel and the average room air temperature. This obviously draws into question the proposed indoor air quality benefits of such a system. It is however, worth noting that the degree of cooling of the room walls by the chilled ceiling (especially near the top of the wall) must be a function of their geometric separation—how closely the active part of the ceiling abuts the wall. The effect of down-flowing air currants from cooled walls could therefore be expected to be worse in the case of a small room with the active part of the ceiling directly adjacent the walls. This effect may not therefore be so obvious in the case of larger open plan spaces where the chilled ceiling may not extend right up to the walls.

Many of these issues are little understood at the present time. Although not directly concerned with the objective of long term energy simulation, it is hoped that some light may be thrown on these issues by the CFD modeling studies in this work.

## 2.5 Flow in the Lower Part of the Room

It has already been noted that the flow from displacement ventilation diffusers shows some fundamental differences from the forced turbulent jets typical of conventional mixing ventilation systems. It is also the flow in the lower part of the room that presents the greatest risks of discomfort due to draught and exposure to low air temperatures. Researchers have addressed themselves to study both the fundamentals of the flow and the parameters that effect comfort conditions. The flow in the lower part of the room is discussed in the literature in terms of a 'near zone' immediately adjacent to the diffuser where the air leaving the diffuser accelerates towards the floor; and a 'far zone' where the air spreads across the floor towards the walls. Office rooms of the typical two-person size can be supplied with air from a single displacement ventilation terminal. The scenarios that have been mostly studied in the literature involve rooms with either a single flat-faced or semi-cylindrical diffuser mounted midway along one side of the room with the bottom of the diffuser at floor level.

Air is typically supplied from displacement ventilation diffusers at between one and

three degrees Celsius below the nominal room temperature and with an initial velocity in the range 0.1 to 0.5 $m.s^{-1}$. This compares with typical velocities of 2.0 to 4.0 $m.s^{-1}$ in mixing type systems using diffusers that produce jets of air. Thus the inertia forces are much lower with flows from displacement ventilation terminals and the buoyancy forces act to ensure the flow is initially down towards the floor. The performance of such jets can usefully be characterised by considering the inlet Archimedes Number of the flow (the ratio of buoyancy to inertia forces):-

$$Ar_i = \frac{g\beta\Delta T_i H}{U_i^2} \tag{2.7}$$

Where,

$U_i$ —the inlet air velocity, $m.s^{-1}$

$\beta$ —volumetric expansion factor ( $= \frac{-1}{\rho}.\frac{\partial \rho}{\partial T}$)

$\Delta T_i$ —temperature difference between room and supply air, °C

$H$ —height of the diffuser, m

$g$ —gravitational acceleration, $m.s^{-2}$.

Thus for mixing systems the Archimedes number would be expected to be less than 0.05, whereas much higher values in the range 0.2–8.0 would be more typical of displacement ventilation systems. The densimetric Froude number is an alternative dimensionless parameter used to describe such flows and is related to Archimedes number, such that $Fr_d = (Ar)^{-1/2}$.

Mathisen (1988, 1990) and describes test room experiments where flat diffusers were used, of various heights and either 'narrow' or full width of the room and constructed with a perforated face and foam covering. Results are presented in terms of the cooling capacity of the various sizes of diffuser with varying supply flow rate. The velocity field in the 'far zone' was also studied. It was observed that the full width supply opening gave a two dimensional flow pattern and the narrow opening a three dimensional pattern more typical of commercial diffusers. It was also interestingly observed that when the flow impinges on the walls it reverses direction and forms a counter-flowing layer immediately above the coolest layer of air near the floor.

The velocity in the two dimensional case was fairly constant across the floor and neither did the layer of cool air near the floor increase in thickness as one would

expect with a wall-jet type flow. The flow from the 'narrow' diffuser showed a fall in velocity with increasing distance from the diffuser. Mathisen suggested that the maximum velocity at a given distance from the diffuser was a function of the square root of the Archimedes Number—for both the two and three dimensional flow pattern— and proposed the following relationship:–

$$\frac{U}{U_i} = k_1 + k_2 Ar_i^{\frac{1}{2}} \tag{2.8}$$

Where,

$U_i$ – the inlet air velocity, $\mathrm{m.s^{-1}}$

$U$ – the maximum air velocity next to the floor, $\mathrm{m.s^{-1}}$

$Ar_i$ – the inlet Archimedes number

$k_1$ and $k_2$ – correlation coefficients

The coefficients $k_1$ and $k_2$ were given by Mathisen for different distances from the diffuser and for particular widths of supply opening. A limited number of results are given for some commercial diffusers which were found to obey a similar relationship.

A series of scale model water and test room experiments have been conducted by Sandberg and Holmberg (1990) to study the fundamental nature of the flow in the 'near' and 'far' zones. Both two and three dimensional cases were studied. In the water experiment, density differences were modeled by introducing brine solution of different concentrations, and the thermal radiation and surface heat flux that are present in full size rooms were absent. The same conclusion as Mathisen was reached regarding the decay of velocity—there was a definite decay with distance in the three dimensional flow but not in the two dimensional case. The flow was studied over a wide range of Archimedes number and it was found that a critical value existed ($Ar_i = 0.16$) where above this figure the flow became *subcritical.* By subcritical it is meant that the jet of fluid is dominated by the buoyancy forces and reduces in thickness, rather than increases. In the three dimensional case the jet thickness reduces to a level where it remains constant in the 'far zone'. The overall conclusion seems to have been that the flow could be best be described as a 'gravity current' rather that any type of wall jet.

Sandberg and Blomqvist (1989) following on from the above work, studied full size rooms with a variety of flat-faced and semi- cylindrical commercial diffusers

(all producing three dimensional flow patterns). They concluded that generally the velocity decayed exponentially with distance from the terminal. The diffuser shape had a significant effect on the initial angle of spread with some flat-faced diffusers giving a much narrower angle of spread and resulting in a 'near zone' extending far into the room. They also point out that the amount of entrainment of air into the 'near zone' through the free shear layer between the supply flow and the rest of the room may also effect the resulting velocities in the lower part of the room.

Field measurements of the flow field in a selection of twelve rooms were studied in (Melikov and Langkilde 1990) and (Melikov et al. 1990). All the rooms were occupied by at least two people and were used either as offices, meeting rooms or computer rooms. Extensive velocity and turbulence intensity measurements were made using a number of omni-directional temperature compensated probes, in order to study the turbulent structure and statistics and the effect of turbulence on comfort. Diffusers were classified as either, 'low induction' or 'high induction' depending on the velocity conditions measured close to the face of the diffusers. The velocity and turbulence intensity varied over the height of the diffuser— more so with the high induction types. From the details of these measurements given in (Melikov and Langkilde 1990) the two types of diffuser could be classified on the basis of:–

— Initial velocities in the range 0.05 to 0.3 $m.s^{-1}$ and turbulence intensity in the range 0–15% for Low Induction diffusers.

— Initial velocities over a wider range 0.1 to 0.6 $m.s^{-1}$ and turbulence intensity in the range 10–25% for High Induction diffusers.

The conclusions of this study were that in rooms with displacement ventilation the maximum mean velocities were measured near the floor between 0.03 and 0.1m. Above 0.3m most of the velocities were below 0.1 $m.s^{-1}$. The mean velocities were less than the lower limit of measurement accuracy of 0.05 $m.s^{-1}$ at 37 % of the test points—this compares with 20 % in related studies with mixing ventilation. Measurements showed that velocities decrease with distance from the outlet and turbulence intensity increased. Their correlations of turbulence intensity with mean velocity show a generally lower level of turbulence intensity than for displacement ventilation (see figure 2.5). Nielsen (Nielsen 1994) has also tried to study the fundamental nature of the flow from displacement ventilation diffusers

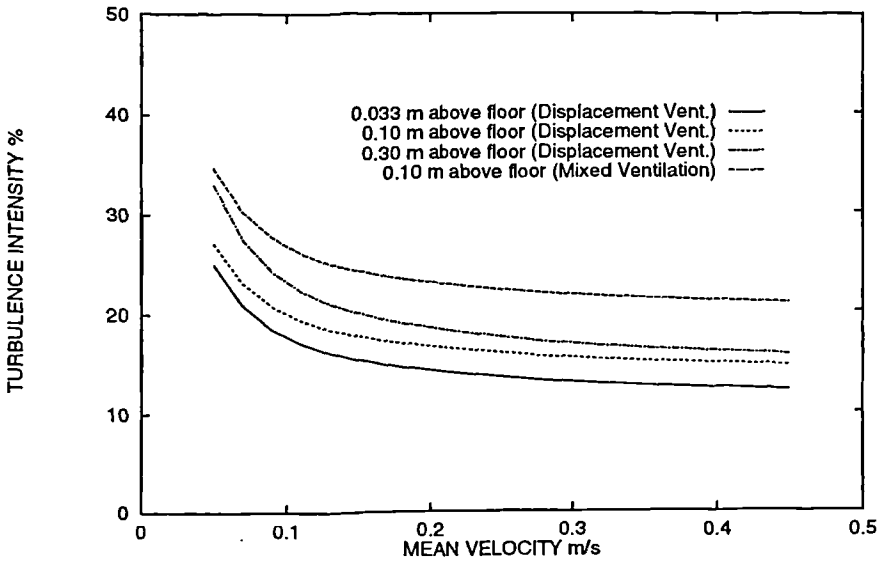


**Figure 2.5:** Turbulence intensity, as a function of mean velocity correlated for different heights in the occupied zone (Melikov et al).

by comparing velocity measurements with the known characteristics of two dimensional and radial wall jets and stratified flow (gravity currents). Neilsen notes that radial wall jets show the characteristic of velocity decaying with distance from the diffuser but differ from displacement ventilation flows in that the length scale of the jet increases with distance due to entrainment of the surrounding air. Jets in stratified surroundings where density differences are more significant show a rapid decay in entrainment past the initial inlet zone as the buoyancy differences tend to damp out any entrainment (Turner 1979). This type of flow is more characteristic of displacement ventilation. Neilsen concludes that in the case of flow from a single diffuser the mean velocity is inversely related to distance from the diffuser but the lengthscale remains constant. He proposes a relationship of the form:–

$$\frac{U_x}{U_i} = K_{dr}\frac{H}{x} \tag{2.9}$$

Where,

$U_i$ – the inlet air velocity, m.s$^{-1}$

$U_x$ – the mean velocity at position $x$, m.s$^{-1}$

$K_{dr}$ – variable coefficient for given diffuser,

$H$ – the height of the diffuser, m

$x$ – distance from diffuser along centre line of flow, m.

Neilsen suggests that these variables are easy to measure and are simple to use as a practical design procedure. The constant $K_{dr}$ varies with inlet Archimedes number and for the example studied was in the range 1.0 to 2.5. $K_{dr}$ will increase with Archimedes number as larger buoyancy forces accelerate the flow from the diffuser into a thinner layer along the floor resulting in larger velocities. This suggests that there is a compromise in diffuser design between the desire to limit the extent of the 'near zone' where temperatures are close to the supply conditions (by having a higher inlet Archimedes number) and the desire to limit velocities in the 'far zone' near the floor.

Of some practical interest is the effect of obstructions in the room at floor level posed by certain types of furniture. Kegel and Schulz (Kegel and Schulz 1989) observed that the effect of desks and bookcases used in their set up of a two person office had the effect of constricting the flow across the floor. Consequently the velocity in the near floor zone was raised significantly and the temperature distribution in the room was also altered in the region beyond the furniture.

## 2.6 Heat and Mass Transfer in Plumes

Displacement ventilation relies primarily on the development of thermal plumes associated with each internal heat load within the room to develop a general upward movement of air and contaminants. It is the characteristics of these plumes that is of greatest interest in understanding the flow mechanisms in the room and thus the characteristic temperature profiles. The study of buoyant plumes has developed firstly from the study of plumes in surroundings of infinite extent where there is no stratification of the surrounding fluid. In a uniform environment the initial buoyancy flux of the plume is conserved. The main assumption in the models of such plumes according to Turner in his book (Turner 1979) is that there is a *similarity* of the velocity and scalar quantity profiles at all heights above the source. The governing parameters for an axisymmetric plume are the initial buoyancy flux $F_o$, the height $z$ and radius $r$, and dimensional analysis leads to the following power law relationships for the vertical velocity $w$, buoyancy $g'$, and

radial extent $b$ :-

$$\begin{aligned} w &= F_o^{\frac{1}{3}} z^{-\frac{1}{3}} f_1\left(\frac{r}{b}\right), \\ g' &= F_o^{\frac{2}{3}} z^{-\frac{5}{3}} f_2\left(\frac{r}{b}\right), \\ b &= \beta z, \end{aligned} \tag{2.10}$$

where $f_1$ and $f_2$ are functions describing the velocity and buoyancy profiles across the plume width, and $\beta$ is a constant to defined for the particular profiles that are used. These profiles are usually taken to be of the 'top hat' type or approximated to be Gaussian. The above equations derived from the similarity assumption indicate that the shape of the plume would be conical above a point source. This has been found to be reasonable some distance away from the source in measured plumes.

In the case of displacement ventilation the behaviour of the plume is modified by the fact that it is both in a confined space and that the surrounding fluid is stratified to some degree. Morton *et al.* (1956) following on from initial work by Sir Geoffrey Taylor were among the first to consider a theoretical model of plumes in a non-uniform environment. In order to develop a solution to the case of a non-uniform environment it is apparently necessary to introduce the *entrainment assumption* rather than the similarity argument mentioned above—the plume can not be similar over its full height in stratified surroundings as it will reach a point of neutral buoyancy where it will spread horizontally. This is discussed by Turner (1986). The entrainment assumption states that the rate of entrainment at the edge of the plume at a given height is proportional to some vertical velocity scale at that height. The entrainment constant $\alpha$ may be defined differently depending on the type of plume and property profiles used. Morton et al develop a model of such plumes based on Gaussian property profiles and a one dimensional version of the conservation equations for a point source. The Gaussian profiles can be expressed in the most general form:

$$\begin{aligned} w(z,r) &= w(z) exp\left(-\frac{r^2}{b^2}\right), \\ g\frac{\rho_0 - \rho}{\rho_1}(z,r) &= g\frac{\rho_0 - \rho}{\rho_1}(z) exp\left(-\frac{r^2}{b^2}\right), \end{aligned} \tag{2.11}$$

where in a stratified fluid $\rho_1$ is the reference density, $\rho_0$ and $\rho$ are the densities

in the ambient fluid and plume respectively at a given height and $w$ is the vertical velocity. With this type of property profile the horizontal scale $b$ for the plume at any particular height is then the distance from the axis of symmetry to points at which the amplitudes are $1/e$ of those on the axis. In this case the entrainment constant $\alpha$ is chosen such that the rate of entrainment of volume at any particular height is $2\pi b\alpha w(x)$. Then, according to Morton et al, the equations representing conservation of volume, momentum and density deficiency when they are integrated over the plume section take the form,

$$\begin{aligned} \frac{d}{dx}(b^2 w) &= 2\alpha b u, \\ \frac{d}{dx}(b^2 w^2) &= 2b^2 g\frac{\rho_0 - \rho}{\rho_1}, \\ \frac{d}{dx}\left(b^2 u g\frac{\rho_0 - \rho}{\rho_1}\right) &= 2b^2 u\frac{g}{\rho_1}\frac{d\rho_0}{dx}. \end{aligned} \tag{2.12}$$

Similar equations are given by Turner (Turner 1979) on the basis of equivalent 'top-hat' profiles.The right hand side of the last equation reflects the dependency of the solution on the density stratification in the surroundings. The most straight forward solution to these equations is when a constant density (temperature) gradient is applied. A solution can be obtained by numerical integration from initial values at a point source. Morton et al give the solution to a non-dimensional form of the above differential equations as shown in figure 2.6. The point of neutral buoyancy is at a non-dimensional height $x_1 = 2.125$ but the plume velocity does not fall to zero until close to $x_1 = 2.8$.

Both the entrainment constant and any constants used in the equations describing the Gaussian property profiles have to be taken from experimental measurements. The values of entrainment constant depend on the type of property profiles used and it is acknowledged that values for plumes are not so accurately known as those for jets. The values determined by Fisher *et al.* (see Turner 1986) for Gaussian profiles are

$$\alpha_{jets} = 0.054, \quad \alpha_{plumes} = 0.083.$$

The entrainment constant can be directly related to the angle of spread so that for jets $db/dx = 2\alpha = 0.107$, and for plumes $db/dx = \frac{6}{5}\alpha = 0.100$. Thus the angle of spread for plumes is only slightly less than for jets, even though the

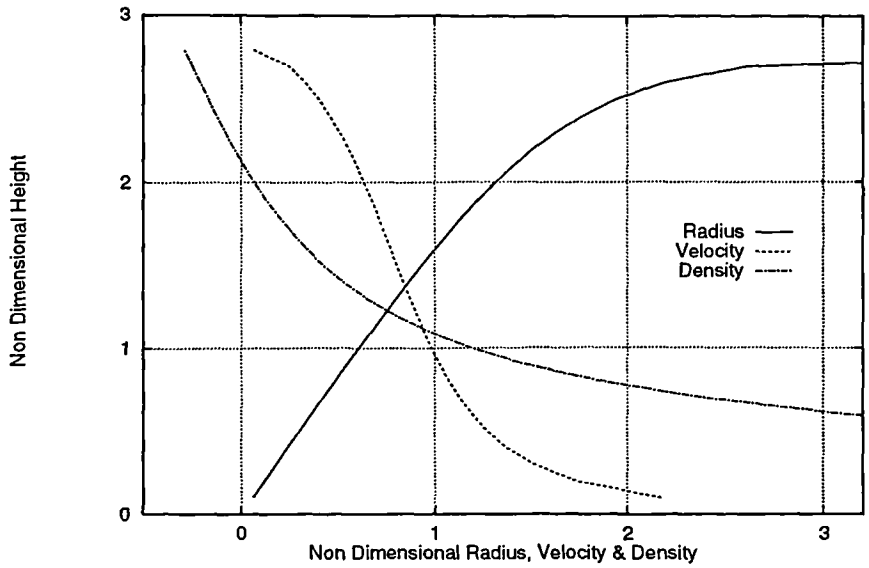


**Figure 2.6:** The variation with height of the plume radius, vertical velocity and density deficiency calculated for a turbulent plume in a uniformly stratified environment (Morton et al).

entrainment constants vary considerably. It has also been noted (Turner 1986) that the entrainment constant does not enter sensitively into many of the calculations.

The basic approach to the study of plumes in stratified surroundings outlined above has been used successfully in the prediction of plume rise height of many geophysical events such as plumes from forest and oil fires and volcanic eruptions. It is interest in geophysical problems and natural ventilation that has apparently spurred the continuation of the work of Morton and Taylor at Cambridge University using experiments conducted with brine solutions introduced into tanks of water to model buoyancy driven flows (so called 'salt bath' experiments) In these experiments density difference is measured throughout the depth of the fluid and would scale with temperature difference such that $(\rho_0 - \rho)/\rho_1 = \beta(T - T_0)$, where $\rho_1$ is the reference density, $\rho_0$ and $\rho$ are the densities in the ambient fluid and plume respectively, with the absolute temperatures $T$ and $T_0$ similarly defined.

Baines and Turner (1969) presented results from brine solution experiments and a theory for the transient and fully developed density profiles produced by a single plumes entering a fully enclosed region of initial constant density (no through-flow of fluid through the enclosure). It was found that the enclosure began to fill from

the bottom with fluid from the plume (the salt bath experiment would represent an inversion of a room model as the brine introduced is of higher density than the surroundings and falls to the bottom of the tank). A front is seen to move through the fluid surrounding the plume until a stable stratification has developed throughout the whole enclosure. This process is indicated in figure 2.7.

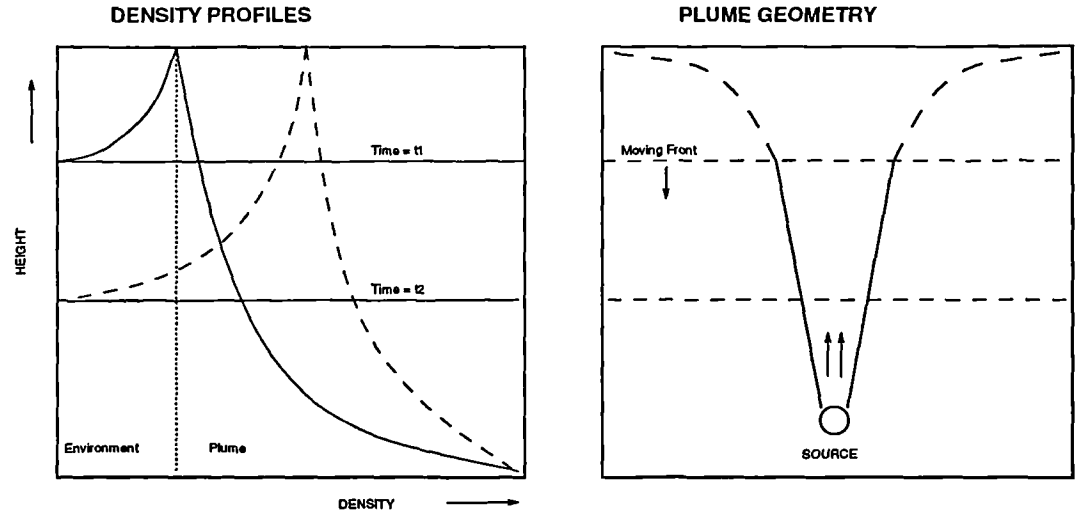


**Figure 2.7:** Development of stable stratification in an enclosure due to a plume from a point heat source shown at two times (Baines & Turner).

The authors developed a mathematical model to predict the time evolution of the front and the final density stratification. The plume fluid motion is complicated by the fact that part of the plume passes through fluid that has previously been convected by the plume itself and whose density has been modified by entrainment of fluid from the surroundings. The authors make use of the 'entrainment assumption' and Gaussian type profiles for the velocity and temperature distributions across the width of the plume. The process of the development of a front in the fluid surrounding the plume is similar to that of displacement ventilation, except that the progress of the front is limited in the latter case by the constant through-flow of supply air into the lower part of the room. It is interesting to note that the application of this theory to ventilation suggested by the authors is one of cooling a room by a line source type plume at high level—an idea not exploited until the introduction of chilled beams nearly two decades later.

More recently Silvana *et al.* (Silvana, Cardoso and Woods 1993) have developed the work of Turner *et al.* described above and describe a similar mechanism where a plume is introduced into an enclosure with an existing stratified fluid. In this

case the plume rises to a height near the point of neutral buoyancy and spreads laterally towards the walls. Where the walls are close enough to the plume axis the horizontal movement of the fluid from the plume can form a growing layer which is well mixed. Two moving fronts are observed; one moving downwards below the plume as before; and one moving more slowly towards the top of the enclosure. The final result is the de-stratification of the fluid: a mixed state of nearly constant density is achieved. The authors conclude that the degree of mixing above the plume is mainly dependent on the kinetic energy of the plume and the efficiency of this mixing process is strongly dependent on the turbulence levels at the upper interface.

In the case of displacement ventilation with a single concentrated heat source it is clear to see that the plume will impinge on the ceiling and form a descending front in the manner described by Baines and Turner. Skåret (1987) suggested that most of the plumes in rooms with displacement ventilation reach their neutral buoyancy height and spread laterally. It is not clear therefore which of these phenomena will predominate as the existence of a neutral buoyancy height for a given plume is dependent on the overall stratification and temperature difference over the height of the room. The overall temperature difference is not determined by the properties of the plume but is dependent on the overall heat balance in the room. The heat balance is affected by heat transfer through the walls as well as the radiant interchange, not just the heat sources that have plumes.

Linden and Cooper (Linden, Lane-Serff and Smeed 1990, Cooper and Linden 1992) have used similar theoretical and experimental methods to those of Turner et al to study the flow mechanisms of natural ventilation. Linden *et al.* (1990) have noted that a displacement ventilation mode can exist in naturally ventilated spaces where there are low level openings for cool ambient air to enter and heat loads are dominated by plume generating sources. Linden et al suggest that in these cases a front descends from the roof of the enclosure in a similar manner to that described by Baines and Turner (1969) except that the front reaches a stable height were the flow in the plume at the front/plume interface is equal to the flow through the room openings—as in mechanical displacement ventilation. In the case of natural ventilation the flow is driven by the buoyancy differences between the room and the ambient conditions outside and is dependent on the properties of the openings.

The authors present a theoretical model for the prediction of the interface height. Of particular interest is their conclusion that the fluid above and below the stationary front (outside the plume) is well mixed so that there is a simple step in

density at the front. Whilst this conclusion is consistent with their result from 'salt bath' experiments, the temperature profiles in full size rooms with displacement ventilation are much closer to a linear variation. Cooper (1992) uses a similar approach to develop a theoretical model for the prediction of interface heights where there is more than one plume and of different strengths. He similarly concludes that further well mixed layers will be formed above a stationary front with plumes from stronger sources passing through the layers deposited by the weaker plumes - the density profile will therefore show several steps.

The apparent discrepancy between the density/temperature profiles suggested by the theory and measurements of Cooper and Linden and the more linear variations measured in full size rooms may be for a number of reasons. Firstly, in full size rooms there may be other buoyant sources in the room such as boundary layers flowing up or down the walls which disturb the environment around the plume. Secondly, in realistic simulations of office rooms there are a number of heat sources of different size and elevation producing plumes of different strengths. Cooper suggested such plumes of different strengths would produce several layers of stratified fluid above the stationary front. This may in fact be happening but with some blurring of the steps in density due to some turbulent mixing at the interfaces. In the simplified theories of plume models no account is taken of general turbulence in the environment surrounding the plume, and in the experiments the fluid was at rest before the introduction of the plume. In full size rooms the environment must be generally more turbulent—and thus there will be greater diffusion of heat—as the supply air diffuser is a source of turbulence, along with convection currents at the floor.

A number of authors have studied the flow in plumes above various heat sources in full size rooms and sought to apply the type of models proposed by Morton (Morton et al. 1956). Meirzwinski (1992) discusses the work of several authors and compares some of the values of measured constants. Meirzwinski and other authors with a building services interest have expressed the plume profiles explicitly in terms of mean vertical velocities and temperature differences so that the Gaussian profiles are,

$$\begin{aligned} \overline{w}/\overline{w_m} &= exp(-m\left(\frac{r^2}{z^2}\right)), \\ \overline{\Delta t}/\overline{\Delta t_m} &= exp(-p\left(\frac{r^2}{z^2}\right)), \end{aligned} \tag{2.13}$$

where $m$ and $p$ are the constants defining the profile widths such that the radial widths of the velocity and temperature profiles are given by, $R_w = m^{-0.5}z$ and $R_t = p^{-0.5}z$ respectively. The constant $m$ is directly related to the entrainment coefficient such that $\alpha = \frac{5}{6}m^{-0.5}$. Meirzwinski reports that measurements of these constants by a number of authors—see also (Kofoed and Nielson 1990)—have varied widely such that $m$ has been reported as being between 55 and 96, and $p$ between 59 and 71. There is general difficulty in measuring plume property profiles due to the wandering of the plume axis with time. Turner also comments on the uncertainty of these constants, stating that their values are dependent on the axial turbulent fluxes which are stronger in plumes than jets and difficult to measure accurately.

An 'improved integral method' for plume calculations has been proposed by Popiolek and Meirzwinski (Popiolek and Meirzwinksi 1984, Popiolek 1987), in which the differential equation for buoyancy is replaced by a form of the energy equation along with a second closing equation describing the changeability of the ratio of profile widths $\lambda$ ($\lambda$ is defined as $R_t/T_w = (m/p)^{0.5}$). This second equation includes a term for turbulent diffusion of heat. Thus the profiles change in a more complex way in their model.

Meirzwinksi identifies three flow zones for plumes in either stratified or uniform environments. This is illustrated in fig 2.8. For a plume in a uniform environment these could be described as:—

A) Boundary layer flow around the heat source. Flow changes from laminar to turbulent and boundary layers join to form plume.

B) The mean motion of the plume starts to become self-similar and axisymmetric, but the spread of the plume is non-linear.

C) Complete self-similarity of the flow. Fully developed turbulent flow exists and the plume spreads linearly.

For a plume in a stratified environment the characteristic zones could be described as:—

A) Boundary layer flow around the heat source as before. Flow changes from laminar to turbulent and boundary layers join to form plume.

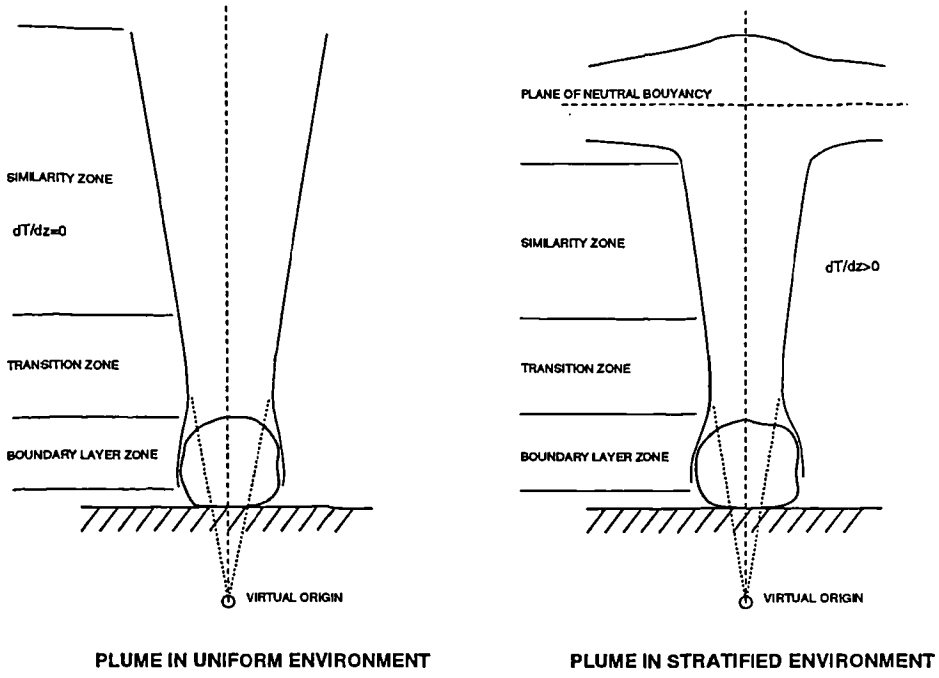


Figure 2.8: Characteristics of Plumes in Uniform and stratified environments.

B) The mean motion of the plume starts to become self-similar and axisymmetric, but the spread of the plume is significantly affected by the stratification.

C) Density equilibrium zone. The plume reaches a height of neutral buoyancy and begins to spread laterally.

The point-source plume models discussed above apply strictly only to the self similar part of the plume. Thus it is strictly necessary to know the position of the start of the self-similar region and to establish a virtual source origin in order to apply these models. In the case of geophysical flows this is not a limitation as the initial transition zone is relatively small in scale. However in ventilation flows the size of the heat source is large relative to the height of the enclosure (especially in office size rooms). A few authors have measured flow in plumes from large scale heat sources (typically light bulbs in black cylinders and boxes) or thermal manakins (Popiolek and Meirzwinksi 1983, Fitzner 1989, Mundt 1990). Meirzwinksi and Popiolek in (Popiolek and Meirzwinksi 1983) concluded from such measurements that the self-similar zone is not reached until 0.5–0.7m above the head.

In the case of displacement ventilation in office rooms (typically 2.7m floor–ceiling

height in British speculative offices) this would imply that the interface of the plume from a person and the 'stationary front' would be below the level where the similarity region of the plume would otherwise exist. Skistad (1994), Skåret (1987) and a number of diffuser manufacturers have suggested using similar models of plumes from point and line sources to calculate the flow rates in plumes—and thus the position of the stationary front—for design purposes. This can not be easy during the design stage, as one does not readily know the temperatures of the heat loads in rooms, nor where the virtual origin of the plume should be assumed. It would also seem therefore, that this approach could only reasonably be used in taller spaces where the plumes reach heights where self-similarity exists and the plume models described above could be applied. In modeling of the flow in rooms with displacement ventilation in office rooms it may therefore be more realistic to use experimental measurements of flow above bodies and equipment such as those of Fitzner (1989) or those of Sandberg and Lindstrom (1990) where the height of the stationary front was directly measured.

It can also be concluded that the effect of an increased temperature gradient in a room, as generally exists in the case of displacement ventilation, has the effect of reducing the flow in the plume over a person. This has been confirmed by Mundt (Mundt 1990) who has measured plumes in test rooms under different stratification conditions. This may have implications for the thermal comfort of occupants as strong temperature gradients are not naturally occurring. It is worth noting that even under stratified conditions the magnitude of the flows over occupants is of the same order and slightly larger (20–50 l/s above the head) than the fresh air rates suggested by most ventilation standards (8–12 l/s per person).

## 2.7 Numerical Modeling of Room Air Flow

The class of numerical modeling techniques known as Computational Fluid Dynamics (CFD) is seeing increasing application in the field of Building Services Engineering. Codes using either finite element (Baker 1983), or the more commonly used finite volume method (Patankar 1980), have now been specifically developed with room airflow applications in mind. Such codes are generally able to deal with prediction of the turbulent, non- isothermal, buoyant air flows found in mechanically ventilated rooms, and are able to model complex geometries. The general development of these numerical methods and their application to room airflows is described by Whittle and Jones (1992) .

The use of this type of numerical technique within this project is seen as having two functions. Firstly, CFD models of individual rooms can provide detailed information concerning air velocities and temperatures for particular boundary conditions. Conducting a CFD analysis of the experimental set-ups used for reference data in this project (with the same boundary conditions) should give a better understanding of the flow and heat transfer conditions. Secondly, provided the level of accuracy of such analysis can be shown to be acceptable, CFD analysis could be used to derive further sets of test data for the thermal models by simulating conditions in the test rooms under a wider range of boundary conditions.

There are a number of published CFD studies of rooms with displacement ventilation, for example, that of Jacobsen and Nielsen (1993), that of Kegel and Shulz (1993), of Davidson and Olssen (1989) , of Niu (1994) and that of Li, Fuchs and Sandberg (1993a). A number of difficulties have been reported in these studies both with modeling of the plumes and conditions at wall surfaces. In the study of Li, Fuchs and Sandberg, the main deficiency in the model was the accuracy of the turbulent flow in the plume. Using the $k$–$\epsilon$ turbulence model the authors found that the axial velocity and turbulent kinetic energy levels predicted in the plume were much higher than measured in the experiment. This resulted in a general over prediction of the amount of mixing in the upper part of the room and some inaccuracy in the vertical temperature gradients predicted. This may be in part due to the deficiency in eddy-viscosity turbulence models to accurately predict the counter-gradient turbulent diffusion found in buoyant plumes—this has been studied by Bergstrom *et al.* (Bergstrom, Stubley and Strong 1993) who found more success with an algebraic stress model.

In order to solve the elliptic non-linear differential equations that describe the velocity and temperature fields in room ventilation flows it is necessary to specify the temperature boundary conditions on all the room surfaces. This requirement can introduce considerable variability between similar CFD studies, as this information is not always accurately known in advance, and can be specified in the CFD model in a number of ways. A second source of variability in modeling wall heat transfer is the treatment of the turbulent boundary layers at wall surfaces, which again can be treated in a number of ways. Both these sources of variability and inaccuracy will have to be minimised in order to develop a useful CFD model of rooms with displacement ventilation and chilled ceilings.

Where eddy-viscosity models of turbulence are used in the CFD simulation, it is conventional to use 'wall functions' to describe the velocity and temperature

gradients between the wall surface and the first nodes of the computational mesh. This alleviates the need to introduce closely spaced grid nodes near the walls to model the steep velocity and temperature gradients in the boundary layers. The wall functions in general use have been developed from empirical studies of forced convection boundary layers. Standard $k$–$\varepsilon$ turbulence models generally use a logarithmic function to describe the velocity profile in the turbulent part of the boundary layer.

A number of variations of wall functions are in use which have different requirements in terms of the recommended distance to the first grid nodes. Renz and Terhaag (Renz and Terhaag 1990) found there was little difference between the velocity fields predicted by these different wall function formulations where the ventilation was by an air jet. Niu (Niu 1994) used a low-Reynolds number $k$–$\epsilon$ turbulence model with wall functions that used a linear function to describe the velocity profiles. He found that it was necessary to fine-tune the position of the first grid nodes, so that they were positioned in the boundary layer at a nondimensional distance of $y^+ = 9.2$, in order to give the best prediction of convective heat transfer. According to Yuan et al (Yuan, Moser and Suter 1993) the difficulty in accurately predicting wall heat transfer with wall functions arises from the fact that the velocity profiles in the boundary layer, and just outside the boundary layer, are somewhat different in the case of natural, as opposed to forced convection. Yuan et al (Yuan 1995)have recently developed a set of alternative wall functions for the case of natural convection from vertical surfaces which have given some promising results.

There are some more recent papers that have dealt with the numerical prediction of the growth of plumes in displacement ventilation. Earlier studies have all used standard formulations of the $k$–$\varepsilon$ turbulence model (Launder and Spalding 1974) which is known to slightly over-predict the spreading rate of axisymmetric plumes. Schaelin (1994) has used the standard form of $k$–$\varepsilon$ turbulence model and made comparisons with experimental measurements of plumes made in a large test chamber (4 m high). He reports good agreement with experimental values. This appears true except near the very start of the plume and approaching the ceiling.

Shankar *et al.* (Shankar, Davidson and Olsson 1994) have made comparisons between different variations of turbulence model and previous experimental data for axisymmetric and plane plumes. To deal with plane plumes they suggest making a modification to the buoyancy production term $G_B$ of the turbulent kinetic

energy equation using the generalised gradient diffusion hypothesis of Daly and Harlow to include a streamwise and cross stream temperature gradient term in $G_B$. They show that this acts to increase the spreading rate for plane plumes. Shankar *et al.* also propose the use of a Normal Stress Amplification approach to the formulation of the $P_k$ term, after Hanjalic and Launder. They show that this tends to decrease the spreading rate for axisymmetric plumes and improve the predictions.

Chen and Chao (1996) have made comparisons between calculations of plumes in displacement ventilation with difference turbulence models, namely, $k$–$\varepsilon$, RNG $k$–$\varepsilon$, and Reynolds Stress models. They report that the most accurate results were obtained with the Reynolds stress model but at computational expense. They also reported that the RNG form of the $k$–$\varepsilon$ turbulence model gave improved results, in terms of plume spreading rate, over that of the standard form.

Specifying room thermal boundary conditions for ventilation flows of the mixing type is commonly done by reference to a separate thermal model or simple hand calculation methods. In rooms with mixing ventilation room surface temperatures differ little (except for window surfaces) and it is usually the velocity field that is of most interest in such simulations, rather than an accurate prediction of heat transfer. In the case of rooms with displacement ventilation the situation is more complex. This is principally because of the stronger radiant heat transfer between the ceiling and floor, and because of the existence of temperature gradients along the walls giving rise to heat flows into and out of each wall. This has been acknowledged by Jacobsen and Nielsen (1993) who used a separate discrete radiant transfer algorithm, and Li, Fuchs and Sandberg (Li, Fuchs and Sandberg 1993a) who used a view factor radiant transfer algorithm within the CFD algorithm, to calculate the effect of the radiant heat transfer in the room.

It is usual to specify thermal boundary conditions at surfaces in a CFD model by either using a constant temperature boundary condition, a constant heat flux, or a mixed condition, i.e. a wall temperature and a heat transfer coefficient. None of these methods is very satisfactory for the case of displacement ventilation, where heat can flow into and out of the same wall, and the flow field is strongly linked to the wall temperature conditions. A more accurate model of heat transfer through the wall surfaces can be modeled by including the solid material of the walls in the numerical analysis, as was done by Li in (Li et al. 1993a). This enables boundary conditions to be applied at the outside of the walls, rather than the inside surfaces, and allows calculation of the heat flow through the wall and

development of temperature gradients to be integrated with calculation of the air flow field.

## 2.8 Nodal Models

Various types of what have become called 'zonal models' have been developed for rooms with convective heat emitters. Allard and Inard have reviewed the development of such models in (Allard and Inard 1992). Lebrun (Lebrun 1970, Lebrun and Ngendakumana 1987) was amongst the first to identify that there was a systematic difference in heat transfer between results predicted by isothermal models of such systems (i.e. with a single air node) and experimental results. Lebrun suggested splitting the room into zones connected by mass conductances to model convection from one part of the room to another. A number of authors have developed this idea, notably Howarth (Howarth 1983) who used a two zone model, and Inard (Inard and Buty 1991) who has used a five zone model and a twelve zone dynamic model of rooms with radiator type heat emitters.

Such models are semi-empirical in that they rely on empirically derived constants in their formulation. It is also true to say that simplified models such as these can only be expected to represent each physical situation when there is a clearly defined air flow pattern—such as the circulation driven by the plume from a radiator. The performance of the heating models discussed by Allard and Inard has recently been compared favorably with the results of CFD simulations in the context of IEA annex 20. Dalicieux (Dalicieux and Bouia 1993) has recently developed a more general model for heating applications by introducing pressure as a state variable and solving the energy and mass balance equations for the order of twenty cells representing the room. Similar approaches have been used to model the macroscopic movement of air within large spaces such as atria (Togari, Arai and Miura 1993, Arai, Togari and Miura 1994).

A further class of models can be identified as 'grey box models', such as those developed by De Moor and Berckmans (1992) for predictive control purposes. In this modeling technique a combination of features described by physical law relationships and mathematical 'black box' methods like neural networks are used. Such models are developed by fitting or training the model using empirical or CFD data. Similarly, a 'black box' modeling method can be conceived, where their is no reliance on prescribed physical law relationships but the model is trained on

experimental or simulation data alone.

A nodal modeling approach has been applied to displacement ventilation by Li, Fuchs and Sandberg who firstly studied the effects of radiant heat transfer in a test cell with black and aluminium coatings on the room surfaces (Li, Sandberg and Fuchs 1993b). The experimental data derived in this study was then used in the development of a number of nodal models (Li, Sandberg and Fuchs 1993c), and also in a CFD/radiant exchange model (Li et al. 1993a). Their experimental arrangement is shown in figure 2.9. The first study highlighted the strong effects of the radiant interchange between the ceiling and floor on both the air flow and temperature profiles in the room. This is illustrated in figure 2.10. Li has kindly made this data available to this project for the purpose of developing a nodal model of displacement ventilation and static cooling.

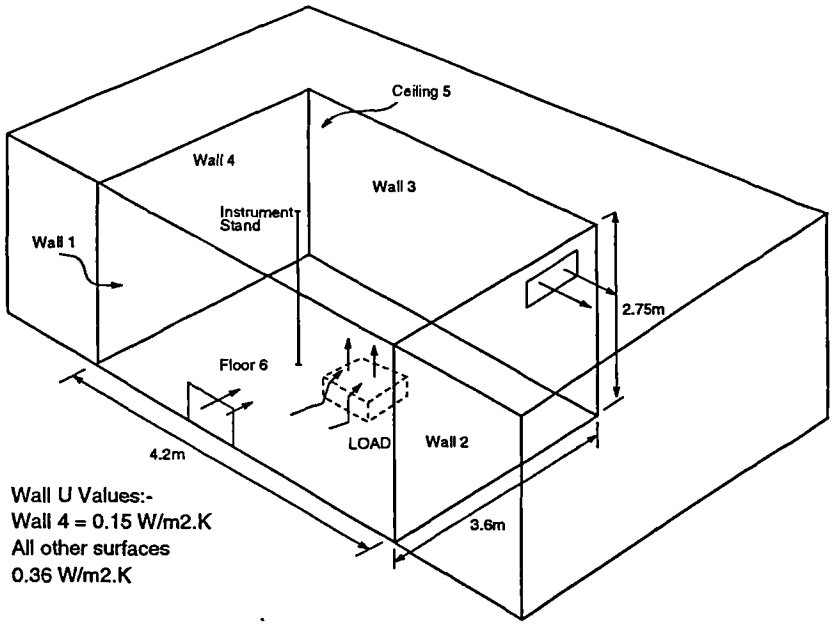


**Figure 2.9:** The experimental arrangement used by Li et al in their study of displacement ventilation.

Li *et al.* (1993c) have developed a number of nodal models of different complexity which are designed to predict the room surface temperatures and air temperatures near the floor, ceiling and at the extract condition. The simplest model they conceive is called a three node model, in which the extract temperature is assumed to be the same as the temperature immediately adjacent the ceiling (probably a reasonable assumption where the extract grille is actually in the ceiling). A more useful model which they call a four node model, defines the extract temperature separately. This gave a better fit to the experimental data which was for the case

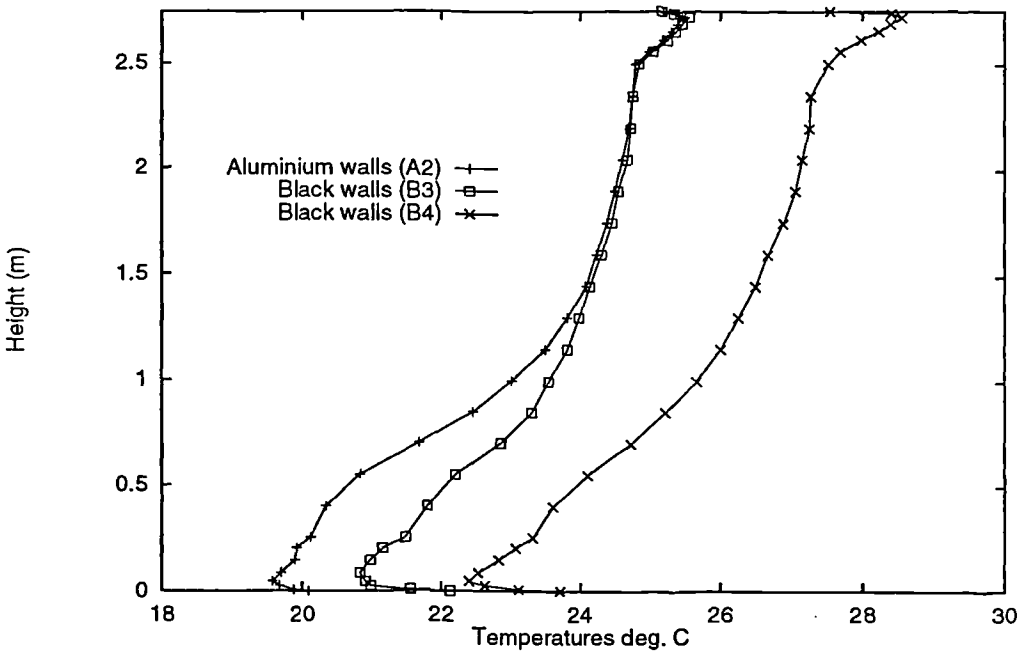


**Figure 2.10:** Room vertical temperature profiles measured by Li et al with different wall coatings.

of a side-wall extract position. Their models used an analytical approach to define algebraic equations for both the radiant and convective heat transfer between each node. Air flow was not explicitly modeled.

In Li et al's four node model (see figure 2.11) it is first of all assumed that the temperature difference between the supply and extract temperature is a function of the overall thermal load on the room air. They secondly assume that all the heat radiated from the ceiling to the floor is convected at the floor to raise the air temperature above the floor above the supply air temperature. Similarly it is assumed that convection at the ceiling is in balance with radiation from the ceiling. This is defined by the following four equations defining the state of the model:–

$$E = \rho C_p q_v (T_e - T_s) \tag{2.14}$$

$$\alpha_r A(T_c - T_f) = \alpha_f A(T_f - T_f^a) \tag{2.15}$$

$$\rho C_p q_v (T_f^a - T_s) = \alpha_f A(T_f - T_f^a) \tag{2.16}$$

$$\alpha_c A(T_c^a - T_c) = \alpha_f A(T_c - T_f) \tag{2.17}$$

where, $\alpha_f$ and $\alpha_c$ are the convective heat transfer coefficients at the floor and

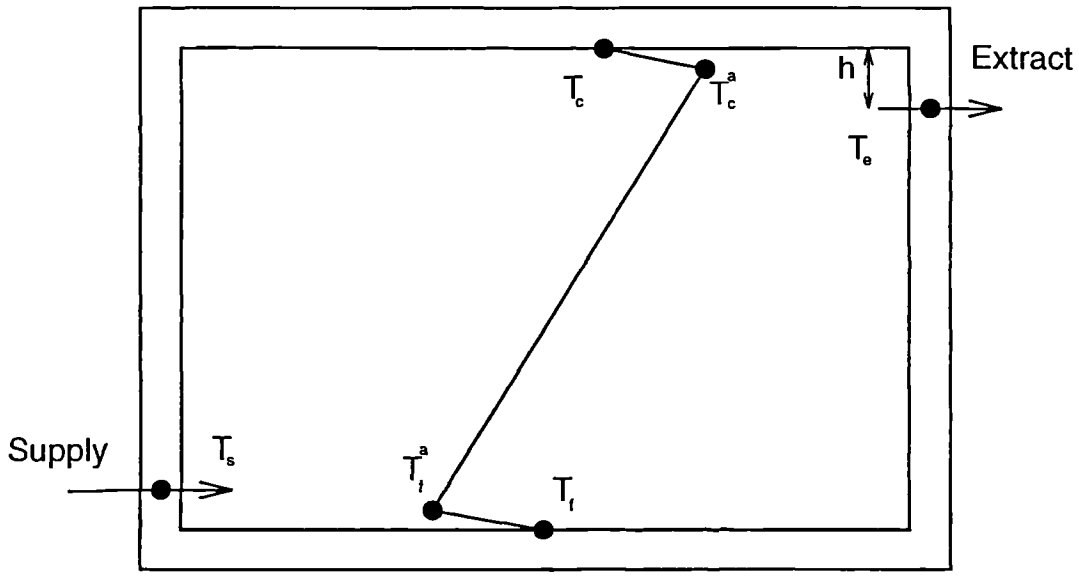


**Figure 2.11:** The general arrangement of nodes in Li et al's four node model of Displacement Ventilation.

ceiling, and $\alpha_r$ is the equivalent radiative heat transfer coefficient between the ceiling and floor based on some assumed temperature difference. $q_v$ is the air volume flow rate, and $A$ is the area of the floor/ceiling. In the four node model the extract temperature is related to the temperature near the ceiling by assuming a constant temperature gradient $s$, so that

$$T_c^a = T_e + sh \tag{2.18}$$

where $h$ is the distance of the extract below the ceiling. The authors define the relative temperature ratio $\lambda$ as the ratio of the temperature near the floor to the overall temperature difference. $\lambda$ can be calculated following manipulation of the above equations and is found to be a function mainly of the heat transfer coefficients for a particular case, thus

$$\lambda \equiv \frac{T_f^a - T_s}{T_e - T_s} = \left[\frac{q_v \rho C_p}{A}\left(\frac{1}{\alpha_f} + \frac{1}{\alpha_c} + \frac{1}{\alpha_r}\right) + 1\right]^{-1} \tag{2.19}$$

and the mean vertical temperature gradient can then be found from

$$s = (1-\lambda)\frac{E}{\rho C_p q_v H} \tag{2.20}$$

where $H$ is the height of the room. Once $\lambda$ and $s$ have been found, the temperatures of the nodes can be found using the four equations of state. Li et al report that the values of $\lambda$ calculated by this model agree fairly well with other experimental results. Thus the model at least gives reasonable estimates of $\lambda$ for

basic design calculations, rather the general value of 0.4 suggested by Jackman (Jackman 1991, Jackman 1990). This model would only be useful in cases where the wall heat transfer is not significant as there are no wall nodes in the model. One issue raised by Li *et al.* in connection with this and similar models is that of convective heat transfer coefficient values. They found that values in the range 5–7 $W.m^{-2}.K^{-1}$ gave best results, whereas Mundt (Mundt 1990) found values in the range 3–5 $W.m^{-2}.K^{-1}$ gave best agreement with experimental results.

Li et al have described how the four node model can be modified to include conduction through the room fabric at the floor and ceiling. At least six nodes are necessary to include heat transfer at the lower and upper sections of the wall. They develop a more general multi-node wall model where each wall is split horizontally into several sections. In the example given in (Li et al. 1993c) the walls are split into eight sections. Splitting the wall into sections requires a more detailed treatment of the radiative heat transfer. They use an absorption factor and shape factor method described in (Li and Fuchs 1991) to calculate the radiative heat transfer in this multi-node model, but assume that the vertical temperature gradient along the wall is constant, and only use two air nodes, as before. This method is able to give reasonable temperatures for cases with heat transfer at the walls, but is not very computationally efficient—reportedly taking 30 seconds on a mid-range IBM workstation.

Mundt (1996) has also developed a nodal model using Li's four node model as a starting point. The model has been extended simply by considering the radiant portions of the load transferred to the floor and ceiling separately. Conduction is also taken into account by assuming the surface temperatures of the walls can be taken to be the average of the floor and ceiling.

Koschenz (1993) has developed a nodal model of displacement ventilation that has been extended to include chilled ceiling panels. The model has the room divided into two parts, the lower of which is from the floor to the interface height. An analytical model of a boundary layer around a cylindrical shaped load is used to calculate the starting plume flow and it is assumed that above the interface height the room air is effectively fully mixed. The model has four air nodes including the supply node. The model has been developed firstly to run within the TRNSYS program (Klein, Beckman and Duffie 1976) and also DOE-2. Within DOE-2 two 'zones' on top of each other have to be defined with a transparent shared surface. There is some difficulty in dealing with radiant heat transfer in this arrangement and reference has to be made to a function derived from previous calculations of

the radiant heat transfer made with TRNSYS. There is little comparison with experimental data except for the predictions of near floor air temperature which follow experimental trends.

A simplified 'zonal model' of displacement ventilation has also been proposed by Manzoni *et al.* (1996, 1997). In this model the room is divided into three horizontal zones. Analytical models of a plume and wall boundary layers are used to calculate the mass balances in each zone. A plume passes from the lower to the upper zone in the model and wall currents pass either to or from the middle zone depending on the temperature differences between the walls and the adjacent air. The plume and boundary layer equations are integrated to find the mass balance in each zone and the height of the interface between each zone. The model essentially predicts step changes in room air temperature. The authors claim good agreement with experimental results but this is not apparent from the comparisons they present.

Hensen and Huygen (1996) have developed a model of displacement ventilation which has four horizontal layers. This model has been developed within the ESP(r) code which has been adapted to deal with the radiant transfer between zones. The air flows between each of the zones in series, from the lowest to the highest, so that there are four room air nodes. They give some dynamic test results which are compared to those of a test chamber experiment. The results are reasonably good. Unfortunately, they do not give any information about how the internal loads and convective heat transfer are dealt with.

## 2.9 Conclusions

The conclusions of the review of the literature can be summarised as follows.

1. The heat transfer and fluid dynamics characteristics of displacement ventilation have been investigated experimentally by a significant number of authors, working both with test chamber experiments and in the field. The flow from the commoner types of wall mounted diffusers is well understood, although it is difficult to make comparisons between results due to dependency on small details of diffuser construction. Flow in plumes in rooms with displacement ventilation has also been investigated by a variety of workers. The theoretical study of plume behaviour is well developed. There remains,

however, a significant range in the reported values of the empirical constants associated with the theoretical models.

2. Although the growth in the application of chilled ceiling systems has been significant in recent years there is comparatively little theoretical or detailed experimental work reported. There is a wide variety of commercial systems and it is acknowledged in the literature that establishment of performance standards has been lacking. Although it is acknowledged in much of the literature that displacement ventilation is very suitable for use with chilled ceiling systems there has been very little work concerning their performance or interaction when used together.

3. Displacement ventilation has been modeled by a number of workers using computational fluid dynamics methods. The numerical methods used have been based on finite volume methods and most commonly using a eddy viscosity turbulence model. There have been a number of approaches to the problem of radiant coupling in these flows. This has ranged from ignoring this effect, dealing with it implicitly, or by explicitly coupling of the flow solver to a radiant exchange solver. Dealing with this type of flow has been demonstrated to be within the capabilities of currently accepted methods. The areas of weakness of the methods used, have been in the prediction of the spreading rate of the plumes, and in the accurate prediction of convective heat fluxes. There have been no specific numerical studies of displacement ventilation used in combination with chilled ceilings.

4. There are a variety of zonal modeling approaches discussed in the literature and which have been applied to a number of systems where intra-zone air flow has been important. A number of attempts have been made to construct nodal models of displacement ventilation. These have varied most notably in there ability to deal with the conducted fluxes. Although the extension of this type of model to deal with chilled ceilings is, in concept, straight forward, no attempt has been made to study the ability of such models to deal with displacement ventilation and chilled ceiling systems.

Although there has been much comment on the energy saving potential of displacement ventilation and chilled ceiling systems there has been little progress towards demonstrating this, either in the field, or by simulation. It is acknowledged that the current generation of annual energy simulation codes are not able to deal with the heat transfer characteristics of displacement ventilation and chilled

ceiling systems. Until computationally efficient models that are able to deal with the particular characteristics of displacement ventilation are developed there can be little progress towards annual energy simulation of these systems. If in the progress of developing such a model, experimental data is collected, and numerical studies made, this should also contribute usefully to the current knowledge and understanding of these systems.

# Chapter 3

# Experimental Method

## 3.1 Introduction

The methodology used to make experimental measurements, the experimental apparatus, design and measurement systems are discussed in this chapter. Calibration and testing of the measurement systems is discussed here and in Appendix A. Experiments have been conducted with two primary purposes in mind:

- to gain understanding of the thermal performance of the displacement ventilation and chilled ceiling system under a range of operating conditions
- to provide data that can be used to determine the structure and parameters of a simplified nodal model

Data gathered for the latter purpose can also be used to provide boundary conditions for, and checking the results of, numerical calculations of room heat transfer (although not being detailed enough to allow full validation).

The summary of current literature showed that very few measurements had been published concerning displacement ventilation and chilled ceiling systems operating together. Although more data concerning displacement ventilation systems is available it is generally in insufficient detail to be used to determine the parameters of any nodal model. Detailed displacement ventilation experimental data were, however, made available from the work of Li, Fuchs and Sandberg from the test chamber at the National Swedish Institute for Building Research (Li et al.

1993c). It seemed worthwhile, therefore, to gather further experimental data—particularly in the case of displacement ventilation operating with a chilled ceiling system—in order to gain a greater understanding of the thermal characteristics of these systems.

One of the key tasks in the development of a room heat transfer model, of the type proposed here, is the determination of the parameters associated with convective heat transfer and bulk air movement. In this work, the values of these parameters have been sought using distributions of radiative, convective and conductive heat fluxes under steady state conditions. In this approach, convection coefficient parameters have firstly been sought by performing a heat balance at the surface nodes of the model using measured air and surface temperatures and calculated radiant and conductive fluxes. Bulk air flow parameters values have been sought by making a heat balance at each air node using measured air temperature data. In principle it is possible to use this approach using either numerically calculated or experimentally measured temperature and heat flux data. However, in view of the uncertainties regarding the accuracy of the numerical convective heat transfer calculations, the primary source of heat flux distribution data has been the experimental work reported here.

The method proposed to determine the model parameters from the experimental data relies on the ability to properly apportion the heat fluxes between the conductive, convective and radiative paths and to find a reasonable correlation between the experimental measurements of temperatures and heat fluxes (which are point measurements) and the corresponding quantities at the nodes in the model (which represent regions of the room or surfaces). This implies a level of detail in the experimental measurements at least corresponding to the degree of complexity of the model. In order to generalise the model it is also necessary to gather data from experiments conducted over a range of system operating conditions. Experiments conducted in an environmental test chamber with a displacement ventilation and chilled ceiling panel system are the most convenient way to obtain the required data. However, this limits the operating conditions to those of the fixed geometry of a small room. This deficiency could be addressed by attempting to generate data from numerical models of rooms of larger size.

## 3.2 Experimental Design

The main experiments in this work consisted of a series of environmental test chamber experiments with a full scale displacement ventilation and chilled ceiling system conducted under steady state conditions—termed 'system performance' experiments here. To obtain data over a range of operating conditions, the internal load size, ceiling temperature, air supply flow rate and temperature were varied. The way in which these variables were varied is described in Section 3.5.

Previously published experimental work has involved similar test chamber experiments and reported measurements of air temperature but not surface temperatures or heat fluxes. Measurement of room air temperatures was necessary in this case for the determination of both the bulk air flow capacity rates and the convective heat transfer coefficients. Since some of the model air nodes may represent air in the plumes, measurements of air temperature in the plumes was also required.

Measurement and segregation of the surface heat fluxes have been attempted by measurement of the conductive fluxes and calculation of the radiant fluxes from surface temperature data. Convective fluxes have then been calculated by performing a heat balance at each surface node. This requires a comprehensive set of surface temperature measurements to be made.

In principle, the influence of conductive fluxes could have been eliminated from the experiments if the test chamber had been very well insulated or the external conditions could have been controlled to maintain adiabatic conditions on all room surfaces. The test chamber available was however only moderately insulated and there was no close control of the external environment. It would have been possible to control the internal surface temperatures to some degree by operating the test chambers 'Frenger' wall panels. (these are lightweight steel panels clipped to water circulation pipework in a similar manner to some types of chilled ceiling panels). In real displacement ventilation and chilled ceiling systems there seem to be distinct surface temperature vertical gradients at the room walls whilst conditions on outer wall surfaces (in corridors or externally) could be expected to be more isothermal. This would result in variation of the conductive heat flux over the height of the walls. Since this is a feature of the system heat transfer which the model should deal with, and it is desirable that the steady state experiments should be conducted with realistic operating conditions, the walls have been used in the passive mode and the conductive flux distribution measured.

Rather than use a large number of heat flux meters to determine the wall conductive heat fluxes, external surface temperatures have been measured and used with the internal surface temperatures and the wall conductive resistance to calculate the conductive flux distribution. This method is economical but relies on the wall conductive resistance being known so that the walls can be effectively used as heat flux meters. The conductive resistances of the walls of the test chamber used were not accurately known as the chamber had been modified since its construction and the information about its wall construction was incomplete. Thus it was necessary to carry out a secondary series of experiments to determine the conductive resistances of the chamber fabric. These experiments have been termed 'co-heating experiments'.

In the co-heating experiment, two heat flux meters were employed to measure directly the conductive heat fluxes on the different test chamber internal surfaces whilst simultaneously measuring the internal and external surface temperatures. This allows conducted fluxes to be compared with temperature differences across each surface and effective conductances determined. Since some of the walls have significant thermal mass the measurements were conducted over several days with the heat flux measurements made at different points on each surface for a number of hours at a time. The test chamber was operated with a fixed thermal load (of sufficient size to generate several degrees temperature difference through the fabric) and the ventilation and chilled ceiling systems turned off.

Although it was unnecessary to make measurements of room air velocities for the purpose of determining the model parameters, a limited set of such measurements was made in an attempt to find a correlation between some of the features of the room air temperature profile and features of the room air movement. For similar reasons, and in particular, to try and observe any recirculation paths of the room air a number of visualisation experiments were conducted with a variety of smoke sources.

## 3.3 Description of the Test Chamber Apparatus

The experiments were conducted in the Department of Civil and Building Engineering environmental test chamber. The chamber is of a size representative of

a two-person office and has internal dimensions of 5.43 m long, 3.09 m wide and 2.78 m high. The long axis of the room is aligned nearly West-East. The room is not quite symmetrical owing to a column part way along the South wall and has a net floor area of 16.7 $m^2$. The chamber is constructed on the first floor of a laboratory building with its southerly wall formed by the external wall of the building and has two small windows to allow day lighting for some types of experiment. These windows have seven panes of glass. The walls of the chamber are of plywood construction with insulating panels on a wood and steel frame. The chamber floor is constructed from commercial raised floor panels over the laboratory floor slab (giving a void of approximately 75 mm) and is carpeted. The roof is constructed with a plywood outer skin and insulating panels on a steel frame with a plenum of 325 mm depth containing ventilation ductwork suspended over the false ceiling. The roof of the laboratory is some 1.5m above the top of the chamber. The general arrangement is sketched in Figure 3.1.

The displacement ventilation system is formed by a semicircular diffuser on the centre-line of the shorter East wall of the test chamber and an 'egg-crate' type extract grille above the door at the other end of the room. The supply diffuser is 700 mm high and 400 mm diameter and is of type QL-180 manufactured by Trox

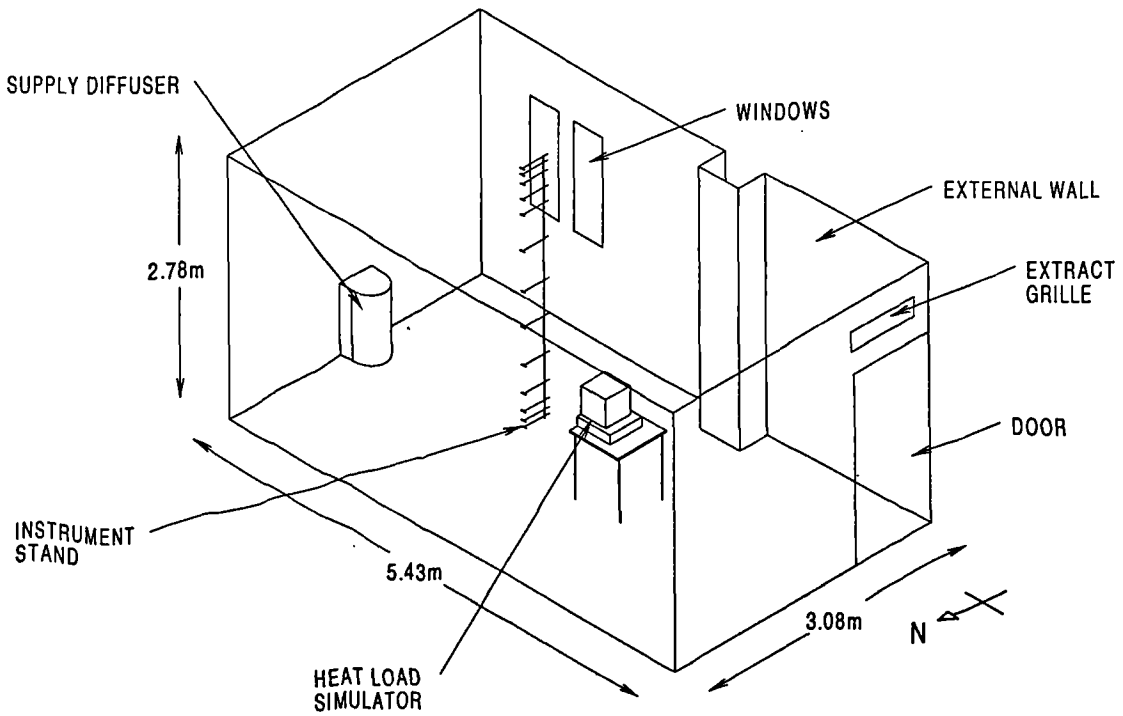


**Figure 3.1:** Sketch of environmental test chamber.

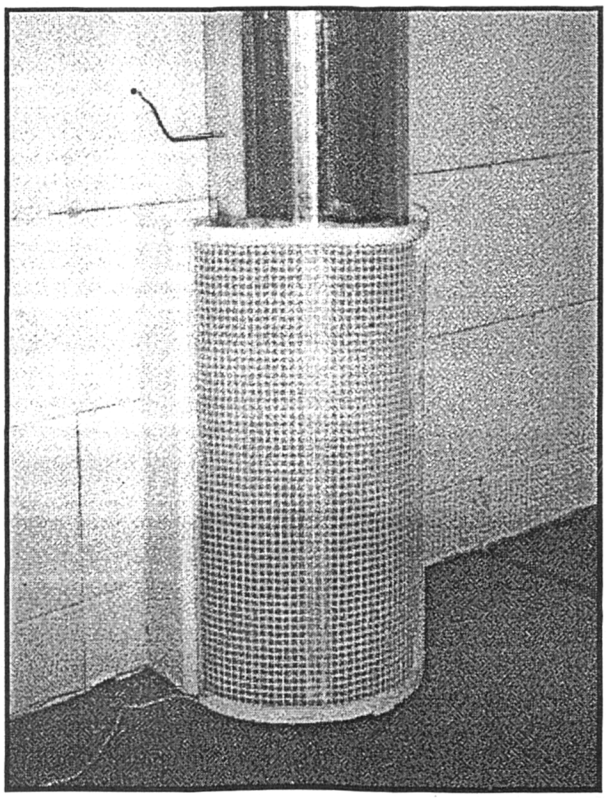

**Figure 3.2:** The displacement ventilation diffuser used in the environmental test chamber.

Brothers Ltd. The extract grille is 125 mm high and 575 mm long with the bottom of the grille 2.53m above floor level. The supply grille is constructed with a perforated metal face with square holes and a foam rubber sheet behind and is illustrated in Figure 3.2. The free area is estimated to be 80%.

The chilled ceiling is constructed from a proprietary system of metal tiles 1.65 m long 0.3 m wide occupying 88% of the total ceiling area (this was the maximum active area that could be achieved after allowing space for the ceiling support system). The panels are of type WK-DU-M manufactured by Trox Brothers Ltd. and consist of a serpentine array of copper tubes fixed to a perforated metal sheet. The tubes are in contact with the rear of the metal ceiling tile and are oval in section to increase the contact area. A foil encapsulated insulating panel 25 mm thick is fixed into the top of the tile over the tubes and backing plate. The panel components are illustrated in Figure 3.3. The manufacturers standard construction has been modified by the addition of a heat conducting paste applied between the tubes and the tile. Further insulation has also been added above the ceiling panels in the form of 100 mm thick fibre glass batts.

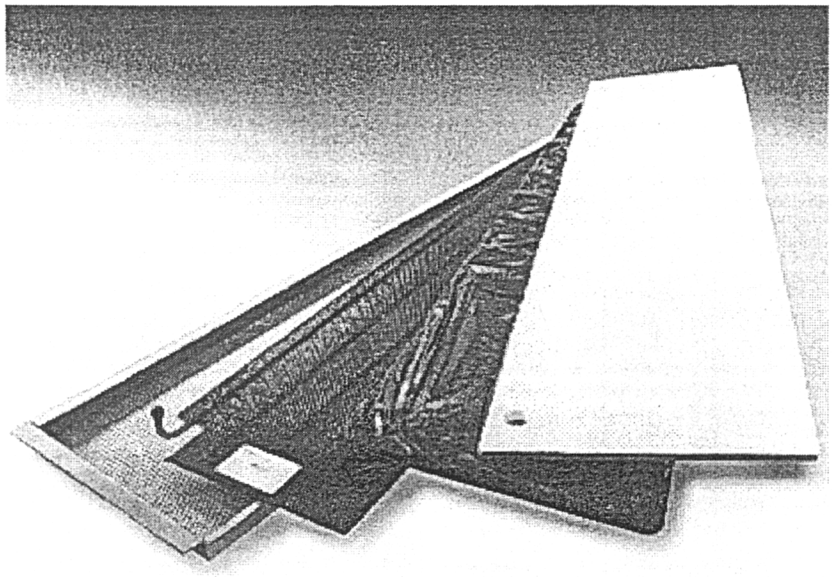

**Figure 3.3:** The chilled ceiling panel construction showing the ceiling panel (bottom), tube matrix and backing plate (next-to-bottom) and insulating panels.

The air supply for the displacement ventilation system is ducted from a laboratory air handling plant consisting of a fresh air inlet and filter, a direct expansion cooling coil, a thermistor controlled electric heating element, and a variable speed supply air fan. Air is ducted from the extract grille through a second variable speed fan and exhausted directly to outside. The arrangement of the plant items is shown schematically in Figure 3.4. Cooling to the air stream is provided using a direct expansion heat exchanger connected to an R134a refrigerant plant with piston compressor and water cooled condenser. (This refrigeration plant is also used to provide primary cooling to the chilled ceiling water system.) The heater batteries and cooling coil are controlled via electronic PID controllers connected to thermocouple sensors. The temperature of the air stream can be controlled to $\pm 0.1$°C when in heating mode and $\pm 0.3$°C when in cooling mode. The air flow rate through the supply and extract streams is measured with a multi-hole orifice device with the pressure drop measured on a fluorocarbon manometer. This arrangement allows the flow rate to be adjusted manually to an accuracy of $\pm 0.9\,\mathrm{l.s^{-1}}$.

Chilled water is supplied to the ceiling panel system from a central chilled water buffer tank. Water is circulated from the tank by a fixed speed pump through a three port mixing valve which is used to control the temperature of the water entering the chilled ceiling panel circuits. The valve has an electric actuator controlled from a separate electronic PID controller using a thermocouple sensor. The pump flow rate is high enough to ensure a temperature difference of only 2–3 K across the chilled ceiling panel system and so minimise any temperature difference across the ceiling surface. The chilled water tank has a refrigerant direct expansion cooling coil connected to the central refrigerant plant. This is controlled via a thermostat and solenoid valve. This arrangement allows the tank temperature to swing by 4–6 K in normal continuous load conditions and the chilled ceiling water supply temperature to be controlled within a $\pm 0.2$ K band. The chilled water supply is divided into six parallel circuits that are in turn connected to groups of five ceiling panels connected in series. Each of the six secondary circuits has a rotameter flow measuring device to enable the division of the flow to be checked and recorded. The chilled water system is also shown schematically in Figure 3.4.

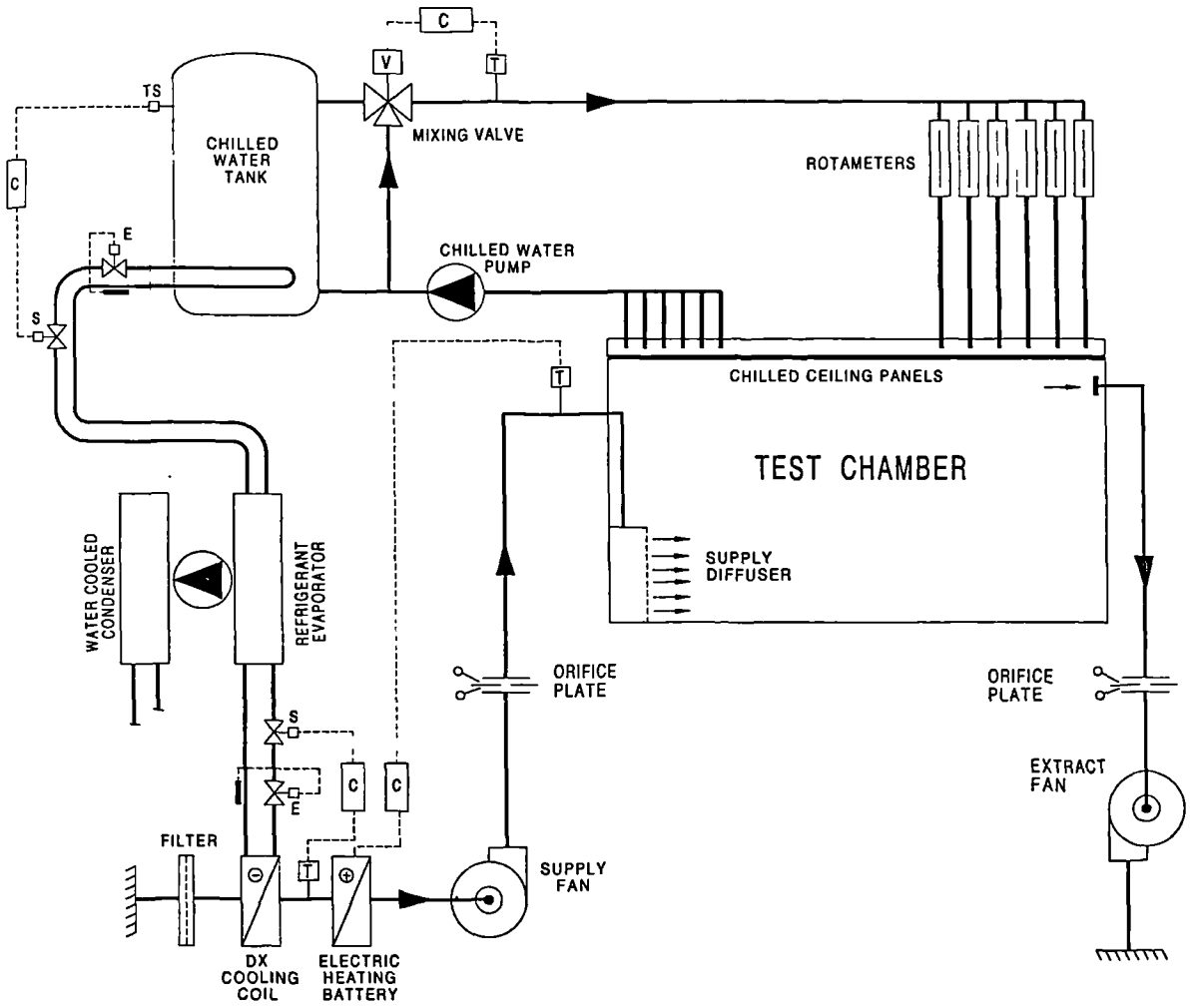


**Figure 3.4:** Schematic diagram of the environmental test chamber apparatus.

## 3.4 Description of the Measurement Systems

### 3.4.1 The Temperature and Heat Flux Sensors

The primary air and wall surface temperature sensors were type 'T' copper-constantan thermocouples. The air temperature sensors were specially constructed with a stainless steel shaft to allow mounting close together. To give some shielding from long wave radiation the thermocouple junction was contained within an open ended stainless steel tube fixed at the end of the shaft. Up to eighteen sensors were mounted on a vertical stand to allow measurement of the room vertical temperature distribution during the steady state experiments. Sensors were closely spaced near the floor and ceiling where the air temperature gradients were expected to be greatest. A second stand with six thermocouple sensors was used for measurement of the air temperature profile in the plumes. The air temperature thermocouple design is sketched in Figure 3.5.

The use of a tube as a radiation shield is only partially effective as the thermocouple junction is well shielded from radiation perpendicular to the tube axis but not from sources near the axis of the tube. The largest radiant asymmetry in these experiments is expected to be from ceiling to floor rather than between vertical surfaces For this reason the sensors were mounted with the tube axis horizontal. (Sample measurements with the sensors in different orientations in fact proved inconclusive as to which orientation is better.)

Surface temperature measurements have been made with purpose made surface

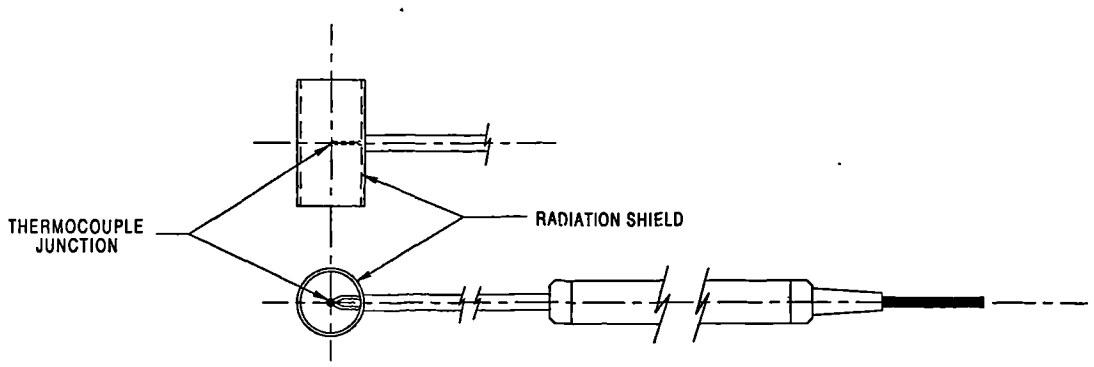


**Figure 3.5:** Diagram of the air thermocouple sensors showing the radiation shield.

temperature measurement thermocouples (type SAF-1 supplied by Omega Inc.). This type of sensor consists of a thermocouple junction that has been flattened after welding and is sandwiched between a high conductivity self adhesive pad and a fabric backing material. The thermocouple assembly was approximately 25 × 20 mm in size and less than 1 mm thick with a junction area of a few square millimetres. Surface temperature thermocouples have been distributed around the walls in vertical lines of four to allow measurement of vertical temperature profiles. Generally two vertical lines of surface thermocouple sensors were installed on each wall surface to ensure some redundancy, and so that the presence of any horizontal temperature gradients could be checked. Thirteen surface temperature thermocouples were installed on the chilled ceiling and six on the floor surface. The position of these internal surface thermocouples is shown in Figure 3.6.

All of the test chamber walls except the South wall had 'Frenger' panels as their internal surface. These panels are thin aluminium clipped to a water pipework matrix and can be easily removed. The surface temperature thermocouples on these walls were attached to the rear of these panels rather than the internal surface. This arrangement has the advantage (besides being neater) that the surface emissivity is not altered at the measurement point by the presence of the thermocouple. The thermal resistance of the aluminium sheet is negligible and can be accounted for, to first order, by the in-situ calibration procedure. The thermocouples on the ceiling panels were mounted on the rear in a similar manner. The south wall of the test chamber is an external wall of the laboratory building and consists of a cavity brick wall which has an additional 150 mm of fibreglass insulation on the inside. The inner surface of this wall consists of thin aluminium sheets supported on wood frame. Thermocouples were fixed to the inside surface of this wall.

Heat flux measurements have been made with 'TNO' type heat flux meters. This type of heat flux meter consists of many thermocouple junctions connected in series (a thermopile) and packed together in a thin plastic encapsulating material of known thermal conductivity. The sensors were approximately 20 mm in diameter and 2 mm thick. This arrangement of thermocouple junctions results in a signal of the order of tens of $mV.W^{-1}.m^2$ which can be measured directly (i.e. without the need for cold junction compensation etc.). The heat flux meters have sufficiently low thermal conductivity so as to not significantly alter the conducted flux locally to their attachment point. In the co-heating experiment the heat flux meters were attached to the internal test chamber surfaces with heat conducting paste in a number of positions adjacent to the surface thermocouples, as shown in Figure 3.6.

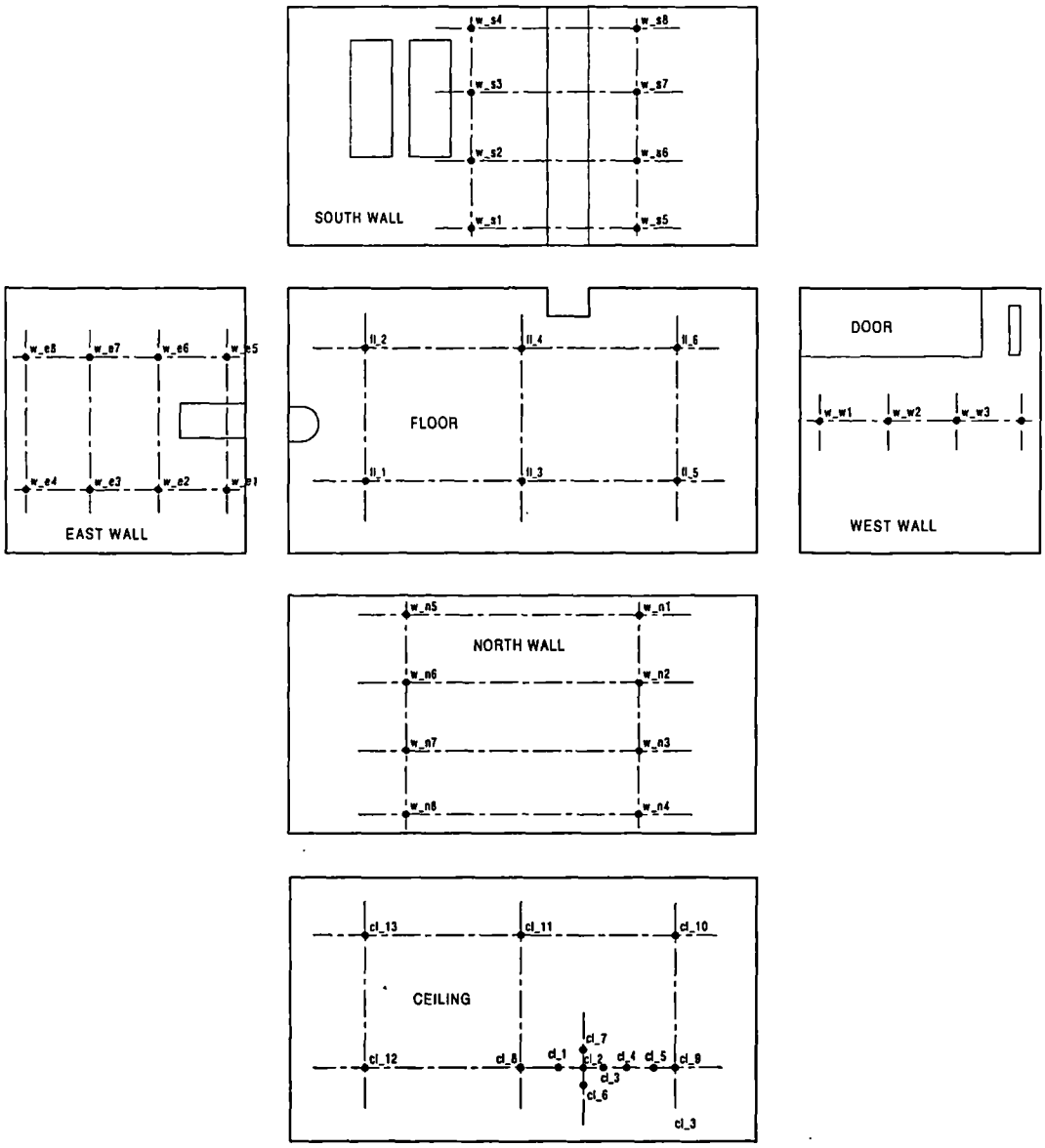


**Figure 3.6:** A net view of the test chamber internal surfaces showing the position of the surface thermocouples.

### 3.4.2 The Signal Processing and Data Logging System

The signal processing and data logging system for the thermocouples was constructed using data acquisition cards designed for use with a personal computer based data logging system. The main components of the system were three multiplexer/signal conditioning cards each with 32 input channels connected into an 8 channel 12 bit Analogue-to-Digital converter card mounted in one of the ISA expansion slots of the personal computer.

The signal processing cards are designed for use with thermocouples and consist of 32 double ended inputs connected through some simple input circuitry and pre-amplifiers into two 16 channel multiplexers each of which is connected into an amplifier. This arrangement means that the 32 thermocouple channels are multiplexed onto 2 channels of the A/D card. The gain of the amplifiers on the signal processing card can be pre-set in the range 10–800 depending on the range of the thermocouple voltage expected. The thermocouple voltages generated in this case were expected to be relatively small and so the gain was set at its maximum. The gain of the A/D card is fixed to give an input voltage range of $\pm 5\,\mathrm{V}$ so that, for the 'type T' thermocouples used here, the full range of the input voltage corresponds to a temperature range of 140 K. The analogue-to-digital converter was of the 12 bit type (i.e. the input voltage scale is mapped onto 0–4096 digital output) so that the resulting resolution of the system was $0.07\,\mathrm{K/bit}$.

The thermocouple signal processing cards each has a thermistor device mounted half way along the edge of the board which can be connected to one of the available A/D channels. This can be used to give a measurement of the temperature of the thermocouple junctions on the card. This information can then be used to calculate the thermocouple temperatures using 'cold junction compensation'. The cold junction compensation algorithm can be summarised as:

1. Select the channel of the multiplexer to read;
2. read the voltage on the channel through the A/D converter and convert the resulting integer output to a voltage;
3. read the signal processing card's thermistor voltage through the A/D converter;
4. convert the thermistor voltage to a temperature reading;

5. convert the thermocouple voltage to a temperature (in this case this is done using a polynomial expression for the 'type T' thermocouple characteristic);
6. add the two temperatures to give a final reading for the 'hot' thermocouple junction.

This method of using the thermocouples is convenient as no external temperature reference is required, and is used in a wide variety of commercial equipment. This method makes the assumption that all the thermocouple junctions on the card being at the same temperature and also that the thermistor operates with a reliably known characteristic. (In this case, the thermistor characteristic is assumed by the library software to be a simple linear one.) With a single thermistor per 32 channels this system has some error is introduced by temperature gradients along the card.

The 'cold junction compensation' method of measurement was used for the first and second series of experiments reported here. In order to regulate the thermal environment that the signal processing/multiplexer cards are exposed to, the three pre-amp/mutiplexor cards were mounted in steel cases with ventilation fans. One card was mounted in an old desktop computer case with its power supply used to power the cards and provide ventilation from its built-in fan. The two other cards were fixed in a wall mounted cabinet incorporating a small ventilation fan.

The alternative system of operating the thermocouples and interface cards, known as an 'ice point' system, does not use the thermistor sensor but an external reference temperature. Ideally the 'cold' junction of each thermocouple would be held at a reference temperature—typically by putting the junction in an ice/water bath. The thermocouple voltage can then be converted directly to a temperature relative to the reference (a Celsius reading when the ice triple point is the reference). However, for a large number of thermocouples it is not practical for every cold junction to be in an ice/water bath. In the system adopted here for the later series of experiments, the ice point reference was taken from one of the thermocouple channels at the centre of each card connected to a 'type T' thermocouple in an ice/water mixture in a vacuum flask. These channels were then used to measure the temperature of the cold junctions at the card terminals relative to the ice melting point. The following procedure was then used to calculate the thermocouple temperature readings.

1. Select the multiplexer channel for the thermocouple;

2. select the channel for the relevant ice point thermocouple;
3. read the ice point thermocouple channel through the A/D card and convert to a voltage;
4. read the thermocouple channel through the A/D card and convert to a voltage;
5. subtract the ice point voltage from the thermocouple channel voltage;
6. convert this voltage to a temperature to give the thermocouple temperature relative to the ice point.

### 3.4.3 Data Logging of the Temperature and Heat Flux Measurements

Data was collected from the A/D converter, processed and logged using a Hewlett Packard personal computer running real time data logging and display software developed by the author. This software was written in the C programming language using the 'Borland Turbo C' compiler. The data logging software combines a number of simple functions. Firstly, a simple timer is used to control the scanning of the input channels. Raw data are collected by scanning a pre-configured number of the total 96 channels once every second. The raw thermocouple data is then processed using either the cold junction compensation or ice point algorithms described above.

The cold junction compensation algorithm was implemented in the data logging software using a library function supplied by the card manufacturer. To implement the ice point algorithm it was necessary to combine a number of simpler library functions. The final step of converting the thermocouple voltage to a temperature reading was done by simply dividing the voltage by a single conversion factor for a 'type T' thermocouple of $40.3\,\mu V.K^{-1}$. Using a linear conversion like this is satisfactory for the narrow range of temperatures encountered in these experiments.

Although input channels were scanned every second, data from each channel were averaged over a longer period (typically 30 seconds) before being logged. Data from selected channels could be displayed in real time on the screen as a time series temperature graph, along with some vertical temperature profiles. This was useful in that it provided a convenient way of monitoring how stable certain

temperatures were, and hence whether the test chamber was approaching steady state conditions. Finally, averaged data for each channel could be logged to a text file—or a number of files when a large number of channels were used. An average reading over the whole of the logging period could also be recorded for each channel. It is the latter figures that are most useful in analysing data from the steady state experiments in which data were logged over a 40–45 minute period.

The heat flux meters were connected to two of the channels of a thermocouple signal processing/multiplexer card and were logged using the same software. The heat flux meters gave a maximum output of the order of $\pm 2\,\mathrm{mV}$ in these experiments and so could be used at the same gain as the thermocouples. The output voltage from the heat flux meters were read through the A/D card using a simple library function and converted to a heat flux reading by a simple linear relationship between voltage and heat flux. Heat flux data were averaged and logged in the same way as the temperature measurements.

### 3.4.4 The Room Air Speed Measurement System

A limited series of air speed measurements were made in the test chamber. These measurements were made simultaneously with the temperature measurements during some of the system performance experiments. The air speed measurements were made using a Dantec 'Multichannel Flow Analyser'. This system consists of a 54N10 flow analyser linked to a personal computer and also connected to twelve 54R10 air flow transducers.

The 54R10 air flow transducer is a combined omnidirectional air speed and temperature sensor designed specifically for measuring room air flows within the velocity range $0.05$–$5.0\,\mathrm{m.s^{-1}}$ and works on the hot sensor anemometer principle. The air speed sensor of the transducer consists of a 3 mm glass sphere coated with a thin film of nickel and a protective quartz outer coating. The Nickel film has a double spiral formed in it so that it can act as an electrical conductor. This sphere is connected electrically to one arm of a Wheatstone bridge, whose opposite arm contains an identical, non-heated, sphere for automatic temperature compensation. The hot sphere is maintained at a constant 30 K above the surrounding air by a heating current passing through the nickel conducting layer, independent of variations in flow velocity or temperature. The power supplied to heat the sphere is then a function of the air speed. The temperature sensor of the transducer is

tor approximately 0.5 mm in diameter suspended by a wire. The transducer head arrangement is illustrated in Figure 3.7

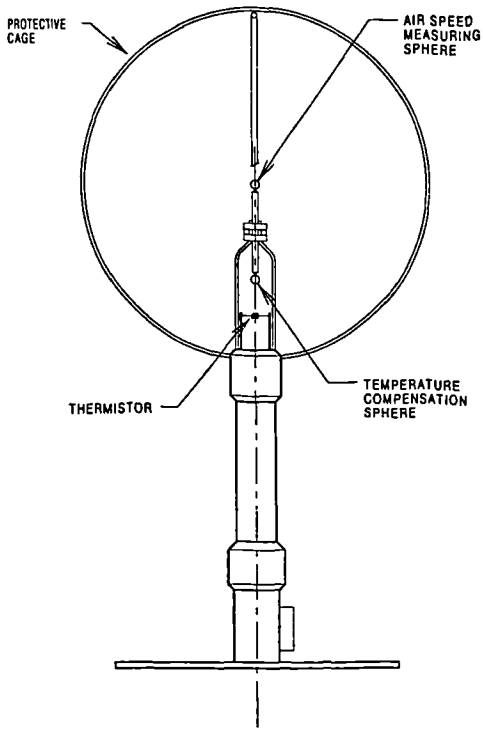


**Figure 3.7:** Illustration of the Dantec 54R10 air speed/temperature transducer.

The flow analyser drives each of the transducers, sampling a velocity reading twice a second. These data are stored over a pre-set sampling interval and the mean and RMS velocity calculated at the end of each interval. The personal computer is used to control remotely the flow analyser and download, display and log the processed velocity and temperature measurements. The sampling period chosen varies depending on the nature of the turbulence in the flow. In a 'steady' turbulent flow a longer sampling time increases the accuracy of the statistical measurement of mean speed and RMS speed (Sandberg 1994). A long averaging time may however mask the effects of genuine unsteadiness in the flow field. In this case, after an initial trial, a sampling time of 210 seconds was used with a 30 second pause between samples. This was thought to be long enough to give reasonable measurements of mean speed in the limited time of the experiments. This is probably not long enough however, to give reasonable values for RMS speed or turbulence intensity—measurements which were of little interest in these studies.

The air flow transducers were mounted on the same vertical stand as the room

air thermocouples and were more closely spaced near the floor and ceiling. In one of the experiments (case DC10) measurements were made at a number of points along the centreline of the room as well as at one position near the side wall of the test chamber (in an attempt to investigate the flow up/down the wall). These positions are shown in Figure 3.8. In some of the experiments a number of the transducers were also mounted over one of the heat sources to measure the plume air speeds.

### 3.4.5 Calibration and Testing of the Measurement Systems

During the progress of the work, a lack of repeatability was found in the first series of temperature measurements, which were made with the cold junction compensation method after initial calibration of the thermocouples on the bench. In particular, although the room air temperature measurements showed good accuracy relative to each other, their absolute accuracy was poor. The accuracy of temperature differences between the air and wall surface temperature measurements was also poor. To improve this situation, an in-situ calibration method was used to calibrate all the thermocouples at the same instance. This improved the accuracy of the surface-to-air temperature difference measurements but not the absolute accuracy of the system. The final solution to this problem was to adopt the ice point measurement technique and calibrate all the thermocouples at the same instance while in-situ. Accordingly, use has only been made of air-to-surface temperature measurements (in the later calculation of convective fluxes) made using the ice point measurement system. The calibration methods used and the testing of the final thermocouple measurement system, along with an estimation of the associated measurement errors, is discussed in detail in Appendix A. Calibration of the other measurement systems is also discussed in Appendix A.

## 3.5 The System Performance Experimental Procedure

The aim of the steady state 'system performance' experiments was to operate the displacement ventilation and chilled ceiling system at a range of operating

conditions with the system and test chamber in a quasi-steady state and collect sets of temperature distribution data. The operating conditions of the displacement ventilation and chilled ceiling system in the test chamber are determined by:

- the flow rates of the air and water streams;
- the supply temperatures of the air and water streams;
- the internal load conditions;
- the conditions external to the test chamber.

The test chamber apparatus has facilities to control each of these variables at a steady level except for the external conditions (as described in Section 3.3). A series of twelve tests were completed with the displacement ventilation system operating alone (designated test cases DV1-12). A further seventeen tests were completed with both the displacement ventilation and chilled ceiling operating (designated test cases DC1–17). The operating conditions for each of the test cases has been tabulated in Tables 3.1 and 3.2. The type of thermocouple measurement system (and calibration method) has been indicated as CJC1 and CJC2 for the cold junction compensation method and the first and second calibration methods respectively, and IP for the ice point method. The air and chilled water supply temperatures are indicated by $T_s$ and $T_{sw}$ respectively.

The chilled water flow rate of the system was fixed at a nominal $0.11\,\mathrm{l.s^{-1}}$ and has been determined to give typical temperature drops across the ceiling panel system of 2–3 K . The flow through each sub-circuit of the chilled water system was measured using the rotameters, recorded at the start of each experiment and checked at the end. There was no measurable fluctuation in water flow during any of the experiments. Changing the chilled water flow temperature, and hence the mean ceiling temperature, is the effective control over the proportion of the load that is absorbed by the ceiling system. The chilled water flow temperature was set at between 12°C and 20°C. In the experiments with only the displacement ventilation system working the ceiling panel system was turned off for several hours prior to the experiment so that it acted as a passive fabric element.

The displacement ventilation flow rate was set at one of three levels: either 1.5, 3.0 or 5 air changes per hour (18.94, 37.88 or $63.13\,\mathrm{l.s^{-1}}$). These flow rates were chosen on the basis that typical design conditions for an office would be in the

| *Test Case* | *Load* W | *Load sites* | $n$ $h^{-1}$ | $T_s$ °C | *Thermocouple System* | *Air Temp. Error (K)* |
|---|---|---|---|---|---|---|
| DV1 | 300 | 1† | 3 | 16.4 | CJC1 | ±0.4 |
| DV2 | 300 | 1‡ | 3 | 17.4 | CJC1 | ±0.4 |
| DV3 | 300 | 1 | 3 | 13.0 | CJC1 | ±0.4 |
| DV4 | 800 | 4 | 3 | 17.6 | CJC1 | ±0.4 |
| DV6 | 400 | 4 | 3 | 20.0 | CJC2 | ±0.4 |
| DV7 | 100 | 1 | 1.5 | 19.8 | IP | ±0.17 |
| DV8 | 200 | 1 | 1.5 | 20.6 | IP | ±0.17 |
| DV9 | 300 | 1 | 1.5 | 19.0 | IP | ±0.17 |
| DV10 | 300 | 1 | 3 | 19.2 | IP | ±0.17 |
| DV11 | 400 | 1 | 3 | 18.6 | IP | ±0.17 |
| DV12 | 400 | 4 | 3 | 18.4 | IP | ±0.17 |

**Table 3.1:** Experimental boundary conditions for the displacement ventilation test cases. († Load at low level. ‡ Load 1.5 m high on floor). $n$ is the air change rate, and $T_s$ the air supply temperature.

range 1.5–3.0 air changes per hour. An air flow of 5 air changes per hour would probably be an upper limit, above which the momentum of the air flow would be high enough to destroy the displacement ventilation flow pattern. The air flow through the supply and extract fans was adjusted at the start of each experiments using the fan variable speed controls, while monitoring the respective flow meter manometer readings. The air flow temperature was set at a nominal 16.0, 18.0 or 19.0°C through the test chamber air plant PID controls. The actual temperature varied slightly from the control set points but was measured in the duct entering the room using one of the thermocouples and logged during each experiment.

Internal loads were simulated using two sizes of cuboid boxes containing single domestic light bulbs of various wattages. The boxes were painted matt black and had a series of ventilation holes around the sides to allow some airflow through the box by natural convection. The boxes were either a 300 mm cube or a flatter cuboid 450 mm square and 150 mm high. When stacked these were intended to simulate a personal computer and monitor and were placed on top of 600 mm square tables at a height of 720 mm. The loads were distributed in the test chamber in one of two plan layouts. For cases with small loads, a single box or stack of boxes was placed on a table on the centre-line of the room approximately two thirds along

| *Test Case* | *Load* W | *n* $h^{-1}$ | *Load sites* | $T_{sw}$ °C | $T_s$ °C | *Thermocouple System* | *Air Temp. Error (K)* |
|---|---|---|---|---|---|---|---|
| DC1 | 800 | 3 | 4 | 14.0 | 17.7 | CJC1 | ±0.4 |
| DC2 | 800 | 3 | 4 | 16.0 | 18.3 | CJC1 | ±0.4 |
| DC3 | 800 | 3 | 4 | 18.0 | 17.8 | CJC1 | ±0.4 |
| DC4 | 800 | 3 | 4 | 14.0 | 20.2 | CJC1 | ±0.4 |
| DC5 | 800 | 3 | 4 | 16.0 | 19.6 | CJC2 | ±0.4 |
| DC6 | 800 | 3 | 4 | 18.0 | 19.4 | CJC2 | ±0.4 |
| DC7 | 800 | 3 | 4 | 20.0 | 20.1 | CJC2 | ±0.4 |
| DC8 | 800 | 5 | 4 | 18.0 | 19.6 | CJC2 | ±0.4 |
| DC9 | 800 | 5 | 4 | 18.0 | 19.9 | CJC2 | ±0.4 |
| DC10 | 1200 | 5 | 4 | 16.0 | 19.8 | CJC2 | ±0.4 |
| DC11 | 800 | 3 | 4 | 16.0 | 19.0 | IP | ±0.17 |
| DC12 | 450 | 3 | 4 | 17.0 | 19.1 | IP | ±0.17 |
| DC13 | 450 | 3 | 4 | 14.0 | 19.0 | IP | ±0.17 |
| DC14 | 600 | 3 | 4 | 14.0 | 15.6 | IP | ±0.17 |
| DC15 | 600 | 3 | 4 | 17.0 | 15.2 | IP | ±0.17 |
| DC16 | 600 | 1.5 | 4 | 17.0 | 16.1 | IP | ±0.17 |
| DC17 | 600 | 1.5 | 4 | 20.0 | 16.4 | IP | ±0.17 |

**Table 3.2:** Experimental boundary conditions for the displacement ventilation and chilled ceiling test cases. $n$ is the air change rate. $T_s$ and $T_{sw}$ are the air and water supply temperatures respectively.

the length of the room from the supply diffuser. For test cases with larger total room loads four sets of boxes were placed on tables set symmetrically about the room center-line. The arrangement of the loads and air temperature measuring positions is shown in Figure 3.8.

The size of the internal loads simulated varied from 100 W in a single box, up to 1200 W distributed equally in four boxes. These loads are equivalent to 6-72 $W.m^{-2}$. The loads were varied in this range by simply using different combinations of boxes and light bulb powers. Loads of 72 $W.m^{-2}$ are towards the upper end of those recommended for systems of this type but are not as high as figures quoted by some chilled ceiling manufacturers for the capacity limit.

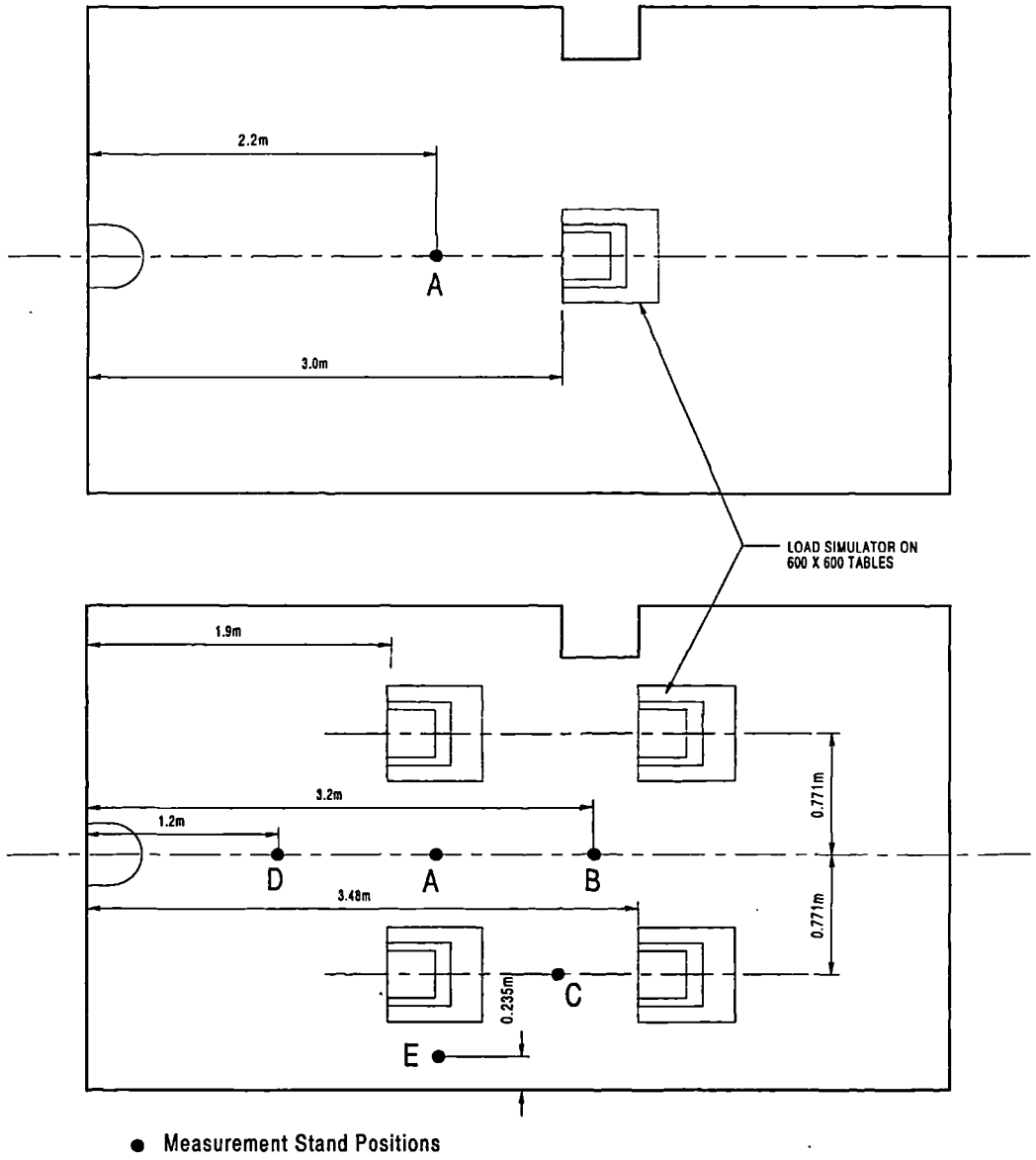


**Figure 3.8:** Plan views of the test chamber showing the layout of the room with single and four load simulator boxes.

Prior to making any measurements, the test chamber plant was set to run at the required operating conditions for approximately twelve hours to allow the chamber to reach a quasi-steady state. The state of the test chamber was monitored by observing the real time plots of selected surface temperatures provided by the data logging system. After leaving the test chamber running at given operating conditions for this length of time (generally overnight), changes to the surface temperatures were at a rate of a few tenths of a degree per hour. Truly steady state conditions could never be reached, as the environment in the lab surrounding the test chamber had to be left to follow its natural diurnal pattern, and one wall is exposed to external conditions.

To collect each set of data, measurements of temperatures and heat fluxes were logged for 40–45 minutes. Data logging was carried out by scanning each channel every second and averaging and logging each measurement over 30 second intervals. Measurements of the room air temperature profile were made with the stand holding the air temperature thermocouples at one of the positions shown in Figure 3.8. When measurements were made of the air temperature profile at a number of points in the room, it was necessary to enter the chamber after one set of measurements was complete, and move the stand manually. In this case the chamber was then left undisturbed for approximately 20 minutes before starting a further period of data logging, so that the air flow pattern could re-stabilise.

## 3.6 The Co-heating Experiment Procedure

The principal aim of the co-heating experiments was to gather simultaneous heat flux and surface temperature data for each surface of the test chamber for use in calculating the conductive heat flux distributions. For the co-heating experiments, a constant load of 1200 W was provided by a number of the heat source boxes in the test chamber. A load of this size was found to be sufficient to ensure a temperature difference across the chamber fabric of the order of 10 K. All the test chamber's cooling systems were turned off and the ventilation inlets and outlets sealed to minimise any infiltration of outside air.

A powerful desk-top fan was used inside the test chamber to promote good mixing of the room air so that each surface approached isothermal conditions. This precaution was taken as temperature difference measurements were to be made between the various thermocouples on each internal surface and the single cen-

trally placed thermocouples on the corresponding outer surface. If the air had been stratified and a vertical temperature gradient existed on the internal surface, then an error would have been introduced by taking a temperature difference using the inside surface thermocouples at their different heights.

The test chamber has a moderate thermal mass which can be attributed mainly to the southerly external wall and the floor. Preliminary measurements showed that a period of approximately 48 hours was required to pass before the chamber had heated through and the internal air and surface temperatures followed a regular diurnal cycle—being driven by the outside and lab temperature cycles. No heat flux measurements were made until 72 hours after switching on the heat load.

To acquire a sufficient data to allow a reasonable average conductances to be calculated, the measurements of heat flux and surface temperature were taken over five diurnal cycles. As there were only two heat flux meters, these were moved to different positions on the internal surfaces next to the various thermocouple sites and measurements made for 1.5–2 hours at a time (and several hours over nights and one weekend). In this way, data representative of the whole diurnal cycle were collected for each surface for the duration of the experiment.

# Chapter 4

# Experimental Results

## 4.1 Introduction

The experimental results from the Loughborough test chamber are presented and discussed in this chapter. The experiments were conducted with two purposes in mind. Firstly, to gain a greater understanding of the thermal performance of the displacement ventilation and chilled ceiling system. Secondly, to gather data that can be used to determine the structure and parameters of the nodal model. There are more published data from similar experiments with displacement ventilation than experiments involving chilled ceilings. Results for the displacement ventilation experiments are accordingly discussed first and some comparisons with published data are made.

The principal results presented are those of the system performance experiments, and are presented primarily in the form of vertical wall and air temperature profiles derived from the thermocouple measurements. The temperature profiles contain a significant amount of information regarding the thermal performance of the system. In particular, besides the overall temperature difference being shown, the relationship between the high level temperature and that near the floor is shown. The temperature and the temperature gradient in the occupied zone and its relationship to the supply temperature are similarly indicated by the temperature profiles. The temperature gradients shown in the temperature profiles also give an indication of the extent of mixing or stratification of the air at different heights.

In order to use experimental data to develop a nodal model structure it is nec-

| *Test Case* | *Load* W | $Q_a$ W | $n$ $h^{-1}$ | $T_s$ °C | $T_e$ °C | $T_N$ °C | $T_S$ °C | $T_W$ °C | $T_E$ °C | $T_F$ °C | $T_R$ °C |
|---|---|---|---|---|---|---|---|---|---|---|---|
| DV1 | 300 | 123 | 3 | 16.4 | 19.0 | 15.7 | -3.3 | 16.0 | 12.8 | † | 14.6 |
| DV2 | 300 | 125 | 3 | 17.4 | 20.1 | 20.6 | -1.1 | 21.0 | 15.6 | † | 26.9 |
| DV3 | 300 | 305 | 3 | 13.0 | 19.6 | 20.8 | 1.0 | 21.6 | 15.8 | † | 27.9 |
| DV4 | 800 | 359 | 3 | 17.6 | 25.3 | 22.8 | 4.3 | 23.2 | 18.5 | † | 28.9 |
| DV6 | 400 | 305 | 3 | 20.0 | 26.6 | 26.5 | 24.0 | 28.0 | 26.4 | 25.2 | 27.6 |
| DV7 | 100 | 43.1 | 1.5 | 19.8 | 21.7 | 21.9 | 15.4 | 21.8 | 19.6 | 21.9 | 24.0 |
| DV8 | 200 | 58.5 | 1.5 | 20.6 | 23.1 | 22.5 | 14.4 | 22.9 | 20.6 | 21.9 | 23.1 |
| DV9 | 300 | 72.5 | 1.5 | 19.0 | 22.2 | 19.1 | 14.6 | 19.2 | 17.9 | 20.2 | 18.7 |
| DV10 | 300 | 134 | 3 | 19.2 | 22.1 | 20.6 | 18.5 | 20.9 | 19.1 | 20.4 | 21.6 |
| DV11 | 400 | 205 | 3 | 18.6 | 23.0 | 20.8 | 12.4 | 20.9 | 19.1 | 21.0 | 20.6 |
| DV12 | 400 | 213 | 3 | 18.4 | 23.0 | 20.5 | 12.6 | 20.9 | 18.8 | 20.6 | 20.6 |

**Table 4.1:** Experimental boundary conditions for the displacement ventilation test cases. †Temperature measurements below the floor were not made for these experiments.

essary to consider the surface temperature and heat flux distributions. The heat transfer at the floor and ceiling surfaces is thought to be of greatest significance in determining the overall thermal characteristics. In particular, it has been suggested (Li et al. 1993b, Mundt 1996, for example), that it is the convective heat transfer at the floor and ceiling, and the radiant coupling between these two surfaces, that is responsible for raising the temperature near the floor above that of the supply. Accordingly, in the analysis and discussion of the results from the displacement ventilation experiments, particular attention is given to the heat transfer at these surfaces. Measurements of plume temperatures are of relevance to the heat transfer at the ceiling, but also—as is later shown in Chapter 7—are sometimes necessary to allow some of the nodal model parameters to be determined. Plume temperature measurements are presented in the form of vertical temperature profiles for each set of test cases.

Further discussion is made of the shape of the air temperature profiles between the boundary layers at the floor and ceiling . There is some significant variation in the shape of profiles reported in the literature—Nielsen's results (Nielsen, Hoff and Pedersen 1988) show a convex shape over most of their height, while Li's results (1993) tend to be concave. The shape of the profile is of some importance in any model of the system as this must partly determine the comfort temperature in the

| *Test Case* | *Load* W | $n$ $h^{-1}$ | $Q_a$ W | $T_{sw}$ °C | $T_s$ °C | $T_e$ °C | $T_N$ °C | $T_S$ °C | $T_W$ °C | $T_E$ °C | $T_F$ °C | $T_R$ °C |
|---|---|---|---|---|---|---|---|---|---|---|---|---|
| DC1 | 800 | 3 | 138 | 14.0 | 17.7 | 20.7 | 23.8 | 9.6 | 23.7 | 18.8 | – | 30.6 |
| DC2 | 800 | 3 | 205 | 16.0 | 18.3 | 22.7 | 26.0 | 5.0 | 26.2 | 20.7 | – | 32.5 |
| DC3 | 800 | 3 | 260 | 18.0 | 17.8 | 23.5 | 23.9 | 3.8 | 23.6 | 18.8 | – | 29.4 |
| DC4 | 800 | 3 | 106 | 14.0 | 20.2 | 22.5 | 24.9 | 21.2 | 26.8 | 25.1 | 22.3 | 26.8 |
| DC5 | 800 | 3 | 249 | 16.0 | 19.6 | 25.0 | 26.5 | 20.2 | 27.1 | 26.9 | 23.8 | 27.4 |
| DC6 | 800 | 3 | 247 | 18.0 | 19.4 | 24.7 | 24.0 | 19.2 | 24.1 | 24.0 | 23.4 | 24.2 |
| DC7 | 800 | 3 | 296 | 20.0 | 20.1 | 26.4 | 25.4 | 17.1 | 25.6 | 25.6 | 24.4 | 25.6 |
| DC8 | 800 | 5 | 397 | 18.0 | 19.6 | 24.7 | 25.4 | 20.0 | 25.7 | 25.4 | 23.6 | 26.5 |
| DC9 | 800 | 5 | 400 | 18.0 | 19.9 | 25.1 | 25.2 | 17.7 | 25.8 | 25.7 | 24.3 | 25.7 |
| DC10 | 1200 | 5 | 286 | 16.0 | 19.8 | 25.9 | 24.0 | 17.1 | 23.8 | 23.9 | 24.1 | 23.4 |
| DC11 | 800 | 3 | 165 | 16.0 | 19.0 | 22.6 | 20.0 | 21.5 | 20.4 | 18.2 | 21.5 | 19.3 |
| DC12 | 450 | 3 | 94 | 17.0 | 19.1 | 21.1 | 20.0 | 17.0 | 20.4 | 17.9 | 21.0 | 20.5 |
| DC13 | 450 | 3 | 9 | 14.0 | 19.0 | 19.2 | 21.1 | 15.0 | 21.8 | 19.4 | 20.9 | 22.2 |
| DC14 | 600 | 3 | 162 | 14.0 | 15.6 | 19.1 | 18.3 | 13.8 | 18.3 | 16.7 | 19.5 | 17.9 |
| DC15 | 600 | 3 | 242 | 17.0 | 15.2 | 20.3 | 19.9 | 14.8 | 20.0 | 18.0 | 19.5 | 20.3 |
| DC16 | 600 | 1.5 | 134 | 17.0 | 16.1 | 21.9 | 19.8 | 17.8 | 20.0 | 18.2 | 20.1 | 19.6 |

**Table 4.2:** Experimental boundary conditions for the displacement ventilation and chilled ceiling test cases.

occupied zone, and also partly determine the convective heat exchange between the air and the wall surfaces. It is believed that the slope of the profile should correlate to the extent of mixing versus stratification at a given height in this zone—greater mixing being indicated by a more vertical profile/lower temperature gradient. Some discussion is accordingly made of the range of profile shapes measured in these experiments and the mechanisms that may govern the extent of mixing at different heights in the room.

The results of the system performance experiments where the chilled ceiling has also been employed are presented in Section 4.3. The additional trends in the data due to the variation in conditions at the ceiling surface associated with different water flow temperatures are discussed. Although there are few experimental data in the current literature regarding displacement ventilation and chilled ceiling systems, some qualitative comparisons are made with the limited data available.

The room vertical temperature profiles in all cases are based on thermocouple

measurements averaged over the full 40–45 minutes of each system performance experiment. In the case of the wall temperature profiles, a single surface temperature result has been derived for each of the four measurement heights by taking an area weighted average of the thermocouple surface temperature readings (7 in total) at each height.

The experimental boundary conditions for the displacement ventilation and displacement ventilation and chilled ceiling system performance test cases were shown previously in Tables 3.1 and 3.2. The external temperature conditions recorded during each experiment and the heat load transferred to the air stream are summarised in Tables 4.1 and 4.2.

## 4.2 The Displacement Ventilation Test Cases

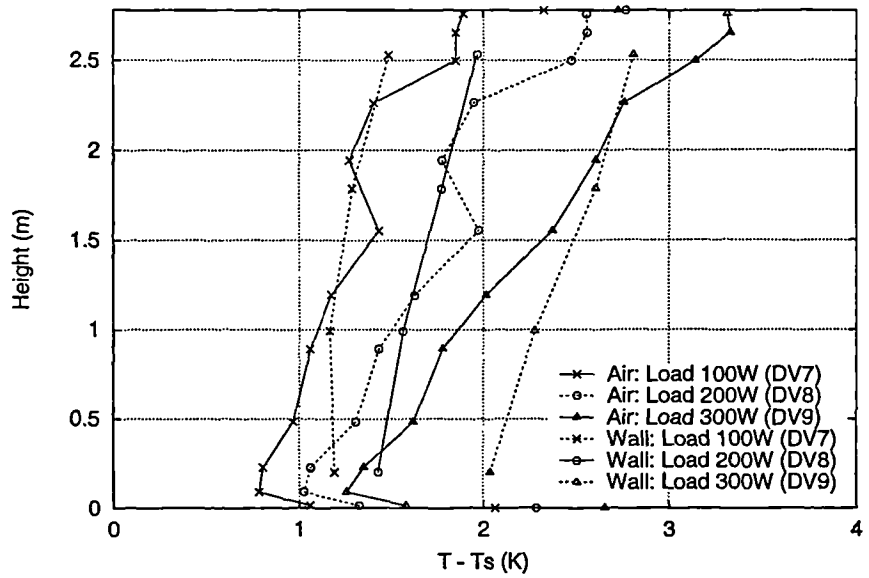


**Figure 4.1:** Air and surface temperature distributions for the displacement ventilation test cases DV7,8 & 9 (air change rate 1.5 per hour).

The air and wall temperature profiles for the displacement ventilation test cases with a supply air flow equivalent to $1.5\,\mathrm{ac.h^{-1}}$ (cases DV7–9) are shown in Figure 4.1. The results for the test cases with a supply air flow of $3\,\mathrm{ac.h^{-1}}$ (cases DV10–12) are shown in Figure 4.2. The average floor and ceiling surface temperatures are shown as points on the bottom and top horizontal axis of these figures respectively. These air temperature profiles were measured on the room centre-line at the position marked as point A in Figure 3.8 for cases DV7–11, and position

B for case DV12. There are a number of features of the air temperature profiles that can be seen to be common to all these test cases. Firstly, the minimum air temperature measured at these positions in the room always occurs at the second thermocouple position above the floor (90 mm). Correspondingly, the maximum temperature always occurs in the zone 100 mm below the ceiling. There is however, some notable variation in the profile shapes between these two points. Consider firstly though, the conditions at the floor.

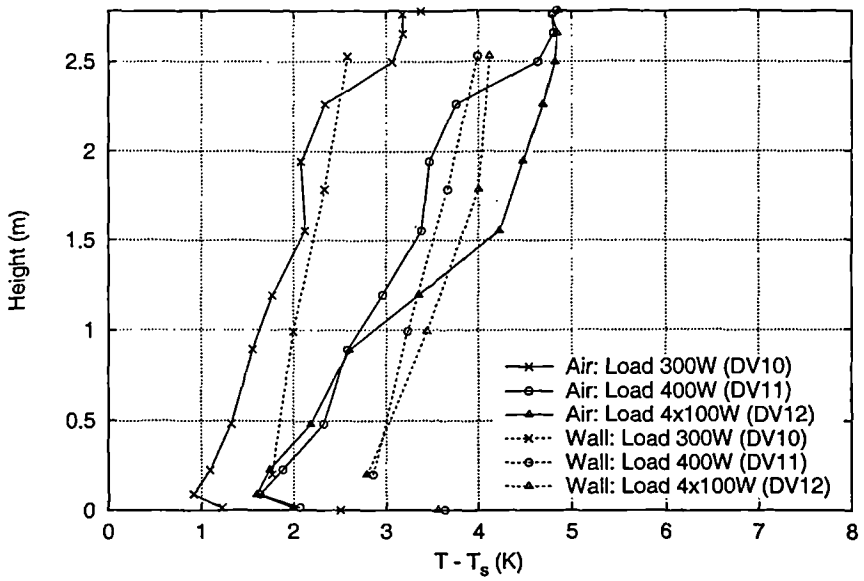


**Figure 4.2:** Air and surface temperature distributions for the displacement ventilation test cases DV10,11 & 12 (air change rate 3 per hour).

Six thermocouples were used to measure floor surface temperatures. It was expected that the floor region nearest the supply diffuser would show the lowest surface temperature, due to the cooling effect of the incoming air, and that there would be some gradual increase in surface temperature further from the diffuser. The individual floor surface temperature measurements are shown in Figure 4.3 where the lines are drawn between the measurements for the north and south sides of the room and the position of the supply diffuser corresponds to the right-hand end of the horizontal axis. It can be seen that the variation in temperature is not very great and that the coolest temperatures are at the end of the room nearest the supply diffuser, as expected. The maximum floor surface temperatures are consistently in the central region of the room. One possible reason for this may be local radiant heating of the floor from the heat sources which were positioned over this region.

Air temperature measurements from the two thermocouples nearest the floor

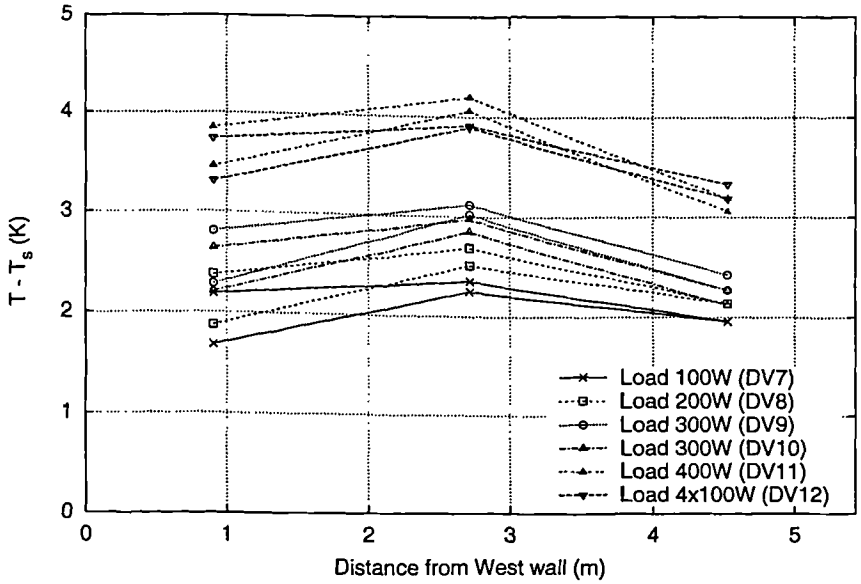


Figure 4.3: Floor surface temperature measurements for cases DV7–12.

(14 mm and 90 mm above the floor) and the average floor surface temperature measurements shown in Figures 4.1 and 4.2 consistently indicate a negative temperature gradient. The difference between the average floor surface temperature measurement and the air temperature above the floor is in the range 1.25–2.0 K (significant compared with the magnitude of the experimental errors). It seems clear then, that in each of these test cases, the direction of the convective heat flux at the floor is from the surface to the layer of air above, as expected.

The convective heat transfer conditions at the ceiling are not so clear. The air temperature measurements at the two thermocouples nearest the ceiling ( 20 mm and 125 mm below the surface) show a temperature gradient that is very small in magnitude—indicating nearly adiabatic conditions. The ceiling is relatively well insulated (U-Value 0.22 $W.m^{-2}.K^{-1}$) but the ceiling plenum and outside surface temperature measurements indicate that the conducted flux at the ceiling would be in the direction out of the chamber in all cases except DV7, where the flux would be into the chamber. (This is consistent with the small positive air temperature gradient measured for case DV7, as shown in Figure 4.1.) However, the average ceiling temperatures are (except for case DV9) up to 0.44 K higher than the corresponding air temperature measurement at the thermocouple nearest the ceiling surface (i.e. suggesting that the convective flux should be from the ceiling surface to the room air).

This apparent contradiction may partly be due to the fact that the ceiling temperature measurement is an average of 13 distributed thermocouples and the air

temperature profile is measured at a single site. Some variation in the convective heat flux and convection coefficient may also be expected between the region of the ceiling where the warm air from the plumes impinges on the ceiling and regions further from the plumes. The air thermocouples were deliberately mounted out of this region and no surface temperature measurements were made directly above the air thermocouple stand position.

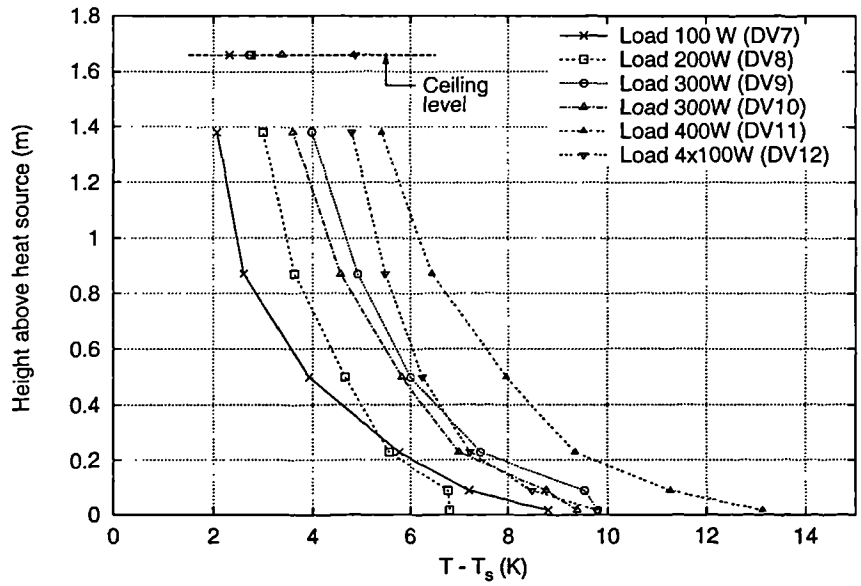


**Figure 4.4:** Temperature measurements along the plume centre line for test cases DV7–12 shown along with the average ceiling surface temperatures.

The variation in conditions at the ceiling surface can be considered further by examining the plume temperatures near the ceiling and the variations in ceiling surface temperature. A number of temperature measurements were taken along the nominal plume center lines (i.e. directly above each heat source) during each system performance experiment. These measurements are shown along with the corresponding average ceiling temperatures in Figure 4.4. The temperatures measured near the top of the plumes can be seen to be either close to or above the corresponding average ceiling temperature (except case DV7 which has slightly different conditions at the ceiling as noted previously). This suggests that the convective flux is into the ceiling nearer the plume centres.

If it is assumed that the convection at the ceiling is mostly balanced by radiation to the floor (and hence convection at the floor) then, even considering the plume temperatures, larger differences in temperature might be expected between the ceiling surface and the adjacent air. Assuming heat transfer coefficients of the same order as at the floor, similar temperature differences would also be expected

(up to 1.5 K). As the measured temperature differences are very much smaller at the ceiling it seems that the heat balance must be rather different than expected. One possibility is that the radiant fluxes to the ceiling from the heat source(s) are sufficient to change the net radiant flux at the ceiling. In other words, although the surface temperature differences indicate a radiant flux from the ceiling to the floor (as expected) the upward radiant flux from the heat source may be sufficient to offset this in the ceiling heat balance.

Nine of the thermocouples on the ceiling surface were positioned in a closely spaced group as shown in Figure 3.6 (thermocouples cl_1 to cl_8). In the test cases DV7–11, where there was a single plume on the room centre line, the plume was offset by 771 mm laterally from this group of thermocouples. In case DV12 (as well as the chilled ceiling test cases) one of the four plumes was directly in line with this line of thermocouples. The variation in ceiling surface temperature along this line of thermocouples is shown in Figure 4.5. The temperature along the ceiling can be seen to follow a similar profile in each test case and generally increase in temperature with increasing load.

It is interesting to note that the ceiling plenum air temperature (shown near the left axis of Figure 4.5) lies between the maximum and minimum surface temperature in each case. This indicates that the conducted flux may change direction over different parts of the ceiling. There is also clearly a minimum in the ceiling surface temperature near, and a maximum either side of, the plume centre line. It is perhaps surprising that the profile does not move much as the plume centreline moves. The variations shown in the results may have been systematic errors (such as a calibration error) but it can be seen that the temperature differences between the minimum and maximums vary between test cases.

A number of studies have been made of convective heat transfer of jets impinging on normal flat plates (mainly in connection with cooling turbine blades). As might be expected, generally the Nusselt number is reported to decay monotonically from a maximum at the axis of a axisymmetric jet. Hollworth and Gero (1985) for example found that the Nusselt number decreased by over 3:1 between the jet axis and a radial position of 4 times the jet diameter. The relative decrease was greater at greater Reynolds number. However, an number of workers (Lytle and Webb 1994, Gardon and Akfirat 1965, Baughn and Shimizu 1989) found a secondary maxima appeared in the radial Nusselt number distribution at a radius of between 1 and 2 jet diameters depending on Reynolds number and spacing from the plate. Gardon and Akfirat (1965), for example, found distinct secondary

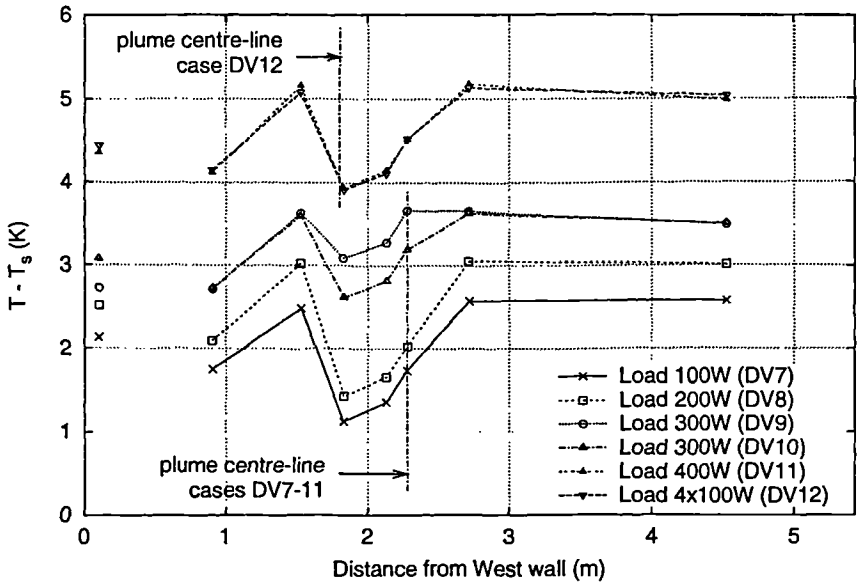


**Figure 4.5:** Ceiling surface temperature measurements showing the variation in temperature near the plumes for test cases DV7–12. The temperatures are normalised with respect to the supply temperature. The ceiling plenum air temperatures are shown adjacent the left axis

maxima with a plate spacing of 2 times the jet diameter and $2800 < Re < 28000$. Lytle and Webb(1994) studied closer spacings (from the base of the jet to the plate), and found that these maxima (at a radius of 1–2 jet diameters) became greater than the Nusselt number at the centre line at close plate spacings and higher Reynolds numbers. The main reason put forward for this phenomena is the penetration of the more turbulent zones at the edge of the jet through the layer of fluid flowing out from the centre line and across the plate.

There is an obvious parallel between the jet impinging on a plate and a buoyant plume impinging on a ceiling. In the case of the plumes generated in the test chamber experiments the spacing between the base of the plume and the ceiling is approximately 2 plume diameters. The secondary maxima in the Nusselt number is dependent on Reynolds number and plate spacing and could be expected to be slightly different in the case of a buoyant plume. This phenomena however may explain the appearance of the maxima in the ceiling surface temperature either side of the plume centre line shown in Figure 4.5. A second possibility (highlighted by time dependent numerical analysis discussed later) is that the plume axis is not stationary but has a periodic motion around the nominal centre line. In this case the maximum of the time averaged convective heat flux may not lie on the centre-line of the heat source.

| *Test case* | *DV7* | *DV8* | *DV9* | *DV10* | *DV11* | *DV12* |
|---|---|---|---|---|---|---|
| Load (W) | 100 | 200 | 300 | 300 | 400 | 400 |
| n ($ac.h^{-1}$) | 1.5 | 1.5 | 1.5 | 3.0 | 3.0 | 3.0 |
| Convective flux ($W.m^{-2}$) | 1.78 | 1.75 | 1.94 | 4.44 | 5.56 | 5.46 |
| Radiant flux ($W.m^{-2}$) | 1.50 | 2.74 | 0.42 | 4.97 | 6.89 | 7.44 |

**Table 4.3:** The approximate convective and net radiant fluxes at the floor

The average ceiling surface temperatures for these displacement ventilation test cases are between 0.22 K and 1.23 K greater than the corresponding average floor temperatures. This temperature difference consistently increases with load. If it is assumed that the floor-to-ceiling radiant coupling is more significant than any other radiant coupling, this would suggest net radiant transfer from the ceiling to the floor. If a radiant heat transfer coefficient of $5.7\,W.m^{-2}.K^{-1}$ is taken along with a view factor of 1.0, then these temperature differences would correspond to heat fluxes from floor to ceiling of between $1.5\,W.m^{-2}$ and $7.4\,W.m^{-2}$ (where the largest total internal load is equivalent to $24\,W.m^{-2}$). If, as in the three and four node models discussed by Mundt (1996), the assumption is made that all the supply flow crosses the floor surface without entrainment then the convective flux at the floor can be approximated by $q_{fc} = \dot{m}\rho C_P(T_{fla} - T_s)/A_{fc}$. This relation has been used to compare the approximate magnitude of the convective flux at the floor with the net radiant flux from ceiling to floor. These fluxes are listed in Table 4.3. It can be seen that both fluxes, approximated in this way, increase with load and are generally of the same magnitude.

The fact that the net radiant heat transfer is downwards in these displacement ventilation test cases, and that heat is transferred convectively from the air to the ceiling and from the floor surface to the air near the floor, can account for the phenomena that in this type of system the air near the floor is always observed to be at a slightly higher temperature than the supply air temperature (Jackman 1990). Heat could be said to 'recirculate' by this path and have the effect of reducing the temperature gradient in the occupied part of the room. This concurs with the findings of Mundt(1990) and Heiselberg and Sandberg(1990).

Considering the maximum and minimum air temperatures (i.e. near the floor and ceiling) shown in cases DV7–9 (Figure 4.1), an interesting trend is that the air temperature near the floor increases much less than near ceiling temperature as

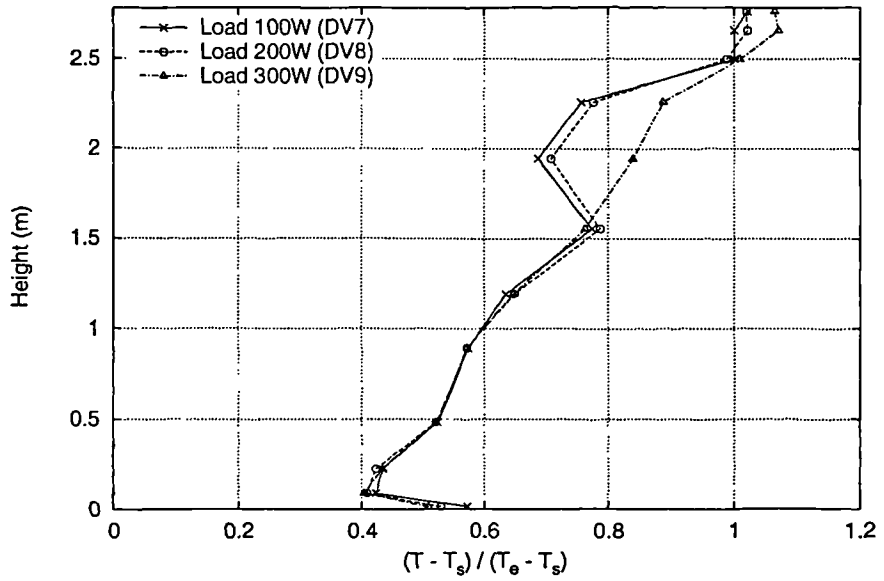


**Figure 4.6:** Normalised air temperature distributions for the displacement ventilation test cases DV7,8 & 9 which have an air change rate of 1.5 per hour.

the load is increased. Figure 4.6 shows these same test case results with the air temperature profile normalised against $(T_e - T_s)$ in each case. It can be seen that with the temperature normalised in this way, the temperature near the floor is nearly the same in each case such that the ratio $(T_{fla} - T_s)/(T_e - T_s) \sim 0.4$. It can also be seen that the normalised temperature gradient in the 0.1–1.6 m zone is also very nearly the same in each case. A similar normalised plot of the air temperature profiles for the cases DV10–12, where the air change rate is 3 ac.h$^{-1}$, is shown in Figure 4.7. There is more variation in the shape of the temperature profiles in these cases but the ratio $(T_{fla} - T_s)/(T_e - T_s) \sim 0.35$.

Mundt(1990) and Li *et al.* (1993) used three and four node models of displacement ventilation respectively to predict this near floor temperature ratio. In Mundt's three node model this ratio is called $\kappa$ and is given by,

$$\kappa = \frac{T_{fla} - T_s}{T_e - T_s} = \left[\frac{\dot{v}\rho C_P}{A}\left(\frac{1}{h_r} + \frac{1}{h_{cf}}\right) + 1\right]^{-1} \tag{4.1}$$

where $\dot{v}$ is the volume flow rate, $h_{cf}$ is the convective heat transfer coefficient at the floor and ceiling, and $h_r$ is the radiative transfer coefficient between the floor and ceiling which has area $A$. According to this model then the near floor temperature ratio $\kappa$ is a function of $\dot{v}/A$ and is independent of the load. The results shown in Figure 4.6 for loads in the range 100 W to 300 W clearly support this hypothesis.

Mundt(1990) showed experimental data from a number of sources for this near floor temperature ratio $\kappa$ plotted against $\dot{v}/A$. Some of this data has been plotted in Figure 4.8 along with data from Li *et al.*'s (1993) test cases and the data of test cases DV7–12. The data points from test cases DV7–12 are on the lower limit of the data group but follow the trend $\kappa \propto (\dot{v}/A)^{-1}$. The spread in the data could be due to the fact that conduction through walls is not taken into consideration in these three and four node models. If some of the load leaves the space by conduction (as a significant portion does in these test cases) this would lower the heat fluxes available to be transferred from the ceiling to floor and to the adjacent air layer so that the temperature of this layer would be nearer the supply air temperature and the ratio $\kappa$ would be lower.

The shapes of the air temperature profiles over the height 0.2–2.7 m show an interesting trend as the load increases. The 100 W and 200 W load displacement ventilation cases DV7 and DV8 have very similar shaped air temperature profiles. There is a very modest temperature gradient ($\sim 0.3\,\mathrm{K.m^{-1}}$) up to the height of 2.3 m, but between 2.3 m and 2.5 m there is a sudden rise in temperature of a further 0.5 K. This is in contrast to the 300 W load cases DV9 and DV10, and the 400 W single load case DV11 which have somewhat more linear profiles.

These changes in the temperature profile shape are indicative of changes in the extent of mixing in the upper part of the room. Linden's plume theory based

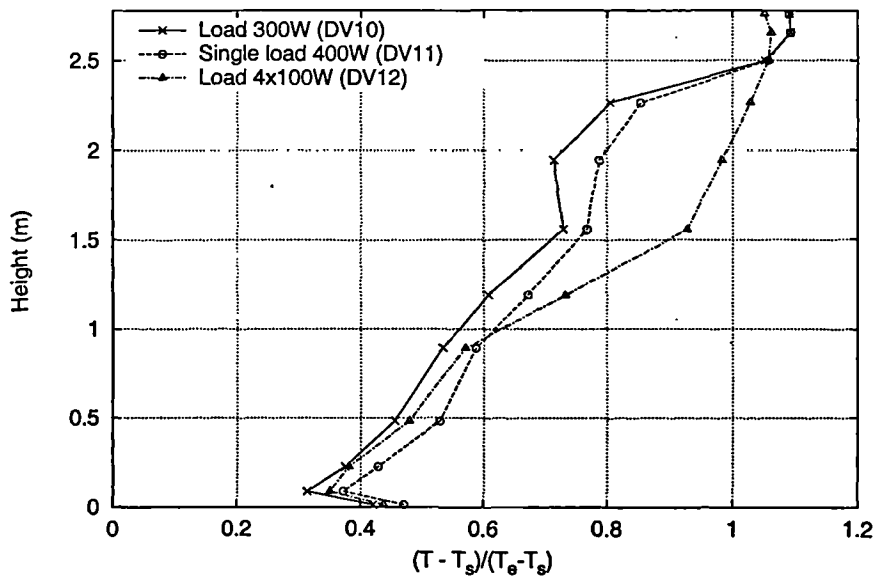


**Figure 4.7:** Normalised air temperature distributions for the displacement ventilation test cases DV9,10 & 12 which have an air change rate of 3 per hour.

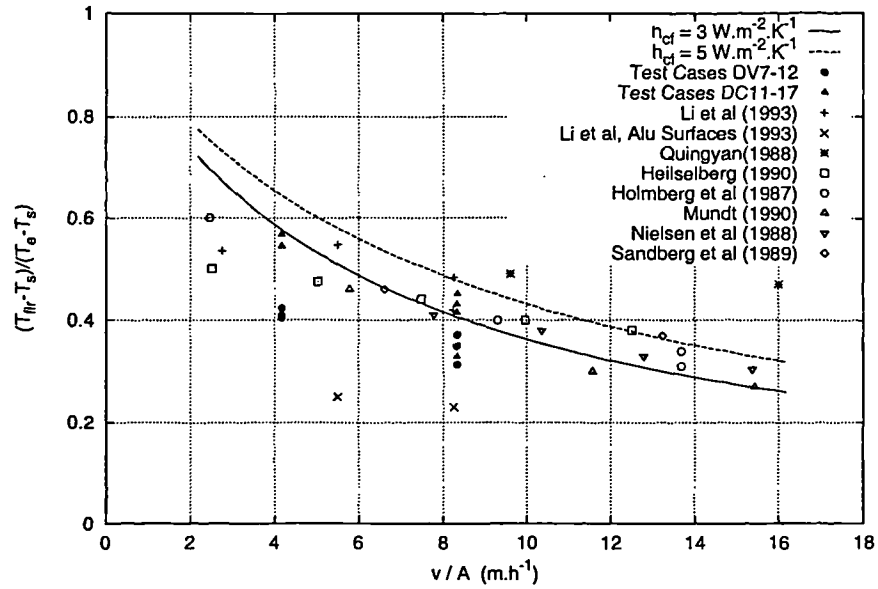


Figure 4.8: The near floor temperature ratio $\kappa$ plotted against $\dot{v}/A$ from a variety of experimental data sources and test cases DV7–12.

models (Linden et al. 1990) and salt bath experiments suggest that there is a well mixed layer of warm air near the ceiling so that there should be a step change in temperature gradient in the upper part of the room. Also the height of the step should reduce as load increased and rise as the air flow rate increased. Such a flow regime may explain the sudden changes in temperature between 2.3 and 2.5 m shown by the profiles of the 100 W and 200 W load cases at 1.5 ac.h$^{-1}$ (DV7 & 8). The nearly linear profile of the 300 W case (DV9) shown in Figure 4.1 and the 400 W single load case (DV11) in Figure 4.2 can not be explained in this way. In these cases, although the plumes have greater momentum and a deeper mixed layer might be expected, there is no sudden increase in temperature but the air is more stratified.

The difference between the air temperature profile shapes of the two 400 W load cases (DV11 & 12) shown in Figure 4.2 is very noticeable in the upper part of the room. A nearly linear profile shape occurs where the 400 W load is confined to a single location (i.e. one plume). The temperature gradient becomes much steeper over the height 1.0–1.5 m where the 400 W load is distributed over four sites of 100 W each. Over the 1.5–2.5 m region the temperature gradient in this case is much reduced, indicating that there may be a deeper well mixed zone adjacent the ceiling. In this case where there are multiple plumes one would expect a greater level of mixing at a given height since, in a plume, $\dot{v} \alpha P^{1/3}$ so that at a given height the volume flow in four plumes of 100 W would be 2.52 times that of a

single plume of 400 W power.

## 4.3 The Displacement Ventilation and Chilled Ceiling Test Cases

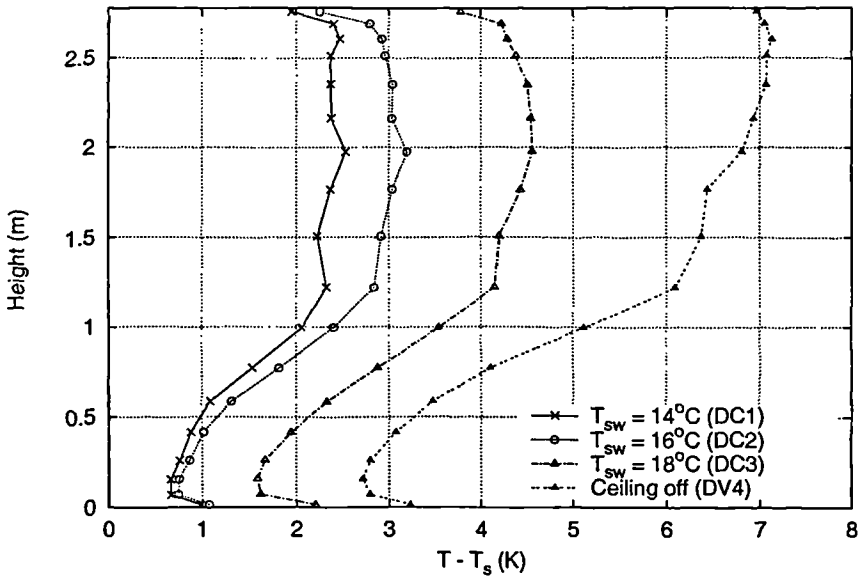


Figure 4.9: Air temperature distributions for test cases DC1–3 and displacement ventilation test case DV4. Load 800 W, air change rate 3 per hour.

For the test cases where the chilled ceiling was also operated, the experimental results are firstly presented for cases where the load and air change rate is constant but the chilled ceiling temperature is varied. Air temperature profiles for the cases measured with the cold junction compensation system are given in Figures 4.9 and 4.10 where the load was 800 W (equivalent to 48 W.m$^{-2}$). The air and surface temperature profiles measured with the ice point system are shown in Figure 4.11 where the load was 450 W (26.8 W.m$^{-2}$) and Figure 4.12 where the load was 600 W (35.8 W.m$^{-2}$). It should first be noted that, although the loads are lower in the latter cases, the air temperature differences are much lower due to the lower outside temperatures (i.e. the conductive heat fluxes out of the chamber were more significant). This was simply due to the latter experiments being carried out during colder weather.

There are a number of features of these air temperature profiles that are common to those where the chilled ceiling is not operating. Firstly the air temperature is

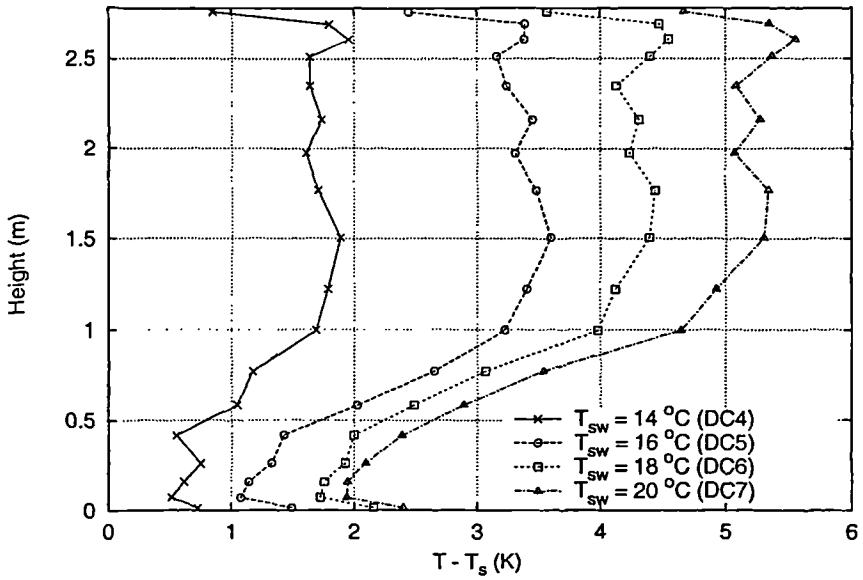


**Figure 4.10:** Air temperature distributions for test cases DC4–7. Load 800 W, air change rate 3 per hour.

at a (local) minimum in the zone just above the floor. In the cases with smaller loads (Figures 4.11 and 4.12) the minimum is clearly at or near the second thermocouple above the floor as in the displacement ventilation test cases. At the higher load of 800 W the transition from a negative to a positive temperature gradient is more gradual and extends up to a height of approximately 400 mm (Figures 4.9 and 4.10).

There is a similar distinction to be made between the 800 W load cases and those of lower loads when considering the position of the maximum air temperature in the room. The results for the lower loads show—in a similar way to the displacement ventilation cases—the maximum temperature at the position of the second or third thermocouple (125 mm and 282 mm) below the ceiling surface. The higher load cases however, show a temperature profile in the upper part of the room which is approximately vertical so that the position of the maximum is less well defined. In cases DC2 & 3 for example, the maximum air temperature is at approximately 2 m.

For one of the displacement ventilation and chilled ceiling test cases, DC10, the air temperature distribution was measured at a number of positions along the length of the room to detect any lateral temperature changes. The load in this test case is 1200 W (equivalent to 72 $W.m^{-2}$) and the air change rate is 3 per hour. These

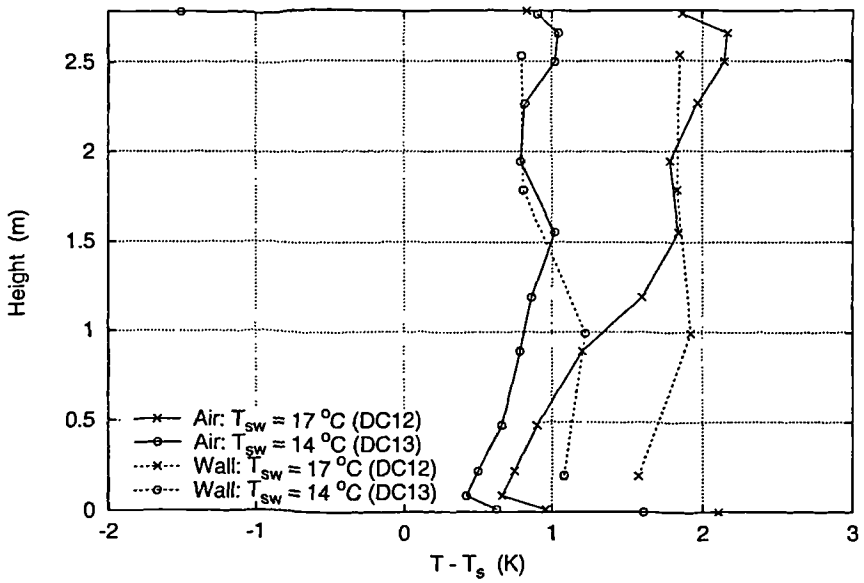


Figure 4.11: Air and wall temperature distributions for test cases DC12 & 13. Load 450 W, air change rate 3 per hour.

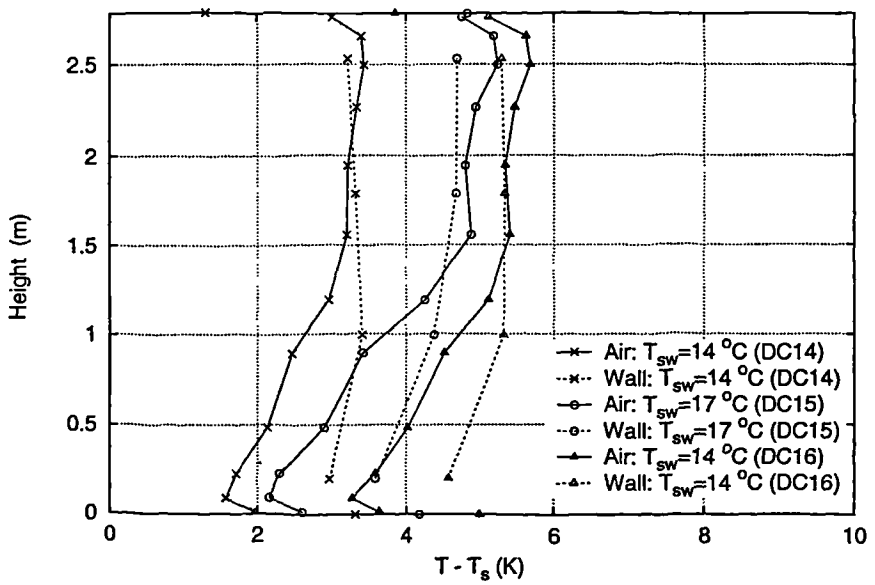


Figure 4.12: Air and wall temperature distributions for test cases DC14–16. Load 600 W. Cases DC14 & 15 have an air change rate 3 per hour, cases DC16 & 17 have an air change rate 1.5 per hour

measurements are plotted in Figure 4.13 where the dimension 'X' is the horizontal distance along the centre-line from the East wall, which is the wall with the supply diffuser mounted on it. Position E is between one of the heat loads and the north

wall as illustrated in Figure 3.8. It can be seen that the lateral variations in room temperature are confined to separate zones. Firstly, the temperature in the zone up to 400 mm above the floor increases with distance from the diffuser, with the largest temperature difference measured between 0.7 m and 1.5 m. Between this zone and the 1.0m level the profile at each position is remarkably similar with a linear gradient of approximately $3\,K.m^{-1}$. Above the 1.0m level there is a notable change in temperature gradient such that the profile is nearly vertical. Finally, near the ceiling there is a strong negative temperature gradient indicative of convective cooling at the ceiling. The temperature profile near the wall varies little from that along the centre-line of the room.

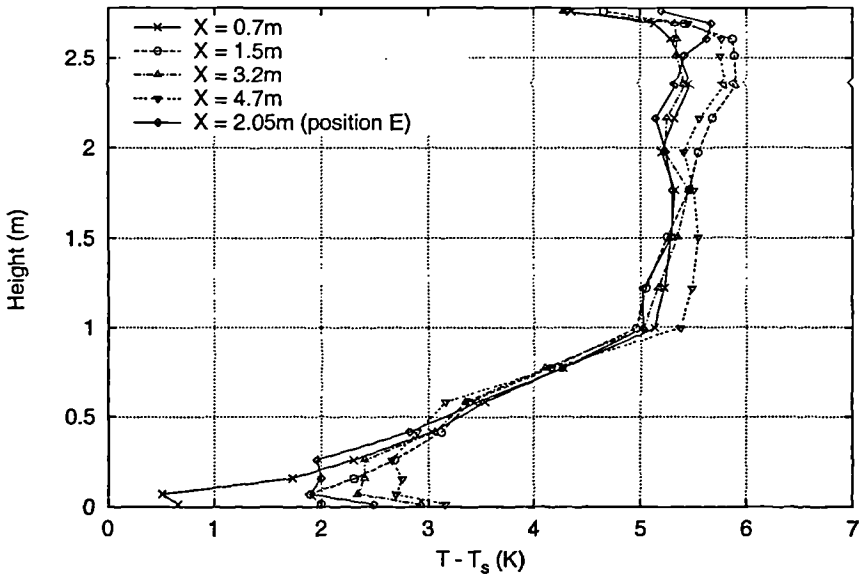


**Figure 4.13:** Air temperature distributions for test case DC10 measured at different horizontal positions. Load 1200 W, air change rate 3 per hour.

The variation in floor surface temperature for cases DC11–17 is shown in Figure 4.14 where the data is plotted in the same ways as in Figure 4.3 for the displacement ventilation cases. These results show that for a particular test case there is less variation in temperature along the floor. Again the maximum temperatures are in the middle of the room nearer the heat sources and the minimum temperature is mostly towards the supply diffuser. The results also show a greater range in floor temperature overall with the floor surface temperatures for the 600 W/1.5 air change rate cases being notably high relative to the air supply temperature.

The convective heat transfer conditions at the floor appear to be similar to that shown in the displacement ventilation results. Firstly, a consistently negative

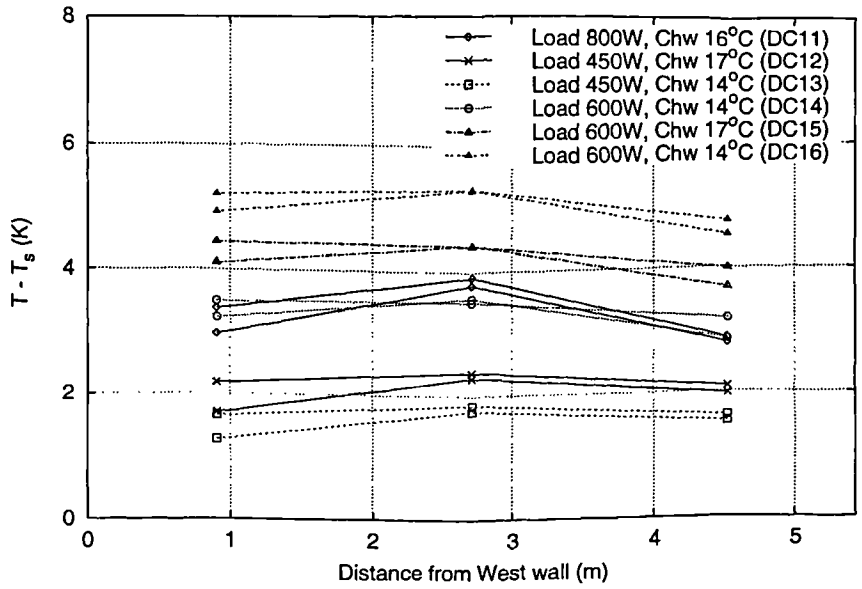


Figure 4.14: Floor surface temperature measurements for cases DC11–16.

temperature gradient is shown between the floor surface and first two air thermocouple measurements just above the floor. The temperature differences between the floor surface and adjacent air temperature are in the range 1.2-2.5 K so that the convective flux clearly acts to heat the air flowing over the floor.

Considering the air temperature profiles near the ceiling and the relative ceiling surface temperatures, the convective heat transfer conditions at the ceiling are somewhat clearer than in the case of the displacement ventilation results. Firstly, the air temperature profiles show a clearly negative temperature gradient in the zone approximately 250 mm below the ceiling. The temperature differences between the ceiling surface and the air in this zone are in the range 1.3–2.9 K.

The temperature distribution across the ceiling is shown for the chilled ceiling test cases DC11–16 in Figure 4.15 in a similar manner to that of Figure 4.5. The operation of the chilled ceiling has resulted in a much wider range of average ceiling temperature (in case DC13 the average temperature is some 2 K below the air supply temperature). It can also be seen that the same trend in variation of temperature along the length of the ceiling occurs as in the case of the displacement ventilation test cases. In the region of the centre-line of the plume the surface temperature is depressed by approximately 1 K below the maximum surface temperature, which occurs a few hundred mm either side of the centre-line. It should be noted that, in Figure 4.15, the data points at the right are not joined to the rest.

It would be unreasonable to suggest a linear variation over this region as another plume impinges on the ceiling at 3.38 m but there were no other thermocouples directly over this plume.

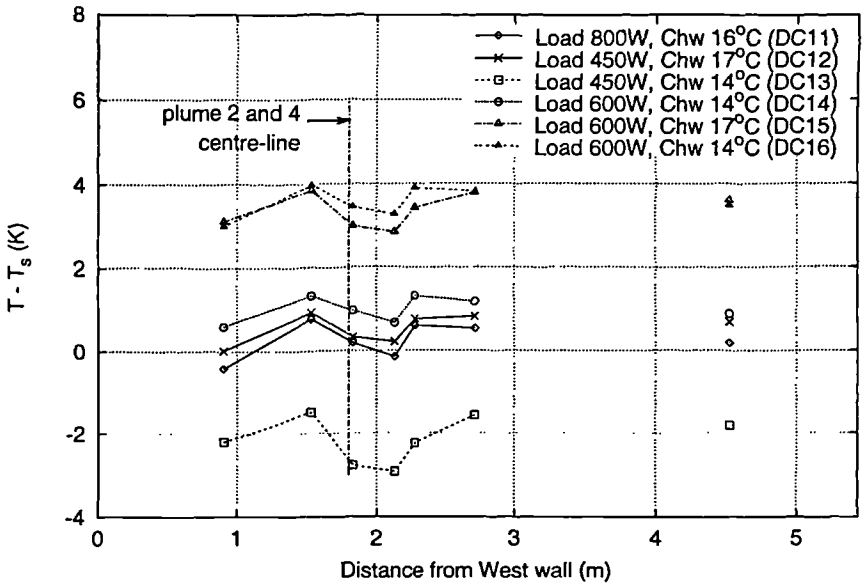


**Figure 4.15:** Ceiling surface temperature measurements showing the variation in temperature near the plumes for test cases DC12–16. The temperatures are normalised with respect to the supply temperature.

The plume temperature measurements and corresponding average ceiling temperatures for the chilled ceiling cases DC11-16 are shown in Figure 4.16. The larger plume air temperatures near the base are a reflection of the greater loads (i.e. larger bulbs used in the heat load simulator boxes) used in the chilled ceiling test cases. Considering these results and those for the displacement ventilation test cases (Figure 4.4) it can be seen that some measurements are grouped together near the base of the plume but diverge nearer the ceiling. There is some correlation between the load used in the upper box of the heat load simulator and temperatures at the base of the plume, and between plume temperatures nearer the ceiling and the surrounding air temperature in the upper part of the room. This would indicate that the load surface temperature has a dominant effect on the temperature at the base of the plume, whereas entrainment of the surrounding air is dominant nearer the top.

A significant difference between the displacement ventilation test cases and those with the chilled ceiling operating is in the difference between the ceiling and floor temperatures. The sign of this temperature difference is in fact reversed, being

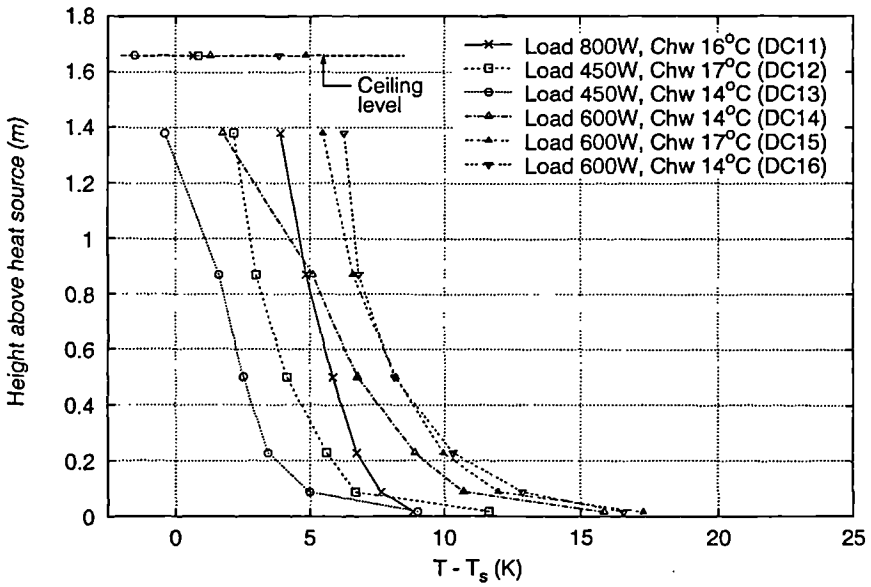


**Figure 4.16:** Temperature measurements along the plume centre line for test cases DC11-16 shown along with the average ceiling surface temperatures.

in the range $-0.42$ to $-3.1$ K for test cases DC11–16. In the displacement ventilation test cases, the ceiling surface was always warmer than the floor, so that the expected dominant radiant flux was from the ceiling to the floor. In the cases with the ceiling system operating the situation is reversed. This is unsurprising in itself—being due to the direct action of the chilled ceiling system—and has implications for thermal comfort (possibly improving comfort over equivalent displacement ventilation conditions).

In view of the ceiling surface being generally cooler than the floor one might expect the dominant net radiant flux to flow up from the floor to the ceiling. However,

| *Case* | *DC12* | *DC13* | *DC14* | *DC15* | *DC16* |
|---|---|---|---|---|---|
| Load (W) | 450 | 450 | 600 | 600 | 600 |
| $n$ (ac.h$^{-1}$) | 3.0 | 3.0 | 3.0 | 3.0 | 1.5 |
| $T_c$ °C | 17 | 14 | 14 | 17 | 17 |
| Ceiling (W) | 128.8 | 247.4 | 199.6 | 104.0 | 159.02 |
| Floor (W) | -23.3 | -78.9 | -22.5 | 43.7 | -0.73 |
| Floor Convective Flux (W) | -33.4 | -27.5 | -81.1 | -94.1 | -80.7 |

**Table 4.4:** Net radiant fluxes at the floor and ceiling calculated for the displacement ventilation and chilled ceiling test cases.

it has already been noted that the convective flux at the floor acts to heat the air near the floor and the air temperature in the lower part of the room is accordingly offset above that of the supply. This convective flux must mainly be balanced by a net radiant flux to the floor surface as the temperature difference between the floor surface and the floor void is small.

The floor and ceiling radiant fluxes calculated using the discrete transfer method (including the effect of the heat sources) along with the convective flux at the floor (calculated as in Table 4.3 for the displacement ventilation test cases) are shown in Table 4.4. The calculations were made using the measured surface temperatures as boundary conditions and the geometry equivalent to that used in the numerical flow calculations (further details are given in Chapter 5). It can be seen that the calculated ceiling flux differs significantly from that of the floor. This suggests that (even though the floor fluxes do not show the expected sign) the radiation field is significantly altered by the presence of four heat sources. It would seem that much of the radiant load is absorbed directly at the ceiling and, though the ceiling is cooler than the floor, the floor and the lower part of the walls are heated by radiant coupling with the load sources.

The air temperature profiles shown in Figures 4.9–4.12 clearly show that the reduction of the ceiling temperature by the operation of the chilled ceiling system reduces the room air temperatures relative to those of the equivalent displacement ventilation conditions. To see whether the change in conditions brought about by the operation of the chilled ceiling changes the relationship between the temperature near the floor and near the ceiling (i.e. the floor temperature ratio $\kappa$) the temperature profiles for cases DC11-16 have been plotted in normalised temperature form in Figure 4.17.

Near the floor the normalised temperatures for cases DC11,14 & 15 fall in a grouping about 0.43, whereas the temperature for case DC16 is at approximately 0.63. These groups of cases are at different loads and ceiling temperatures but at air change rates of 3 and 1.5 respectively. This trend is similar to that shown in the displacement ventilation cases although the values are slightly higher. However, the curve for case DC12 lies outside of these groupings. Unfortunately, the case DC13 (similar to DC12) could not be plotted in this way as the extract temperature ($T_e$) thermocouple developed a fault during the test. These values of non-dimensionalised temperature near the floor ($\kappa$) have also been plotted in Figure 4.8. It can be seen in Figure 4.8, that the data for the chilled ceiling cases fit closely with the theoretical predictions of Mundt/Li's simplified model as well as

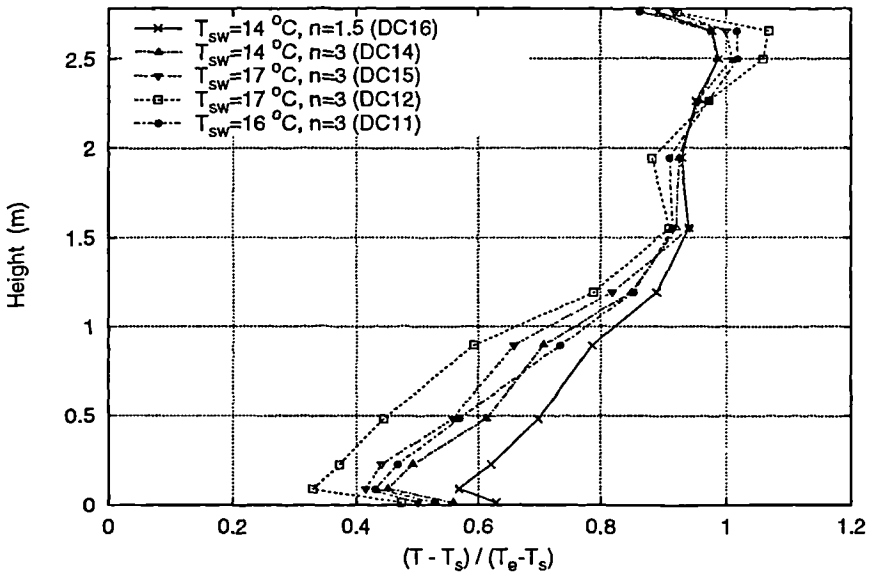


**Figure 4.17:** Normalised air temperature distributions for test cases DC11–16.

with the measured data for displacement ventilation.

It was previously noted that the values of $\kappa$ for the displacement ventilation test case were relatively low because of the significant conducted loss from the test chamber recorded in these tests. However, the outside conditions (see Table 4.1 and 4.2), and hence conduction losses, were very similar in the displacement ventilation cases and the chilled ceiling cases. Hence there may be a more systematic reason why the values for the chilled ceiling test cases are higher than those for the purely displacement ventilation test cases. One explanation for this phenomena is as follows. Consider first the actual size of the temperature differences between the supply and the air near the floor $(T_{fla} - T_s)$. This temperature difference has a similar range of 0.5–4.0 K in both the displacement ventilation and the chilled ceiling results. If $\kappa$ $(= (T_{fla} - T_s)/(T_e - T_s)$ ) is increased in the chilled ceiling results then it follows that it is the temperature difference in the upper part of the room $(T_e - T_{fla})$ that is being reduced by the action of the chilled ceiling. This implies strong convective coupling between the ceiling and the air in the upper part of the room and also increased mixing of the air in the upper zone.

Plotting the non-dimensionalised temperature profiles for the displacement ventilation test cases revealed some interesting differences in the upper part of the room. Consideration of the non-dimensionalised temperature profiles for the chilled ceiling test cases DC11–17 in Figure 4.17 shows rather different trends. Firstly, in

the lower part of the room the temperature gradients vary but the profiles are relatively linear over the height 0.15–1.0 m. Notably linear profiles are also shown for other cases in Figures 4.9, 4.10 and 4.13 where the loads are higher. Secondly, from a height of approximately 1.2 m up to 2.6 m the temperature profiles become very similar with only a small positive temperature gradient. (This is contrast to the displacement ventilation cases shown in Figures 4.6 and 4.7 where the profiles in the lower part of the room are very similar, but differ in the upper part of the room.) The combination of these two features results in a 'kink' in the temperature profiles of the displacement ventilation and chilled ceiling test cases at approximately 1.2 m where the gradient changes significantly.

Much of the temperature rise in the room air appears to take place in the lower part of the room, over the height 0.15–1.0 m where the temperature rise is nearly linear with height. This is essentially the zone below the position of the heat sources and so this temperature rise then can only be accounted for by two mechanisms. The heat associated with this temperature rise can be either conducted from the layer of warm air above (sustained by the heat sources) or convected from the surrounding wall surfaces. The feasibility of these two possibilities can be examined by considering the order of magnitude of the potential conducted and convective heat fluxes.

Firstly it seems reasonable to assume all the supply air flow must rise vertically over this height (i.e. there is vertical plug flow below the plumes). If the typical temperature rise over this height is taken to be 1.5 K (from the measurements), an air flow of 3 ac.h$^{-1}$ would require a heat input of $\sim$70 W to sustain this temperature difference. The heat flow by conduction, with this same temperature difference, from the zone above is calculated to be less than 1.0 W (i.e. two orders of magnitude smaller). To consider the potential convective flux it is first noted that Figures 4.11 and 4.12 show the wall surfaces to be of order 1.0 K warmer than the air in the lower part of the room. Given this driving temperature difference over the lower part of the walls a convection coefficient can be calculated to give the required 70 W heat input. This is found to be 3.3 W.m$^{-2}$.K$^{-1}$, which is certainly of the expected order of magnitude for room conditions.

It seems likely then that it is convection from the walls that drives the temperature increases in the lower part of the room below the heat sources. Although the same clear distinction between the upper and lower parts of the room is not shown in the displacement ventilation results, the wall surface and air temperature differences in the lower part of the room are very similar (see Figures 4.1 and 4.2) and the same

convection mechanism may be at work. It is also interesting to note that the wall–air temperature differences always reduce to zero at between 1.2–1.5 m and become very small or negative above this height in both the displacement ventilation and chilled ceiling cases. Although convection may account for the temperature rise in the lower part of the room it, does not fully explain why the temperature rises are also linear, and with similar gradient, in the upper and lower regions of the room.

Consider now the characteristics of the temperature profiles in the upper part of the room. It has been noted that in the chilled ceiling test cases the profiles over the height 1.2–2.6 m are nearly vertical. This is apparent not only from Figure 4.17 but also from the test cases with higher loads shown in Figures 4.9, 4.10 and Figure 4.13. It can also be seen that the height at which the temperature profile becomes vertical is independent of heat load and chilled ceiling temperature. The fact that the temperature profile is nearly vertical (very small vertical temperature gradient) is indicative of significant mixing and recirculation in this zone. There are two possible contributory driving forces that may work to increase the degree of mixing in this zone above that present in the lower load displacement ventilation cases. These are the additional momentum of the plumes associated with the heat sources and the additional negative buoyancy given to the air near the ceiling by the convective action of the chilled ceiling panels. To estimate the significance of these two driving forces the temperature profiles of some displacement ventilation and chilled ceiling test cases can be compared with those of displacement ventilation test cases under similar load and flow conditions (i.e. similar conditions but with the chilled ceiling system off).

The non-dimensional temperature profiles of cases DV12 and DC12, which have moderate loads of 400/450 W and air flow of 3 ac.h$^{-1}$, are compared in Figure 4.18. It can be seen that, at this load level, there is no noticeable change in temperature gradient between the lower and upper regions of the room. The effect of the chilled ceiling is seen mainly in the zone immediately below the ceiling, where the temperature gradient becomes reversed.

The non-dimensional temperature profiles of cases DC1-3 and DV4, which have higher loads of 800 W and air flow of 3 ac.h$^{-1}$, are compared in Figure 4.19. It can be seen that, at this load, the change in the temperature profile at 1.2 m is distinct, both when the chilled ceiling is on and when it is off. The effect of the reduced ceiling temperature is evident in the zone extending to 500 mm below the ceiling, where the temperature gradient becomes negative at lower ceiling temperatures.

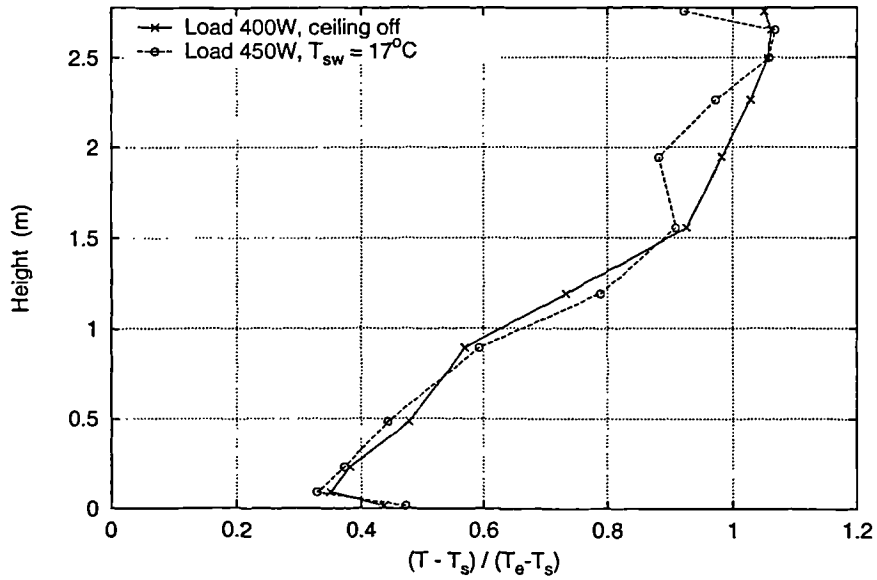


Figure 4.18: Normalised air temperature distributions for test cases DV12 and DC12. Load 400 W, air flow 3 ac.h$^{-1}$.

Comparing Figures 4.18 and 4.19 it can be seen that the temperature gradient in the upper part of the room is sensitive mostly to load size. The effect on the temperature gradient by the action of the chilled ceiling is much less significant.

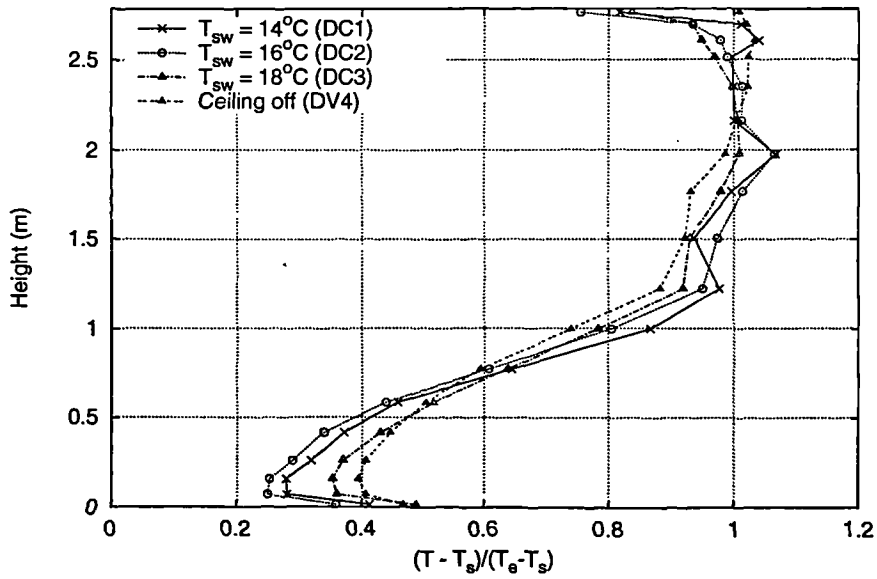


**Figure 4.19:** Normalised air temperature distributions for test cases DC1–3 and DV4. Load 800 W, air flow 3 ac.h$^{-1}$.

The other feature of the displacement ventilation and chilled ceiling results, as

noted earlier, is that the temperature gradient changes at a consistent height of approximately 1.2 m. This height is very close to the height of the top of the load simulator boxes. The base of the load simulator is at table top height, 0.72 m, and the top at 1.12 m. The plumes develop over this height, firstly as a boundary layer up the side of the box before becoming free plumes. This suggests that the lower limit of the relatively well mixed upper zone (at least with the load sizes tested here) may be determined by the height of the base of the plumes. This would in turn imply that the total flow entrained into the plumes is greater than that of the room air supply, such that the fluid entrained into the plumes would need to be recirculated from within this upper zone.

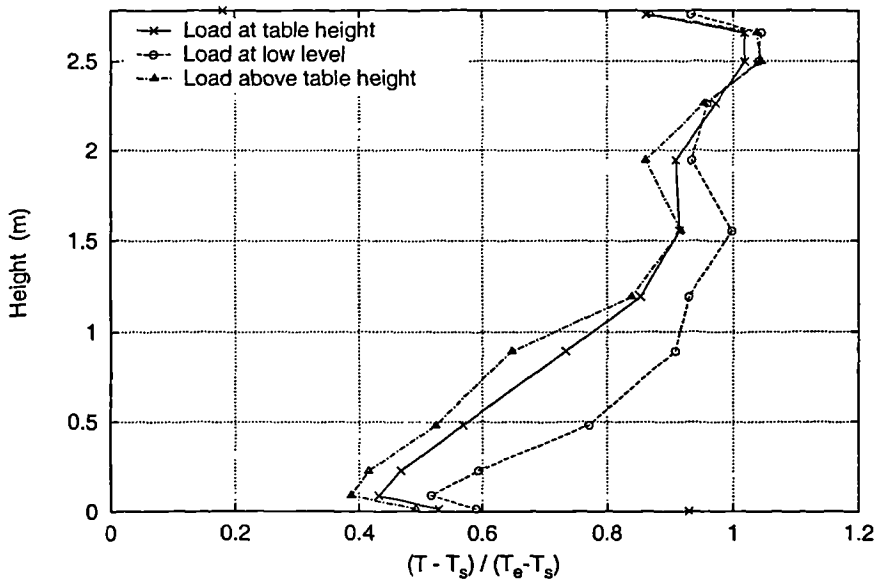


**Figure 4.20:** Normalised air temperature distributions for test case DC11 with the loads at different vertical positions.

To test the hypothesis that the lower extent of the mixed zone in the upper part of the room is determined by the height of the base of the plumes a further experiment was performed. In this experiment the height of the tables and heat load simulators was moved to higher and lower positions (load simulator tops at 1.55 m and 0.69 m respectively). The conditions were otherwise identical to test case DC11. The results of this experiment are shown in Figure 4.20. Where the load has been raised the changes in the temperature profile are only slight. However, where the load was lowered it can be seen that the lower extent of the mixed zone is correspondingly lowered. In this latter case it is also interesting that the floor temperature is relatively higher. This is presumably because of the increased radiant coupling between the heat sources and the floor. This experiment

demonstrates that the above hypothesis may be true.

## 4.4 The Flow Visualisation Experiment

Attempts were made to visualise the flow with the test chamber configured as in test cases DV10 (single load position) and DC10 (four load positions). Observations were made with smoke introduced inside the heat sources, in the supply duct and at high level. Some of the visualisation experiments were recorded with a video camera.

It proved very difficult to visualise the whole of the flow field, particularly the areas adjacent to the plumes where there was mixing and the smoke became diffuse. It was possible however, to visualise the flow near the sources of the smoke and at room surfaces. Some limited conclusions could be drawn:

- near the supply diffuser, the incoming flow was strongly downward and spreading over the floor,
- the flow in the plumes above the heat sources is relatively strong and the velocities here are probably the largest in the room,
- the flow from the plumes impinges on the ceiling with significant velocity and forms a boundary layer moving from the plume centres to the walls and corners of the room with little decay in velocity,
- at the top of the walls, the flow was downward, lower down the walls the direction of the flow was difficult to determine,
- there was generally more mixing in the upper part of the room
- the velocities in the lower part of the room (below the tables) were very small and there was less mixing but it was difficult to define a clear boundary between the upper and lower zones.

These observations are summarised in the sketches shown in Figure 4.21.

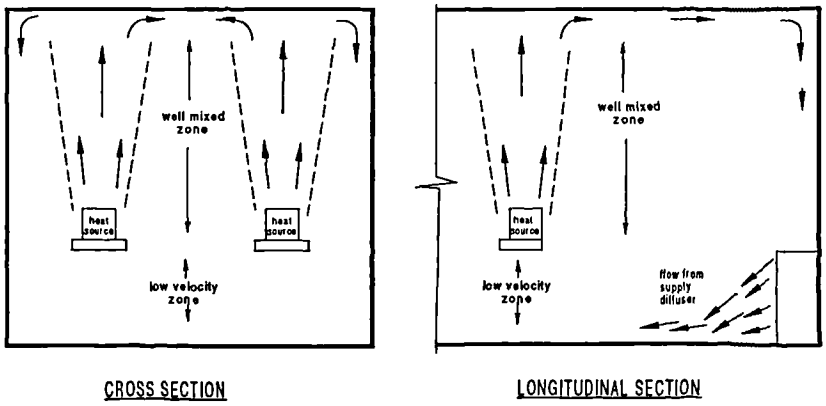


**Figure 4.21:** Sketch showing the principal air movements observed in the flow visualisation experiments.

## 4.5 The Room Air Speed Measurements

Limited air speed measurements were made. These measurements are presented for case DC10 at different horizontal positions in Figure 4.22. These measurements were made at the same time and at the same positions (along the room but outside the plumes) as the temperature measurements presented in Figure 4.13.

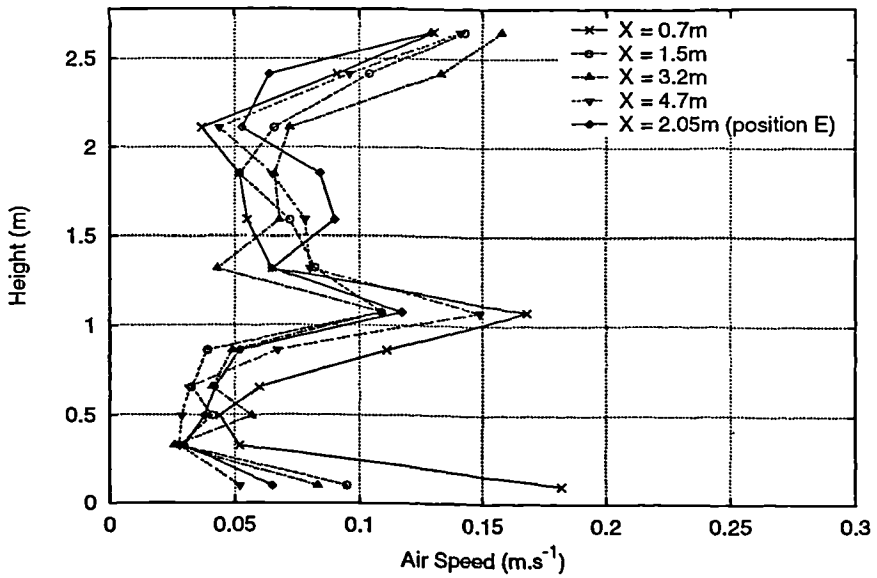


**Figure 4.22:** Air speed measurements for test case DC10 at different horizontal positions.

There are a number of features in the air speed profiles that are repeated at each

of the measuring positions. First it is worth noting that the velocities are all relatively low, being below $0.2\,\mathrm{m.s^{-1}}$. In the zone nearest the floor (0.1 m sensor height) the air speed is at a local maximum which is largest near the supply diffuser and reduces further away. In the zone above this (sensor heights of 0.325–0.86 m) the speed falls to approximately $0.04\,\mathrm{m.s^{-1}}$ indicating very little air movement in this zone. There is a similar zone, with little air movement, in the upper part of the room (sensor heights 1.32–2.11 m) where the air speed is approximately $0.07\,\mathrm{m.s^{-1}}$. The two sensors near the ceiling indicate higher velocities in the range $0.129–0.158\,\mathrm{m.s^{-1}}$ nearest the ceiling. At approximately 1.0 m there is another distinctive maxima in the air speed with measurements in the range $0.109–0.168\,\mathrm{m.s^{-1}}$ at a height of 1.075 m.

The measurement of local maxima in the air speed at the floor and ceiling could be expected in view of the supply flow over the floor and the air from the top of the plumes spreading across the ceiling. The measurement of a peak in the air speeds near the 1.0 m level is more interesting as this height must be close to the height of the base of the plumes. In the visualisation experiments, no particularly noticeable air movement was detected at this level (motion near the centre of the room being difficult to judge). However, below this height a zone of relatively clearer air (less well mixed) was observed. This latter zone seems to correspond to the zone with the very low air speed measurements discussed above (sensor heights of 0.325–0.86 m). Since there is some separation of the fluid between this low level zone and levels above it seems reasonable to assume that the direction of the higher speed air motion detected at 1.075 m is lateral rather than vertical. This suggests some shearing of the fluid at the interface between the upper well mixed zone and the fluid below.

## 4.6 The Coheating Experiment Results

The coheating experiment was performed over a period of seven days. During this period two heat flux meters were used, and moved to a number of points on each room internal surface. This allowed sample measurements of heat fluxes to be made at each surface during different parts of the room diurnal temperature cycle. Measurements were taken over extended periods during night times and over one weekend at the end of the seven days.

A sample of the temperature data showing the diurnal cycles over the seven day

period is shown in Figure 4.23. The data logging started at midday on Monday until the following Monday morning. The room air temperature reached 33°C while the outside air temperature varied between 9°C and 16°C such that a temperature difference of approximately 10 K was maintained between the inner and outer test chamber surfaces. The variations in inner surface temperature followed a similar pattern to the variations in room air temperature and the outer surface temperatures followed the variations in outside temperature more closely. The floor void temperature interestingly lies between the other inner and outer surface temperatures—the suspended floor being relatively low thermal mass and higher conductance.

It can be seen from Figure 4.23 that a steady diurnal temperature pattern does not develop after switching on the heat sources until Wednesday. The temperature pattern also changes slightly at the weekend with the temperatures falling slightly. This is due to the heating system being turned off in the surrounding building zones (the heating system was switched off in the test chamber lab at all times) and a slight fall in outside temperature. As a consequence, data from the first 48 hours has not been used to calculate the fabric conductances.

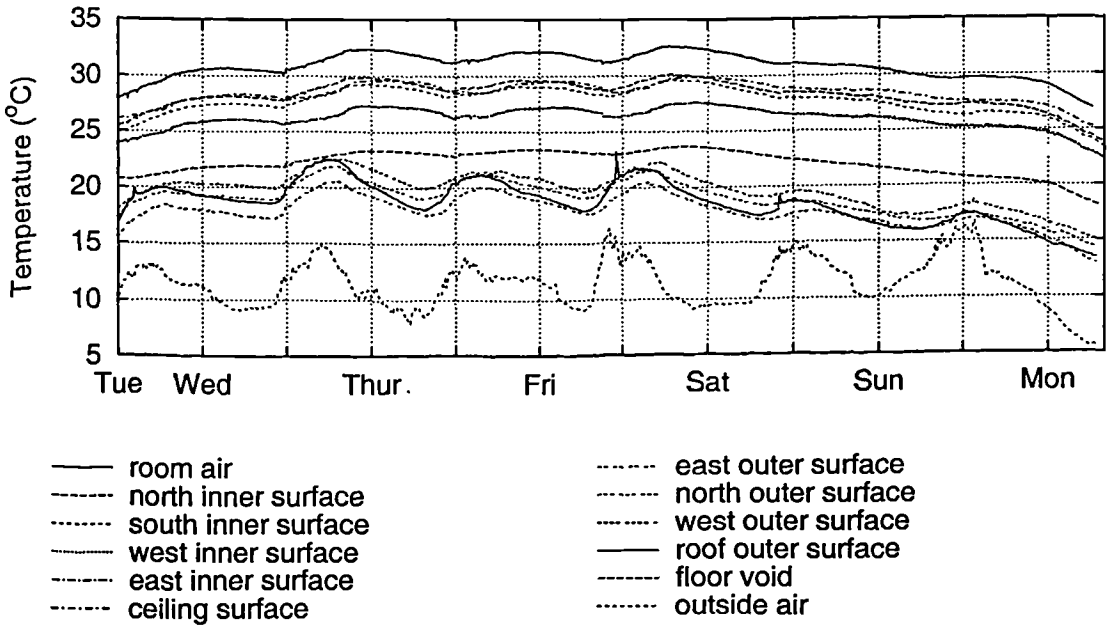


**Figure 4.23:** Internal and external test chamber temperature during the co-heating experiment.

Heat flux data for the floor and ceiling is shown in Figure 4.24. Instantaneous conductances have been calculated using these heat flux measurements and the inner surface and void temperatures. An average conductance has been subsequently

derived. The average conductance has then been used to calculate heat fluxes over this sampling period using the same temperature differences. The difference between the calculated and measured heat fluxes has been plotted and gives an indication of the order of magnitude of error that might occur in using a fixed conductance to calculate the heat flux. In the case of the floor, the error is modest and the measured heat flux correlates well with the measured temperature difference. In the case of the ceiling the correlation is poorer and the error more significant (a maximum of 43.6%). When the outside surface temperature measurement, rather than the ceiling void temperature measurement, is used, the correlation is poorer still. This may be due to an interaction between the lightweight ceiling and the large void above that can not be explained using a simple fixed conductance model.

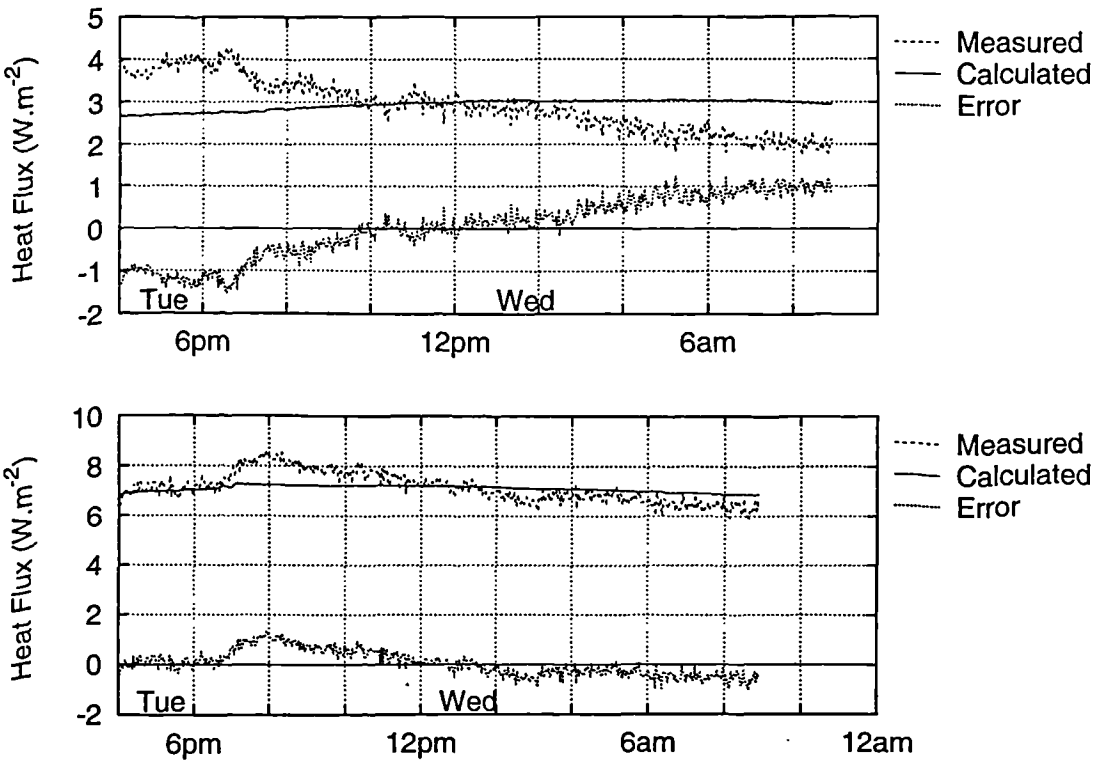


**Figure 4.24:** Measured and calculated conduction heat fluxes for the ceiling (top) and floor (lower) surfaces.

Measured heat flux data for the North, West and East walls is similarly shown in Figure 4.25 along with the calculated heat flux and associated deviation between the measurement and calculated value. In each case the heat fluxes correlate well with the associated temperature differences. This is expected, as each of these walls is believed to have similar lightweight, and poorly insulated, constructions. The temperature differences are very similar in each case but it can be seen that

the heat fluxes are quite high for the West and North walls and more moderate for the East wall.

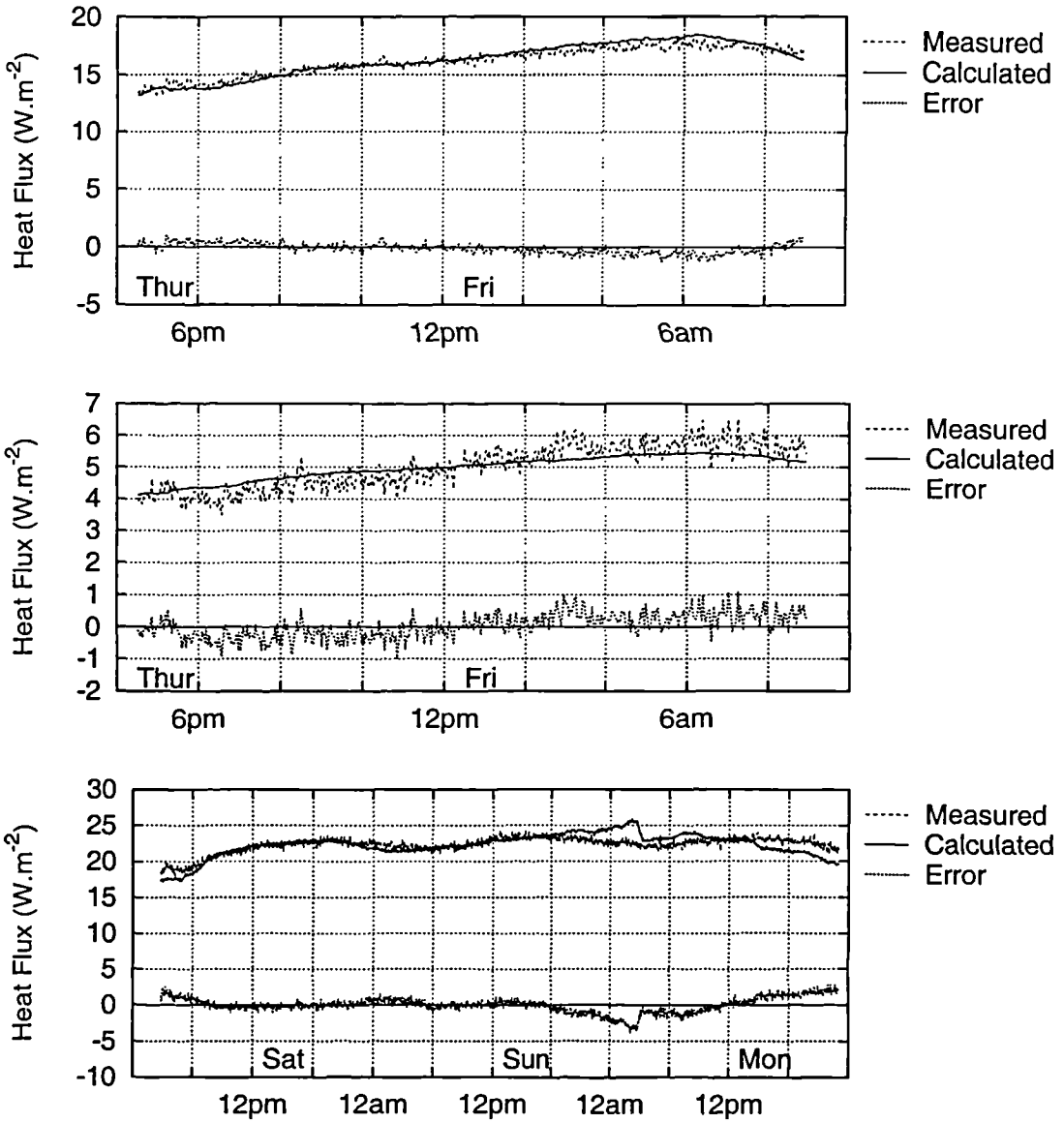


**Figure 4.25:** Measured and calculated conduction heat fluxes for the west (top) and east (centre) and north (lower) wall surfaces.

The South wall of the test chamber is known to be of higher thermal mass than the other surfaces as it incorporates a double thickness of brickwork and additional insulation. The heat flux data for this surface, measured over the latter part of the experiment and plotted in Figure 4.26, shows a poor correlation between the heat flux and the instantaneously measured temperature difference. The temperature difference in this case is taken between the inside surface and the outside air

temperature (no outside surface temperature data being available). The relatively large error in this case is assumed to be because of the dynamic thermal storage effects introduced by the larger thermal capacity of this surface. The heat flux data, during the six hours immediately after the start of measurement on Friday afternoon, shows a rather different trend to the rest of the data. This may be due to the rather different outside temperature cycle shown in the data for Thursday and the change in conditions at the weekend noted previously.

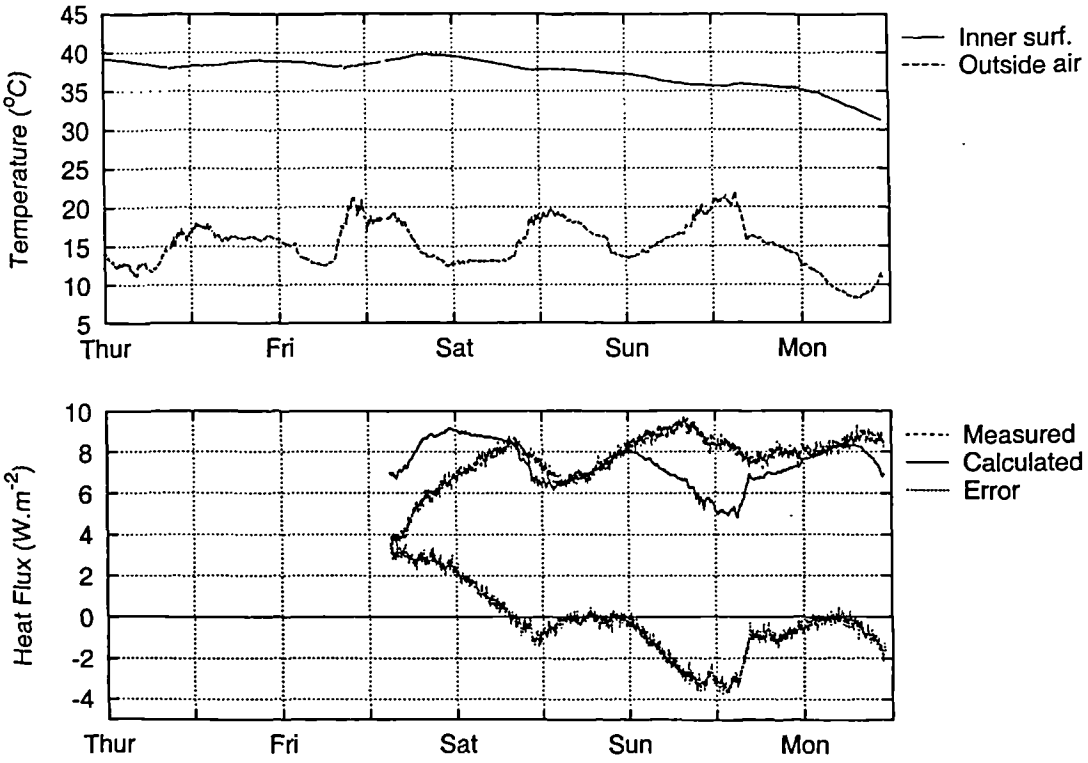


Figure 4.26: Measured and calculated conduction heat fluxes for the South wall surfaces (lower) and the corresponding inside and outside temperatures during the whole experiment (top).

The values of the average conductances calculated from the heat flux and temperature data are given in Tabel 4.5 along with the maximum magnitude of the associated error. These conductances have been used later for two purposes. Firstly, to estimate the conducted heat fluxes at each test chamber surface in a calculation of the resulting convective flux (and associated convection coefficient). In the case of these calculations the significance of the error in the calculation of the convection coefficient depends on the relative size of the radiant flux and the surface-to-air temperature difference and is therefore difficult to assess. Secondly, these conductances are converted to effective wall conductivities in the numerical

| *Surface* | *Floor* | *Ceiling* | *North* | *South* | *West* | *East* |
|---|---|---|---|---|---|---|
| Conductance ($W.m^{-2}.K^{-1}$) | 0.64 | 0.41 | 1.89 | 0.33 | 1.72 | 0.34 |
| Flux Error (%) | 11.9 | 43.6 | 13.3 | 80.6 | 7.2 | 6.1 |

Table 4.5: Test chamber fabric conductances derived from the coheating experiment measurements.

conjugate heat transfer calculations. In this case the significance of the errors depends on the size of the conductive fluxes in relation to the load size. It was later found that the conductive fluxes account for the order of half of the room heat gains, so that the uncertainty in the conductances may result in a similar degree of uncertainty in the calculation of the heat load transferred to the air.

In the case of the South wall—in view of the significance of the dynamic storage effects—the heat flux meters were used in the later system performance experiments to measure the conducted fluxes directly. It should also be noted that the conductance calculated for the ceiling construction (which has a significant error associated with it) is not used in dealing with the chilled ceiling test cases. In these cases the conducted flux is determined by the chilled water temperatures.

## 4.7 Conclusions

The experimental findings of the displacement ventilation and chilled ceiling test cases are summarised below. The significance of the experimental results is discussed further in the final chapter.

1. The characteristics of the air temperature profiles in the lower part of the room were found to be similar in the displacement ventilation test cases and where the chilled ceiling was operated. The floor surface was found to be always warmer than the supply air temperature such that the convective flux at the floor was always upwards, heating the layer of air flowing across the floor from the supply diffuser.

2. The minimum temperature in the room—at a given lateral position—was found in the boundary layer flowing across the floor (at a height of ~90 mm). Above this boundary layer and below the height of the heat sources the air

was found to be stratified, with a nearly constant temperature gradient. The heat gains to the room air in this zone are likely to be due to convection at the wall surfaces.

3. The floor temperature ratio ($\kappa$) was found to decrease with increasing supply air flow rate and to be independent of the load size in the displacement ventilation cases. This concurs with the findings of Mundt (1990) and the predictions of the 4 node model of Li *et al.* (1993). Similar results were found for the chilled ceiling cases but further experiments over a wider range of conditions are required to confirm this.

4. Conditions near the ceiling were found to be approximately adiabatic in the case of the displacement ventilation experiments. In the cases where the chilled ceiling was operated, a negative temperature gradient was induced in the layer of air immediately below the ceiling, indicating significant cooling of the room air by convection at the ceiling surface.

5. Reduction of the ceiling temperature in the displacement ventilation and chilled ceiling experiments caused a reduction in the proportion of the load transferred to the air stream and a reduction in the overall air temperature gradient in the room.

6. In the displacement ventilation experiments with smaller loads, the temperature profile suggests a relatively shallow layer of air below the ceiling. At moderate loads the temperature profile was nearly linear. At higher loads and/or a greater number of plumes greater mixing of the air in the upper part of the room was evident.

7. Greater mixing was evident in the upper part of the room in all the chilled ceiling results as indicated by reduced temperature gradients above a height of approximately 1.2 m. The effect of reduced ceiling temperature on increasing the mixing and reducing the temperature gradient is secondary to that of the increased momentum of the plumes caused by the increased load.

8. The lower extent of the upper mixed zone in the displacement ventilation and chilled ceiling experiments seems to correlate with the height of the base of the plumes. This suggests that at the higher loads associated with displacement ventilation combined with chilled ceiling systems the supply flow may be insufficient to raise the 'interface height' above the base of the plumes i.e. there is significant 'starvation' of the flow in the plumes.

9. Thermal conductances could be found for all the test chamber surfaces, and could be used to find conducted heat fluxes with the exception of the heavyweight south wall. The uncertainties in the conductances were found to be of order 10%, and may result in similar degree of uncertainty in the numerical calculation of the wall conductive fluxes and heat transferred to the air stream, using the conjugate heat transfer calculation procedure.

# Chapter 5

# Numerical Methods

## 5.1 Introduction

Numerical methods of calculating room air flow and heat transfer have the advantages that the room geometry and boundary conditions can be easily varied, and that the detailed information is generated for the whole velocity and temperature fields. The aims of making numerical calculations of the room air flow and heat transfer in this work were:-

- to study the flow and heat transfer in the test chamber experiments in further detail,
- to generate further sets of data for other room geometries that could be used in developing the simplified model.

The aim has not been to develop new or innovative numerical models or techniques, but rather to seek the most appropriate models, boundary condition treatment and numerical methods currently available to apply to the modeling of displacement ventilation and chilled ceiling system flow. Accordingly, a commercial CFD package with a multi-block flow solver (CFDS 1996a) and coupled radiant exchange model (CFDS 1996b) has been used in this work.

The approach to the numerical modeling has been firstly to model the test chamber experiments. Comparison of the numerical calculations of the flow, temperature

and heat fluxes in the test chamber experiments of Li *et al* (Li et al. 1993a) with the experimental results is used to make an initial evaluation of the numerical methods. The experiments of Li *et al* are particularly useful in this respect, in that the experiments were set up partly for the evaluation of numerical codes—having a simple geometry and low emissivity heat source—and in that numerical calculation results for these conditions have also been published (Li et al. 1993b). Calculations of the flow and heat transfer in these test chamber experiments are made with a number of computational grids, boundary condition treatments, discretisation methods and solution techniques. These calculations have been evaluated and a refined numerical method established which is used in the numerical modeling of the Loughborough test chamber experiments. Calculations have also been made using the same numerical methods and a hypothetical geometry intended to represent a larger open plan office space.

In this chapter, a summary of the governing equations and numerical methods are first given. The commercial CFD package used in this work (CFDS 1996a) employs a variety of what can be considered standard models and solution methods. These are discussed briefly, with particular attention drawn to differences between the established methods and those used in the code. Where special boundary conditions have been used or adaptations have been made to the standard models, this has been done using special FORTRAN subroutines of the code available for adaptation by the user. Such adaptations are accordingly discussed in more detail.

## 5.2 The Reynolds Averaged Navier-Stokes Equations

The fundamental equations governing fluid flow are the continuity equation and the momentum transport equations, which together are known as the Navier-Stokes equations. The formulation of the Navier-Stokes equations solved in the method used here involves a number of simplifications and modeling assumptions that are commonly made in dealing with problems such as room air flows. Firstly the Navier-Stokes equations are formulated in their Reynolds Averaged form by separating the velocity components into mean (noted by upper case variables) and fluctuating parts (noted by lower case variables)and time averaging the equations. The time averaging treatment of the momentum equations results in additional terms involving the fluctuating velocity components $\rho\overline{u_i u_j}$ —the Reynolds stresses.

These Reynolds stresses need to be determined by the use of a turbulence model of some form (discussed in section 5.3). The Reynolds Averaged Navier Stokes (RANS) equations can be stated in Cartesian tensor notation as

$$\frac{\partial \rho}{\partial t} + \frac{\partial U_i}{\partial x_i} = 0 \tag{5.1}$$

$$\frac{\partial \rho U_i}{\partial t} + \frac{\partial \rho U_i U_j}{\partial x_j} = -\frac{\partial P}{\partial x_i} + \frac{\partial}{\partial x_j}\left(\mu \frac{\partial \rho U_i}{\partial x_j} + \frac{\partial \rho U_j}{\partial x_i}\right) + \rho g_i - \frac{\partial}{\partial x_j}(\rho \overline{u_i u_j}) + S_i \tag{5.2}$$

It is also assumed that the flow can be treated as incompressible. This simplification means that the first term of the continuity equation is eliminated and that $\rho$ in most of the terms of the momentum equation can be replaced by a constant reference density $\rho_0$ determined by a constitutive relation at a reference temperature $T_0$. For buoyancy effects to be modeled the body force term $\rho g_i$ needs a slightly different treatment. Firstly, $\rho g_i$ is written as $\rho_0 g_i + (\rho - \rho_0) g_i$ and the $\rho_0 g_i$ term is absorbed into the pressure gradient term. Density changes are then related to temperature difference by use of the thermal expansion coefficient $\beta$, so that the body force term becomes $\rho_0 \beta (T - T_0) g_i$ (the Bousinesq assumption).

The model of turbulence used in this work is based on the eddy viscosity hypothesis. The eddy viscosity hypothesis makes an analogy between molecular viscous stresses and turbulent shear stresses by introducing the idea of turbulent viscosity, $\mu_t$, so that the Reynolds stresses are proportional to the mean rates of strain,

$$-\rho \overline{u_i u_j} = \mu_t \left(\frac{\partial U_i}{\partial x_j} + \frac{\partial U_j}{\partial x_i}\right) - \frac{2}{3}\rho_0 \delta_{ij} k. \tag{5.3}$$

Closure of the Reynolds Averaged Navier-Stokes equations using an eddy viscosity turbulence model then becomes a question of modeling and solving further equations for the turbulent viscosity. When the Bousinesq assumption and an eddy viscosity turbulence model are employed the RANS equations can then be expressed as

$$\frac{\partial U_i}{\partial t} + \frac{\partial U_i U_j}{\partial x_j} = -\frac{1}{\rho_0}\frac{\partial P'}{\partial x_i} + \mu_{\text{eff}} \frac{\partial}{\partial x_j}\left(\frac{\partial U_i}{\partial x_j} + \frac{\partial U_j}{\partial x_i}\right) + \beta (T - T_0) g_i + S_i \tag{5.4}$$

with an effective viscosity $\mu_{\text{eff}}$ defined by $\mu_{\text{eff}} = \mu_t + \mu$ and the pressure modified so that

$$P' = P + \frac{2}{3}\rho_0 k - \rho_0 g. \tag{5.5}$$

## 5.3 The Turbulence Model

The turbulence model used here is based on the two equation eddy viscosity model of Launder and Spalding (Launder and Spalding 1974). In eddy viscosity models such as this the basic hypothesis is that turbulent viscosity is proportional to a turbulence velocity scale, $V_c$, multiplied by a length scale (representative of the larger eddy sizes), $L_c$, such that $\mu_t = \rho V_c L_c$. In the $k$–$\varepsilon$ model used here the velocity scale is the square root of the turbulent kinetic energy $k$ (where $k = \frac{1}{2}\overline{u_i u_i}$) and the length scale is defined as $L_c = k^{\frac{3}{2}}/\varepsilon$, where $\varepsilon$ is the rate of dissipation of $k$. A modeling constant $C_\mu$ is also introduced such that

$$\mu_t = \rho C_\mu \frac{k^2}{\varepsilon}. \tag{5.6}$$

Exact transport equations for both $k$ and $\varepsilon$ can be obtained buy manipulation of the Reynolds Averaged Navier-Stokes equations. Both exact equations contain higher order correlations of fluctuating velocities and so closure requires modeling assumptions to be introduced to deal with such terms. Models such as this are therefore semi-empirical in nature. Where Reynolds stresses appear in the $k$ equation they are modeled again according to the effective viscosity hypothesis, so that $\mu_t$ itself appears in the final modeled $k$ equation. Production terms involving higher order correlations are modeled using the generalised gradient diffusion hypothesis (Daly and Harlow 1970). The modeled $k$ equation, after introducing a modeling constant $\sigma_k$, is then of the form

$$\frac{\partial \rho k}{\partial t} + \frac{\partial U_j k}{\partial x_j} - \frac{\partial}{\partial x_j}\left((\mu + \frac{\mu_t}{\sigma_k})\frac{\partial k}{\partial x_j}\right) = P_k + G - \rho\varepsilon, \tag{5.7}$$

where $P_k$ is the production due to strain term given by

$$P_k = \mu_{\text{eff}}\left(\frac{\partial U_i}{\partial x_j} + \frac{\partial U_j}{\partial x_i}\right)\frac{\partial U_i}{\partial x_j}, \tag{5.8}$$

and $G$ is the production due to buoyancy forces given by

$$G = \frac{\mu_{\text{eff}}}{\sigma_T}\beta g_i \frac{\partial T}{\partial x_i}. \tag{5.9}$$

The exact $\varepsilon$ equation contains several higher order correlations of fluctuating velocities which are difficult to measure or calculate. In the high Reynolds number form of the epsilon equation used here, several terms are neglected on the basis of

| Constant | $C_\mu$ | $C_{\varepsilon 1}$ | $C_{\varepsilon 2}$ | $\sigma_k$ | $\sigma_\varepsilon$ |
|---|---|---|---|---|---|
| Value | 0.09 | 1.44 | 1.92 | 1.0 | 1.217 |

**Table 5.1:** Constants used in the $k$–$\varepsilon$ Turbulence Model

their small order of magnitude. The generation rate of $\varepsilon$ is assumed to be proportional to $P_k$, the generation rate of $k$. The destruction rate of $\varepsilon$ is assumed to be proportional to $\varepsilon$. The resulting modeled epsilon equation is

$$\frac{\partial \rho \varepsilon}{\partial t} + \frac{\partial \rho U_j \varepsilon}{\partial x_j} - \frac{\partial}{\partial x_j}\left((\mu + \frac{\mu_t}{\sigma_\varepsilon})\frac{\partial \varepsilon}{\partial x_j}\right) = C_{\varepsilon 1}\frac{\varepsilon}{k}P_k - C_{\varepsilon 2}\rho\frac{\varepsilon^2}{k}, \tag{5.10}$$

The constants $C_\mu$, $C_{\varepsilon 1}$ and $C_{\varepsilon 2}$ are found from empirical observations and here have the values given in table 5.1.

## 5.4 The Energy Equation

The energy equation in its most general form is usually expressed in terms of total specific enthalpy[1] $H$ ($H = h + \frac{1}{2}U^2$). Here, however, the energy equation is formulated in terms of static (thermodynamic) enthalpy $h$, as the flow is being treated as low Mach Number (hence incompressible), and the kinetic energy term $\frac{1}{2}U^2$ in the total enthalpy can be assumed to be relatively insignificant. Similarly the pressure work and kinetic heating terms of the general equation are ignored. The energy equation given these simplifications, and subjected to a similar time averaging treatment to the RANS equations, can be expressed in terms of static enthalpy as

$$\frac{\partial \rho h}{\partial t} + \frac{\partial \rho U_j h}{\partial x_j} - \frac{\partial}{\partial x_j}\left(\frac{\lambda}{C_p}\frac{\partial h}{\partial x_j} + \overline{\rho u_j h}\right) = S_e, \tag{5.11}$$

where $-\overline{\rho u_j h}$ are the turbulent enthalpy fluxes which arise from the time averaging of the non-linear convection term in a similar manner to the Reynolds stresses of the RANS equations. $S_e$ is a source term which might be used to include such phenomena as radiant heating of the air, but is used here only for the introduction of heat at the location of internal heat sources.

[1] $H$ is used to denote total specifc enthalpy (J/kg) rather than total system enthalpy (J) as in thermodynamics texts.

The energy equation must be closed by using a calorific equation of state defining the relationship between static enthalpy and temperature and pressure, $h = h(T, p)$. It is usually assumed that the static enthalpy is a function of temperature only and is expressed as some function of specific heat $C_p$. The code (CFDS 1996a) allows $C_p$ to be defined by a variety of expressions, but a constant value is used here in view of the very small temperature range of the flow. Hence total enthalpy is related to temperature only, so that $h = C_pT$. The energy equation, given this simplification of the calorific equation of state, could be expressed in terms of temperature only, rather than enthalpy. However, since the code uses the enthalpy form internally for the sake of generality (i.e. discretises this form of the equation and solves for $h$), this form is retained below.

With a two equation eddy viscosity model, such as that used here, the turbulent heat fluxes are modeled using the eddy diffusivity hypothesis (analogous to the treatment of the turbulent momentum fluxes) so that

$$-\rho\overline{u_j h} = \frac{\mu_t}{\sigma_H}\frac{\partial h}{\partial x_j}, \tag{5.12}$$

where $\mu_t$ is calculated with the turbulence model and $\sigma_H$ is $C_p$ multiplied by $\sigma_T$ the turbulent Prandtl number.

Given the use of the $k$–$\varepsilon$ turbulence model and the modeling of the turbulent enthalpy flux as defined in equation 5.12 the modeled Reynolds averaged energy equation becomes

$$\rho\frac{\partial h}{\partial t} + \rho\frac{\partial U_j h}{\partial x_j} - \frac{\partial}{\partial x_j}\left(\frac{\lambda}{C_p} + \frac{\mu_t}{\sigma_H}\right)\frac{\partial h}{\partial x_j} = S_e. \tag{5.13}$$

## 5.5 The Solution Procedures

Solution of the governing flow and heat transfer equations by numerical means requires firstly, discretisation of the differential equations, linearisation of the resulting algebraic equations and application of the boundary conditions before final application of algebraic solver algorithms to the large sets of simultaneous algebraic equations. The solution methodology can be thought of consisting of a number of sub-processes or algorithms which together constitute a method of producing a solution to the coupled non-linear partial differential equations. Many of these sub-processes are algorithms that have been extensively tested and reported upon

in the literature and for this reason are described and discussed only briefly in this section

### 5.5.1 Discretisation of The Equations

Numerical solution of the governing partial differential equations results in values of the fundamental variables of these equations being found at discrete points in a geometric mesh of the flow field. There are several approaches to discretising the equations (e.g. Finite Difference or Finite Element methods). The method used here is known as the 'Finite Volume' method. The finite volume formulation is to be preferred over other methods on the basis that the consistency and conservation properties of the original differential equations are guaranteed to be preserved in the discrete analogue (Patankar 1980). In the finite volume formulation the partial differential equations are firstly integrated over a finite control volume. The resulting algebraic equations then describe the transport of *fluxes* of the fundamental quantities.

The governing equations can be expressed as a generalised convection-diffusion equation such as

$$\frac{\partial \rho\phi}{\partial t} + \frac{\partial \rho U_j \phi}{\partial x_j} - \frac{\partial}{\partial x_j}\left(\Gamma \frac{\partial \phi}{\partial x_j}\right) = S_\phi, \tag{5.14}$$

where $\Gamma$ is the appropriate diffusion coefficient and $S_\phi$ the source term with appropriate dimensions.

The finite volume formulation can be illustrated by reference to a one dimensional example. The first step in discretising this type of equation by the finite volume method is to integrate it over the cell volume. Equation (5.14) in its one dimensional form and integrated in this way becomes

$$\int \frac{\partial \rho\phi}{\partial t}\, dx + \int \frac{\partial \rho U_j \phi}{\partial x}\, dx - \int \frac{\partial}{\partial x}\left(\Gamma \frac{\partial \phi}{\partial x}\right) dx = \int S_\phi\, dx. \tag{5.15}$$

A notional one-dimensional control volume is shown in figure 5.1 over which the above integrated equation is to be evaluated to find the value of $\phi$ at point $P$. (Constant cell spacing is shown but the extension to variable spacing is straight forward.) First it should be noted that a number of assumptions are made in forming the algebraic equations (Patankar 1980):

1. $\phi$ is constant over the face of the cell

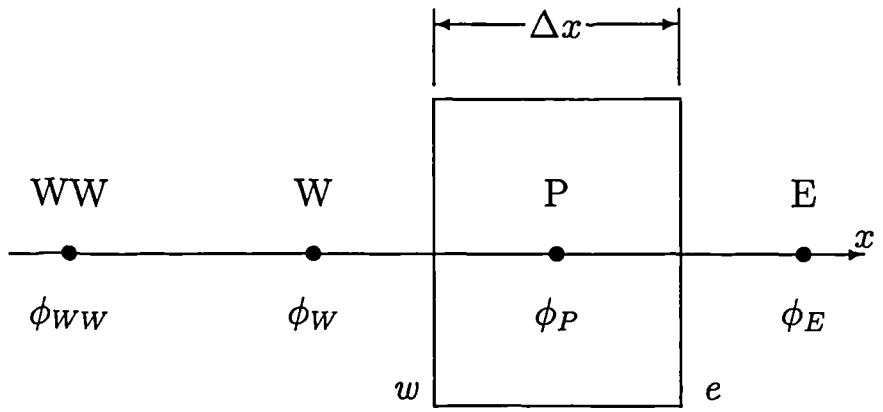


**Figure 5.1:** A notional one-dimensional control volume with constant node spacing.

2. The source term $S_\phi$ is constant over the control volume, at a value determined at the cell centroid $P$

3. The diffusion coefficient $\Gamma$ varies linearly between grid nodes if it is dependent on $\phi$.

Firstly, the source term of equation (5.14) is normally arranged to allow for a dependency on the variable and linearised so that,

$$S_\phi = B^*\phi_P + C^*. \tag{5.16}$$

The integrated source term in equation (5.15) is then

$$\int S_\phi \, dx = B\phi_P + C, \tag{5.17}$$

where the dimensions of $B$ and $C$ are suitably modified from that of $B^*$ and $C^*$. Taking the diffusion term of equation (5.15) next, this becomes

$$\int_w^e \frac{\partial}{\partial x}\left(\Gamma\frac{\partial\phi}{\partial x}\right) dx = \left[(\Gamma\frac{\partial\phi}{\partial x})_w - (\Gamma\frac{\partial\phi}{\partial x})_e\right], \tag{5.18}$$

and the convection term becomes

$$\int_w^e \frac{\partial\rho U_j\phi}{\partial x}\, dx = [(\rho U\phi)_w - (\rho U\phi)_e]. \tag{5.19}$$

From the integration of the convection and diffusion terms it is apparent that it is necessary to find an algebraic expression for the values of $\phi$ (and its gradients) at the cell faces involving only values at other cell centres. These expressions or interpolating polynomials are defined by a differencing scheme.

### 5.5.2 The Differencing Schemes

The differencing schemes used here are known as the Central Differencing Scheme (CDS), upwind differencing scheme (UDS), hybrid differencing scheme (HDS) and Higher Order Differencing scheme (HOD). These are defined as follows.

#### Central Differencing Scheme (CDS)

In this differencing scheme the values of $\phi$ at the cell faces are calculated as the average of the values of $\phi$ at the cell centres either side. Referring to the example illustrated in Figure 5.1 then

$$\phi_w = \tfrac{1}{2}(\phi_W + \phi_P), \qquad \phi_e = \tfrac{1}{2}(\phi_P + \phi_E). \tag{5.20}$$

A Taylor series analysis of this differencing scheme shows that it results in a discretised equation that is second order accurate (the error being proportional to the mesh spacing squared). The CDS is an obvious enough form of differencing scheme but it has been found that when used to discretise the convection terms it can lead to numerical instabilities and unphysical solutions at anything but very low velocities (Roache 1982, Patankar 1980). The CDS is used here to discretise all of diffusion terms of the governing equations.

#### Upwind Differencing Scheme (UDS)

The Upwind differencing scheme was proposed by Courant *et al* (Courant, Isaacson and Rees 1952) in an attempt to overcome the difficulties of the CDS in dealing with convection effects. In this scheme the value of $\phi$ at the cell face takes the value of $\phi$ at the neighbouring cell centre depending on the direction of flow so that

$$\begin{aligned} \phi_e &= \phi_P \quad \text{for} \quad U_e > 0, \qquad \phi_e = \phi_E \quad \text{for} \quad U_e < 0. \\ \phi_w &= \phi_W \quad \text{for} \quad U_w > 0, \qquad \phi_w = \phi_P \quad \text{for} \quad U_w < 0. \end{aligned} \tag{5.21}$$

Again, using a Taylor series expansion technique, it may be shown that the truncation error using this approximation is proportional to mesh spacing $\Delta x$, and so is said to be first order accurate with respect to mesh spacing. On a uniformly spaced mesh the error is

$$Error = U\frac{\Delta x}{2}\frac{\partial^2 \phi}{\partial x^2}. \tag{5.22}$$

This error involves a second order derivative and is therefore of similar form to the diffusion terms in the equations and can be said to represent 'false diffusion'. This type of false diffusion error can hide the true performance of the turbulence model and often results in smearing of features in the flow such as steep cross stream gradients (Raithby 1976, Leschziner 1980).

### Hybrid Differencing Scheme (HDS)

The hybrid differencing scheme was proposed by Spalding (Spalding 1972) and is an attempt to combine the best features of the central and upwind schemes. It can be shown that when the central differencing scheme is used to discretise both convection and diffusion terms the limit on numerical stability of the resulting set of algebraic equations is determined by a cell Peclet number of 2. The cell Peclet number $Pe_c$ is a non-dimensional number and is defined as the ratio of convection to diffusion so that in this example

$$Pe_c = \frac{\rho U \Delta x}{\Gamma}. \tag{5.23}$$

The hybrid scheme is designed such that where $|Pe_c| < 2$ the CDS is applied, and where $|Pe_c| \geq 2$ the UDS is applied. In this case of the west face in Figure 5.1 then

$$\begin{aligned} \phi_w &= \tfrac{1}{2}(\phi_W + \phi_P) && \text{for } \mathrm{Pe_c} < 2, \\ \phi_w &= \phi_W && \text{for } \mathrm{Pe_c} \geq 2, \mathrm{U_w} > 0, \\ \phi_w &= \phi_P && \text{for } \mathrm{Pe_c} \geq 2, \mathrm{U_w} < 0. \end{aligned} \tag{5.24}$$

This arrangement has the advantage that where convection dominates the flow numerical stability is promoted (although there is a risk of false diffusion errors) and where diffusion dominates (across streams and in areas of low flow) second order accuracy is retained.

### Higher-order Upwind Differencing Scheme (HUDS)

This is a second order accurate upwind scheme. In order to increase the order of accuracy over that of the UDS/HDS it is necessary to include the two upwind cell centroid values so that for the west face

$$\phi_w = \frac{3}{2}\phi_W - \frac{1}{2}\phi_{WW}. \tag{5.25}$$

These differencing schemes are evaluated in calculating the flow and temperature distribution in some of the test chamber experiments of Li *et al* and discussed in section 6.2.2.

### 5.5.3 Assembly of the Algebraic Equations

Returning to the example one-dimensional equation (5.18), the diffusion term in equation can be evaluated by using a central difference approximation for the gradients of $\phi$ at the faces of the cell so that

$$\int_w^e \frac{\partial}{\partial x}\left(\Gamma\frac{\partial\phi}{\partial x}\right) dx \approx \left[(\Gamma_w\frac{(\phi_P-\phi_W)}{\Delta x}) - (\Gamma_e\frac{(\phi_E-\phi_P)}{\Delta x})\right], \tag{5.26}$$

where $\Gamma$ may be linearly interpolated so that $\Gamma_w = (\Gamma_W + \Gamma_P)/2$ and $\Gamma_e = (\Gamma_P + \Gamma_E)/2$. The convection term can be evaluated using the Upwind scheme so that,

$$[(\rho U\phi)_w - (\rho U\phi)_e] \approx [(\rho U)\phi_W - (\rho U)\phi_P], \tag{5.27}$$

assuming that $U > 0$ at each face.

It is now possible, after expressing the discretised equation in terms of values of $\phi$ at neighbouring cells, to gather together terms using a series of coefficients $a_{nb}$ associated with the neighbouring cells so that the whole equation is

$$\begin{aligned}\frac{\partial}{\partial t}(\rho\phi\Delta x) &= a_E(\phi_E-\phi_P) + a_W(\phi_W-\phi_P) + B_P\phi_P + C_P \\ &= \sum_{nb} a_{nb}(\phi_{nb}-\phi_P) + B_P\phi_P + C_P,\end{aligned} \tag{5.28}$$

where $\sum_{nb}$ implies summation over the neighbouring cells. In a three dimensional case this would simply include terms for the other six neighbouring cells.

To accommodate the temporal term an implicit backward differencing approach is used here, so that where the superscript $n$ indicates the current time step,

$$\frac{\rho\Delta x}{\Delta t}(\phi^n - \phi^{n-1}) = \left[\sum_{nb} a_{nb}(\phi_{nb}-\phi_P) + B_P\phi_P + C_P\right]^n. \tag{5.29}$$

This can be re-written as an expression for $\phi$ at the current time step by absorbing the $\phi_P^{n-1}$ term into the source term,

$$(A_P - S_P)\phi_P = \sum_{nb} a_{nb}\phi_{nb} + S_U, \tag{5.30}$$

where,

$$\begin{aligned} A_P &= \sum_{nb} a_{nb}, \\ S_P &= B_P - \frac{\rho \Delta x}{\Delta t}, \\ S_U &= C_P + \frac{\rho \Delta x}{\Delta t} \phi^{n-1}. \end{aligned}$$

The discretised equations for each cell form a large set of algebraic equations that can be expressed in matrix form as,

$$[A]\,[\phi] = [B]\,, \tag{5.31}$$

where $[A]$ is the coefficient matrix (and is generally dependent on $\phi$), $[\phi]$ is the vector of unknowns, and $[B]$ is the vector of source terms.

The sets of equations to be solved in this case are formulated in terms of the fundamental variables $U, V, W, h, P, k$ and $\varepsilon$. Each of these equations are coupled together and made non-linear by velocity appearing in the coefficients of the convection terms. In the case of the $k$ and $\varepsilon$ equations these are also made non-linear by $\mu_t$ appearing in the coefficients, and the nature of the source terms. In order to deal with these non-linearities in the solution procedure an iterative approach is used where the algebraic equations are successively re-linearised. At each iteration step, values from the previous iteration are used to re-calculate the equation coefficients before re-applying a linear algebraic equation solver algorithm.

The coefficient matrices $[A]$ are narrowly banded and amenable to the application of a number of linear equation solver algorithms. These linear equation solver algorithms typically require a number of iterations to solve the algebraic equations (to a given tolerance). Thus the solution procedure consists of (at each time step in a transient solution) an outer iteration loop where the equation sets are linearised and coefficient matrices reformed, and a series of inner iteration loops where each of the equation sets is solved, in sequence, by the application of a linear algebraic solver algorithm.

The algebraic solver algorithms used here are the Line Relaxation algorithm (applied to the $k$ and $\varepsilon$ equations), the STONE algorithm (applied to the momentum and energy equations) and the ICCG Preconditioned Conjugate Gradients method (applied to the pressure correction equation).

### 5.5.4 The Pressure Correction Algorithm

The governing equations to be solved here are formulated in terms of the fundamental quantities $U, V, W, h, P, k$ and $\varepsilon$. The equations in their original general form are also coupled together by the density $\rho$. In a compressible flow calculation $\rho$ could be solved for using the continuity equation, and the pressure found from the ideal gas law ($P = \rho RT$). However, here the flow is treated as being incompressible and density is effectively fixed so that the pressure field can not be found in this way. The first problem in calculating the pressure field then, is the choice of an appropriate independent equation. Pressure appears only as a gradient term in the momentum equations—the natural equations to use to find the velocities. The momentum equations could be manipulated to derive a Poisson for pressure but this would not help as this would not be an independent equation.

The second problem concerning the pressure field is that at low Mach numbers the momentum field is very sensitive to changes in the pressure field, and hence to errors in its solution. To ensure numerical stability it is therefore necessary to solve the pressure field relatively accurately and ensure that the momentum equations are forced towards satisfying continuity.

These problems in calculating the pressure field in an incompressible flow calculation are typically overcome by adopting a pressure correction procedure. In this type of procedure an independent equation for pressure is found by substituting a form of the momentum equation into the continuity equation giving an equation for a pressure correction $\delta P$. This equation is discretised and solved in a similar manner to the other equations. The velocities are then calculated in a two step process. The procedure used here is known as SIMPLEC (Van Doormaal and Raithby 1984) which is a refinement of the SIMPLE[2] algorithm (Patankar and Spalding 1972) .

In this type of pressure correction procedure the velocity field is first calculated with the existing pressure field $P^n$ to give a first estimate of the velocity $U^*$ which will not satisfy the continuity requirement. The aim is to find a pressure correction $\delta P$ such that $P^{n+1} = P^n + \alpha_P \delta P$ and a corresponding velocity correction $\delta U$ such that the new velocity field given by $U^{n+1} = U^* + \delta U$ satisfies continuity. An equation for the velocity correction can be found by subtracting the momentum

[2]Semi-Implicit-Method-for-Pressure-Linked-Equations. The additional C of the SIMPLEC acronym stands for 'Consistent'.

equation for $U^*$ from the momentum equation for $U^{n+1}$. In discretised form this would give for the $U$ velocity correction,

$$\left(\frac{\Delta x\Delta y\Delta z}{\Delta t}+a_{nb}^{U}\right)\delta U_P=-\sum_{nb}a_{nb}^{U}\delta U_{nb}-\Delta y\Delta z(\delta P_e-\delta P_w), \qquad (5.32)$$

and similarly for the $\delta V$ and $\delta W$ velocity corrections. In the SIMPLE algorithm the $\sum a_{nb}^{U}\delta U_{nb}$ term is simply dropped to find an explicit form of velocity correction equation. In the SIMPLEC algorithm a more accurate approximation to equation (5.32) is sought by subtracting $\sum_{nb} a_{nb}^{U}\delta U_P$ from both sides and dropping the $\sum_{nb} a_{nb}^{U}(\delta U_{nb}-deltaU_P)$ term from the right-hand side to give,

$$\delta U_P=dip(\delta P_w-\delta P_e) \qquad (5.33)$$

where

$$dip=E\Delta y\Delta z/[(1+E)a_P^U-E\sum a_{nb}^{U}] \qquad (5.34)$$

and

$$E=\Delta t\, a_{nb}^{U}/\Delta x\Delta y\Delta z. \qquad (5.35)$$

Substitution of $U^{n+1}=U^*+\delta U$ etc. into the continuity equation gives the pressure correction equation, a Poison equation for $\delta P$, which in tensor notation is

$$\frac{\partial}{\partial x_i}\left(\frac{\partial \delta P}{\partial x_i}\right)=\frac{1}{\Delta t}\left(\frac{\partial U_i^*}{\partial x_i}\right) \qquad (5.36)$$

The pressure correction procedure can therefore be summarised as:

1. solve momentum equations to find approximate velocity field $U^*$ etc. using current pressure field $P^n$,
2. solve pressure correction equation (5.36) to find $\delta P$,
3. use $\delta P$ to make velocity corrections using equation (5.35),
4. update the pressure field using $P^{n+1}=P^n+\alpha_P\delta P$ , where $\alpha_P$ is a relaxation factor.

A smaller relaxation factor $\alpha_P$ is required when correcting the pressure field when using the SIMPLE algorithm compared to the SIMPLEC algorithm due to the less accurate form of the velocity correction equation. Van Doormaal and Raithby (1984) showed that although more work per iteration was involved in the SIMPLEC algorithm, less iterations were required and there was an overall saving in computational effort. Here the SIMPLEC algorithm has been used exclusively and $\alpha_P$ has been set at 1.0.

### 5.5.5 The Body Fitted Co-ordinate System

Discretisation of the governing equations on a simple rectangular coordinate system is unsuitable for the representation of flow in many complex geometries. The method used here to accommodate more complex geometries is a body fitted coordinate system. In this method a mapping is defined which transforms the geometric grid in the physical domain onto a cubic mesh in the computational domain. The Cartesian system $x^i(x, y.z)$ is transformed into a $\xi^i(\xi, \eta, \zeta)$ system where the physical boundaries are mapped onto planes of constant $\xi^i$ and the grid spacing in the computational domain is normalised so that $\Delta\xi^i = 1$. This is illustrated in two dimensions in Figure 5.2.

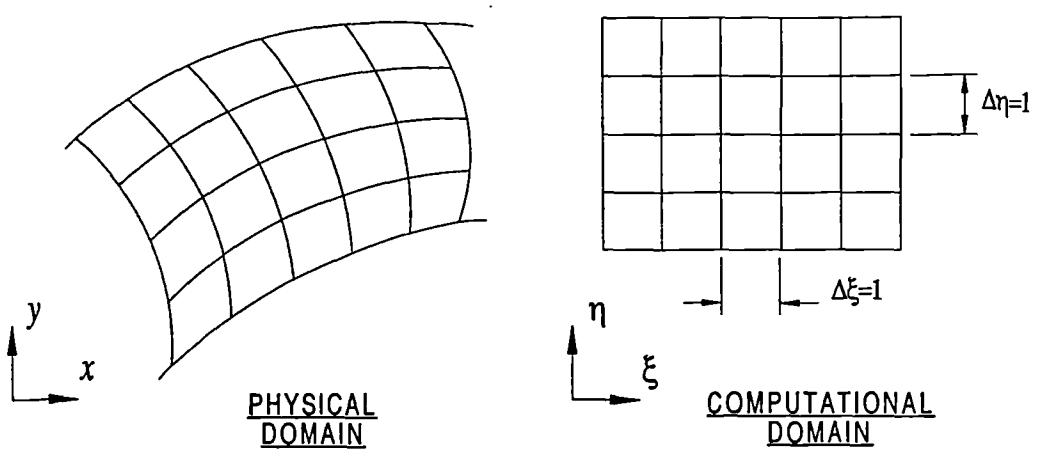


**Figure 5.2:** An Example two-dimensional body fitted grid and its transformation in the computational domain

For such a mapping system to be usable the transformation has to be non-singular so that the functions $\xi^i(x^i)$ and $x^i(\xi^i)$ are one-to-one. Given that it is possible to generate a suitable grid and compute the associated mapping (a non-trivial task in itself but not discussed here) it should be possible to transform the governing equations so that they are discretised in the computational domain. The primary variables are not transformed but spatial gradients have to be transformed into computational gradients. The spatial gradients can be related to the computational gradients by applying the chain rule of differentiation so that:

$$\frac{\partial\phi}{\partial\xi^i} = \frac{\partial x^j}{\partial\xi^i}\frac{\partial\phi}{\partial x^j} = J_i^j\frac{\partial\phi}{\partial x^j} \tag{5.37}$$

$$\frac{\partial\phi}{\partial x^i} = \frac{\partial\xi^j}{\partial x^i}\frac{\partial\phi}{\partial\xi^j} = \overline{J}_i^j\frac{\partial\phi}{\partial\xi^j}. \tag{5.38}$$

where $J_i^j$ is the Jacobian matrix and $\overline{J}_i^j$ is the inverse Jacobian matrix. Of these two equations (5.38) is more useful as it shows how spatial gradients are transformed into computational space gradients. The Jacobian matrix and its determinant effectively define the nature of the coordinate transformation.

Some further notation and a number of useful identities can be defined as follows:

$$\begin{aligned}
(x^i) &= \text{Cartesian physical space coordinates} \\
(\xi^i) &= \text{General non} - \text{orthogonal computational space coordinates} \\
J_i^j &= \frac{\partial x^i}{\partial \xi^j} = \text{Jacobian matrix} \\
\overline{J}_i^j &= \frac{\partial \xi^i}{\partial x^j} = (J^{-1})_j^i \text{ Inverse Jacobian matrix} \\
|J| &= \det(\mathrm{J_j^i}) = \text{Jacobian determinant} \\
A_j^i &= |J|\overline{J}_i^j = \text{ Adjugate Jacobian matrix} \\
V'^i &= \overline{J}_i^j V_j = \text{ the contravariant components of vector} \mathrm{V_j} \\
V_i' &= J_i^j V_j = \text{ the covariant components of vector } \mathrm{V_j} \\
\hat{V}^i &= A_j^i V_j = \text{ the normal components of vector } \mathrm{V_j} \\
g_{ij} &= J_k^i J_k^i = \text{ the metric tensor} \\
g^{ij} &= \overline{J}_k^i \overline{J}_k^i = \text{ the inverse metric tensor} \\
A^{(i)} &= \text{ the area vectors normal to the cell surfaces}
\end{aligned} \tag{5.39}$$

It can further be shown that the inverse metric tensor is related to the cell area vectors such that,

$$g^{ij} = \frac{A^{(i)}.A^{(j)}}{|J|^2} \tag{5.40}$$

and given that the grid cells have unit size in computational space,

$$g = |g_{ij}| = |J|^2 \;\Rightarrow\; \sqrt{g} = |J| = vol(\Omega) \tag{5.41}$$

where $vol(\Omega)$ is the volume of the physical (parallelepiped) cell. Also, the cartesian components of the cell area vectors $A^{(i)}$ are given by:

$$A^{(i)} = |J|\overline{J}_k^i = A_k^i \tag{5.42}$$

i.e. they are the rows of the adjugate Jacobian matrix.

In order to transform the governing equations into computational space a conventional approach would be to apply equation (5.37) successively so that for example the flux form of the general first order two-dimensional differential equation

$$\frac{\partial U}{\partial t} + \frac{\partial F}{\partial x} + \frac{\partial G}{\partial y} = S \tag{5.43}$$

would become

$$|J|\frac{\partial U^*}{\partial t} + \frac{\partial F^*}{\partial \xi} + \frac{\partial G^*}{\partial \eta} = |J|\, S^* \tag{5.44}$$

However, the equation becomes more complex as a result of the transformation as the terms $F^*$ and $G^*$ involve the derivatives of $\xi^i$ with respect to $x^i$. The Jacobian matrix $J_i^j$ $(\partial x^j/\partial \xi^i)$ would be found from taking central differences in computational space using the physical grid node location information. This could be described as the 'Computational Space Approach'—see (Thompson, Warsi and Mastin 1982) and (Fletcher 1988, pages 64–69) for example. Where it is necessary to use the cell face areas and volumes these would be computed from the Jacobian determinant and the adjugate Jacobian matrix using the geometric identities given above.

A second approach is possible where the analysis is carried out entirely on the distorted grid in physical space and which could be called the 'Physical Space Approach'. The equations are then discretised by applying the physical space conservation laws to each of the distorted control volumes, with geometric information computed in terms of the physical volumes and normal area vectors of the control volumes.

The code used in this work (CFDS 1996a) uses a combination of these ideas. In particular, the discretisation is performed in computational space but using geometric information calculated from physical space. In this approach the first step is to use the physical grid information (i.e. co-ordinates of the grid nodes) to calculate directly the cell face areas and volumes (by a series of simple vector operations). The geometric identities of equations (5.39)–(5.42) are then used when necessary to find the Jacobian determinant and inverse metric tensor.

Both of these approaches make the assumption that each cell can be approximated by a parallelepiped. The computational space approach makes this assumption implicitly by assuming the coordinate transformation is approximated well in the neighbourhood of point P by its linearisation (the Jacobian matrix calculated at P). This is only true if the cell is approximately a parallelepiped. The physical space approach makes this assumption explicitly in its derivation. The computational space approach is said to be second order accurate in physical space provided the grid is sufficiently smooth. However, where the grid is more distorted it is argued that the physical space approach is more accurate by virtue of approximating the geometric information more accurately.

The governing equations can be transformed into computational space as follows.

The equations are first expressed as a prototype convection-diffusion equation in tensor form:

$$\frac{\partial}{\partial x^i}(\rho U^i \phi) = \frac{\partial}{\partial x^i}\left(\Gamma \frac{\partial \phi}{\partial x^i}\right) + S, \tag{5.45}$$

which can be written in a more convenient form as,

$$\frac{\partial I^i}{\partial x^i} = S, \tag{5.46}$$

where $I^i$ is the total convective and diffusive flux given by,

$$I^i = (\rho U^i \phi) - \Gamma \frac{\partial \phi}{\partial x^i} \tag{5.47}$$

Now it can be shown that the divergence of a vector can be related to its covariant ($I'^i$) and normal ($\hat{I}^i$) forms by the following,

$$\frac{\partial I^i}{\partial x^i} = \frac{1}{\sqrt{g}} \frac{\partial}{\partial \xi^i}\left(\sqrt{g} I'^i\right) = \frac{1}{\sqrt{g}} \frac{\partial \hat{I}^i}{\partial \xi^i}. \tag{5.48}$$

This can be used to transform the general equation (5.46) into computational space and in terms of the normal flux vectors,

$$\frac{\partial \hat{I}^i}{\partial \xi^i} = \sqrt{g} S, \tag{5.49}$$

and,

$$\hat{I}^i = \sqrt{g} I'^i = \rho \hat{U}^i \phi - \sqrt{g} g^{ij} \Gamma \frac{\partial \phi}{\partial \xi^j} \tag{5.50}$$

The term $\sqrt{g} g^{ij} \Gamma$ can be noted as $\Gamma^{ij}$ which is effectively the *anisotropic diffusivity* and can be calculated with help of equation (5.40). The normal velocities $\hat{U}^i$ are simply given by $U.A^{(i)}$. The governing equations can be seen to be of similar form when transformed into computational space in this way, except that the scalar diffusivity has been replaced by an anisotropic diffusivity.

The body fitted grid system idea has been further extended in the code used here into a 'multi-block' system. In this system the physical space grid is sub-divided into blocks of cells (which may be of different size and orientation) which are 'glued' together. Each block is then effectively subjected to a co-ordinate transformation onto separate grids in computational space. This system allows better control of the grid node distribution in situations were there are sudden expansions or bifurcations in the geometry. Junctions between adjacent blocks are dealt with by the addition of dummy cells in computational space at the grid boundaries.

These cells notionally overlap with the first cells in the adjacent block at block junctions, and are used to apply boundary conditions. At each iteration of the flow calculation each block is treated in sequence, with variable values from the previous iteration being used in the dummy cells at block junctions. This feature of the code however, is not extensively used in the current work as the whole of the test cell geometry can be defined in one block. A second block of cells has been used only to model the extract duct of the test chambers.

The use of a body fitted grid system has implications for both the storage of information within the code and the associated question of pressure-velocity decoupling. The problem of pressure-velocity decoupling can arise in the following manner.

Where the pressure gradient is calculated in the discretised momentum equations at the cell centroid (e.g. point P in Figure 5.1) a $2\Delta\xi$-centered difference would involve the pressures in the two neighbouring cells (W and E). When the pressure gradient in the neighbouring cell (W say) is calculated in turn, the discretisation would exclude the pressure value at P but include the two neighbouring cells again (WW and P). The pressure gradients in neighbouring cells thus use alternate sets of nodes and the pressures on the even and odd grids become decoupled. This makes the discrete equations insensitive to higher frequency fluctuations in the pressure field and the momentum equations can effectively become decoupled from the pressure field, leading to physically unreal solutions.

This velocity-pressure decoupling problem has been recognised for some time. The approach of Patankar (1980) in applying the SIMPLE calculation method was to use separate staggered grids for the pressure (and other scalars) and each of the velocity components. In this approach the velocity cell faces coincide with the usual cell centroids. $1\Delta\xi$-centered differences can then be used to calculate the pressure gradients in the momentum equations and the decoupling problem is avoided.

When using a body fitted grid system however, there are computational and storage overheads arising from the additional geometric information. The transformation of the equations in a staggered grid system also give rise to the need to calculate additional velocity components. Thus storing and calculating the geometric information of the multiple grids of the staggered grid system is acknowledged to be prohibitively expensive. The storage of the primary variables is therefore normally—as in the code used here—arranged in a co-located cell centred fashion

so that all variables are defined at the cell centroids. Given this preference for a co-located storage scheme over that of a staggered grid an alternative solution to the velocity-pressure decoupling problem must be found. This is described in the following section.

### 5.5.6 The Pressure Smoothing Procedure

The procedure adopted here to overcome the problems of pressure-velocity decoupling is known as the Rhie-Chow Pressure Smoothing procedure (Rhie and Chow 1982). The principle of the procedure is to introduce higher order even derivatives of the pressure field into the discretised momentum equations and thereby increase the amount of coupling. The method can be best explained by reference to the one-dimensional example shown in Figure 5.1.

Consider the evaluation of $U_w$ at the west face of the control volume at P. This can simply be calculated $U_w = (U_W + U_P)/2$ where $U_W$ and $U_P$ are the solution of the discretised momentum equations,

$$U_W = \frac{1}{a_W^U}\left(\sum_{nb(W)} a_{nb}^U U_{nb} - \frac{P_P - P_{WW}}{2\Delta x} + S_W^*\right), \tag{5.51}$$

and,

$$U_P = \frac{1}{a_P^U}\left(\sum_{nb(P)} a_{nb}^U U_{nb} - \frac{P_E - P_W}{2\Delta x} + S_P^*\right), \tag{5.52}$$

where the pressure gradient has been separated from the source term $S^*$. (It can be seen from these two equations how the pressure gradients would always be calculated on odd and even grids without further treatment.) Following the initial approximation of $U_w$,

$$\begin{aligned} U_w \;=\; & \frac{1}{2a_W^U}\left(\sum_{nb(W)} a_{nb}^U U_{nb} - \frac{P_P - P_{WW}}{2\Delta x} + S_W^*\right) + \\ & \frac{1}{2a_P^U}\left(\sum_{nb(P)} a_{nb}^U U_{nb} - \frac{P_E - P_W}{2\Delta x} + S_P^*\right). \end{aligned} \tag{5.53}$$

The pressure gradient is then modified by 'replacing' the average of the two pressure gradients centred at W and P with the simple pressure gradient at w, so that

$$U_w \;=\; \frac{1}{2a_W^U}\left(\sum_{nb(W)} a_{nb}^U U_{nb} - \frac{P_P - P_{WW}}{2\Delta x} + S_W^*\right) + \tag{5.54}$$

$$\frac{1}{2a_P^U}\left(\sum_{nb(P)} a_{nb}^U U_{nb} - \frac{P_E - P_W}{2\Delta x} + S_P^*\right) +$$
$$\frac{1}{2a_W^U}\left(\frac{P_P - P_{WW}}{2\Delta x}\right) + \frac{1}{2a_P^U}\left(\frac{P_E - P_W}{2\Delta x}\right) -$$
$$\frac{2}{a_W^U + a_P^U}\left(\frac{P_P - P_W}{\Delta x}\right).$$

This can be simplified again using the original equations (5.51) and (5.52) so that,

$$\begin{aligned} U_w &= \frac{U_W + U_P}{2} + \\ &\frac{1}{2a_W^U}\left(\frac{P_P - P_{WW}}{2\Delta x}\right) + \frac{1}{2a_P^U}\left(\frac{P_E - P_W}{2\Delta x}\right) - \\ &\frac{2}{a_W^U + a_P^U}\left(\frac{P_P - P_W}{\Delta x}\right). \end{aligned} \tag{5.55}$$

Equation (5.55) now contains a modified pressure gradient so that it contains a $\Delta x$ based difference and not just a $2\Delta x$ difference—effectively mimicking the effect of the staggered grid. This expression for the cell face velocities would then be used in calculating any convection terms in the momentum equation, and the source terms in the pressure correction equation.

### 5.5.7 The Buoyancy Induced Instability Problem

It has already noted that the general form of the governing equations are coupled by the density. In making the Bousinesq approximation this coupling is removed. Where the flow is non-buoyant sequential solution of the momentum and energy equations is straight forward. Where it is necessary to model the effects of buoyancy—as in rooms flows with displacement ventilation—additional numerical problems arise as the energy equation becomes weakly coupled to the momentum equations through the body force term. Sequential solution of the equations can then lead to numerical instabilities under certain circumstances.

The nature of the buoyancy induced instability problem has been illustrated and analysed by Papadimitriou (Papadimitriou 1985) for the two-dimensional case. The error induced instability growth mechanism can be illustrated qualitatively by considering a lateral flow with stable thermal stratification ($\partial T/\partial y > 0$). Suppose firstly that the flow and temperature fields are at the exact solution and that there is a perturbation ($\Delta T$ say) in the temperature at a particular cell. First solution

of the vertical momentum equation would result in transport of the warmer fluid into the cell above due to the excess buoyancy. Subsequent solution of the energy equation would result in calculation of a temperature in the upper cell colder than the exact solution. The next solution of the vertical momentum equation would result in generation of a downward velocity bringing warmer fluid back to the lower cell. An oscillatory process can thus be established. Papadimitriou showed how the critical growth of instability errors may depend on the Grashof and Reynolds numbers of the flow and the vertical grid spacing.

It should be noted that in the displacement ventilation flows being modeled here the existence of this instability mechanism does not necessarily correspond to where the strongest buoyancy forces exist. In the plumes, where buoyancy is strongest, the vertical temperature gradient is reversed ($\partial T/\partial y < 0$) from that of the surrounding stratified fluid, due to the mixing processes in the plume. Fluid is therefore always strongly convected upwards. (The flow equations are in fact parabolic in nature in the plume region.) In much of the region surrounding the plumes the flow is thermally stratified but recirculating laterally at low velocity (moving from the wall regions towards the plumes). It is in these regions that the flow is very similar to the stably stratified lateral flows described by Papadimitriou

One possible solution to the buoyancy induced instability problem is to seek a simultaneous solution of the momentum and energy equations. McGuirk and Whittle comment on several such approaches (McGuirk and Whittle 1991), but these are all computationally expensive. There are three approaches to dealing with the buoyancy induced instability problem that are commonly used when the equations are solved sequentially. These are (in order of increasing effectiveness and computational cost):

- strong under-relaxation
- false time stepping
- full transient solution

If the discretised equations in matrix form (as equation 5.31) are expressed in terms of a matrix of diagonal coefficients $[A_P]$ and of off-diagonal coefficients $[A_{OD}]$, then in the steady form the equations are

$$[A_P]\,[\phi]^{n+1} + [A_{OD}]\,[\phi]^{n+1} = [B]\,. \tag{5.56}$$

Under-relaxation consists of 'mixing' of the new solution with a proportion of the previous solution, so that after relaxation has been applied the steady state equations become

$$[A_P]\,[\phi]^{n+1} + \omega\,[A_{OD}]\,[\phi]^{n+1} = \omega\,[B] + (1-\omega)\,[A_P]\,[\phi]^n\,, \tag{5.57}$$

where $\omega$ is the under-relaxation factor. In non-buoyant flows $\omega$ is 0.3–0.7 but in buoyant flows much smaller factors are used. Numerical stability is promoted by the fact that the diagonal terms of the coefficient matrix are increased relative to the off-diagonal terms.

In the 'false time stepping' or 'pseudo-transient' procedure the time derivative terms are included in the discretised equations so that,

$$\frac{\rho}{\Delta t}\{[\phi]^{n+1} - [\phi]^n\} + [A_P]\,[\phi]^{n+1} + [A_{OD}]\,[\phi]^{n+1} = [B] \tag{5.58}$$

$$\Rightarrow \quad \{\frac{\rho}{\Delta t}[I] + [A_P]\}\,[\phi]^{n+1} + [A_{OD}]\,[\phi]^{n+1} = [B] + \frac{\rho}{\Delta t}[\phi]^n \tag{5.59}$$

and diagonal dominance of the coefficient matrix is again promoted (more so with smaller $\Delta T$). As the steady state is approached the time derivative terms diminish in significance.

Comparing the two forms of the equations it can be shown that there is a false time step $\Delta t^*$ equivalent to the relaxation factor $\omega$ given by,

$$[\Delta t^*] = \frac{\omega\rho}{(1-\omega)\,[A_P]} \tag{5.60}$$

Thus under-relaxation could be thought of as applying a spatially varying false time step, and conversely use of a false time stepping approach can be seen to be equivalent to application of a spatially varying under-relaxation factor. In the false time stepping approach the time step is incremented at each outer iteration so that time accuracy is not preserved at intermediate steps—different equations may in fact be treated with different false time steps. Application of this approach does however require some knowledge of the time scale of the problem.

In a true transient approach the equations are solved to a certain tolerance at each time step. Several 'outer' iterations are then required at each time step to deal with the non-linearities of the equations. All the equations are solved with the same time step, so that a time accurate solution is available at every time step. It may then be necessary to march through time for several times the mean particle residence time before a steady state is approached.

## 5.6 Boundary Conditions

Given the set of governing equations and a particular geometry, it is the boundary conditions that determine the nature of the solution to the flow and temperature field. Heat transfer is of particular interest in this work and so the thermal boundary conditions are of particular significance. The treatment of boundary conditions for the momentum and energy equations are described in this section.

### 5.6.1 Inlet Boundary Conditions

In an incompressible flow, all the primary variables except pressure need to be specified using Dirichlet boundary conditions (set at a constant value) at inlets. Determining the inlet temperature is straight forward as this is a independent design variable and was under independent control during the experiments. To determine the inlet velocity it necessary to ensure firstly that the overall mass flow is correct. Since the inlet temperature is known the reference density can also be found. If the inlet opening is a simple plain opening the inlet velocity could simply be found from the mass low rate divided by the density and face area of the cells at the inlet ($U_{in} = \dot{m}/\rho_0 A_f$), and $U_{in}$ would be normal to the face of each inlet cell.

The situation is, however, more complicated here due to the displacement ventilation inlet diffuser having a perforated metal face. The effect of the perforated metal face is to reduce the effective free area and locally increase the momentum of the flow. The inlet velocity if calculated by the above method would therefore be lower than that local to the diffuser but correspond to the correct overall mass flow rate (Li *et al* call this the 'mass method'). To try and model correctly the effect of the locally increased momentum and maintain the correct mass flow it is necessary, when forming the discrete momentum equations at the inlet cells, to multiply the cell face area by the degree of perforation. This has been called the 'momentum method' (Chen and Moser 1991). The effect of these alternative treatments is investigated in section 6.2.3.

Whichever method of calculating the inlet velocity is used, the same velocity is set across the whole of the inlet—a so called 'top hat' velocity profile. In the absence of detailed velocity measurements at the diffuser face this is a reasonable approximation. Firstly, the perforated face of the diffuser could be expected to

evenly distribute the flow over the whole face. Also, it seems that buoyancy effects dominate the flow adjacent to the inlet.

Experimental information is not directly available to enable the turbulence quantities $k$ and $\varepsilon$ to be determined at the inlet. The turbulent kinetic energy can be approximated from the kinetic energy of the inlet flow and an approximation of the turbulence intensity so that,

$$k_{in} = \frac{1}{2}\left(\frac{U_{in}TI}{100}\right)^2 \tag{5.61}$$

where $TI$ is the turbulence intensity (%). A consistent value of $\varepsilon$ at the inlet can then be estimated from

$$\varepsilon_{in} = \frac{k_{in}^2}{0.3D} \tag{5.62}$$

where $D$ is the hydraulic diameter of the inlet. In most rooms $TI$ could be expected to be in the range 1–30%. The flow is not, in fact, sensitive to the value of turbulence intensity at the inlet and was set at 5% in most cases here.

### 5.6.2 Outlet Boundary Conditions

At the outlet Neumann boundary conditions (constant gradient) are imposed on all variables. A zero gradient is specified for $T, k$ and $\varepsilon$. When using a pressure correction procedure, it is important that there is global mass continuity in order that the pressure correction equation is well posed. This requires that the velocity gradient is modified from a zero gradient condition to a constant normal gradient in order to ensure global mass continuity. The velocity gradients at the outlet cells are modified as follows:

1. Apply a nominal zero gradient boundary condition $\frac{\partial U_i}{\partial n} = 0$.
2. Calculate the discrepancy between the actual mass flow and the total inlet flow.
3. Add an increment to $U_i$ in the direction of the outward facing unit normal to give the correct outflow.

This is equivalent to applying the boundary condition

$$\frac{\partial U_i}{\partial n} = \lambda n_i \tag{5.63}$$

where the constant $\lambda$ is chosen to give the correct outward mass flow rate.

Applying Neumann boundary conditions at the outlet in this way implies that the flow is fully developed approaching the outlet. Conditions will be very different at the usual type of air flow exit from a room. For this reason it has been necessary to model a short length of extract duct in most of the calculations made here.

### 5.6.3 The Generalised Wall functions

To establish boundary conditions for the momentum and energy equations at wall boundaries it is necessary to know the velocity and temperature gradients in the boundary cells. Velocity and temperature gradients vary rapidly at wall boundaries and to resolve accurately the gradients near walls would be expensive in computing time and storage. Wall functions are empirical non-dimensionalised functions that can be used to define the relationships between a variable (e.g. $U_P$ or $T_P$) at some distance from the wall and its flux at the wall ($\tau_w$ or $Q_w$). Wall functions are used then to define the wall boundary conditions with the first cell centroid placed some significant distance from the wall.

Bakhmeteff (1936) found a logarithmic law defining the velocity profile in forced convection wall boundary layers of the form

$$u^+ = \frac{u}{u_\tau} = C_1 log(y^+) + C_2, \tag{5.64}$$

where $u^+$ is the non-dimensional velocity parallel to the wall and $y^+$ is the non-dimensional distance normal to the wall surface given by

$$y^+ = \frac{y u_\tau}{\nu}, \tag{5.65}$$

and $u_\tau$ is the friction velocity given by,

$$u_\tau = \sqrt{\frac{\tau_w}{\rho}}. \tag{5.66}$$

The log law is found to be valid in the range $30 < y^+ < 300$. In the viscous sublayer ($y^+ < 11.6$) the velocity profile is linear (between these limits the profile is less well defined).

A more generalised form of wall function is can be found by normalising using the turbulent kinetic energy on the basis that in a boundary layer the shear stress is

related to $k$ by $\tau^2 = C_\mu \rho^2 k^2$. This is the form of wall function used by Launder and Spalding (1974) and is the default model in this work. A new quantity $\tau_k$ is defined such that

$$\tau_k = \rho C_\mu^{1/2} k. \tag{5.67}$$

This can then be used to define $u^+$ and $y^+$,

$$u^+ = -\frac{(\rho\tau_k)^{1/2}}{\tau} U, \tag{5.68}$$

$$y^+ = \frac{(\rho\tau_k)^{1/2}}{\mu} y. \tag{5.69}$$

The velocity wall function is then given by

$$u^+ = \begin{cases} y^+ & \text{for } y^+ < 11.6, \\ \frac{1}{\kappa} log(E y^+) & \text{for } y^+ \geq 11.6 \end{cases} \tag{5.70}$$

$E$ is a constant dependent on the roughness of the surface (9.0 for a smooth surface).

Using this form of non-dimensionisation means that $k$ can be calculated in the normal way in the cells adjacent the wall (except that the velocity gradients in the $P_K$ term are calculated according to the wall function) and equation (5.67) used to find the shear stress. The turbulent dissipation $\varepsilon$ can be found from $k$—on the basis that the production of $k$ is in equilibrium with its dissipation—using the relation

$$\varepsilon = \frac{C_m u^{3/4} k^{1/2}}{\kappa y} \tag{5.71}$$

The treatment of enthalpy (and other scalars) is handled in an analogous way to the velocity wall function so that

$$\phi^+ = \begin{cases} Pr_\phi y^+ & \text{for } y^+ < 11.6, \\ \frac{\sigma_\phi}{\kappa} log(E_\phi y^+) & \text{for } y^+ \geq 11.6, \end{cases} \tag{5.72}$$

where $Pr_\phi$ is the turbulent Prandtl number $\mu/\Gamma_\phi$. $\phi^+$ is defined in a similar way to $u^+$

$$\phi^+ = \frac{(\rho\tau_k)^{1/2}}{J_\phi}(\phi_w - \phi), \tag{5.73}$$

where $\phi_w$ is the value at the wall and $J_\phi$ is the flux of $\phi$ at the wall $\left(\frac{\partial\phi}{\partial n}\right)_w$.

The turbulent Prandtl number $Pr$ however is not constant in the region close to the wall. The exact nature of its variation is in some dispute in the literature but

the commonly adopted formula of Jayatilleke (1969) is used here. The variation is defined by

$$E_\phi = Eexp\left[9.0\kappa((\frac{Pr}{\sigma_\phi})^{0.75} - 1)(1 + 0.28exp(-0.007(\frac{Pr}{\sigma_\phi}))\right] \quad (5.74)$$

where $E$ is the constant the velocity 'log law' wall function.

## 5.7 Calculation of Radiant Heat Fluxes

In view of the importance of radiant coupling between surfaces in the displacement ventilation and chilled ceiling systems studied some of the numerical calculations have been carried out using a general radiation calculation procedure coupled to the flow calculation. The radiation calculation procedure used here is known as the 'discrete transfer' method (Shah 1979). The discrete transfer method was originally developed for the treatment of radiation in combustion calculations and can be applied to complex geometries as well as treating absorption and scattering effects (Lockwood and Shah 1980). The discrete transfer method has also been applied to calculation of room radiant heat transfer (Malalasekera and James 1993). The method relies on tracing rays along predetermined angles from one surface to another and integrating the radiant intensity along each path.

The fundamental equation for the transfer of thermal radiation can be expressed as:

$$\frac{dI}{ds} = -(K_a + K_s)I + K_a\frac{E_g}{\pi} + \frac{K_s}{4\pi}\int_{4\pi} P(\Omega,\Omega')I(\Omega')\,d\Omega' \quad (5.75)$$

where $I$ is the radiant intensity in the direction $\Omega$, $s$ is the distance in that direction and $E_g$ is the black body emissive power of the gas ($\sigma T_g^4$). $K_a$ and $K_s$ are the gas absorption and scattering coefficients and $P(\Omega,\Omega')$ is the probability that incident radiation in the direction $\Omega'$ will be scattered into the increment of solid angle $\delta\Omega$ about $\Omega$.

This equation can be expressed more concisely as

$$\frac{dI}{ds^*} = I\frac{E^*}{\pi} \quad (5.76)$$

where an extinction coefficient ($K_e = K_a + K_s$) is defined so that distance is expressed as optical depth ($ds^* \equiv K_e ds$) and $E^*$ is a modified emissive power given by

$$E^* = \frac{1}{K_e}\left(K_a E + \frac{K_s}{4}\int_{4\pi} P(\Omega,\Omega')I(\Omega')\,d\Omega'\right) \quad (5.77)$$

To discretise Equation (5.77) the flow domain is divided by a series of planes crossing each other to form a number of zones (which are arranged to be the union of a number of flow cells in a coupled flow-radiation calculation) and divide each surface into a number of panels. A number of uniformly distributed rays are traced back from reference points on each surface panel (at which the ray is imagined to have arrived), along a straight path passing through a number of intermediate zones, until another surface is encountered. Equation (5.77) is discretised by integrating along the ray to yield the recurrence relation:

$$I_{n+1} = I_n e^{-\delta s^*} + \frac{E^*}{\pi}(1 - e^{-\delta s^*}) \tag{5.78}$$

where $n$ and $n+1$ indicate positions where the ray enters and leaves each zone.

The recurrence relationship is applied as follows. An initial estimate of the intensity leaving the source surface panel is made from the current temperature field using the relation

$$I^n = \frac{\epsilon_s \sigma T_w^4}{\pi} \tag{5.79}$$

The intensity at each point along the ray path and at the surface panel is then found by applying the recurrence relation. Surface heat fluxes are then arrived at by integrating the effect of all the rays arriving at each panel such that the irradiation $G$ is obtained from

$$G = \sum_{j=1}^{nj} I_j(\Omega_j.n)\delta\Omega \tag{5.80}$$

where $I_j$ is the calculated intensity in the discretised angle $\delta\Omega$ and $n$ is a unit vector normal to the surface. For a 'grey' wall the local radiosity $J$ is given by

$$J = (1 - \epsilon_s)G + \epsilon_s \sigma T_s^4 \tag{5.81}$$

where $\epsilon_s$ is the surface emissivity.

Where the method is used apart from any flow calculation to calculate radiant fluxes the calculated radiosity $J$ is used to find a new value for the intensity leaving the surface (from the relation $I = J/\pi$) This is then used as the new initial intensity when re-applying the recurrence relation. This procedure is repeated until the change in the $G$ from one iteration to the next falls below a certain tolerance. At the end of the procedure the net flux on each surface panel can be found from $q_s = G - J$.

In a combined flow-radiation calculation, the coupling is achieved by passing heat flux information from the flow solver to the radiation solver and temperature

information in the reverse direction (or vice versa). The information from one solver is then used to form the boundary conditions for the next calculation in the other. Usually the radiation calculation does not need to be carried out at every iteration of the flow calculation, and because many iterations are required to solve the flow field it becomes unnecessary to use iteration within the radiation calculation.

There are two types of thermal boundary condition involving the calculation of radiation at the walls. The energy balance at a wall element can be expressed in general terms as

$$\lambda_c \frac{\partial T}{\partial n} + \lambda_a \frac{\partial T}{\partial n} + q_s = 0, \tag{5.82}$$

where the first term represents conduction through the wall, the second terms represents convection, and the third is the net radiant flux. The first boundary condition of concern is an adiabatic wall condition, in which case the first term becomes zero and the convective flux must be in balance with the radiant flux. The second condition is one of conjugate heat transfer, where the radiant flux must balance both the conductive and convective fluxes. An energy balance at each surface can be assured by passing temperature and heat flux information in opposite directions between the flow and radiation codes and as the solution progresses towards convergence the heat fluxes calculated by one code will become consistent with the temperatures calculated by the other. The question remains as to which code calculates the surface temperatures and which calculates the surface fluxes.

The most obvious form of boundary condition treatment is for temperatures to be passed from the flow solver to the radiation solver. In this case the temperatures would then be used in equation (5.79) to find the next estimate of the intensity. Where conduction and convection wall fluxes dominate this procedure can be used successfully. However, where the radiant flux is more dominant instability can arise due to the radiant flux being sensitive to the fourth power of temperature and the other fluxes being sensitive to simple temperature difference[3]. In these cases it is necessary to pass heat fluxes from the flow solver to the radiation solver. In this case, if $q_s^n$ is the required flux passed from the flow solver, the next estimate of intensity can be found using the previous estimate of $G$ thus,

$$I^n = \frac{J}{\pi} = \frac{1}{\pi}(G^{n-1} - q_s^n) \tag{5.83}$$

[3]This problem might not arise in rooms with small temperature differences, but could certainly arise in combustion calculations, for which the method was devised

After the recurrence relationship has been applied, $G^n$ can be calculated using equation (5.80). The temperature to be passed back to the flow solver can then be calculated as follows,

$$J = G - q_s \tag{5.84}$$

and substituting for $J$ using equation (5.81),

$$(1-\epsilon)G^n + \epsilon E = G^n - q_s^n \tag{5.85}$$

$$\epsilon\sigma T^4 = \epsilon G^n - q_s^n \tag{5.86}$$

so that after applying some under-relaxation

$$T^{n+1} = \alpha\left(\frac{1}{\epsilon\sigma}(\epsilon G^n - q_s^n)\right)^{\frac{1}{4}} + (1-\alpha)T^n \tag{5.87}$$

Although it is possible to treat the effects of absorption and scattering in the medium using the discrete transfer method, in rooms of office size such effects can be neglected. Accordingly, in the implementation of the discrete transfer algorithm used here (CFDS 1996b) the absorption and scattering coefficients were set at zero. Also, it is possible to use the method to calculate radiation in a number of wavelength bands with different properties in each band. It was not thought necessary to consider variations in emissivity and absorptivity with wavelength here in view of the small range of temperatures encountered, and so a single band grey model was used in this work.

# Chapter 6

# Numerical Results

## 6.1 Introduction

The results of the numerical calculations of air flow and heat transfer are presented in this chapter. Calculations have been made for some of the displacement ventilation test chamber experiments of Li *et al.* (referred to here on as the NSIBR[1] test chamber experiments), and for some of the experimental test cases from the Loughborough test chamber. The objectives in making these calculations have been, firstly, to study the flow and heat transfer in the test chamber experiments in more detail than that possible with the experimental data alone, and also to examine the suitability of the numerical method and see if the data from the calculations can be used in developing the simplified model.

Li, Fuchs and Sandberg published results of numerical calculations for their test chamber experiments (Li et al. 1993b) in which they used a conjugate heat transfer calculation procedure. The objective of making similar calculations here was to evaluate different numerical treatments and make some comparisons with the experimental and numerical results of Li *et al.* before making similar calculations for the Loughborough test chamber experiments. Accordingly, these results are presented first with a discussion of the different computational meshes, differencing and boundary condition treatments. Details of the flow and temperature fields from a conjugate heat transfer calculation for two of the NSIBR test cases are presented and the interesting features of the flow discussed.

[1]National Swedish Institute for Building Research

The principal differences between the NSIBR and Loughborough test chamber experimental arrangements (besides the fact that there was a chilled ceiling present in the latter chamber) is in their geometry and the number of heat sources used in the experiments. In the case of the NSIBR test chamber the geometry is a simple cuboid and a rectangular mesh system could be used in the calculations. In the case of the Loughborough test chamber calculations the geometry was more complex and a body fitted co-ordinate mesh system had to be used. The calculation procedure adopted for the displacement ventilation test cases from the Loughborough test chamber was otherwise very similar to that used for the NSIBR test chamber and results from a conjugate heat transfer calculation are presented. In the case of the displacement ventilation and chilled ceiling cases from the Loughborough test chamber (with higher loads and four heat sources, as well as a cold ceiling temperature) it was found necessary to adopt a different approach. In these cases it was necessary to make fully transient calculations (discussed in Section 6.4) and the additional time required to complete the calculations did not allow a full conjugate heat transfer calculation to be attempted.

## 6.2 Calculation of the NSIBR Test Cases

The geometry of the room used by Li, Sandberg and Fuchs at the NSIBR is shown schematically in Figure 6.1. The room had internal dimensions 4.2 m long, 3.6 m wide and 2.75 m high and was enclosed within a larger room to allow control of the external temperatures. The room had a flat rectangular displacement ventilation diffuser positioned midway along the longer wall, and a extract opening on the adjacent wall at a height of 2.5 m. A single load was placed 0.11 m off the floor opposite the inlet and towards the back of the room. The heat source was designed to give a high convective output and consisted of a number of 25 W electric bulbs in an aluminium frame and surrounded by aluminium chips. Aluminium and black wall coverings were used in the experiments to investigate the significance of the longwave radiation (Li et al. 1993b) but only the cases with black walls are considered here. The experimental boundary conditions for the test cases made use of here are shown in Table 6.1.

Li *et al.* have presented results of calculations (Li et al. 1993a) using a conjugate heat transfer calculation procedure. A conjugate heat transfer calculation involves an explicit calculation of conduction through the room fabric and explicit calculation of the heat balance at the room internal surfaces including the surface long

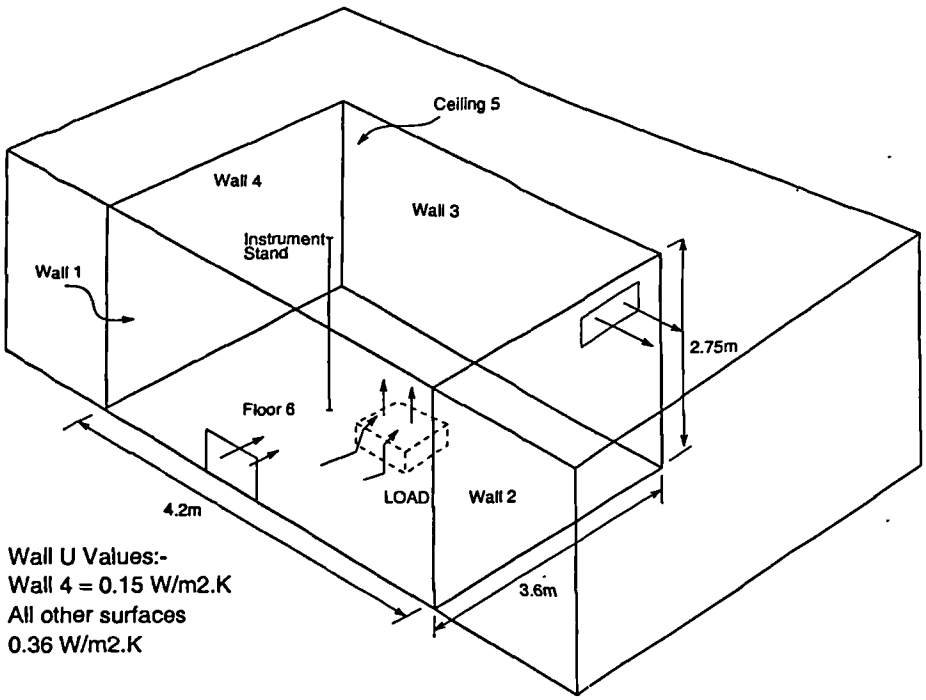


Figure 6.1: Sketch of the environmental test chamber arrangement used by Li, Sandberg and Fuchs (1993a) at the NSIBR. The inlet opening is 450 × 500 mm and the extract opening 525 × 220 mm at a height of 2.5 m. The load is positioned 110 mm off the floor.

wave radiation component. This allows the specification of the thermal boundary conditions as fixed outside surface temperatures and calculation of the temperature gradients along the internal surfaces—seeking to mirror what happens in the real test chamber. Here a similar approach is taken, except that the discrete transfer radiation calculation procedure was used rather than the view factor/radiosity method used by Li. To examine the effects of wall thermal boundary condition treatment calculations have also been made without modeling wall conduction explicitly. The simplest treatment adopted for these cases was to use a zero convective heat flux boundary condition (often referred to as an adiabatic condition). A slightly more realistic boundary condition was to fix the wall temperature using experimentally measured surface temperatures. Another intermediate level of complexity used was to link the flow and radiation calculations but with an adiabatic boundary condition (i.e. convective and radiant fluxes balanced at every surface node).

| *Test Case* | *Load* W | $Q_a$ W | $n$ $h^{-1}$ | $T_s$ °C | $T_e$ °C | $T_{os1}$ °C | $T_{os2}$ °C | $T_{os1}$ °C | $T_{os3}$ °C | $T_{os5}$ °C | $T_{os6}$ °C |
|---|---|---|---|---|---|---|---|---|---|---|---|
| B3 | 300 | 283 | 3 | 18.0 | 24.8 | 19.8 | 22.5 | 22.8 | 22.6 | 20.0 | 19.8 |
| B4 | 450 | 370 | 3 | 18.0 | 26.9 | 19.8 | 23.0 | 22.4 | 22.5 | 19.8 | 19.8 |

**Table 6.1:** Experimental boundary conditions for the displacement ventilation tests made by Li, Sandberg and Fuchs (1993a). $T_s$ and $T_e$ are the air supply and extract temperatures respectively and $Q_a$ is the load measured in the air stream.

### 6.2.1 The Computational Meshes

As the geometry of the NSIBR test chamber arrangement is simple and involves only flat surfaces it was possible to use a rectilinear mesh in all these calculations. The different wall treatments required slightly different meshes—additional cells being added the boundaries for the conjugate heat transfer calculations. The effects of mesh refinement were examined using three meshes and a calculation of the flow with fixed wall temperature boundary conditions. These meshes are shown in Figures 6.2–6.3 and have 67650, 120000 and 218000 cells. The meshes are generally more densely packed in the lateral directions where steeper velocity gradients were expected—at the edges of the plume and around the inlet. In the vertical direction the meshes are more closely packed near the floor and ceiling. To control the smoothness of the mesh, the sizes of adjacent cells were adjusted to differ by less than 1:1.2. Successful convergence in buoyancy dominated flows such as these is known to be dependent on vertical grid spacing (Papadimitriou 1985). Preliminary calculations showed that it was necessary to include at least 50 cells in the vertical direction to achieve convergence. This has resulted in the smallest cell dimension usually being in the vertical direction in these meshes.

Test calculations were made with the three meshes and the same boundary conditions (Li *et al.* case B3). Three alternative differencing schemes were also used involving different treatment of the momentum and energy equation convection terms. In all cases the hybrid differencing scheme was used with the $k$ and $\varepsilon$ equations. They can be summarised as:

a.) 'Hybrid' differencing of all equations,

b.) 'Higher Order Upwind' differencing of the momentum equations and 'Hybrid' differencing of all other equations,

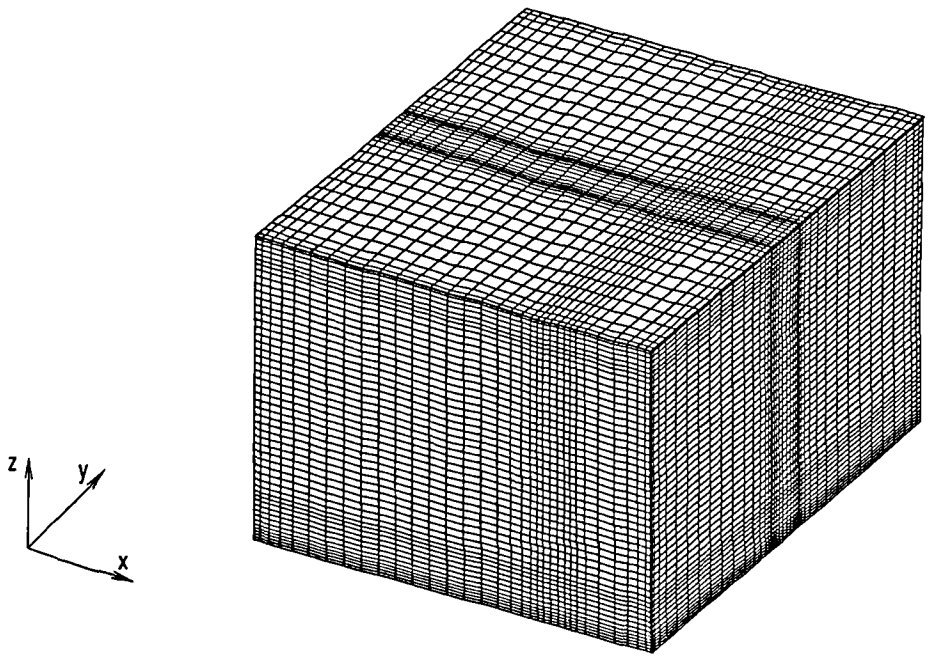


**Figure 6.2:** The $33 \times 41 \times 50$ mesh (67650 cells) used for the NSIBR test chamber calculations.

c.) 'Higher Order Upwind' differencing of the momentum and enthalpy equations and 'Hybrid' differencing of all other equations.

These trial calculations showed that the use of false time stepping with time steps of 0.35–0.7 s was necessary to achieve convergence. The calculations were accepted as converged when the mass residual had fallen below 1% of the total supply mass flow and the enthalpy residual had fallen by four orders of magnitude. (The mass residual is defined in this case as the summation of the absolute value of the net mass fluxes into or out of every cell in the flow.) It was generally the enthalpy residual that converged at the slowest rate.

With the smallest mesh (67650 cells) successful convergence could be achieved with all of the differencing schemes—smaller false time steps being necessary for scheme 'c'. Differencing schemes 'a' and 'b' could be successfully used with the 120000 cell mesh. However, the convergence performance deteriorated noticeably with the 218000 mesh. The difference in the global enthalpy change between the calculations made with the 67650 and the 128000 cell mesh was only 0.05%. As this difference is very small and it seemed more desirable to retain the benefits of the second order accuracy of scheme 'c' further calculations have been based on

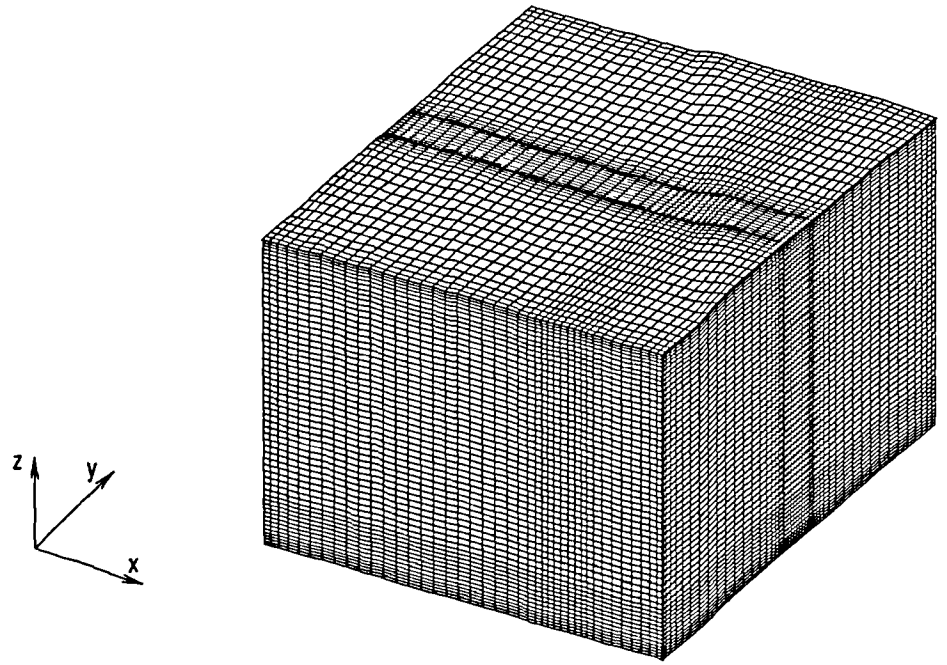


**Figure 6.3:** The 40 × 50 × 60 mesh (120000 cells) used for the NSIBR test chamber calculations.

the 67650 cell mesh. (Li *et al.* calculations were, in fact, based on a 22 × 20 × 58 25520 cell mesh). The mesh used for the conjugate heat transfer calculations of the NSBIR test cases is shown in Figure 6.5 and is essentially identical to the 67650 cell mesh, but with the addition of a further 2 cells at each of the room boundaries to represent the room fabric. These cells have been given an arbitrary thickness of 0.3 m and given the thermal conductivity required to give the specified overall wall conductance.

The flow in the zones adjacent the room surfaces was expected to be dominated by buoyancy effects in some areas, and momentum effects in others—a mixed convection regime. Standard wall functions (See equations 5.6.3 and 5.6.3) have been used in all the calculations reported here. As these functions are based on fully turbulent momentum driven boundary layer flows there was some concern about their effectiveness. An initial check was made—using the trial calculations with the 67650 cell mesh—on the value of $y^+$ calculated at the nodes adjacent each wall surface. The values of $y^+$ have been plotted for the floor, ceiling and two room vertical walls (the wall opposite to, and to the left of, the inlet position) in Figure 6.6.

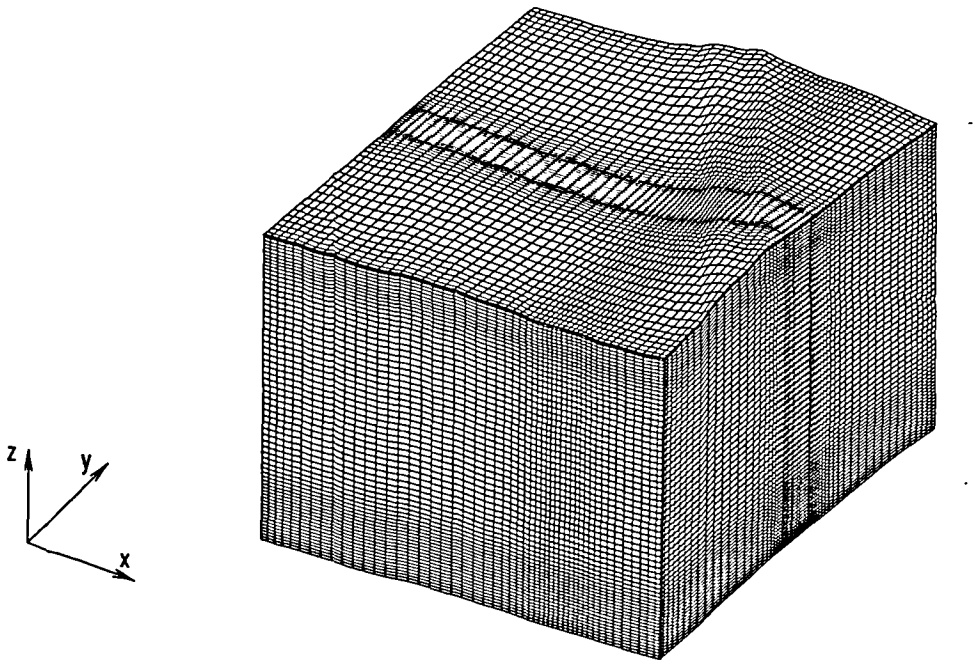


**Figure 6.4:** The 55 × 61 × 65 mesh (218000 cells) used for the NSIBR test chamber calculations.

It is accepted that in momentum driven zero pressure gradient boundary layer flows that the flow is laminar where $y^+ < 11.6$ and fully turbulent where $y^+ > 30$. Between these values there is a transition region where $u^+$ is neither described by a linear or 'log law' function. The usual intention is that the first node adjacent wall surfaces is positioned in the fully turbulent zone ($30 < y^+ < 300$). Figure 6.6 shows firstly, that $y^+$ over the floor surface is mostly between 7.5 and 12.5. At the ceiling there is a single peak of $y^+ = 42.5$ in the zone where the plume impinges on the ceiling, falling to a low value of approximately 7.5. On the wall opposite the inlet there is a peak in the value of $y^+$ near the floor in the zone where the gravity layer across the floor impinges on the bottom of the wall. The values on the other wall are mostly between 15 and 25.

In summary, the values of $y^+$ were found to be rather low, with the values over much of the surfaces falling in the range associated with the transition zone in conventional boundary layers. The wall functions are implemented in the code used here (CFDS 1996a) in such a way that a linear function is applied where $y^+ < 11.6$ and the usual 'log law' (see equation 5.6.3) applied where $y^+ > 11.6$. This arguably results in an over-prediction of $u^+$ where $y^+$ falls in the transitional range, as is the case over much of the walls here.

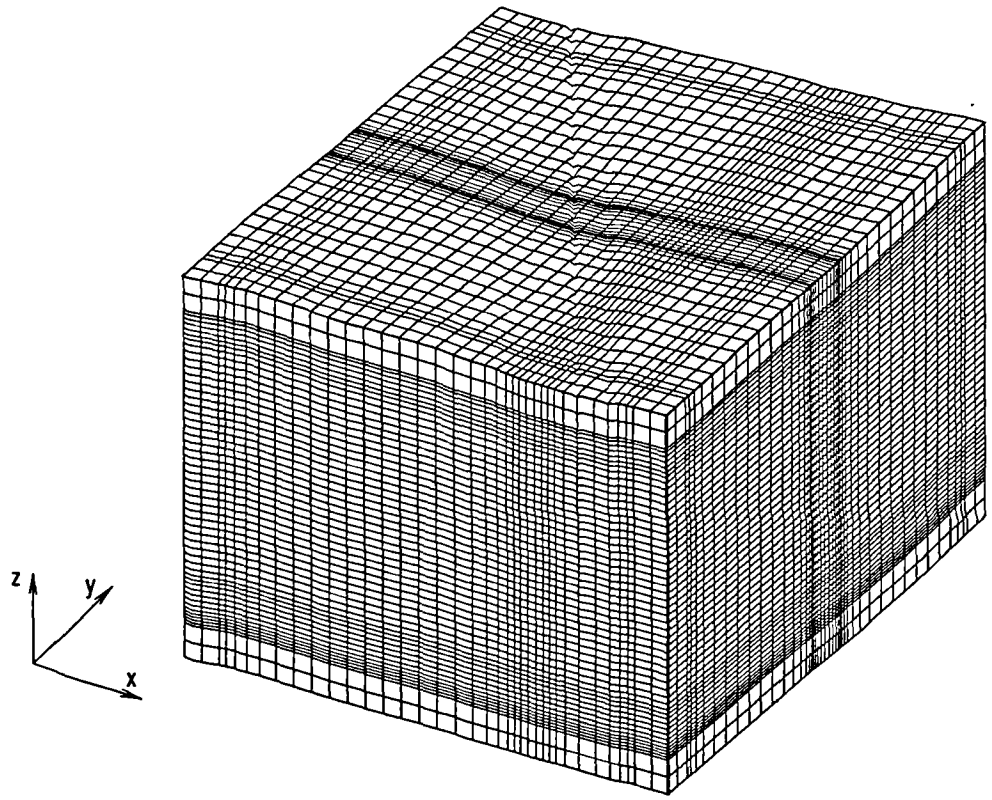


**Figure 6.5:** The $37 \times 45 \times 54$ mesh (89000 cells) used for the NSIBR test chamber conjugate heat transfer calculations.

One obvious solution to this would be to increase the spacings between the surface and the first grid nodes. However, at the vertical walls the spacing to the first grid node in the 67650 mesh is not particularly small (approximately $\frac{1}{3}$ of the largest spacing in the mesh). Increasing this dimension (up to reasonable limits) would not ensure that $y^+ > 30$ everywhere. At the floor and ceiling surfaces, where the cell dimension perpendicular to the surfaces is smaller, there is a conflict between the desire to be able to accurately resolve the steeper temperature and velocity gradients, and the desire to achieve higher $y^+$ values. At the floor in particular, the boundary layer is expected to be relatively thin. As the bottom of the heat source is only 0.11 m above the floor and at least 3 cells are need to resolve the rapidly changing temperature gradient the cell vertical spacing is restricted. In view of these restrictions it was necessary to use the 67650 mesh, with these cell spacings, as shown in Figure 6.2 and accept the low $y^+$ values.

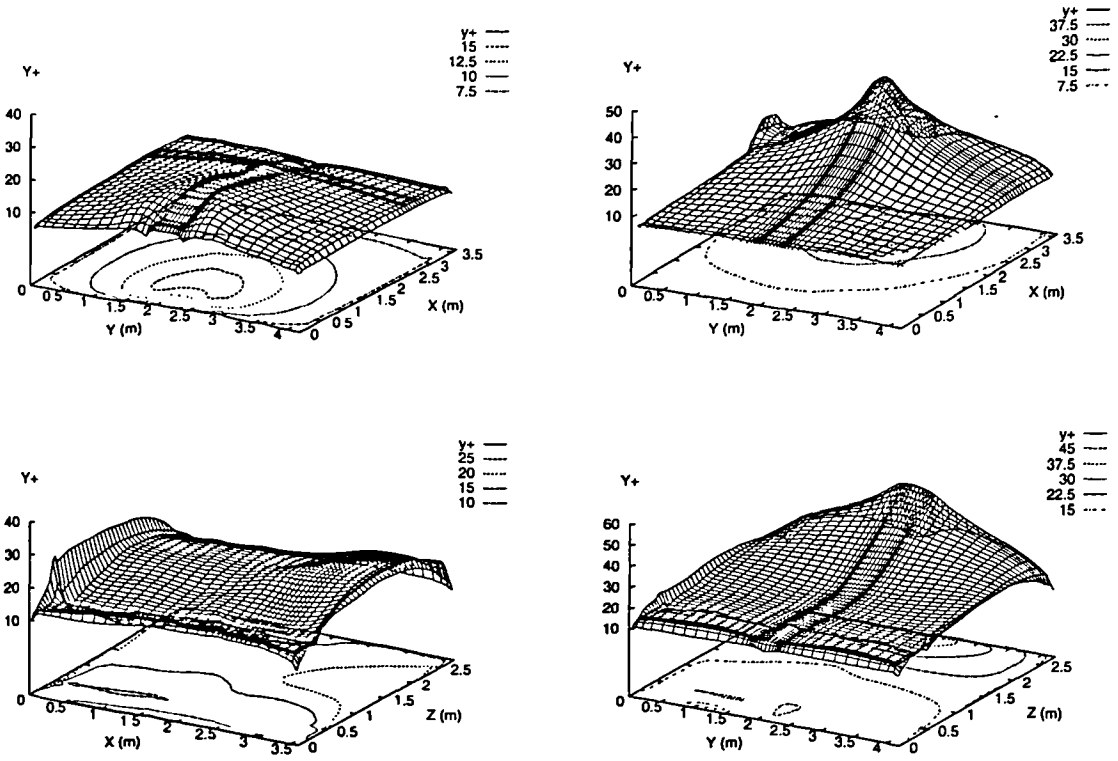


Figure 6.6: $Y^+$ calculated on 33 × 41 × 50 mesh of the NSIBR test chamber (case B3) plotted over the floor (top left), ceiling (top right), wall4 (bottom left), and wall 3 (bottom right).

### 6.2.2 Alternative Differencing Schemes

To evaluate alternative differencing schemes further trial calculations were made using test case B3 boundary conditions and the 67650 cell mesh and fixed wall temperatures. The differencing schemes tested involved different combinations of the 'Hybrid' and 'Higher Order Upwind' schemes as defined as schemes 'a', 'b' and 'c' above. To evaluate the effects of these different schemes the prediction of plume temperatures was examined. The plume is the dominant source of momentum in these test cases and it is near the base of the plume that the largest velocities and the strongest convection occurs. The choice between upwind and central differencing in the hybrid scheme is dependent on cell Peclet number. Upwind differencing is applied where $Pe_c > 2$. The 'false diffusion' effects associated with the first order accurate upwind/hybrid differencing scheme may be expected to be most evident in areas of strong convection. The calculated temperatures on the notional plume centre-line (i.e. the vertical axis at the centre of the heat source)

have firstly been plotted in Figure 6.7. The temperatures on a horizontal line above the centre of the heat source, and at three heights, have been plotted in Figure 6.8.

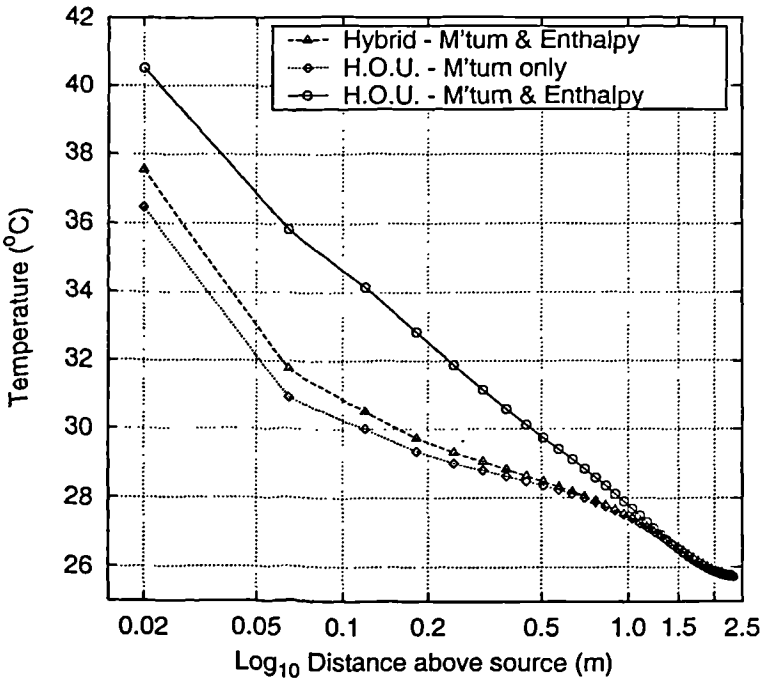


**Figure 6.7:** Temperature decay along the plume centre-line calculated with different differencing schemes.

There is little difference in the temperature distributions predicted using differencing schemes 'a' and 'b' in both the lateral direction and along the plume centre-line. The lateral temperature distributions shown in Figure 6.8 show both the decay in the peak temperature in the plume and the lateral growth of the plume with increasing height. Figure 6.7 shows some significant difference in the plume centre-line temperatures near the base of the plume when using differencing scheme 'c' when compared to using either 'a' or 'b'.

The lateral temperature distributions predicted using differencing schemes 'a' and 'b' are very nearly symmetrical about the notional plume centre-line. The lateral temperature distribution predicted using scheme 'c' however, can be seen in Figure 6.8 to be increasingly skewed to the right of the centre-line with increasing height. This is not unreasonable in view of the fact that the room extract is positioned to the right (viewed as shown in Figure 6.8) of the plume and at high level, making the overall flow unsymmetrical.

Of the different differencing schemes tested the 'Higher Order Upwind' treatment

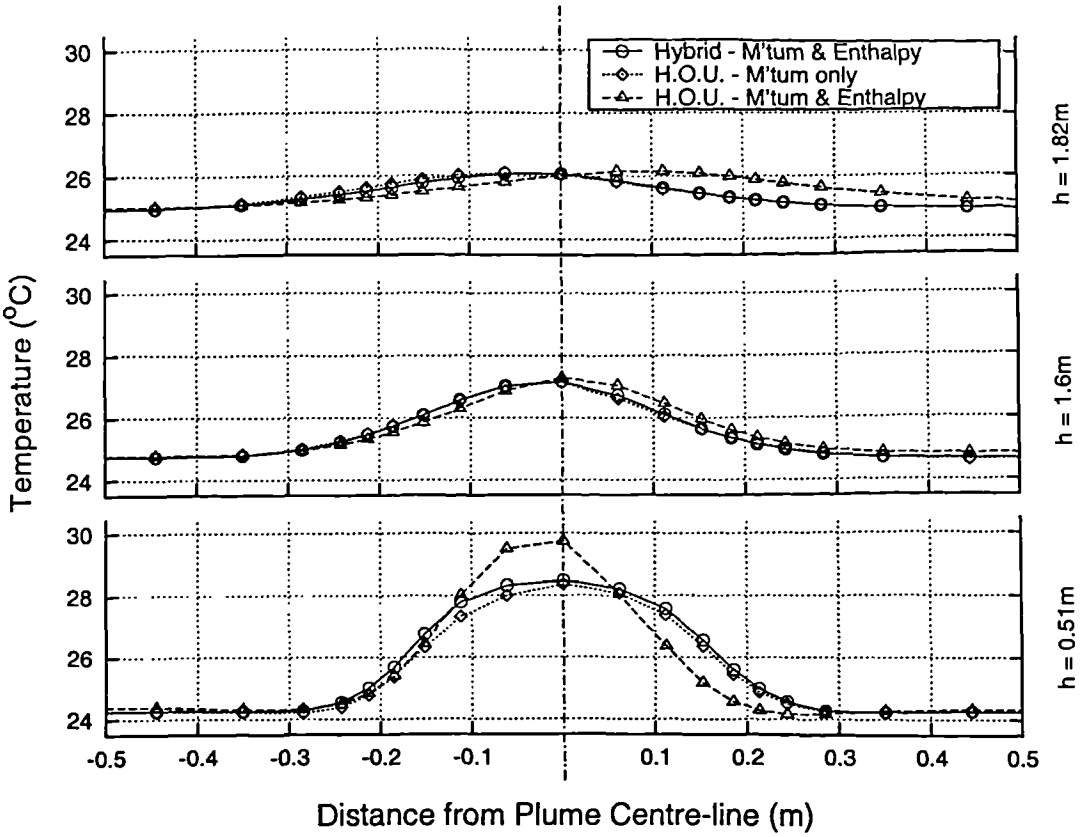


**Figure 6.8:** Temperature distribution across the plume centre-line at three heights calculated with different differencing schemes.

of the enthalpy equation of scheme 'c' produced the most significant difference in the results. The slower rate of decay of plume centreline temperature is indicative of the strength of convection vs. diffusion in the plume also probably indicates the presence of 'false diffusion' effects near the base of the plume when using the 'Hybrid' differencing scheme for the enthalpy equation.

Of the computational meshes and differencing schemes tested, although complete grid independence has hot been demonstrated, the difference between the results with the 67650 cell mesh and those with the 120000 cell mesh are very small. In view of the benefits of using a second order differencing scheme, it is concluded that the best overall numerical accuracy can be obtained using the 67750 cell mesh and differencing scheme 'c', which involves second order differencing of both the momentum and energy equations.

### 6.2.3 Inlet Conditions

In their experiments Li *et al.* made air speed measurements along the axis normal to the supply diffuser at four positions to study the prediction of velocities near the diffuser. These measurements were made using a Dantec 55R76 fibre-film probe which gives omni-directional air speed data. Li *et al.* made comparisons of their experimental measurements with calculated air speeds using what they called the 'mass method' inlet boundary condition and the 'momentum method' (Chen and Moser 1991) boundary condition. In the latter treatment the effect of locally increased momentum at the perforated diffuser face is taken into consideration (see Section 5.6.1). A similar comparison is made here, where the velocities have been taken a conjugate heat transfer calculation for Li *et al.*'s test case B4. The results are shown in Figure 6.9 for both inlet boundary condition treatments.

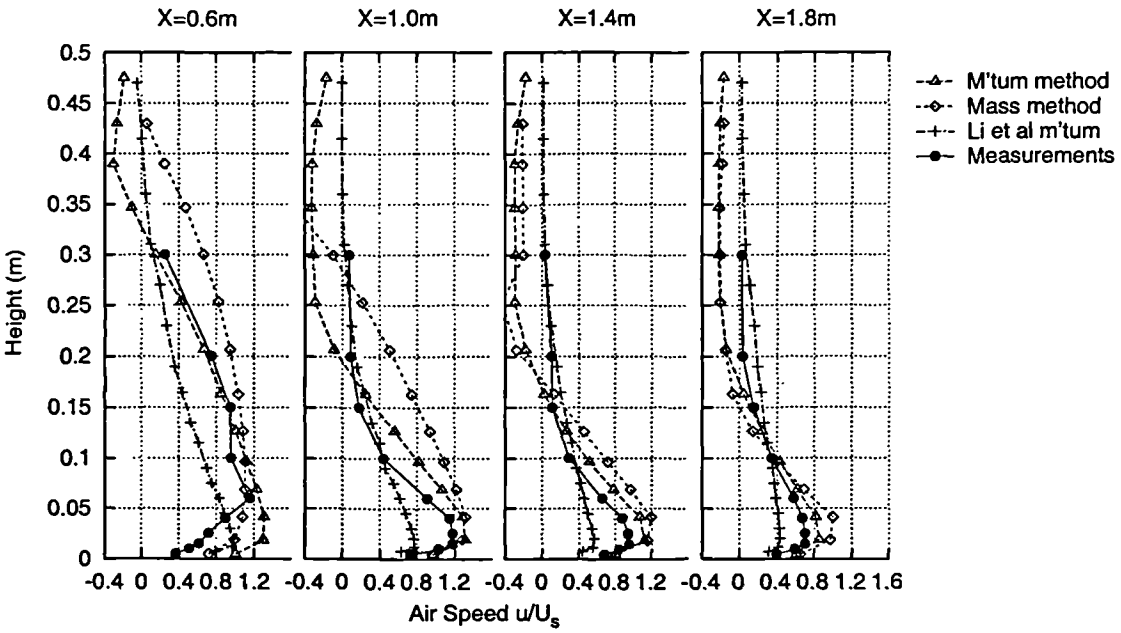


**Figure 6.9:** A comparison of calculated U velocities with the experimental measurements of Li *et al.* test case B4 along the axis normal to the supply diffuser ($U_s = 0.154\,\mathrm{m.s^{-1}}$.

The largest differences between the calculated velocities and the measurements can be seen nearest the diffuser where the velocities are greatest ($x = 0.6\,\mathrm{m}$). At this position the velocities calculated using the 'mass method' fall well above that of those calculated using the 'momentum method'. The magnitude of this difference might be expected very near to the diffuser as it has a free area of only 45%. Over the height 0.1–0.3 m there is good agreement between the experimental

measurements and the velocities calculated with the 'momentum method'. Above this height and up to 0.45 m negative U velocities have been calculated but the measured air speeds are very small ($u < 0.05\,\mathrm{m.s^{-1}}$) and positive. These negative U velocities in the calculation results are associated with a flow towards the supply diffuser above the gravity current immediately above the floor (see Figure 6.10 for similar flow in case B3). It is worth noting that Li *et al.*'s calculation did not show such a flow. Since the measurements were made with an omni-directional sensor it is not possible to conclude what the direction of this part of the flow in the experiments actually was. It is also worth noting that the velocities calculated here for the main gravity current (nearer the floor) are in closer agreement with the measured air speeds than those calculated by Li *et al.*. This difference between the calculated results of Li *et al.* and those presented here may be due to the difference in the wall function treatment or the probably improved numerical accuracy here due to the denser mesh. Unfortunately Li *et al.* did not publish details of their wall functions or their implementation.

The 'momentum method' of inlet boundary condition treatment is clearly a more realistic treatment of the inlet conditions than that of the 'mass method' where the effect of the restricted free area of the diffuser is significant. Accordingly, the 'momentum method' has been used in subsequent calculations, although the difference between the two treatments is likely to be less significant in the case of the Loughborough test chamber, as the free area of the diffuser was much higher (88%).

### 6.2.4 The Predicted Velocity Field

The predicted velocity field for the NSIBR test chamber is shown in the form of a series of vector plots in Figures 6.10–6.13 and are the results of the conjugate heat transfer calculation for test case B3. For the purposes of discussion the flow can be considered in two zones. Firstly, the flow in the upper part of the room above the level of the top of the supply diffuser and including the plume. Secondly, the flow near the floor up to the height of the top of the supply diffuser and including the heat source.

Cross sections of the room passing through the heat source position are shown in Figures 6.10 and 6.11. The plume can be clearly seen as the dominant source of momentum in the upper part of the room. The plume above the heat source

can be seen to grow steadily until very near the ceiling. As the plume impinges on the ceiling the flow spreads out into a relatively thin boundary layer spreading laterally in all directions across the ceiling. This boundary layer has sufficient momentum to reach the walls and drive some flow vertically downwards. This boundary layer moves down from the top of the walls, and reduces in thickness in the direction of flow, down to a height of approximately 0.7 m.

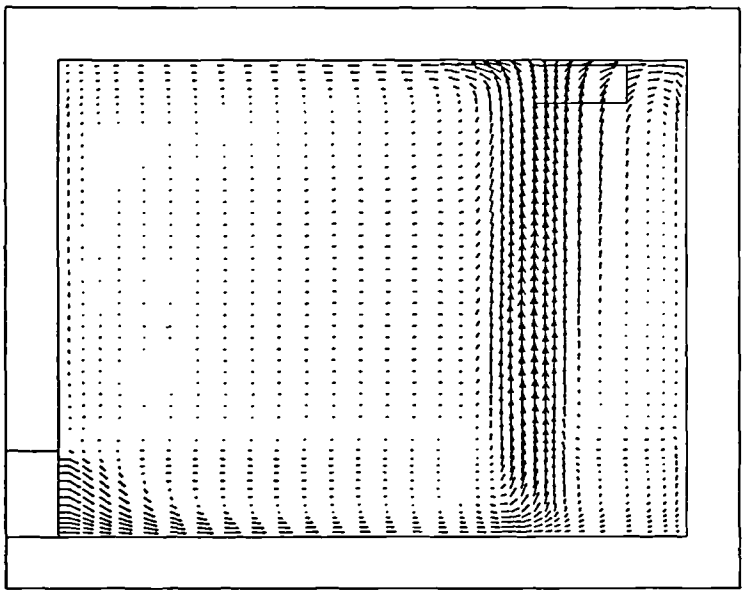

Figure 6.10: A vector plot of the velocity field for case B3 projected on a vertical plane at the centre-line of the room ($y = 2.1$ m).

Although the experimental measurements indicated that in the upper part of the room the wall surface temperature was always below that of the air temperature (this is also indicated in the numerical results) this does not seem to result in sufficient driving force to accelerate the flow down the walls. If this were the case the boundary layer could be expected to thicken as further air is entrained and it has already been noted that the contrary occurs. It is also interesting that the flow in the plume and the surface boundary layers do not induce much mixing in the upper region of the room surrounding the plumes. In this region the flow is mostly lateral towards the plume and at very low velocity. This flow is subsequently entrained into the plume.

Consider now the flow in the lower region of the room. Figure 6.10 shows the

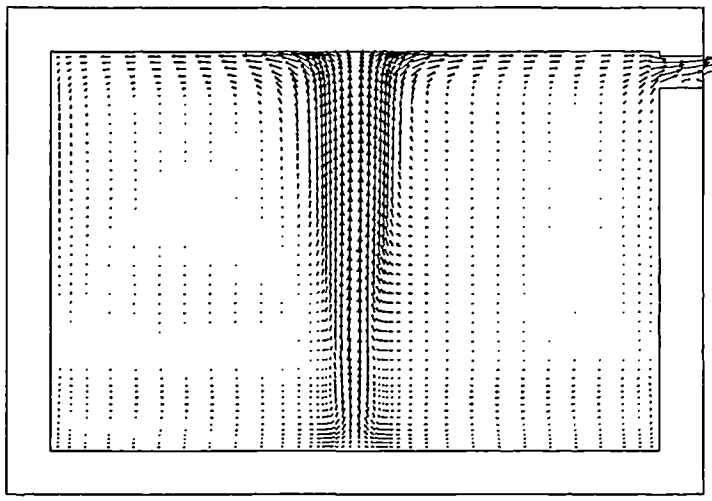

Figure 6.11: A vector plot of the velocity field for case B3 on a projected on a vertical plane through the heat source and extract outlet ($x = 2.85$ m).

flow from the supply diffuser falls towards the floor under the effect of buoyancy within a small horizontal distance (~0.7 m). Beyond this distance the air moves in a boundary layer across the floor. This layer can be seen in Figure 6.10 to have a constant thickness of approximately 100 mm. Figure 6.12 is plotted in a horizontal plane 50 mm above the floor and shows the flow to be spreading radially from the supply diffuser. This flow pattern extends across the whole of the floor and is disrupted in the region directly below the heat source (the bottom of the heat source being only 0.11 m above the floor in this case) where some air is entrained into the bottom of the plume.

It was noted previously (see Section 6.2.3) that the velocity profiles on the room centre-line showed some flow towards the diffuser above the boundary layer moving over the floor surface. This flow can be seen in Figure 6.10 between the heights 100 mm and the top of of the diffuser (500 mm). At the diffuser this flow appears to be entrained into the supply flow as it falls towards the floor. Experimental work concerned with diffuser performance has also shown that air is strongly entrained into the flow from the supply diffuser in this location (Melikov and Langkilde 1990). From Figure 6.10 it is not clear where all of this flow towards the diffuser originates from. Figure 6.13 shows the flow in a horizontal plane at a height of 225 mm. In this plane it can be seen that there is a lateral recirculation pattern such that air moves from the side walls towards the load and back along the centre of the room towards the diffuser.

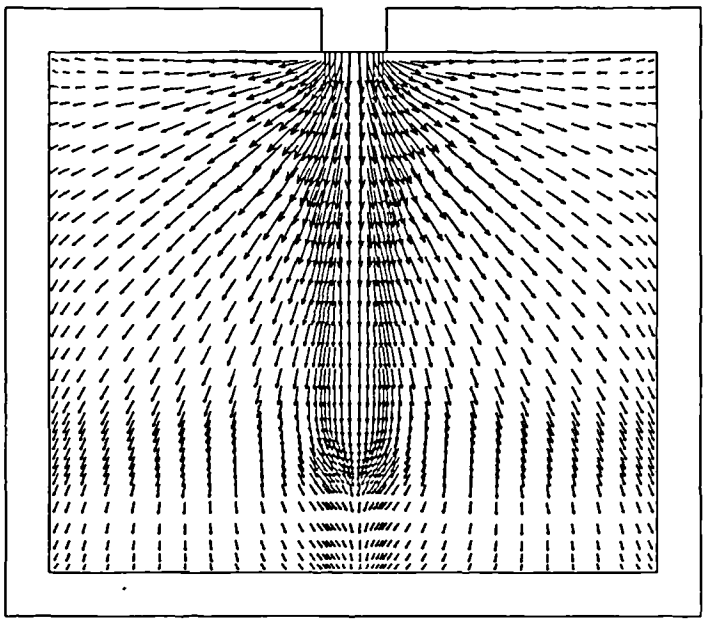

Figure 6.12: A vector plot of the velocity field for case B3 projected on a horizontal plane just above the floor ($z = 0.05\,\mathrm{m}$).

### 6.2.5 The Predicted Temperature Field

The ability of the numerical method to successfully predict the temperature field and overall heat transfer in the modeled room is important if such a method is to be used alone to produce data for development of a simplified model. Comparisons with the measured temperature data have firstly been made for Li *et al.*'s experimental test case B3. A series of calculations were made using different thermal boundary condition treatments with different levels of sophistication. These can be summarised as follows.

i) Zero convective heat flux (often referred to as an adiabatic boundary condition).

ii) No explicit modeling of wall conduction or surface radiation. Wall surface temperature fixed using experimental data.

iii) Zero conducted flux. Surface radiation is modeled so that the net radiant flux is balanced with the convective flux everywhere—an adiabatic boundary condition.

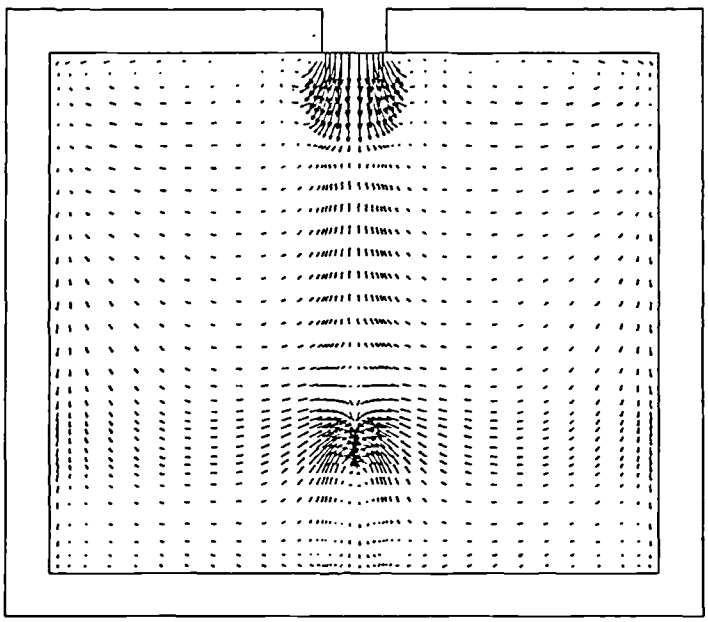

Figure 6.13: A vector plot of the velocity field for case B3 projected on a horizontal plane 225 mm above the floor ($x = 0.225$ m).

iv) Wall conduction and surface radiation modeled explicitly so that radiant, convective and conductive fluxes are balanced at wall internal surfaces—a conjugate heat transfer calculation. Experimentally measured external surface temperatures are used as the boundary conditions.

The results of these calculations are firstly examined by comparing the vertical air temperature profile measured by Li *et al.* with the temperature calculated on a vertical line in the same location. The temperature profiles for the calculations are compared with the experimental measurements in Figure 6.14. (The position at which the measurements were made is shown in Figure 6.1).

Considering the predicted temperature profiles in order it can firstly be seen that where the zero convective heat flux condition is used the temperature near the floor is drastically below that measured ($\sim$ 3 K). This calculation serves mainly to show the importance of including the effects of the radiant coupling between the air and the surfaces. Secondly, the air temperature at the ceiling, for the fixed wall temperature calculation, is close to the measured value. Near the floor the temperatures are $\sim$0.5 K lower than the measured values but the shape of the

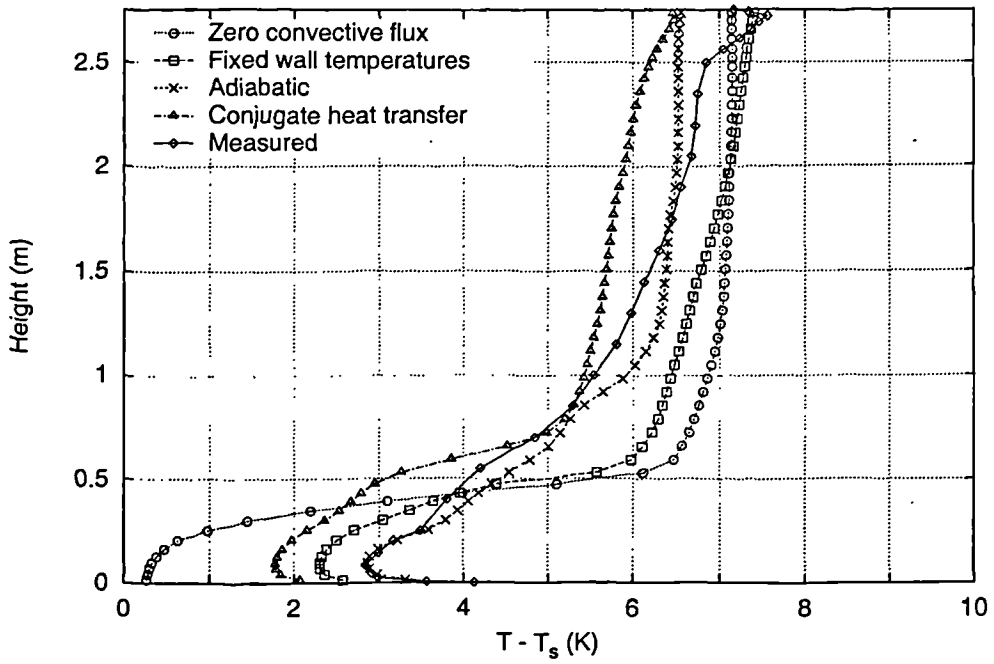


Figure 6.14: Calculated temperature profiles compared with the experimental measurements of Li *et al.* for case B3.

profile up to 0.3 m from the floor is very similar. Above a height of 1 m and up to 2.5 m the shape of the temperature profile is also similar to that measured, but with temperatures in excess by ~0.5 K. The temperature gradient between 0.3–0.6 m is correspondingly much larger than that measured over this height and the air temperature poorly predicted in the occupied zone of the room (i.e. up to 1.1 m).

The results from the adiabatic calculation show very close agreement with the measured temperatures near the floor. In the upper part of the room the agreement with the measured temperatures is also good but the temperature gradient is lower, suggesting some over-prediction of the extent of recirculation and mixing. Immediately below the ceiling the calculated temperature is ~0.5 K low. In the occupied space the temperature gradient predicted is in good agreement with the experimental data.

The air temperatures calculated using the conjugate heat transfer procedure are lower than the measured temperatures and those predicted in the other calculations. The temperature is ~1 K lower than that measured near the floor and ~0.5 K lower than that measured near the ceiling. The calculated temperatures can be expected to be lower than in the results of the adiabatic calculation, as in

this case the outside temperature are slightly lower than those inside and a net heat loss by conduction was measured in the experiment. The difference between the adiabatic calculation results and the conjugate heat transfer results appears mainly near the floor. The temperature gradient in the occupied zone is correspondingly high. Near the ceiling (above 2.5 m) there is a notable change in the measured temperature gradient and a peak in the air temperature very close to the ceiling surface. (This is probably the effect of the boundary layer of warm air from the plume moving across the ceiling.) It is only the conjugate heat transfer calculation results that reproduce this feature in the temperature profile, although not to the full extent.

The overall heat transfer conducted through the walls and carried by the air stream is shown in Table 6.2. Comparison of the values of total heat transferred to the air stream ($Q_a$) in Table 6.2 with the temperature profiles shown in Figure 6.14 shows a correlation between the total heat transfer and the temperature in the upper part of the room (air leaves the room at 2.5 m in fact). The conjugate heat transfer calculation results in the lowest net heat transfer of heat to the air stream, and the fixed wall temperature the highest. Li *et al.* similarly over-predicted the wall fluxes and reported a value of 256 W for $Q_a$ from their conjugate heat transfer calculation for this test case. It might have been expected that the calculation with the fixed wall temperatures gave a more reasonable temperature profile and a prediction of net heat loss through the walls. In this case it is the wall functions alone that determine the relation between the wall surface temperature, the adjacent air temperature and the heat flux through the wall, and might therefore be at fault.

| *Conditions* | $Q_a$ *(W)* | $Q_c$ *(W)* |
|---|---|---|
| Measured | 283 | 17 |
| Zero Convective flux | 300 | 0 |
| Fixed Wall Temperatures | 310 | -10 |
| Adiabatic | 300 | 0 |
| Conjugate Heat Transfer | 266 | 34 |

**Table 6.2:** The net heat transfer to the air stream and conducted through the room walls, $Q_a$ and $Q_c$ for the different calculations for case B3.

It could also have been expected that with the adiabatic boundary condition the air temperature in the upper part of the room be higher that measured. This could possibly be due to systematic differences between the temperatures measured in

the profile and the extract temperature. There is some evidence of this in the numerical results. The spatial temperature distribution in the room is shown in the form of contour plots of the temperature field in Figures 6.15 and 6.16. It is also worth considering the uncertainty in the measured overall heat balance, as this is very close to an adiabatic condition. Li *et al.* estimate errors in the temperature measurement of $\pm 0.2\,\mathrm{K}$ and $\pm 2\%$ in the flow measurement. In this case this amounts to an overall error in the heat balance of $\pm 14\,\mathrm{W}$. In view of this it is quite possible that the experimental conditions were closer to adiabatic than indicated.

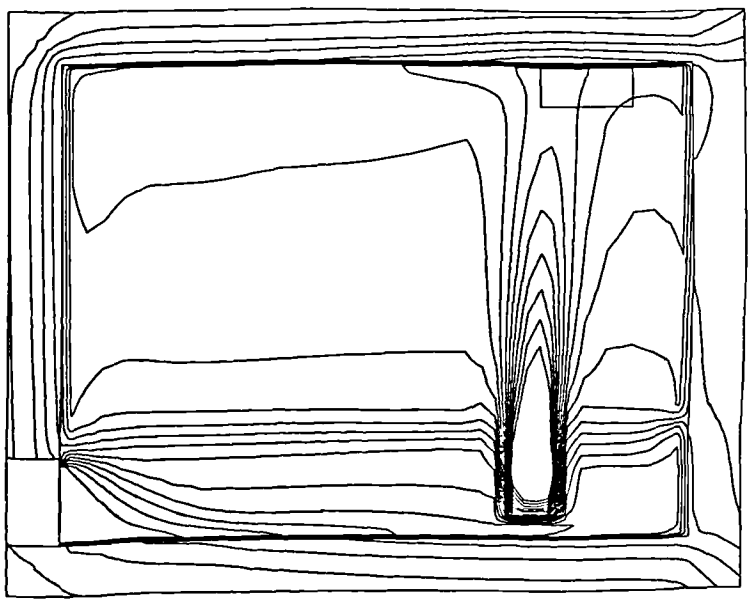

**Figure 6.15:** A contour plot of the temperature field for case B3 on a vertical plane at the centre-line of the room ($y = 2.1\,\mathrm{m}$). Contours are plotted at $0.5\,\mathrm{K}$ intervals in the range 18–28°C.

There are a number of uncertainties and sources of error relating the calculated temperature and heat flux data when making a comparison with the experimental data. These include

- experimental error in the air and surface temperature measurements
- uncertainty in the wall conductances
- uncertainty in the floor boundary conditions

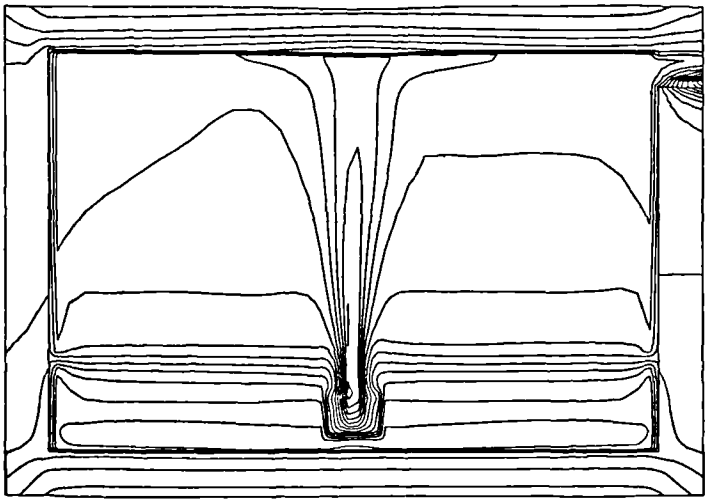

**Figure 6.16:** A contour plot of the temperature field for case B3 on a vertical plane through the heat source and extract outlet ($x = 2.85\,\mathrm{m}$). Contours are plotted at 0.5 K intervals in the range 18–28°C.

- uncertainty in calculation of the convective heat fluxes

The experimental errors in temperature measurement not only effect the comparison of the air temperatures but also the application of the measured surface temperatures in the fixed surface temperature boundary condition calculation. Li *et al.* give an estimation of experimental error in their temperature measurements of 0.2 K.

In the case of the conjugate heat transfer calculation the number of uncertainties is increased by modeling the walls explicitly. Firstly the conduction calculation is dependent on the solid walls conductivity which has been derived from the published U-value. It is not known whether the published U value was calculated or measured but in either case there must be some uncertainty associated with its value. Also in the case of the conjugate heat transfer calculation uncertainty in the specification of the outside surface temperatures may account for some error in the predication of the overall heat transfer. In this case there is particular uncertainty about the specification of the floor outside surface temperature. Li *et al.* published the outside temperatures for all the surfaces except the floor. Li has subsequently provided an approximate temperature for use in these calculations (Li 1995)

Calculation of the conducted flux is dependent on the heat balance at the internal surfaces and so also on the calculation of the radiant and convective fluxes. The

radiant flux acts mainly to redistribute heat within the rooms—mainly from ceiling to floor in this case—and errors arising from the discretization of the radiation field will affect this distribution, but have negligible impact on the overall heat transfer. (The numerical method always enforces a balance between the radiant, conducted and convective fluxes) .) The radiant distribution could also be affected by the fact that the heat source is modeled as entirely convective (no physical surfaces). In the experiment although the heat source was of low emissivity and porous (hence surprising the surface temperature) it undoubtedly gave some radiant output. In particular as the heat source was so close to the floor the heat balance at the floor surface (at least local to heat source) could have been influenced by its' radiant output. A conjugate heat transfer calculation made using a solid heat source (with emissivity 0.3) showed this local effect but resulted in an increase in the predicted heat loss of 4.5 W.

The calculation of the convective flux is strongly dependent on the formulation and implementation of the wall functions. There must be some concern about the applicability of the universal wall functions (equations 5.6.3 and 5.6.3) to all of the room surfaces under the flow conditions found in these calculations. Also it has already been noted that the values of $y^+$ are somewhat lower than is desirable. The universal wall functions (Launder and Spalding 1974) have been derived for forced convection boundary layers without buoyancy effects. There are a number of places in the displacement ventilation flow modeled here where wall conditions differ from this. Firstly at the floor the boundary layer is significantly different in that buoyancy effects are strong enough to damp out entrainment so that the layer does not grow in thickness. At the ceiling heat transfer around the point of impingement of the plume on the ceiling is of some significance. At the point of impingement there is a stagnation point around which the Nusselt number can be expected to vary significantly (Lytle and Webb 1994, Gardon and Akfirat 1965). At the walls there is also sufficient temperature difference between the surfaces and the air and sufficient height for buoyancy to effect the development of the boundary layers.

In view of this it is likely that the application of the universal wall functions at all surfaces gives rise to errors in the prediction of the convective fluxes. Li *et al.* come to a similar conclusion. Similar problems have also been reported by Djilali *et al.* (Djilali, Gartshore and Salcudean 1989)

## 6.3 Calculation of the Loughborough Displacement Ventilation Test Cases

In this section the results of calculations of the experimental test cases from the Loughborough test chamber without the chilled ceiling in operation are presented. Although there may be more interest in the calculation of the flow for the test cases including the chilled ceiling, calculation of these cases allows firstly, a reasonably direct comparison with the NSIBR test cases, and secondly, the differences in the flow between the cases with and without the chilled ceiling (and greater magnitude and number of loads) to be highlighted.

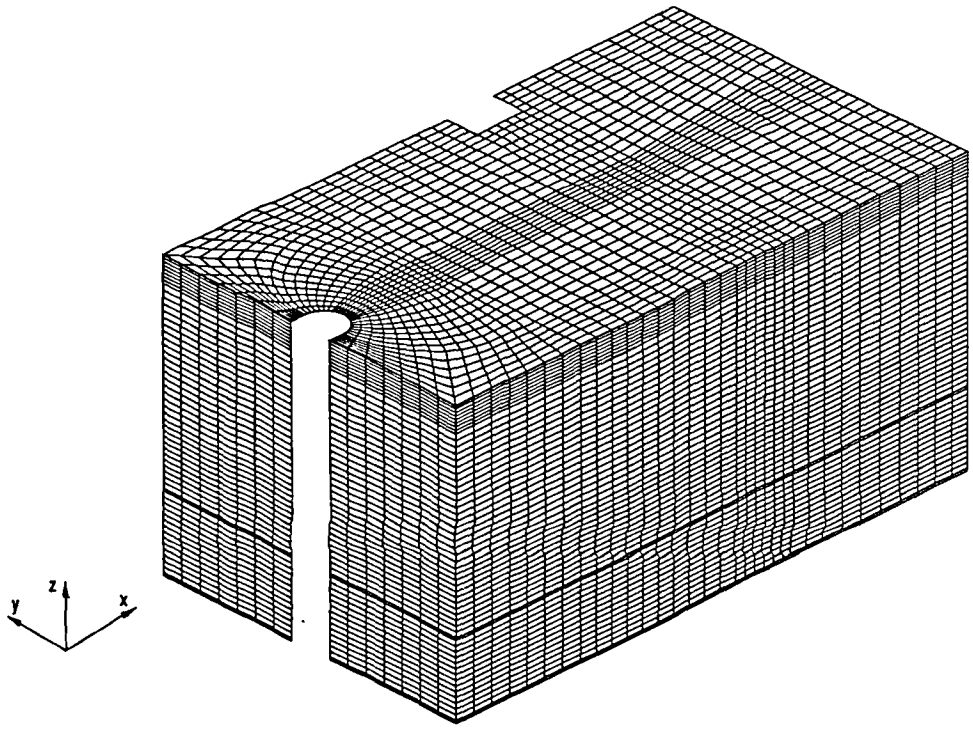


**Figure 6.17:** The 40 × 36 × 56 mesh (80640 cells) used for the Loughborough displacement ventilation test case calculations.

A similar approach has been taken to the calculation of these test aces as with the NSIBR test aces. Calculations have been made with the thermal boundary conditions previously denoted (ii) and (iv), i.e. fixed wall temperatures and conjugate heat transfer boundary conditions. Similarly, a false time stepping iterative procedure has been used, with the same convergence criteria as before. The results presented here are for test case DV9 which had a total load of 300 W and supply

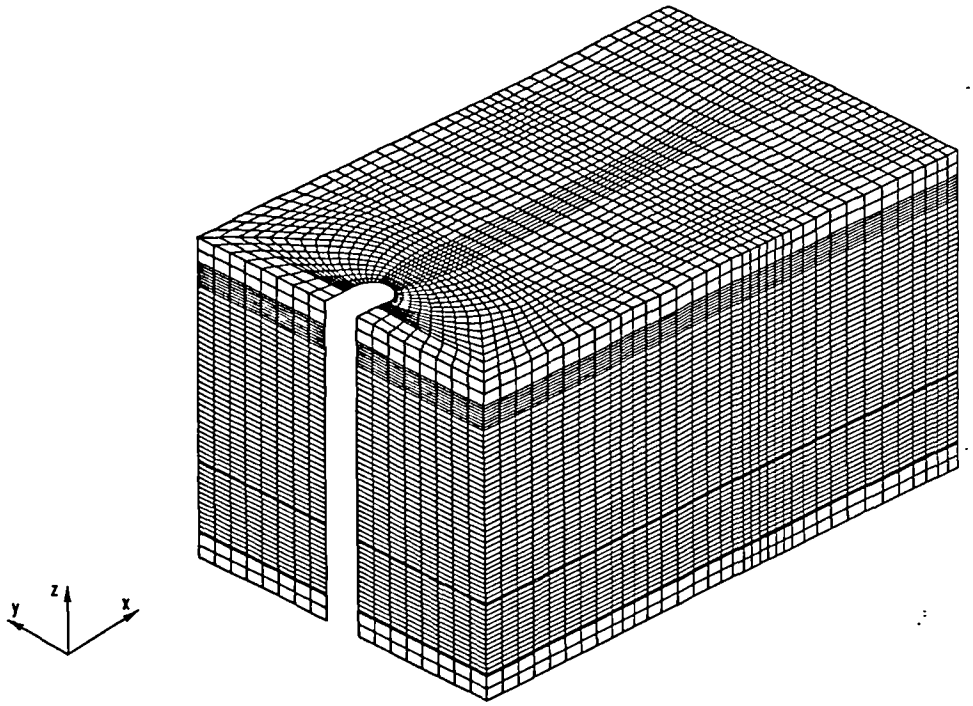


**Figure 6.18:** The 44 × 40 × 60 mesh (105600 cells) used for the Loughborough displacement ventilation test case calculations of conjugate heat transfer.

air flow of $1.5\,\mathrm{ac.h^{-1}}$. Hybrid differencing has been used in this case—differencing scheme 'a'.

### 6.3.1 The Computational Mesh

The principal difference between the calculation of the NSIBR test cases and the Loughborough displacement ventilation test cases is due to the more complex geometry. The geometry of the Loughborough chamber is made more complex by the inlet having a semi-cylindrical shape and is also made unsymmetrical by the presence of a column protruding part way along the south wall. As the shape of the inlet is of particular importance a body fitted mesh has been used in these calculations.

The increased complexity of the geometry has also resulted in slightly larger mesh sizes. A mesh of 80640 cells has been used for the calculations with fixed wall

temperature boundary conditions and is shown in Figure 6.17. A similar mesh of 105600 cells with additional cells representing the room fabric has been used in the conjugate heat transfer calculations and is shown in Figure 6.18. Distortion of the cells in both these meshes has been controlled to a reasonable level. The most distorted cells are in the corners of the room adjacent the supply diffuser. This was not of concern, as these corners are rather distant from the main features of the flow. In much of the geometry the mesh is, in fact, rectilinear. The calculations on these meshes have shown a similar problem with low $y^+$ values as in the NSIBR calculations, with $y^+$ falling in the range $10 < y < 40$. For the conjugate heat transfer calculations the conductivity of the walls has been set using the conductances derived from the results of the coheating experiment.

### 6.3.2 Prediction of the Velocity Field

Results from the steady state conjugate heat transfer calculations of flow are presented here in the form of vector plots showing the main features of the flow. Vectors on vertical sections through the heat source are shown in Figures 6.19 and 6.20. As no velocity measurements were made for this test case, no detailed quantitative comparisons with the calculated results have been possible.

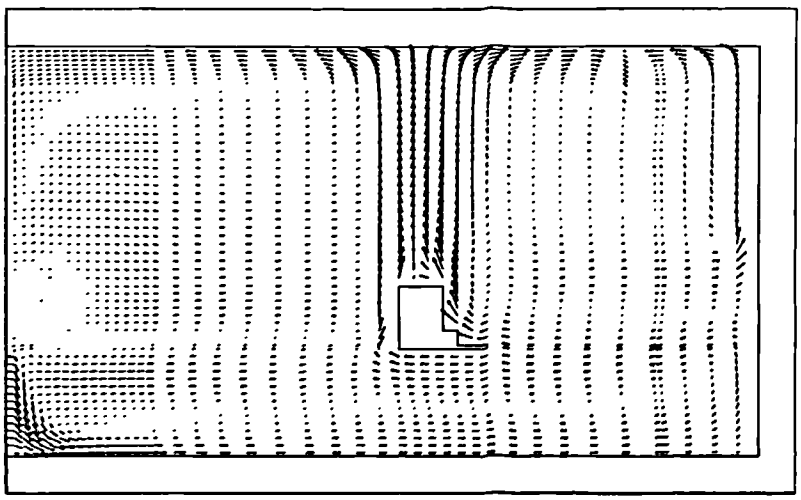

**Figure 6.19: A vector plot of the velocity field for case DV9 on a vertical plane along the room centre-line (y=1.54 m).**

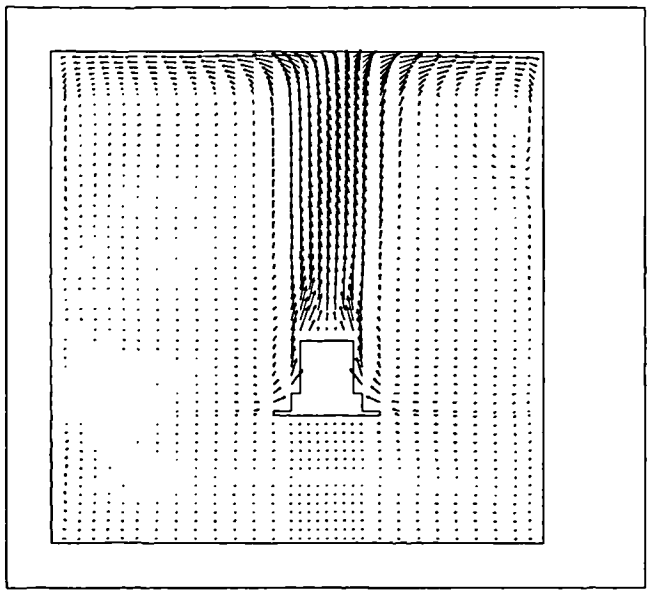

Figure 6.20: A vector plot of the velocity field for case DV9 on a vertical plane through the heat source (x=3.05 m).

Figure 6.19 shows clearly the flow from the supply diffuser falling towards the floor, and within a small horizontal distance (< 0.5 m). The flow from the diffuser continues along the floor to the very back of the room in a boundary layer on the floor, and without being disturbed as it passed below the heat source. At the rear (west) wall of the room this flow can be seen to reverse direction and flow back over the floor boundary layer towards the heat source where it appears to be drawn into the base of the plume. Figure 6.21 shows vectors in a horizontal plane 50 mm from the floor. The wide radial spread of the flow near the diffuser is very clear. It is interesting that, because of the narrow aspect ratio of the room, part way down the room the flow into the floor boundary layer becomes parallel so that the velocity is nearly constant beyond $x \sim 2$ m.

The flow in the upper part of the room (above 0.7 m) is very similar in nature to that found in the NSIBR test case results. The flow is dominated by the plume. After the plume has impinged on the ceiling a boundary layer can be seen (see Figure 6.19) to flow across the ceiling and extending to each wall. This boundary layer can be seen flowing down the walls to a height of $\sim 0.75$ m where the flow is drawn back towards the plume. In the region outside these boundary layers and

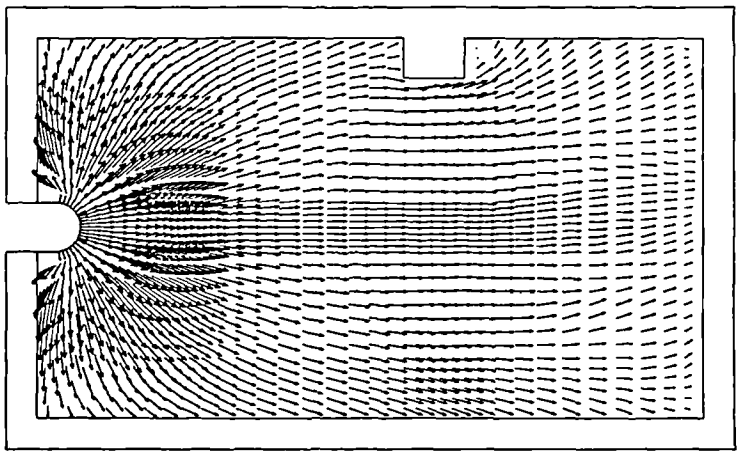

**Figure 6.21:** A vector plot of the velocity field for case DV9 on a horizontal plane just above the floor (z=0.05 m ).

the plume the flow is mainly horizontal and a very low velocity towards the plume. Figure 6.20 shows the recirculation in the room more clearly where the width of the room is slightly more restricted. Some distortion of the plume can be seen in this view, so that the peak velocity in the plume is to the left of the heat source centre-line in this view. Some asymmetry can also be seen in the recirculating flow patterns. The room dimensions appear to be small enough in this plane, in relation to the plume size, that the recirculating flow external to the plume effects the plume internal flow structure.

### 6.3.3 Prediction of the Temperature Field

The temperature calculations for test case DV9 are presented here firstly in the form of room air temperature profiles The predicted temperature profiles from the fixed wall temperature calculation and conjugate heat transfer calculation are compared with the experimentally measured profile in Figure 6.22. In this test case the heat flux conducted out of the room was significant. The measured value of $Q_a$, the heat transferred to the air stream, was only 72.5 W of the total 300 W .

The temperature profile predicted by the fixed wall temperature calculation shows the temperature in the upper part of the room noticeably over-predicted ($\sim$ 1 K). The temperature near the floor is only slightly over-predicted ($\sim$ 0.3 K). The temperature gradient in the occupied zone of the room is correspondingly over-

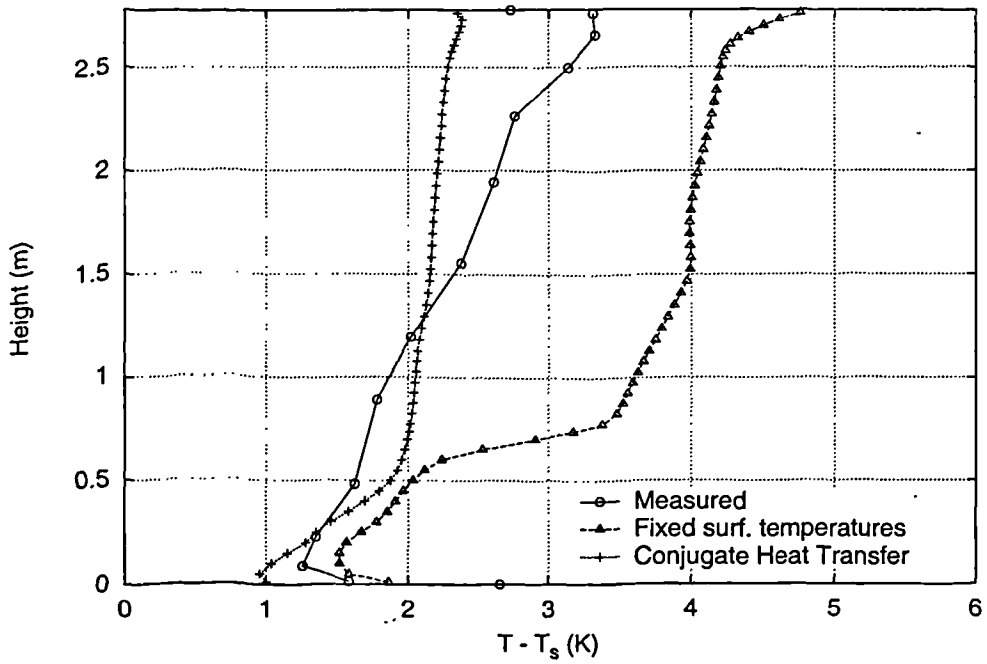


**Figure 6.22:** Calculated temperature profiles compared with the experimental measurements for case DV9.

predicated. The fixed wall temperature results also show a feature adjacent the ceiling, where the air temperature rapidly increases, that is not evident in the experimental results.

The temperature profile predicted by the conjugate heat transfer calculation show temperatures slightly lower than that measured in the upper region of the room. The temperature gradient is also lower than that measured in these region—suggesting over-prediction of the mixing and diffusion processes. The prediction of the temperature near the floor is notably low ($\sim$ 0.4 K) and the shape of the profile near the floor rather different than that measured. Also at $\sim$ 0.6 m there is a noticeable change in temperature gradient in the calculated results. This is somewhat over emphasised and at a lower level in the room than that shown in the measured profile. This is consistent with over-prediction of the mixing and recirculation in the upper region of the room—leading to lower temperature gradients and prediction of the recirculation to a lower level in the room.

The overall heat transfer to the air stream ($Q_a$) calculated using the fixed wall temperature boundary conditions was 94.4 W, compared to the measured value of 72.5 W. This degree of over-prediction is implied from the temperature profile results. The conjugate heat transfer calculation predicted a value of $Q_a$ of

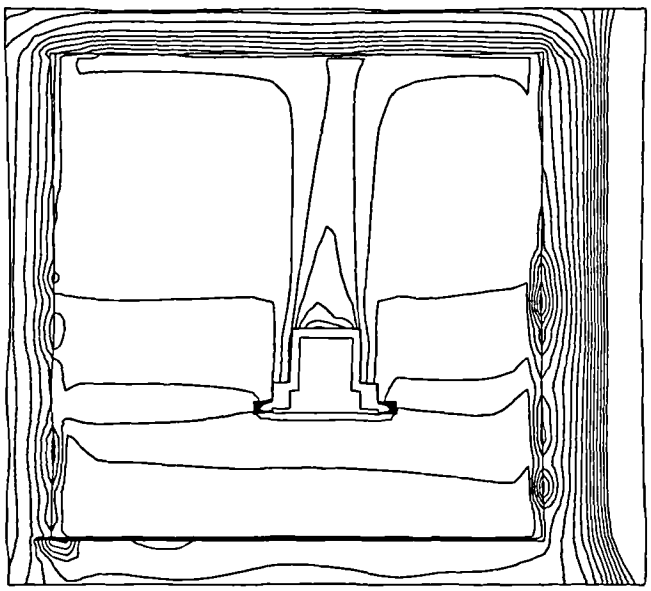

**Figure 6.23:** A contour plot of the temperature field for case DV9 on a vertical plane through the heat source ($x = 3.05\,\mathrm{m}$). Contours are plotted at 0.25 K intervals in the range 19–24°C

45.2 W. The heat transfer results of the calculations for test case DV9 thus show similar trends to those of the NSIBR calculations, in that the fixed wall temperature calculation tends to over-predict, and the conjugate heat transfer calculation under-predict, the heat transferred to the air stream.

Temperature contours on a vertical planes through the heat source are shown Figures 6.23. These figure shows the results of the conjugate heat transfer calculation. The significance of the heat transferred through the walls can be seen by the noticeable temperature gradients through the room fabric.

## 6.4 Calculation of the Displacement Ventilation and Chilled Ceiling Test Cases

The displacement ventilation and chilled ceiling test cases from the Loughborough test chamber have been modeled using a body fitted mesh. This was necessary, as in the Loughborough displacement ventilation test cases, to accommodate the

curved face of the supply diffuser. The mesh further complicated in the chilled ceiling test cases due to the presence of four heat sources rather than one. This has resulted in a mesh of $45 \times 41 \times 56$ (103320 cells), which is shown in Figure 6.24.

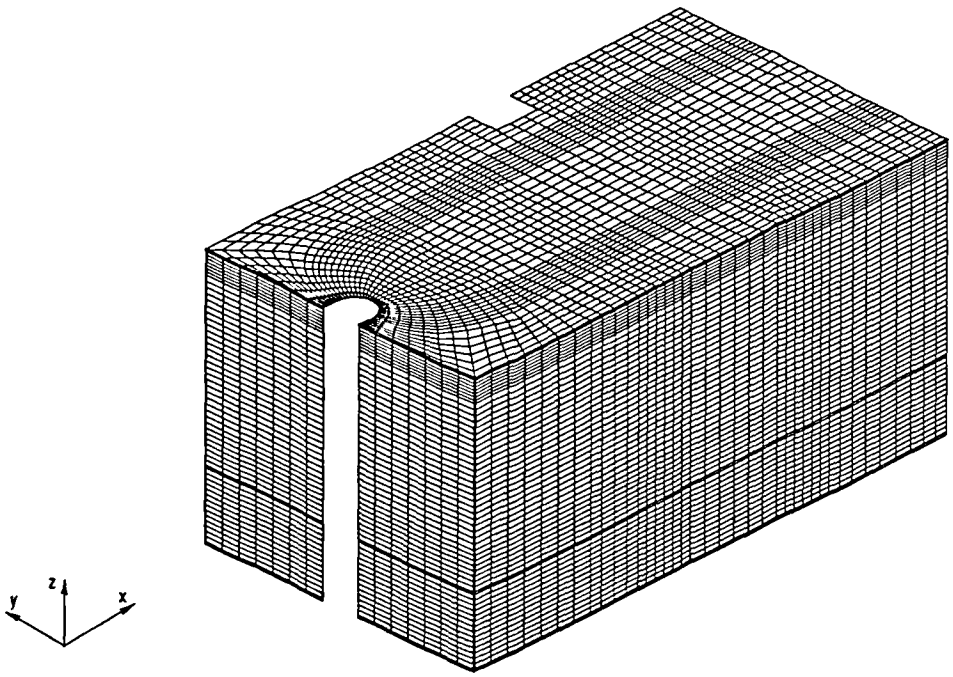


**Figure 6.24:** The $45 \times 41 \times 56$ mesh (103320 cells) used for the Loughborough displacement ventilation and chilled ceiling test chamber calculations.

Initially the same false time stepping solution procedure was adopted as used with the other test chamber calculations. However it was found that this method could not reduce the equation residuals to the required level. Examination of the spatial distribution of the equation residuals did not reveal any particular regions in the flow that could be causing convergence difficulties. This situation could be explained by transient effects in the flow, such that a true steady state could no longer be defined. To examine this possibility a fully transient solution procedure was adopted.

When using a fully transient solution procedure the objective is to find a time accurate solution at each time step. To this end the temporal derivative terms of each equation are properly discretised and a spatially constant time step applied. A fully implicit first order backwards differencing scheme was used to discretise the temporal derivative terms of the equations and under-relaxation no longer

applied. The same convergence criteria were used as in the other calculations so that, at each time step, the mass residual was checked until it had fallen below 1% of the net flow through the room, and the enthalpy equation residual had fallen by four orders of magnitude.

A calculation of the flow and temperature fields for test case DV11 was made using this transient solution procedure and fixed wall temperature boundary conditions. In this test case there were four heat sources of 200 W total output. When using fixed temperature boundary conditions an assumption has to be made about the radiant output of the heat source and a value of 50% was used here. (Measurements with a hand held radiometer later showed the radiant output to be 53%.) The heat source boundary conditions were applied in two stages so that during the first 40 minutes of solution time only heat sources one and four were activated (the numbering of the heat sources and corresponding plumes is indicated in Figure 6.25). It was found that satisfactory convergence could be maintained with time steps of up to 3.0 seconds. Time steps of 3.0 seconds required 16 iterations per time step so that the procedure was computationally very expensive, progressing an order of magnitude slower than real time. Time steps of 1.0 seconds have also been used where greater temporal resolution of the data was required.

To monitor the progress of the transient solution a number of points were chosen at which the field values of each solution variable were recorded at each time step. Firstly, four points at high level in each plume were selected. The position of these monitoring points is shown in Figure 6.25

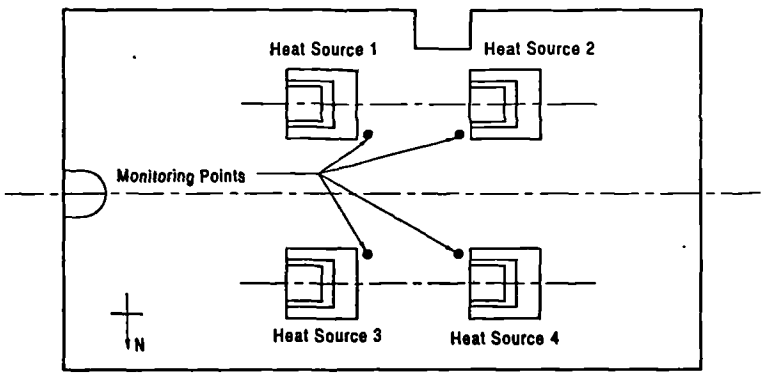


**Figure 6.25:** A plan view of the Loughborough test chamber showing the position of the plume monitoring points (at a height of 2.77 m) and the numbering of the heat sources.

The initial conditions of the calculation were zero velocity and a constant tem-

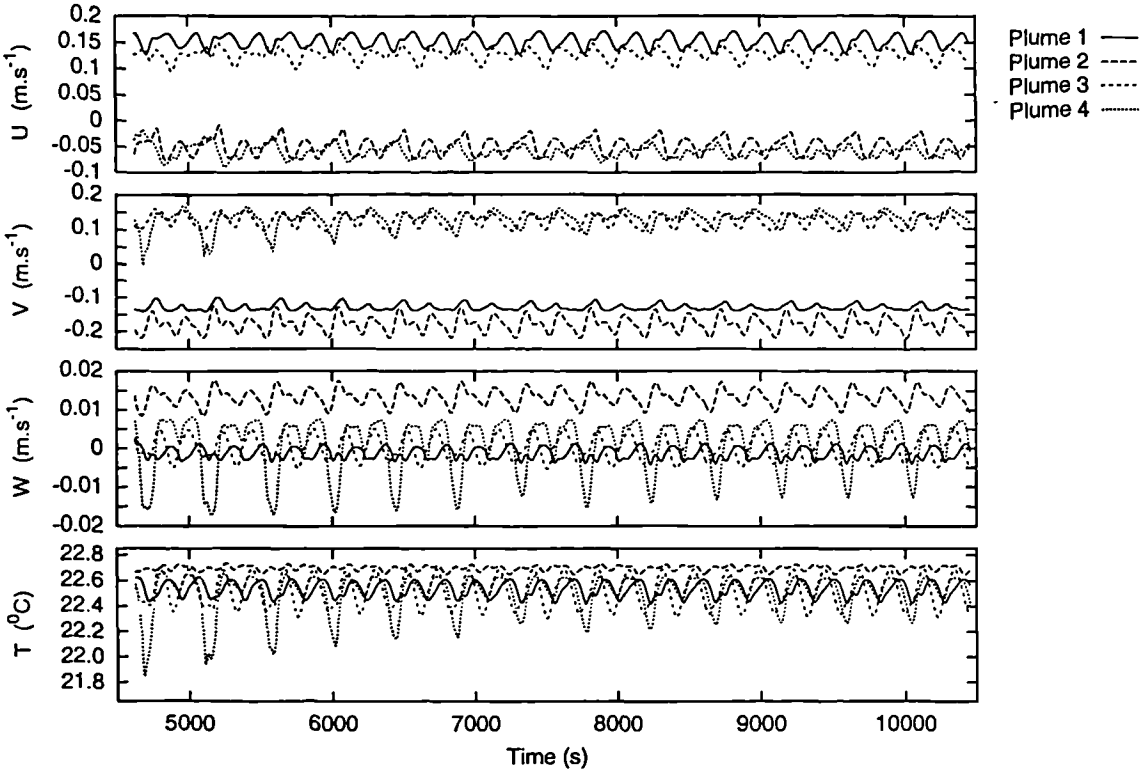


**Figure 6.26:** The cyclic variations of the U, V and W velocity components and Temperature at the four monitoring points during the progress of the transient calculation.

perature throughout. One hour after the activation of all the heat sources was allowed for the flow to develop. As the objective of the calculation was to find data representative of the measured conditions data from this initial period was disregarded. Examination of the data at the plume monitoring points showed that by this time in the solution (~4600 s) periodic fluctuations in the flow had evolved with a period of 450 seconds. These fluctuations continued and were observed in each solution variable but with the largest amplitude in the V velocity data. This data has been plotted in Figure 6.26. It was found that both the V velocity and temperature data obtained from the monitoring point in plume four were decaying. The calculation was therefore continued until a steady periodic cycle was observed (from 8000s onwards, see Figure 6.26). It may be noted that the amplitude of the fluctuations, particularly of the U and V velocities, is significant given that the maximum velocities near the base of the plumes are $\sim 0.3\,\mathrm{m.s^{-1}}$.

A notable feature in the shape of the velocity and temperature signals at each monitoring point is that, within each cycle, there are two maxima and two cor-

responding minima (see Figure 6.27). To analyse the fluctuating motion of the plumes further a set of animation data was generated on a vertical plane through the centre of heat sources two and four (plane $x = 3.65\,\mathrm{m}$). Animated shaded contours of each velocity component and temperature were then viewed. The plumes could be clearly seen to move from side to side in the room, but plume four more so than plume two. The timing of the movement of plume four—either towards the north wall, upright or towards the room centre—was noted from the animated data. This information has been noted on a plot of the U, V and W velocity data from the plume four monitoring point in Figure 6.27.

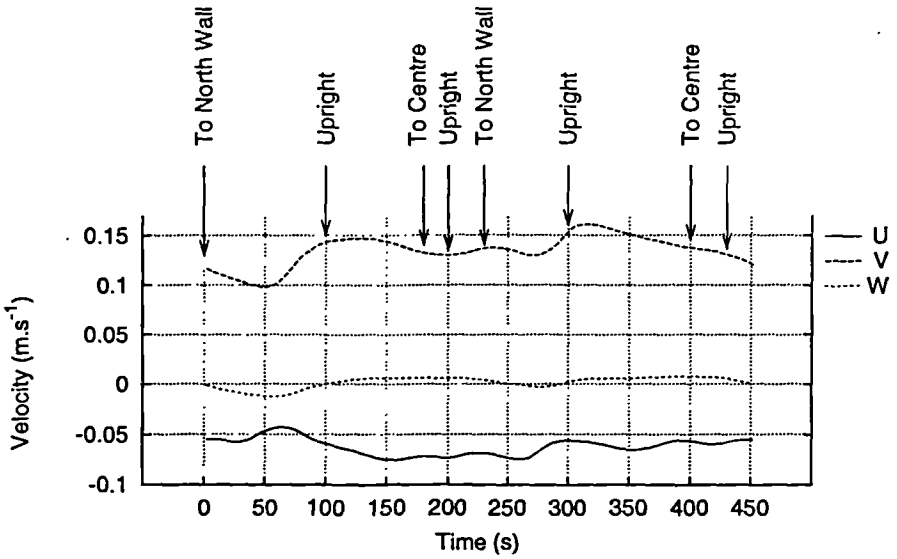


**Figure 6.27:** Progress of the motion of plume four through one period of the observed steady periodic fluctuations.

A notable feature of the observed motion of plume four is that the time taken to traverse from one side to the other differs at different parts of the cycle. For example, at ~200 s in the cycle the plume moves from its maximum deflection towards the room centre, to its maximum northerly position over ~50 s, whereas, starting at time $t = 50\,\mathrm{s}$ in the cycle it takes more than 100 s to complete its movement in the opposite direction.

In order to find the cause, or driving forces producing this periodic motion two possibilities were first considered,

- resonance in the plumes (jet column instability),
- vortex shedding caused by flow perpendicular to the axis of the plumes

Impinging jets (and similarly plumes) have been found to show instability under certain circumstances (the suggestion is made that the jet can be thought of a cylindrical bar undergoing buckling on impingement). Crow and Champagne (1971), through externally exciting a round free jet found that lateral perturbations were amplified in the jet up to a maximum level for a Strouhal number ($ST = fD_{\text{jet}}/U_{\text{jet}}$ where $f$ is the frequency of the oscillations) of 0.3 and at a distance of 3.7 $D_{\text{jet}}$ downstream. More recent research work (Gutmark and Ho 1983) has established a range of Strouhal number between 0.24 and 0.51 where jet instability has been observed.

The feasibility of the existence of this phenomena in this case was examined by making an approximate calculation of the frequency given a Strouhal number of 0.3. This suggested a frequency of 0.2 Hz which is two orders of magnitude higher than fundamental frequency observed here (0.0022 Hz). It is therefore unlikely that this could be the principle mechanism driving the observed fluctuations.

A second possibility is that of a vortex shedding phenomena, in which it may be possible that the lateral flow through the room, from the inlet to exhaust, in the room causes vortices to be generated as this flow crosses the region dominated by the plumes. In this case the Strouhal number might be expected to be $\sim$0.1 (and $ST = fD_{\text{plume}}/U_{\infty}$). If $U_{\infty}$ is calculated from the net flow through, and cross sectional area of, the room a frequency of 0.001Hz is suggested. Although lower than that observed this phenomena could give rise to oscillations with a frequency of the correct order of magnitude.

To analyse the oscillating motion of the plumes further data was collected at the plume monitoring points over several steady periodic cycles. From this data discrete Fourier transforms were calculated for each velocity component and temperature. The discrete Fourier transforms for plume four are shown in Figure 6.28.

It can be seen that, besides the fundamental frequency which shows as a large peak at the far left of the horizontal axis, there are further peaks in the spectrum at 4, 8 and 16 Hz. The largest peak occurs in the transform of the temperature data at 8 Hz. These higher order harmonics are a reflection of the complex nature of the fluctuations but do not necessarily suggest specific phenomena at these frequencies. The higher frequency peaks may well arise from the asynchronous interaction of two or more phenomena.

To examine the features of the flow observable at each stage of the periodic motion

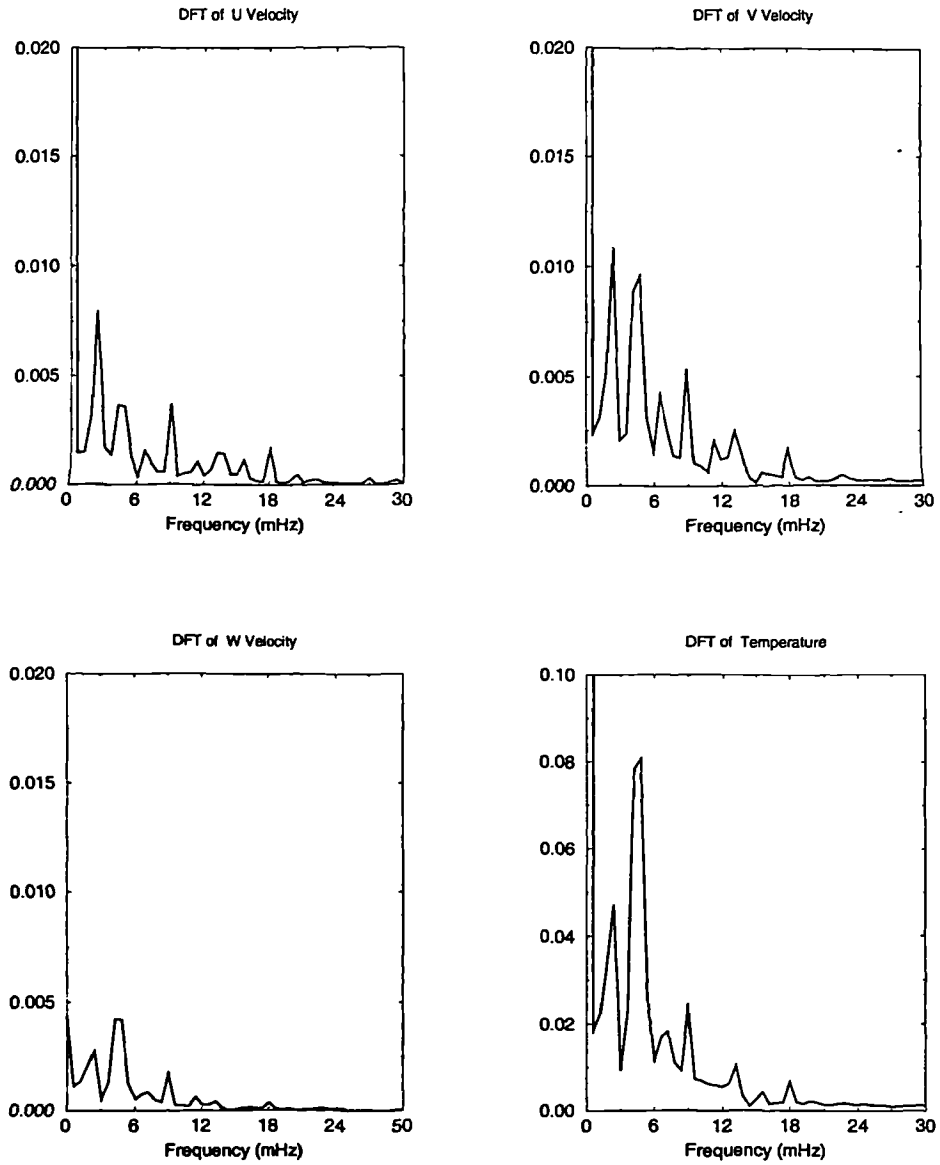


**Figure 6.28:** Discrete Fourier Transforms of the calculated U, V and W velocity components and Temperature at the monitoring point in Plume number 4 for case DC11.

of the plumes, the flow field has been plotted in vector and contour form, at each of the eight steps identified in Figure 6.27. The data has been plotted on a horizontal plane part way up the plumes ($z = 1.7\,\mathrm{m}$) and on a vertical plane through plume two and four ($x = 3.65\,\mathrm{m}$). Speed and W velocity contours are shown in Figures 6.29– 6.31 and vector plots in Figures 6.32– 6.34.

The progression through the 450 s cycle can most easily be followed by reference to the motion of Plume four which at time zero in the cycle—actually solution time 10000 seconds—is positioned towards the north wall (the left and bottom wall in

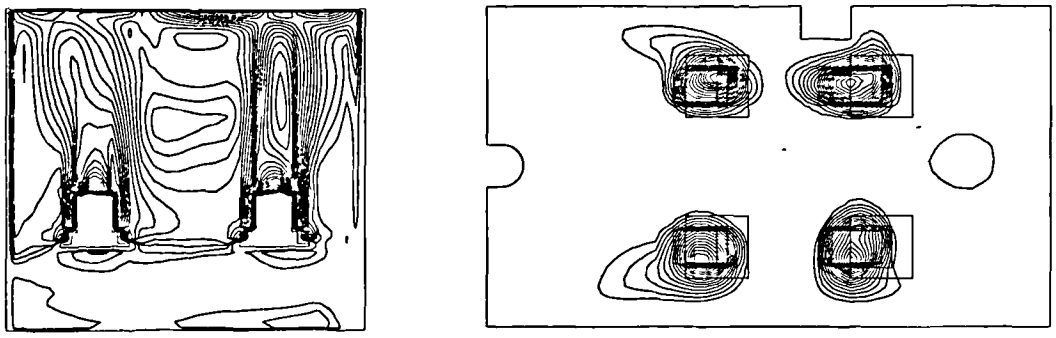

$t = 0\,\mathrm{s}$

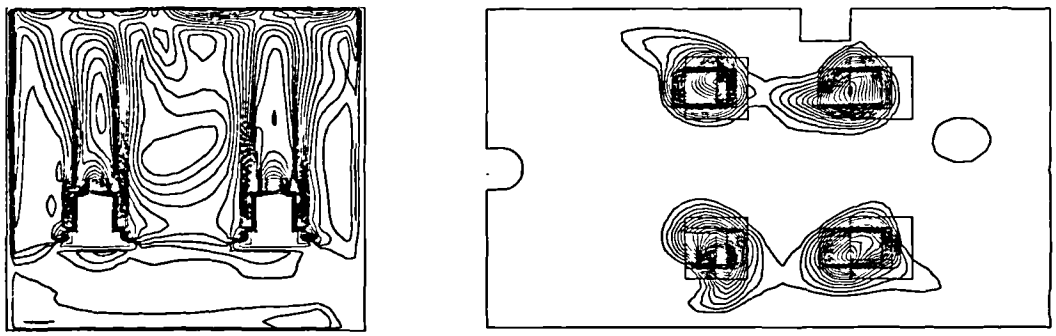

$t = +100\,\mathrm{s}$

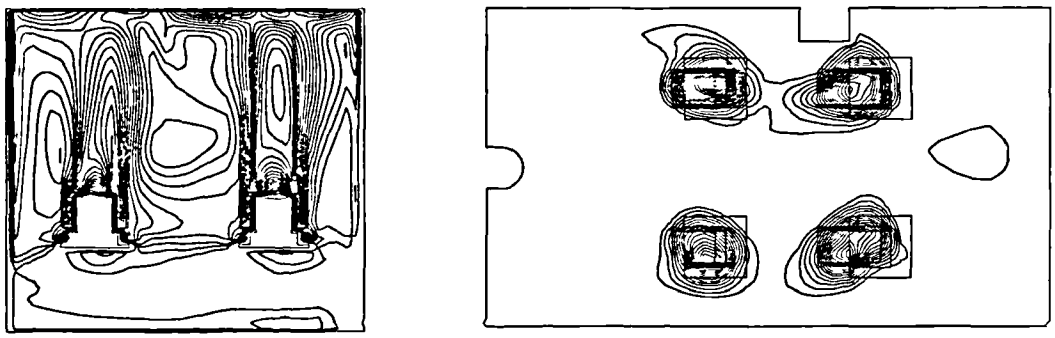

$t = +180\,\mathrm{s}$

**Figure 6.29:** Speed contours at plane $x = 3.65\dot{\mathrm{m}}$ (left) and W velocity contours at plane $z = 1.7\,\mathrm{m}$ (right). Contours are 0.03–0.33 m/s in $0.015\,\mathrm{m.s^{-1}}$ increments.

the section and plan views respectively). The position of the plume centres can be clearly seen in Figures 6.29– 6.31 in the horizontal plane W velocity contours. At time 100 s plume four is upright and moves towards the centre of the room by $t = 180\,\mathrm{s}$. This motion is reversed except on a shorter time scale between times 180 s and 250 s. Plume four moves to an upright position again at $t = 300\,\mathrm{s}$ and slowly towards the room centre by 400 s. The motion is then quicker from this position to upright (430 s) and north again by 450 s. The contours at $t = 450\,\mathrm{s}$

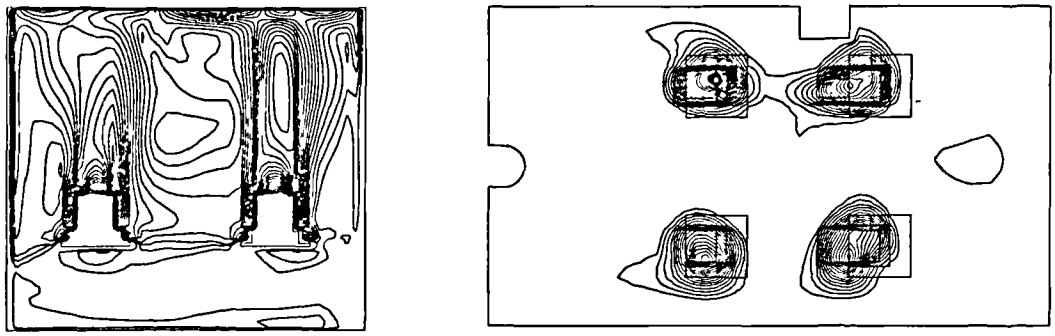

$t = +200\,\mathrm{s}$

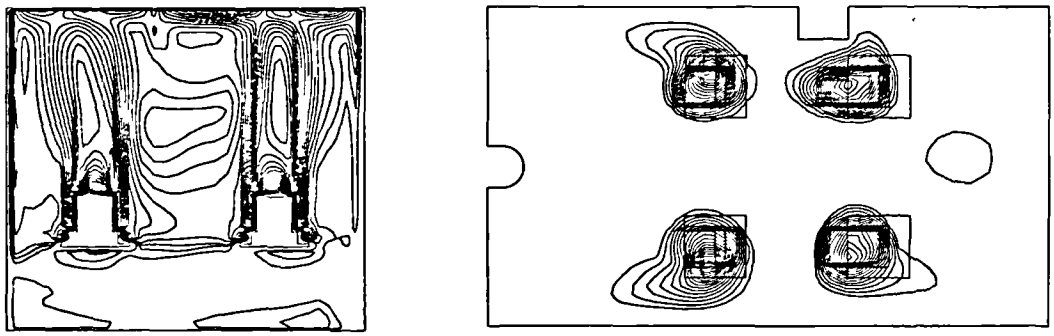

$t = +250\,\mathrm{s}$

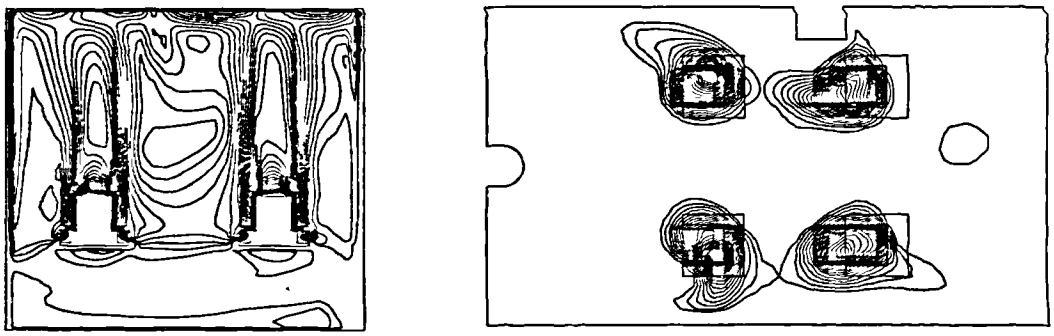

$t = +300\,\mathrm{s}$

**Figure 6.30:** Speed contours at plane x=3.65m (left) and W velocity contours at plane Z=1.7m (right). Contours are 0.03–0.33 m/s in 0.015 m/s increments.

can be seen to be identical to those at $t = 0\,\mathrm{s}$. Of the other plumes, plume three seems to move in the same direction as plume four, while plume one moves in the opposite direction. Plume two also moves in the opposite direction to plume four (so that they move towards the centre of the room together, then apart) but by a much smaller amount.

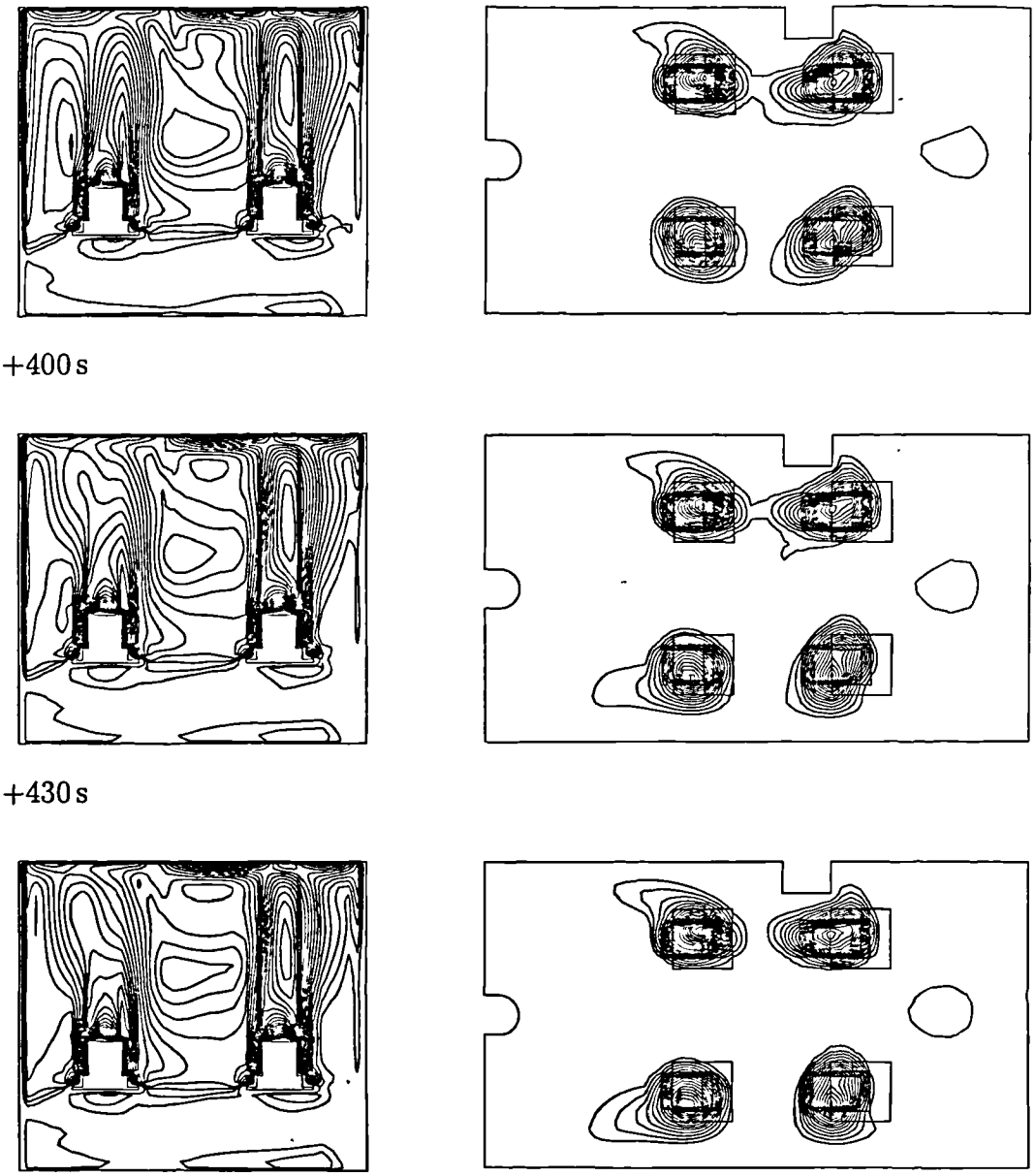

$t = +400\,\mathrm{s}$

$t = +430\,\mathrm{s}$

$t = +450\,\mathrm{s}$

**Figure 6.31:** Speed contours at plane x=3.65m (left) and W velocity contours at plane Z=1.7m (right). Contours are 0.03–0.33 m/s in 0.015 m/s increments.

Study of the vector plots on these planes in Figures 6.32–6.34 shows further details of the plume movement and its effect on the surrounding flow. Firstly, it can be seen that plume four, at each stage in the cycle, does not penetrate so vigorously towards the ceiling as plume two. It can also be seen that throughout the cycle there is no particular variation in the flow observable beneath the heat sources (0–0.7 m height), and that the velocities in this region are much lower in magnitude.

magnitude.

Between plume four and the north wall there is a noticeable recirculation pattern which seems most vigorous at 100 s and 300 s when the plume is in an upright position. Between plumes two and four the flow from each plume across the ceiling impinges and results in a swirling motion at high level. This swirling motion varies in strength (again it seems most vigorous at 100 s and 300 s) but always rotates in the same direction so that it acts in favour of the mean flow in plume two and against the mean flow of plume four. This probably accounts for the lack of penetration of plume four to the ceiling. The recirculating flows surrounding the plumes exist over a height from 0.7m and up to the ceiling and recirculate air to the very base of the plumes.

The vectors plotted on the horizontal plane in Figures 6.32–6.34 firstly show that the recirculating flow surrounding the plumes is not just a vertical movement but has a strong horizontal component. This is particularly noticeable between the north wall and the adjacent plumes where the flow is along the wall towards each corner of the room. This flow is also sufficient to impart a noticeable degree of swirl, at this height, to plumes three and four. A similar situation also exists around plume one, where there is a flow along the wall away from the column, and a corresponding swirl around the plume—although not so strongly as plumes three and four. This swirl around plume one varies more noticeably throughout the cycle and is hardly evident at 100 s and 400 s. The flow at plume two is distorted and deflected from the axis of the heat source but there is little swirl or flow along the adjacent wall. In this case the motion of the plume seems to be stabilised by its proximity to the column.

The recirculating flow in the room that is entrained into the plumes is mostly drawn from the west and east walls where some vertical flow down the walls (from above) is evident. The fluctuations in the plume are evidently strong enough to cause fluctuations in this flow outside the plumes—compare the regions next to the diffuser at 250 and 400 seconds for example.

From the study of this data it appears that, with four heat sources in the test chamber, that the flow entrained into the plumes is sufficiently large compared to the supply flow that firstly, recirculating flows are generated in the upper region of the room that fall to the base of the heat sources. Secondly, the recirculating flows, besides the expected vertical velocity components, also have significant horizontal components. These flows are strong enough to generate swirling effects in

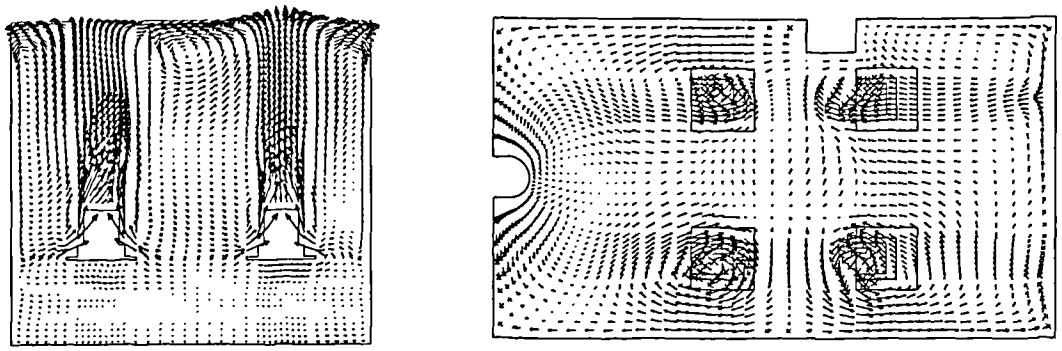

$t = 0\,\mathrm{s}$

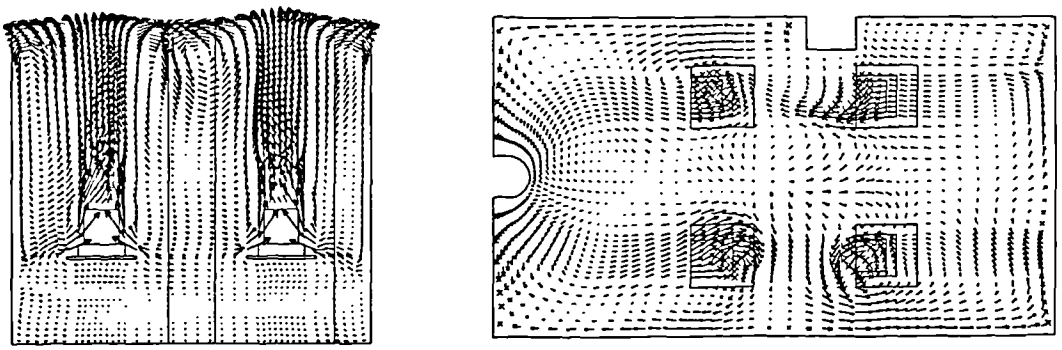

$t = +100\,\mathrm{s}$

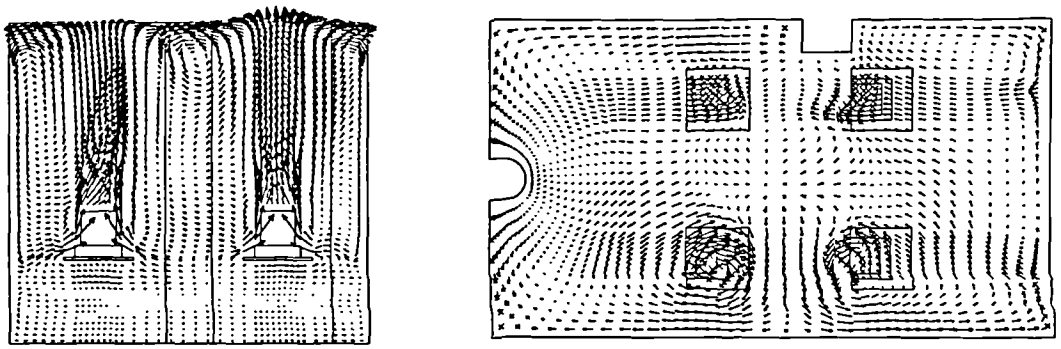

$t = +180\,\mathrm{s}$

**Figure 6.32:** Velocity vectors at plane x=3.65m (left) and at plane Z=1.7m (right). Vectors are scaled ×5 to show the smaller velocity vectors more clearly.

places. It also seems true that it is the interaction of the plumes with the recirculation flows and with each other that is causing the growth of the plumes to be unstable. There is some similarity between the observed flow and vortex shedding phenomena, in that, the recirculating flow around the plumes causes some swirling motion in the plumes and causes fluctuation with a frequency of the same order of magnitude. However, the results of the calculation do not show any separate

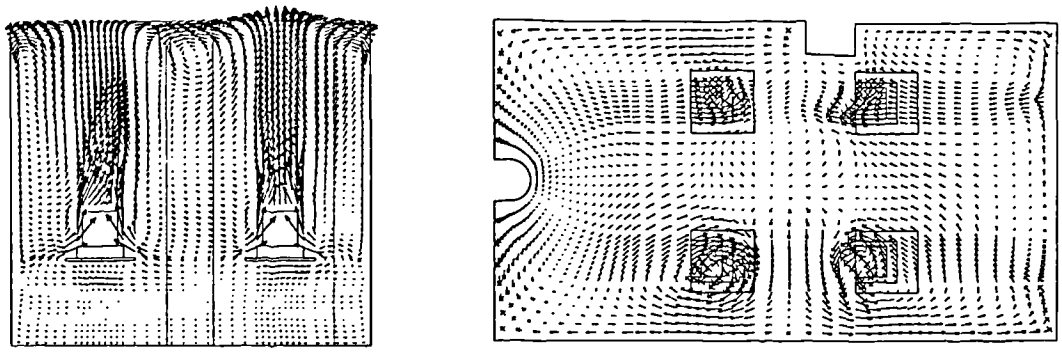

$t = +200\,\mathrm{s}$

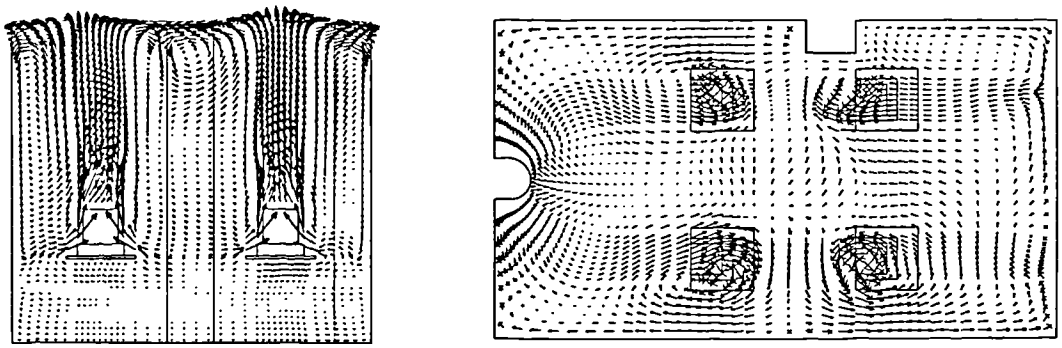

$t = +250\,\mathrm{s}$

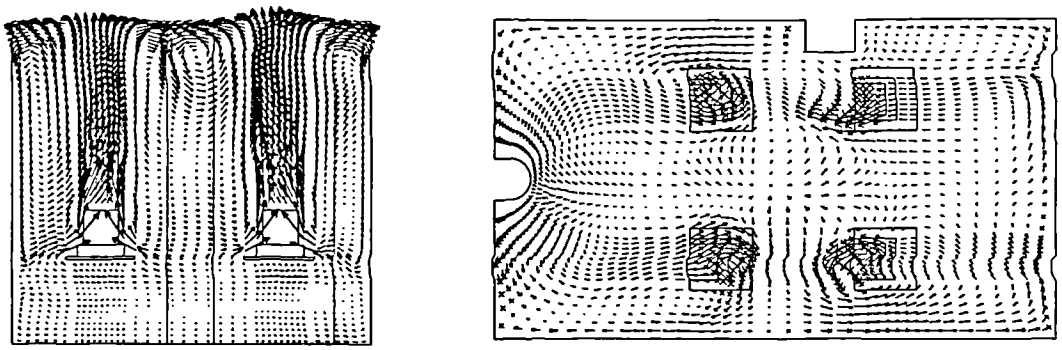

$t = +300\,\mathrm{s}$

**Figure 6.33:** Velocity vectors at plane x=3.65m (left) and at plane Z=1.7m (right). Vectors are scaled ×5 to show the smaller velocity vectors more clearly.

vortices, only those around the plumes.

Although the fluctuations in the calculated velocity and temperature at the plume monitoring points have been studied, no direct comparison with the experimental data is possible as no measurements were made at these points for case DC11. Some comparison with experimental data can be made, however, at the temper-

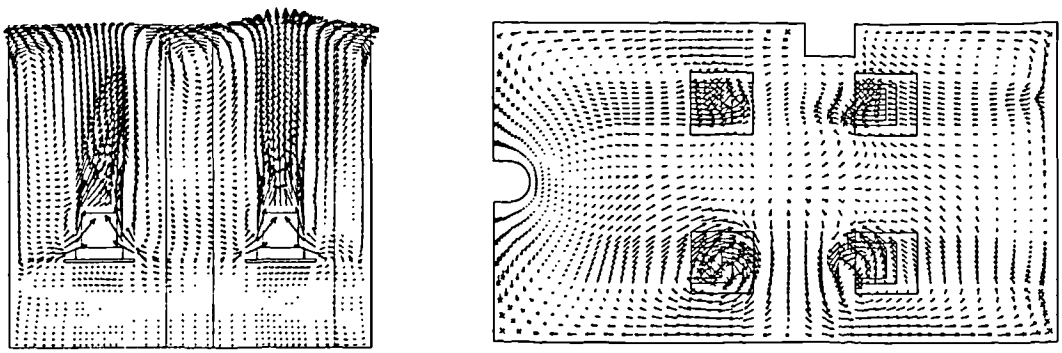

$t = +400\,\mathrm{s}$

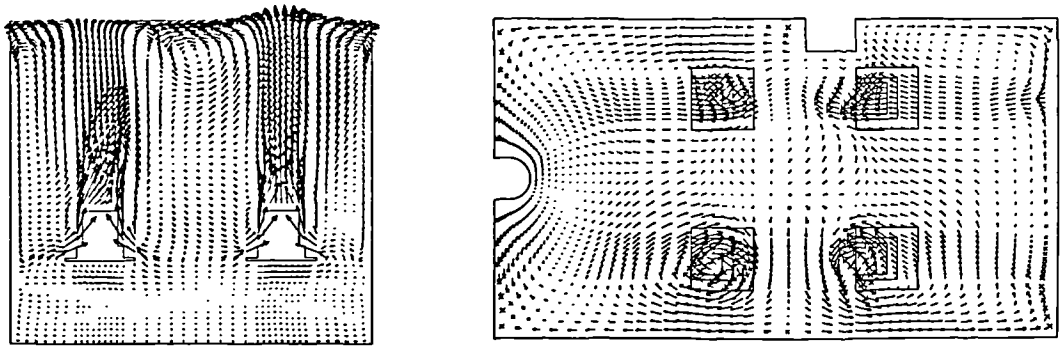

$t = +430\,\mathrm{s}$

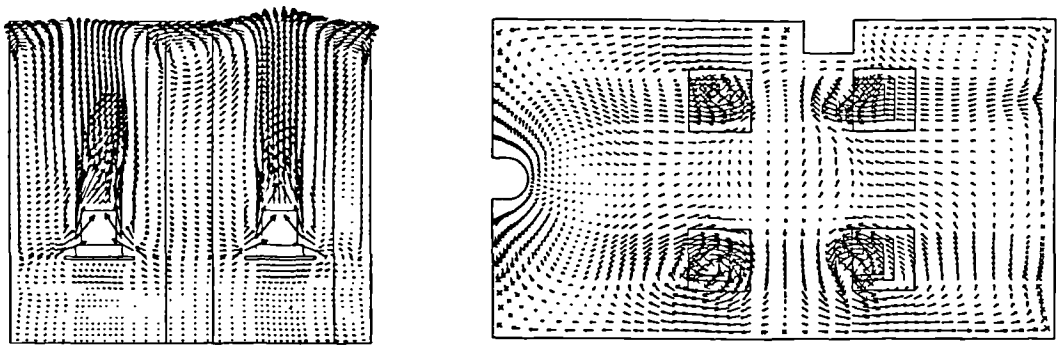

$t = +450\,\mathrm{s}$

**Figure 6.34:** Velocity vectors at plane x=3.65m (left) and at plane Z=1.7m (right). Vectors are scaled ×5 to show the smaller velocity vectors more clearly.

ature measuring positions on the room centre-line. Calculated data have firstly been taken from six points equivalent to the position of six of the thermocouples. The calculated fluctuation in the temperature data at these points over several cycles is shown in Figure 6.35.

It can be seen that the fluctuations at low level in the room are very small in mag-

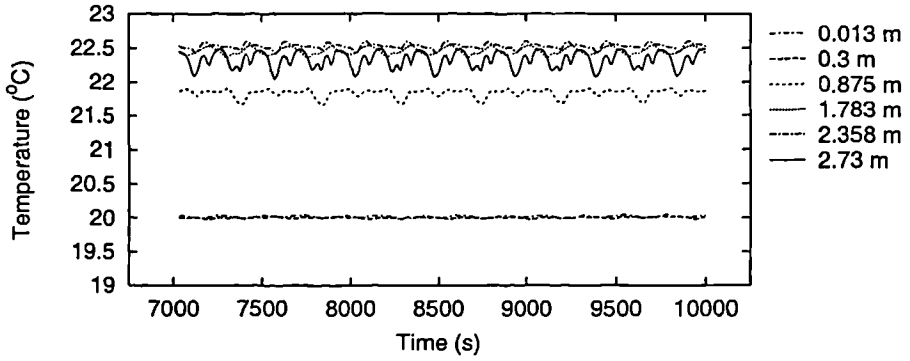


**Figure 6.35:** Calculated temperature fluctuations at a number of thermocouple positions for case DC11.

nitude compared to those at high level. The largest amplitude fluctuations appear at 2.73 m in the calculated data. In the experiment temperatures were recorded over a period of approximately 45 minutes (fortunately long enough to include several of the predicted temperature fluctuation cycles) with measurements made every second but averaged over 30 seconds before being logged. The recorded data is therefore at 30 second intervals and some of the fluctuations have been effectively filtered out. Nevertheless, fluctuations are present in the recorded experimental data from higher levels in the room. A discrete Fourier transform has been calculated for the data from 2.73 m and is plotted in Figure 6.36 along with the discrete Fourier transform of the equivalent calculated data. Comparing these spectral distributions shows that the harmonics at 5, 10, 15 and 18 mHz found in the calculated data are at very similar frequencies and magnitudes to those shown in the experimental data. As these fluctuations were not originally observed in the experimental data, this is a good example of how CFD predictions can be successfully made and used to enhance the understanding of the physical phenomena of experiments.

### 6.4.1 Calculation of Test Case DC10

Test case DC10 is similar to that of DC11 but each heat source has an output of 300 W rather than 200 W, giving a total load of 1200 W (equivalent to 71 $W.m^{-2}$). It was thought useful to make a calculation for this test case as velocity measurements were made, along with temperature measurements, at a number of positions along the room centre-line that could be used to make a comparison with the calculated data. The same fully transient solution procedure, as used described for

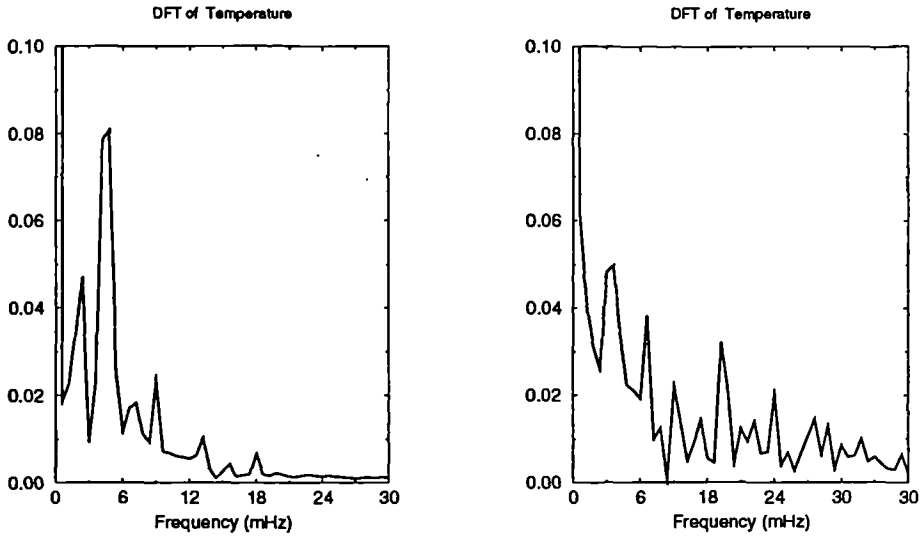


**Figure 6.36:** Discrete Fourier Transforms of the calculated temperature at 2.73 m height and X=3.2 m (left) and the experimental temperature data at the same point (right).

test case DC11, was used in this calculation except that all four heat sources were activated at the start of the calculation. The same 103320 mesh was also used.

In this case it was found that steady periodic fluctuations developed in the data at the four plume measuring positions after approximately 1800 seconds. The calculation was continued for a further 3200 seconds. The data from the plume four monitoring position is shown in Figure 6.37. It can be seen that the period of the fluctuations is, in fact, shorter at 383 seconds. The shortening of the period is not surprising in view of the increased momentum in each plume. Given that the supply flow rate is the same in case DC11, and the other boundary conditions are similar, the reduction in the period of the fluctuations suggests that it is the momentum of the plumes that drives the recirculation flow and the fluctuations.

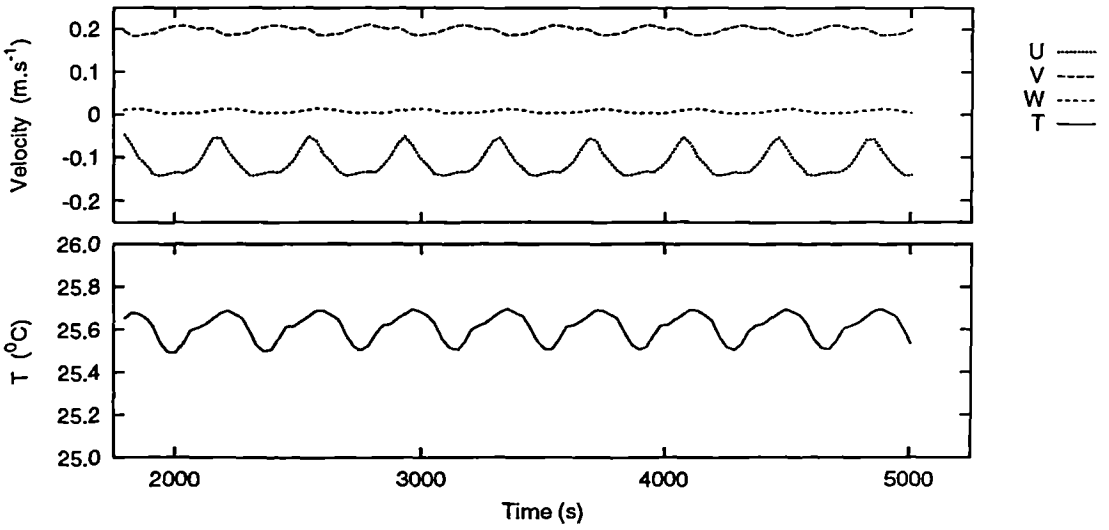


**Figure 6.37:** The cyclic variations of the U, V and W velocity components and Temperature at the plume four monitoring point during the progress of the transient calculation for case DC10.

The discrete Fourier transform of several cycles of data from the plume four monitoring point is shown in Figure 6.38. The presence of distinct peaks is clearer in this case, with harmonics shown at (in order of decreasing magnitude) 5, 10, 15, 20 and 25 mHz.

Temperature and velocity profiles were measured in the experiment along the room centre-line at four different distances from the supply diffuser. To make a comparison with this temperature data the numerically calculated temperatures have been averaged over a whole cycle. The calculation was first made for this

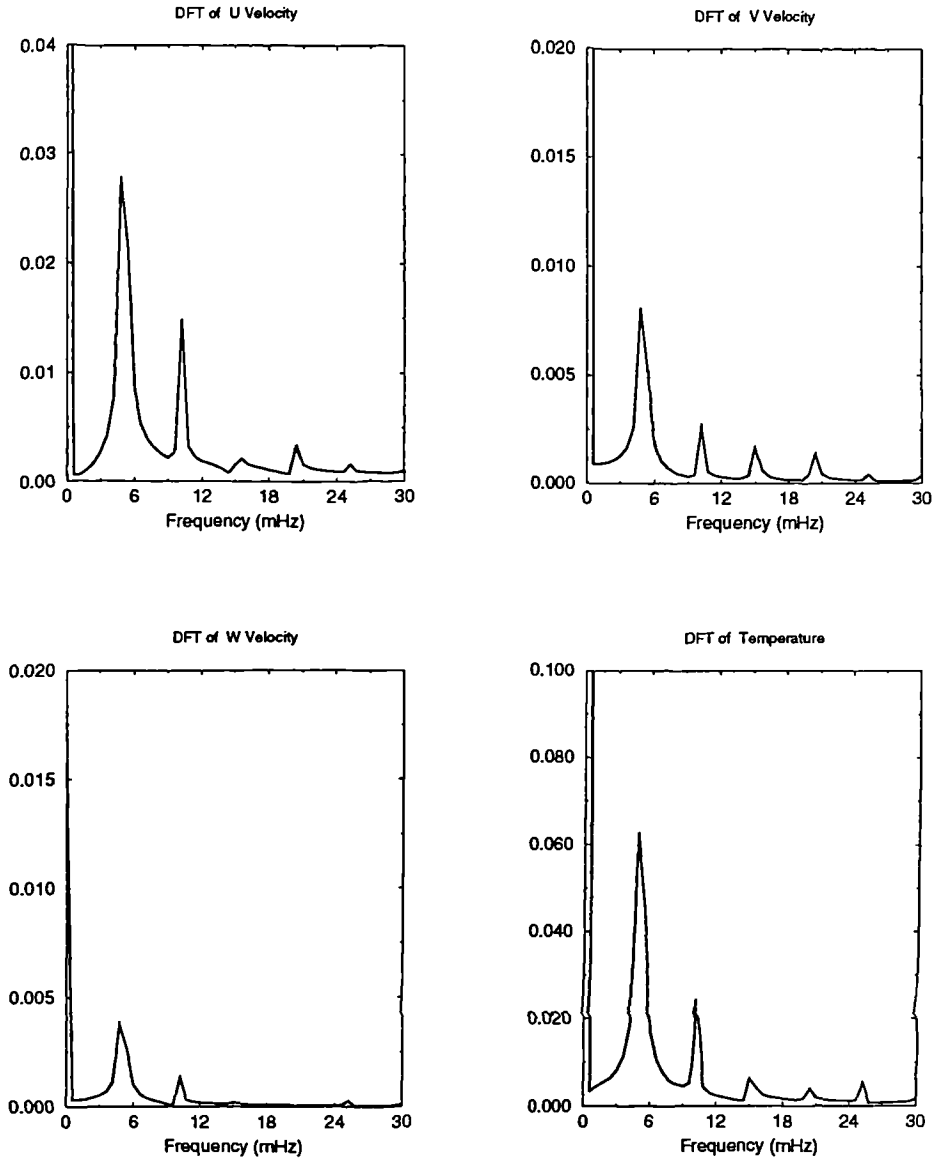


**Figure 6.38:** Discrete Fourier Transforms of the calculated U, V and W velocity components and Temperature at the monitoring point in Plume number 4 for case DC10.

test case using hybrid differencing of the convective terms of all equations. The calculation was continued for several cycles further using higher order differencing (defined previously as schemes 'b' and 'c') and further temperature and velocity data extracted.

The temperature profiles are compared at the four different positions in Figure 6.39. From the floor up to a height of 1 m there is close agreement between calculated and experimental data except at $x = 4.7$ m (near the rear wall of the chamber) where the temperature near the floor is under-predicted. In the upper

part of the room (above 1 m) the air temperature is over-predicted in the calculations by up to 0.8 K at $x = 3.2$ m. This degree of over-prediction is similar to that of the other calculations where fixed wall temperatures have been used as the thermal boundary conditions. The experimental results also show a change in temperature gradient at approximately 1 m. This effect is shown in the calculated results but at a lower level of ~0.75 m. There is very little difference between the results of the alternate differencing schemes.

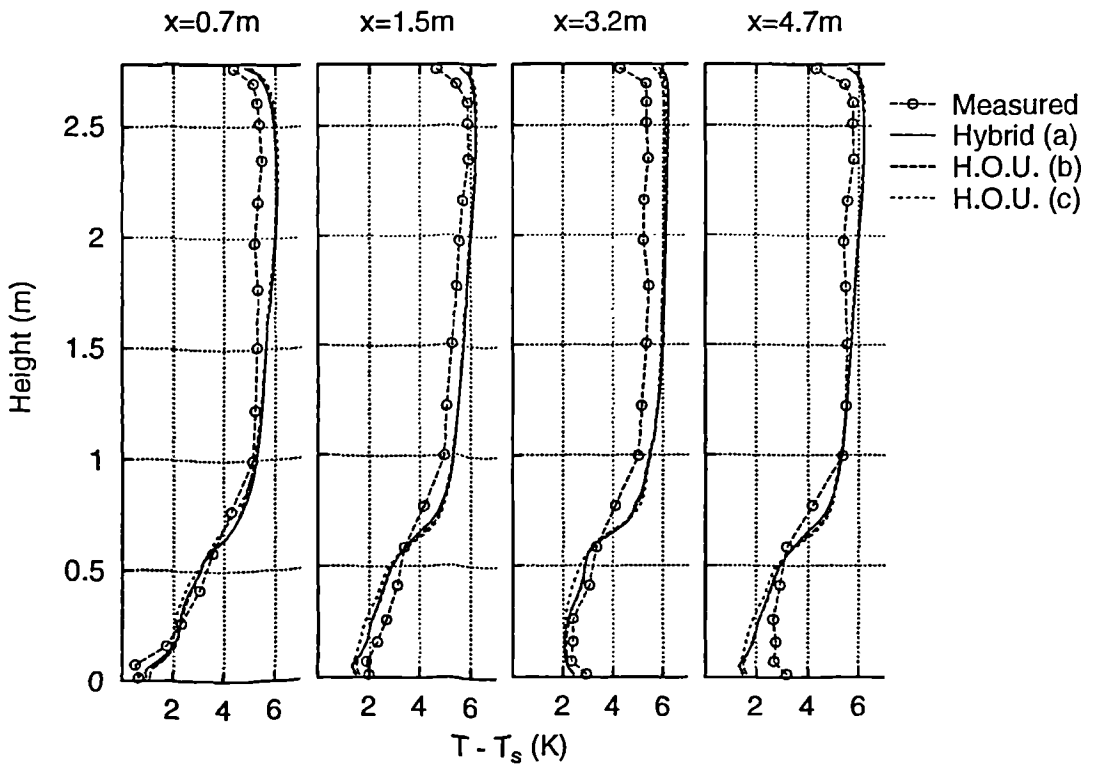


**Figure 6.39:** A comparison of the predicted temperature profiles and experimental data for case DC10 at different distances from the supply diffuser, and with alternative differencing schemes.

The mean air speed profiles are compared, at the four different positions, for test case DC10 in Figure 6.40. As the experimental measurements were made with an omnidirectional probe, the numerically calculated velocities have been used to calculate air speeds, and then averaged over one whole period of the dynamic cycle. Comparison of these results with the experimental data shows some of the same principle trends—namely that there are peaks in the air speed approaching the floor and ceiling, and there is a local maximum part way up the height of the room.

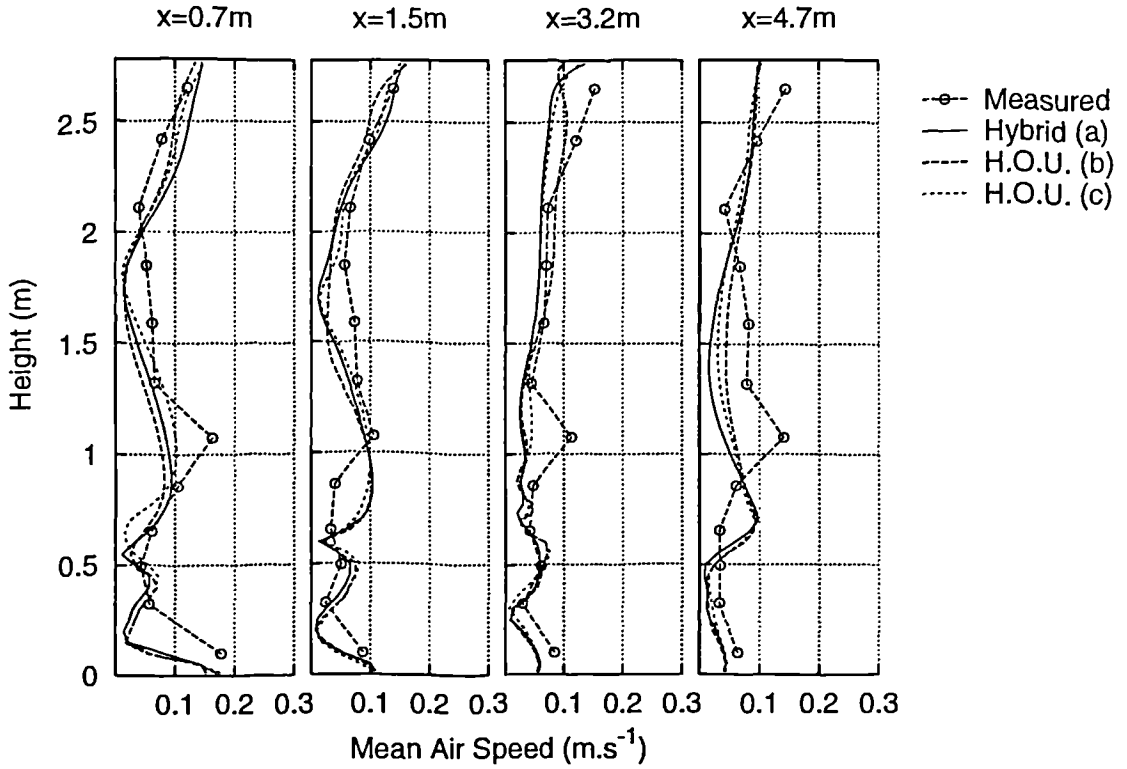


**Figure 6.40:** A comparison of the predicted air speed profiles and experimental air speed measurements for case DC10 at different distances from the supply diffuser, and with alternative differencing schemes.

Near the floor the numerical results show a similar trend to the experimental data in that the speed immediately adjacent the floor surface reduces with distance from the supply diffuser. The agreement with the experimental data up to 0.5 m is generally very good. There is also good agreement above a height of 2 m except at a distance of $x = 4.7$ m. Where a local peak in air speed was measured consistently at $\sim$ 1.1 m the numerical results show peaks that are both lower in the room ($\sim$ 0.7 m) and lower in magnitude. At $x = 3.2$ m no particular peak part way up the height of the room is predicted at all. The difference in results from using the alternative differencing schemes is not great but scheme 'c' could be said to offer slightly better results.

It is interesting that both the calculated change in temperature gradient, and the local maximum in the air speed, are predicted at a lower height in the room than that measured ($\sim$0.7 m compared with $\sim$1.1 m measured). It seems likely that these features are associated with the bottom of the recirculating flows in the upper region of the room (i.e. the bottom of a well mixed zone surrounding the

factor of plumes, and hence the magnitude of the surrounding flow. For a given supply flow rate this would require a flow to be recirculated down to a lower level in the room than would actually occur.

## 6.5 Conclusions

Steady state calculations of flow and heat transfer have been made for two of the NSIBR test cases and one of the Loughborough displacement ventilation test cases. Transient calculations have been made for two of the Loughborough displacement ventilation and chilled ceiling test cases. From the results of these calculations a number of things can be concluded regarding both the nature of the flows under the different boundary conditions, and regarding the ability of the numerical procedures used here to successfully calculate the room heat transfer.

1. The results of all the calculations show that the flow is separated into two distinct regions of the room. These regions can be identified as firstly, near the floor and up to the height of the top of the supply diffuser, where the flow is dominated by that from the diffuser, and secondly, above this height and up to the ceiling, where the flow is dominated by the plumes from the heat sources.

2. In the lower part of the room the flow is dominated by the inlet flow from the supply diffuser. The buoyancy effects in the zone around the supply diffuser are evident in the calculation results such that the flow can be seen to fall rapidly towards the floor. The flow from the diffuser is found to spread radially in a thin boundary layer over the floor. This boundary layer spreads at constant thickness across the full width of the room. These observations from the calculation results concur with the experimental observations reported by Mathisen (1988, 1990) and Sandberg and Holmberg (1990).

3. In the case of the Loughborough test chamber calculations the radial spread of this boundary layer is modified to a parallel flow part way down the room, due to the narrowness of the room, so that the velocity in the boundary layer decays little before reaching the end wall of the room.

4. Where detailed comparison of the calculated velocities with experimental data has been made the agreement has been very good in the lower part

4. Where detailed comparison of the calculated velocities with experimental data has been made the agreement has been very good in the lower part of the room when a 'momentum method' (Chen and Moser 1991) has been used to apply the inlet boundary conditions.

5. Above the floor boundary layer a counter-flowing stratified layer can be seen to flow in the opposite direction. In the NSIBR test cases this layer flows back towards the supply diffuser and is partly re-entrained into the supply flow. In the Loughborough displacement ventilation calculations this layer is seen to flow back towards the bottom of the heat source and is entrained into the plume. Similar flows were reported by Mathisen (1990).

6. In all the displacement ventilation calculations, where a single heat source was modeled, the flow in the upper region of the room was found to be dominated by the plume. The plume impinges on the ceiling and develops into a thin boundary layer flowing across the whole ceiling.

7. In all the displacement ventilation calculations thin boundary layers a evident flowing down all the walls. The boundary layers are unusual in that they do not increase in thickness, but diminish as some of the air in the outer part of the boundary layer is drawn back towards the plume.

8. A rather different situation was found to exist in the upper region of the room in the results of the displacement ventilation and chilled ceiling test cases. A transient solution procedure was necessary to calculate the flow in these cases and periodic variations in the flow were found. These fluctuations were found to be due to the oscillation of the four plumes. This oscillating motion was found to be mainly laterally (perpendicular to the supply flow).

9. The behaviour of each plume in the displacement ventilation and chilled ceiling case was found to vary. In particular the fourth plume was found to move the greatest and to be diminished in strength. The presence of the column on the south side of the room appeared to have a stabilising effect on the motion of the adjacent plumes.

10. The dynamic motion of the plumes seems to be due to the interaction between the plumes and the larger recirculating flows arising when there are four plumes in the room. The movement of the plumes was seen to induce dynamic fluctuations in the flow in all parts of the upper region of the room. The lateral movement of air in the recirculating flow surrounding the plumes was significant enough to induce some swirling of the plumes.

11. The predictions of the fluctuations in the temperature field near the ceiling, induced by the motion of the plumes, was found to be very similar in magnitude and frequency to the fluctuations in the experimental data. This demonstrates how numerical methods can be used to make genuine predictions and enhance the understanding of the physical phenomena in experiments.

12. Some of the predicted air temperature and velocity profiles from the transient calculations when compared with experimental data show evidence that the vertical extent of the recirculating flow in the upper region of the room is slightly over predicted. This is most likely due to the known tendency of turbulence models like the $k$–$\varepsilon$ model used here to over-predict the spreading rate of the plumes by up to 20%.

13. The calculated vertical temperature profiles have shown firstly the importance of the radiant coupling between the room surfaces (mainly the floor and ceiling) and the flow. Calculating the flow and heat transfer using fixed wall temperature boundary conditions consistently resulted in an over-prediction of the room air temperatures and an under-prediction of the wall heat fluxes.

14. Calculating the flow and heat transfer using a conjugate heat transfer procedure consistently resulted in an under-prediction of the room air temperatures and an over-prediction of the wall heat fluxes. Although the accuracy of the conjugate heat transfer procedure in calculating the overall heat transfer is reasonable, and it offers the most generalised way of applying the thermal boundary conditions, additional uncertainties are introduced by relying on specification of the wall conductances and surface emissivities.

15. It seems most likely that it is the calculation of the convective heat fluxes that is mostly at fault in the calculation of the overall heat transfer. This is partly explained by the low values of $y^+$ found at most of the walls in the results, but is more likely due to the conditions in these flows being rather different than that in the simple boundary layers for which the universal wall functions were divised. In particular the strong buoyancy effects in the floor boundary layer, the temperature gradients on the walls and the effect of the plume(s) impinging on the ceiling.

In comparing the flow regime in the displacement ventilation cases with those where the chilled ceiling was also modeled it is the difference in the recirculation and mixing processes in the upper region of the room that seems of particular

significance. Clearly, although the overall loads in the room are only moderately high (48 and 71 $W.m^{-2}$), the mixing of the air in the upper region of the room is noticeably more vigorous than in the test cases with displacement ventilation alone and smaller loads. Not only has this resulted in lower temperature gradients in this part of the room but also has implications in terms of room air quality and the ability of the system to transport pollutants out of the normal breathing zone.

# Chapter 7

# The Nodal Model

## 7.1 Introduction

The overall objective of the work has been to develop a thermal model of office rooms with displacement ventilation and chilled ceiling panel systems. For the model to be useful in simulating system thermal performance, it has to be simplified (at least relative to CFD models) in order to be computationally efficient.

The model proposed here is of the type that has been called a nodal model. A nodal model consists of a series of interconnecting nodes which represent points on the room surfaces or in the room at which heat balances are made to find temperatures and heat fluxes. The nodes of such models are identified with either particular room surfaces, or the room air (or subdivisions of the room air volume or room surfaces), and can be conceptualised as part of a network of interconnecting heat flow paths. The interconnections between surface and air nodes are conductances representing convective heat transfer paths[1]. Air nodes may be interconnected with 'one-way' conductances associated with particular bulk air flow movements. Each surface node, in general, has multiple connections to the other surface nodes which represent the radiative heat transfer paths. The network of such models is usually drawn in a two-dimensional form but without showing radiative links (for the sake of clarity).

Some nodal models (Dalicieux and Bouia 1993) seek to make a momentum-

[1]It is tempting to make an electrical network analogy but this is not helpful as there is no equivalent for bulk air flow (capacity rate) connections.

pressure balance at the room air nodes using a reduced form of the Navier-Stokes equations. This is not done here however (as with most of the nodal models in the literature) so that the capacitance rates between interconnected air nodes are parameters of the model that have to be pre- defined.

In this chapter, the numerical methods underlying the nodal model and its implementation are discussed first. A nodal model, such as that presented here, is defined by its structure (i.e. the distribution of the nodes and interconnections) and its parameters (i.e. the value of the conductances, capacity rates etc.). The development of the model structure and the derivation of the parameter values can be thought of as two separate processes with the latter following on from the former (although there is some interaction between the two, as will be shown later). Accordingly, the development of the model structure is discussed first. A final section of this chapter is given to the testing and demonstration of the model.

## 7.2 The Numerical Method

Within this project the initial approach has been to use a zonal modeling method along similar lines to that of Li et al, where a number of nodes are linked by a combination of heat and mass transfer paths. A generalised nodal thermal modeling program LIGHTS, developed by Sowell (1989) has been used to this end. The program was originally developed for the detailed study of the thermal and luminous aspects of building lighting systems and can model the non-linear behaviour of lighting elements—although these features are not used in the present context. The program is capable of modeling thermal systems in either dynamic or steady state conditions. Nodes can be connected in a very general way, with a combination of fluid flow, thermal mass, and convection being either defined or calculated at each node. Radiation between nodes is dealt with in two wave bands in an exact manner on the basis of view factors input by the user (see (Sowell and O'Brien 1972)). In the steady state, the basic formulation used in the program is, in vector-matrix form:

$$Q^O - U^C T - A \sum_j V_j . J_j^o = O \tag{7.1}$$

Here the first term $Q^0$ represents the vector of source powers at each node, and the term $U^C T$ represents conductive/convective transport away from each of these

nodes. $T$ is the vector of nodal temperatures that must satisfy this equation. The summation term represents net radiative transport away from each node in both short and long-wave bands. $A$ is a diagonal matrix of surface areas, $V_j$ are special transfer matrices describing interreflections and transmissions within the enclosure, and $J^o$ is a matrix of source radiation terms at each node and in each wave band. The notation $J^o_j$ means that the $j$th column is involved in the matrix multiplication. The equation is non-linear due to temperature dependence of $Q^o, U$ and $J^o$. The right hand side is zero in the steady state case, and $MT'$ in the dynamic case where $M$ is a diagonal matrix of heat capacitances and $T'$ is the temperature derivative vector. Fluid flows in the LIGHTS program are represented as one-way conductances and always have to be pre-defined.

It is relatively simple using the LIGHTS program to set up a nodal model equivalent to the four node model of Li *et al.* described in Chapter 2. This was done as a simple test and in the LIGHTS model the radiation from the ceiling to the floor was modeled using view factors calculated from standard values and interaction with the walls disregarded. A comparison was made in this way between this simple LIGHTS model, and hand calculation of the Li et al four node model using the geometry of Li et al's experiment. This required a total of five nodes—three air nodes and two surface nodes. The resulting temperatures for the surfaces and air temperatures at floor and extract were found to be accurate to four significant figures. The very small differences are probably due to the different treatment of the radiant coupling—the accuracy of the radiant heat transfer coefficient used in Li et al's model mainly depends on the accuracy of the initial guess of the surface temperatures.

## 7.3 The Model Structure

In the development of the model structure, it has been found that a usable structure (and it is acknowledged that there may be a number of usable alternatives) can be found by consideration of the following:-

- The output requirements of the model.
- The degree of detail required to adequately represent the heat transfer phenomena of interest.
- Bulk air flow movements observed in the experiments and numerical results.

The first two items act as constraints on the number and positioning of the nodes, and the last is a source of information that can be used to determine the interconnections between the air nodes. A further consideration is that, when applying the model to the experimental data, the second law of thermodynamics is always observed. It should also be said that a hypothesis in developing the model has been that a similar structure can be used to represent a room with a displacement ventilation system, both with, and without a chilled ceiling panel system.

It is first worth considering what is entailed, in a nodal model of a room with a fully mixed air conditioning system, and the associated assumptions usually made. A diagram of such a nodal model is shown in Figure 7.1. The assumptions commonly made—for example in programs such as (BLAST 1986) and (DOE-2 1982)—are that firstly the air is fully mixed and hence only one air node is required. Also that each internal surface has a uniform temperature and that conduction through the surface is one-dimensional (hence only one node per internal surface). The outputs of such a model might be either temperatures or net heat fluxes at each of these nodes so that for example the overall heat transfer could be calculated for a given room air temperature. It can be seen then, that in this case the structure of the model, given these assumptions, is simplified so that it is mainly determined by the output requirements of the model.

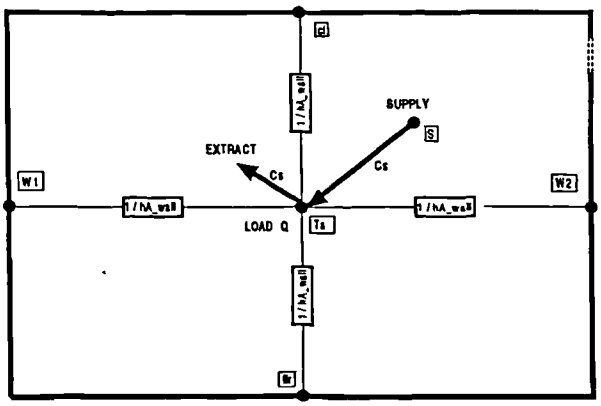


**Figure 7.1:** A nodal model of a room with a fully mixed air conditioning system (connections to the other walls are not shown for clarity).

The structure of a nodal model of a displacement ventilation and chilled ceiling system has to be more complex than that of a conventional fully mixed system because, firstly the output requirements are different, and secondly, the assumption of isothermal surfaces is no longer valid. One of the output requirements is the room operating/comfort temperature (this is required for monitoring and/or con-

trol in a simulation environment). This temperature lies somewhere between the supply and extract temperatures, at a height of 1.1 m conventionally, and depends on the room air temperature gradients. This imposes a requirement to either place an air node at that height, or a node above and below and use interpolation to find the temperature. The other basic output requirements of the model are the air and water stream heat flows, and so inlet and outlet air and water nodes are also required.

The assumption of isothermal surfaces and the corresponding use of a single node at each wall surface is no longer valid in the displacement ventilation in view of the wall surface temperature gradients typically present. Li *et al.*'s data indicates, for example, conduction of heat into the bottom of the walls and out of the top. Since the air and wall surface temperature gradients are in the vertical directions only, it seems appropriate to sub-divide the room into a number of horizontal layers or zones.

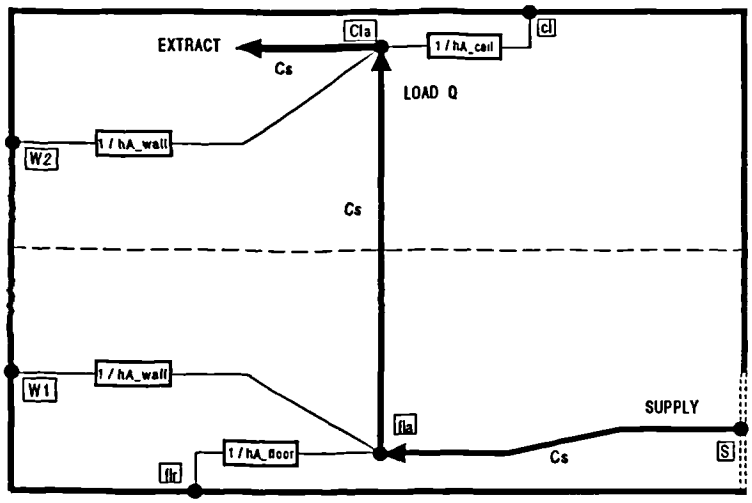


**Figure 7.2:** A simple nodal model of a room with displacement ventilation showing the room divided into two horizontal layers (connections to the other walls are not shown for clarity).

A nodal model with two horizontal zones is illustrated in Figure 7.2. Here the bottom part of the walls and the whole floor are convectively coupled to the lower room air node, and similarly the upper walls and ceiling are convectively coupled to the upper air node. In this model the air flow path is from the supply node to the bottom, the top room air nodes. This serial mode of connecting the air nodes is equivalent to assuming one-dimensional 'plug flow' vertically upwards in

the room.

Some results from this model—when implemented in the LIGHTS program with the boundary conditions for Li *et al.*'s case B3—are shown in Figure 7.3 compared with the experimental results. It can be seen that the predicted air temperatures at high and low level are in reasonable agreement but the wall surface temperatures are noticeably under-predicted. It can also be seen that assuming a linear temperature gradient between the upper and lower room air nodes would give an erroneous prediction of the air temperature at 1.1 m.

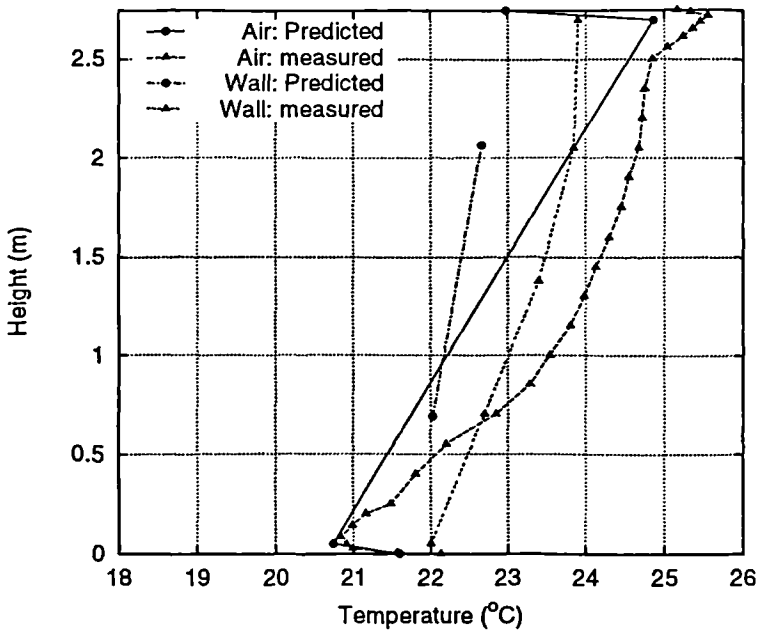


**Figure 7.3:** Results from the nodal model of a room with displacement ventilation with the room divided into two horizontal layers.

An improvement on this model would firstly be to increase the number of horizontal divisions of the room. Also, the fact that the floor and ceiling have buoyancy dominated boundary layers flowing over them suggests that separate treatment of these surfaces is required rather that connection to a mixed zone. Accordingly, separate floor and ceiling air nodes and temperatures have been defined ($T_{\mathrm{fla}}$ and $T_{\mathrm{cla}}$). A model incorporating these features and with the room divided into four horizontal zones is shown diagrammatically in Figure 7.4, again with the room air nodes connected in serial fashion. The heat load is injected at the lowest room air node as this was the position in the relevant experiments. The results from this model, for case B3, are shown in Figure 7.5. This arrangement is, in fact, similar to that in the model of Hensen and Huygen(1996).

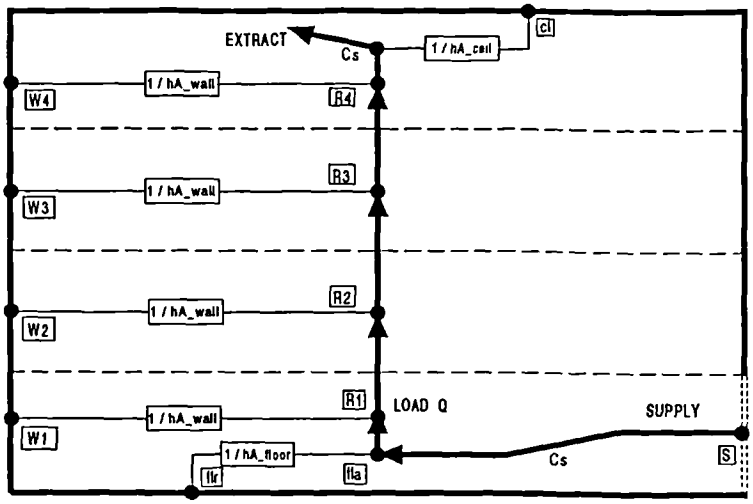


Figure 7.4: A nodal model of a room with displacement ventilation showing the room divided into four horizontal layers and one-dimensional vertical air flow (connections to the other walls are not shown for clarity).

With this one-dimensional 'plug flow' arrangement it can be seen that although the air temperature just above the floor and just below the ceiling are reasonably

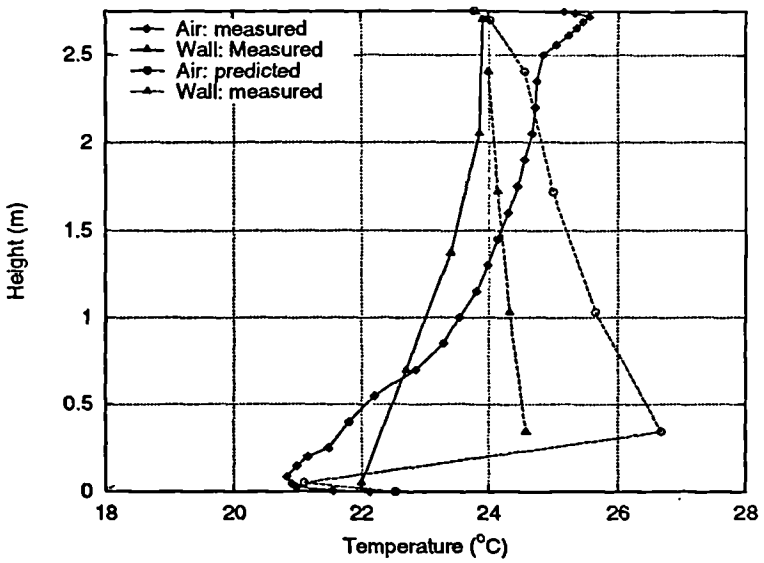


Figure 7.5: Results from the nodal model of a room with displacement ventilation with the room divided into four horizontal layers and one-dimensional vertical air flow.

predicted, the room air and wall temperatures are significantly over-predicted[2]. The excessive air temperatures predicted in the lower part of the room are a consequence of the room air nodes here having a direct connection with the heat load. In rooms with displacement ventilation (and also where combined with a chilled ceiling) there is some decoupling of the heat loads from the room air (the air surrounding the plumes that is) by virtue of the heat being transported to high level directly by the plumes.

In order to account for this decoupling effect, a second set of air nodes to represent conditions in the plume(s) in a more explicit manner was introduced. These plume air nodes are connected to each other and with the room air nodes. Vertical connections were introduced between adjacent plume nodes to represent air flow in the plume(s). Lateral connections were introduced from the room air nodes to the adjacent plume air nodes to represent entrainment of air into the plume from the surrounding air. This allows the nodal network to mimic the normal plume behaviour, growing in volume, and reducing in temperature with increasing height. This model structure is shown in Figure 7.6. The upper zone of the room is shown as being well mixed. This feature was incorporated on the initial assumption that the 'stationary front' would be approximately three quarters of the way up the room.

Results for this form of the nodal model are shown in Figure 7.7. In this case the capacity rates are set so that half of the supply flow splits off into the base of the plume and the entrainment capacity rates are equal. These results show good agreement of the air temperatures at the first two nodes and near the ceiling but otherwise too small a temperature gradient in the lower part of the room. The experimental data, however, generally shows the steepest air temperature gradients to be in the lower part of the room. This can not be accounted for if the direction of the flow in the air surrounding the plume (i.e. between nodes R1 and R2, R2 and R3 in Figure 7.6) are in all cases upwards. This is because the only temperature gains with increasing height are due to the convective fluxes at each level. Consideration of these convective fluxes shows that they could not be large enough (with reasonable convection coefficients) to raise the temperature gradient to that recorded experimentally.

It has already been noted that in displacement ventilation the air next to the ceiling is expected to be reasonably well mixed warm air due to the action of the

[2]Alternative distributions of the load to other room air nodes in this model structure were tried and found to give equally poor under-predictions of the temperatures

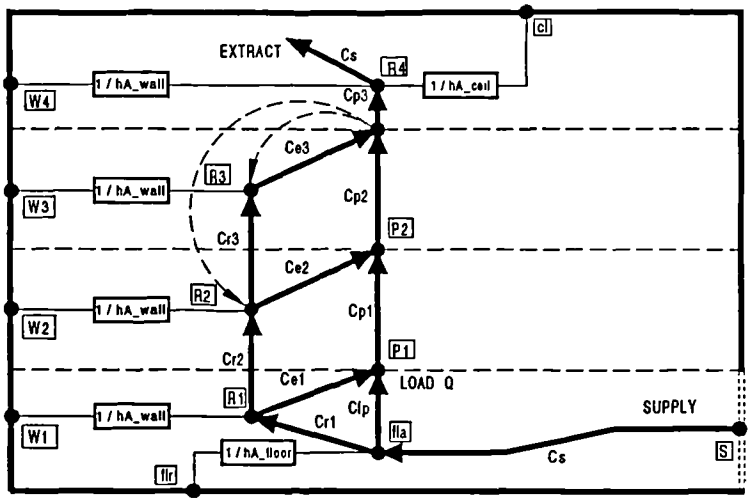


Figure 7.6: A nodal model of a room with displacement ventilation showing separate plume and room air nodes. (connections to the other walls are not shown for clarity).

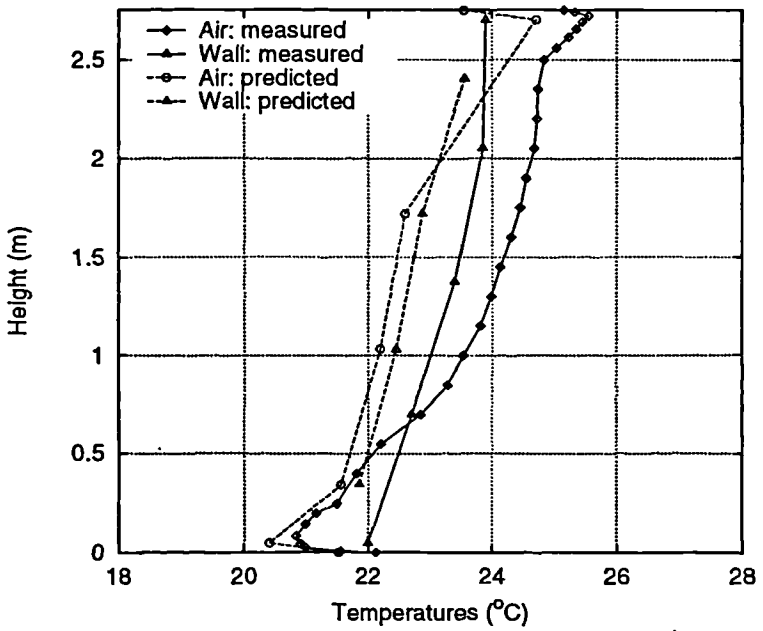


Figure 7.7: Results from the nodal model of a room with displacement ventilation with separate plume and room air nodes (no recirculation).

plumes delivering a stream of heat and momentum directly form the heat sources. It would seem that the only mechanism that can account for sufficient heat being transferred to the middle and lower part of the room, is bulk movement of air

from the warm layer near the ceiling to lower in the room. In other words, by a larger degree of mixing and recirculation than had originally been thought. (This explanation also concurs with the extent of recirculation shown in the numerical results.)

Analytical analysis (Linden et al. 1990) shows that the extent of recirculation in the room—and so the size of any upper mixed zone—depends on the size of the heat load in relation to the supply air flow rate. It can also be concluded from experimental results that room air temperature profiles vary in shape somewhat, so that the extent of the upper mixed region is no easy to define. A flexible means of including the effects of recirculation is therefore required.

The path between air nodes by which air is recirculated from the upper to lower parts of the room is not obvious. In the work previously published (Rees and Haves 1995, Haves, Rees and Harrington 1995) recirculation was simply introduced in the model structure by making two connections from the room air node in the upper zone to the air nodes in the middle zones. This arrangement is shown by the dotted lines from node P3 in Figure 7.6. The parameter values for this model used to find the published results were found by trial and error, assuming constant entrainment flow at each level. The results with different levels of recirculation (expressed as a percentage of the supply flow rate) are shown in Figure 7.8. With an assumed recirculation level of 60% the correct temperature gradients and coupling with the walls is reproduced.

This recirculation path may not be the most physically reasonable arrangement as air is shown in the numerical results to be recirculated via the boundary layers down the walls. In order to be able to refine the structure of the air flow network one would ideally like sets of detailed experimental air velocity data for the whole room. This would require the use of techniques such as hot wire anemometry or LDA to gather such data. This would require considerable resources. Here further use has been made of the numerically calculated velocity data to help refine the air flow network in the nodal model.

The numerical velocity field data has been processed by dividing the room up with a few hypothetical surfaces to form large control volumes. These large control volumes have been arranged so that the flow through each surface is at a position representative of the flow into and out of the plume or between each horizontal layer. The numerical velocity data was then integrated over these large control volume faces to find the net mass fluxes. This flow has been further integrated

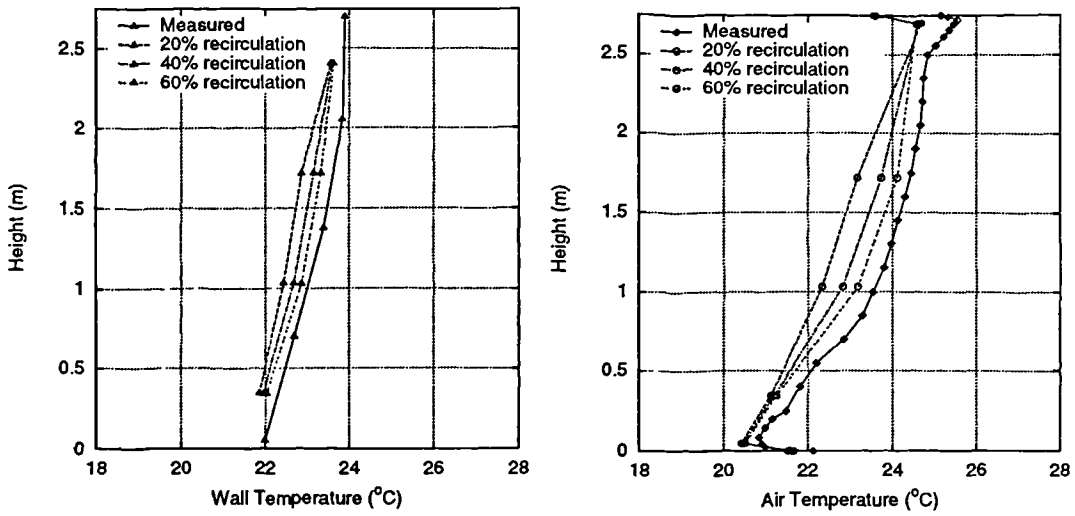


Figure 7.8: Results from the nodal model of a room with displacement ventilation with separate plume and room air nodes—previously published in (Rees and Haves 1995)—showing wall (left) and air temperature (right) predictions for different degrees of recirculation.

and illustrated in two-dimensional form in Figures 7.9 and 7.10 for test cases B3 (Li *et al.*) and DV9. From both these figures it can be seen that there is strong recirculation from the upper layer to the two middle layers. The size of this recirculating flow is also large compared to the supply/extract flows.

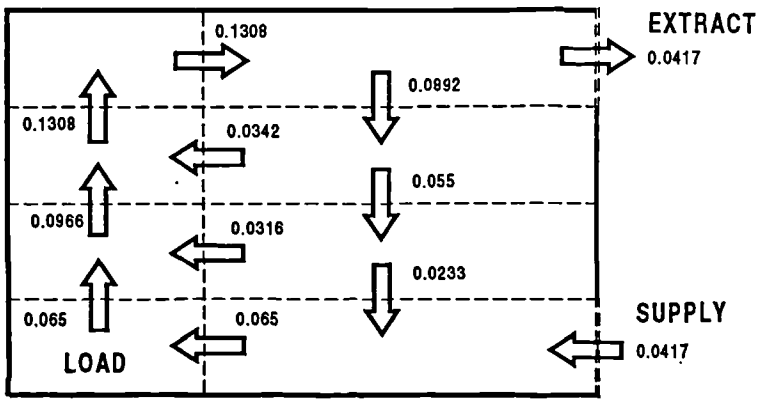


Figure 7.9: Integrated air flows calculated for Li *et al.*'s test case B3 from the numerical results. Note that the plume is represented on the left. The units are $kW.K^{-1}$

Rather than use this data directly to find parameter values the numerical data has been used to confirm the directions of the bulk air flows. A modified air

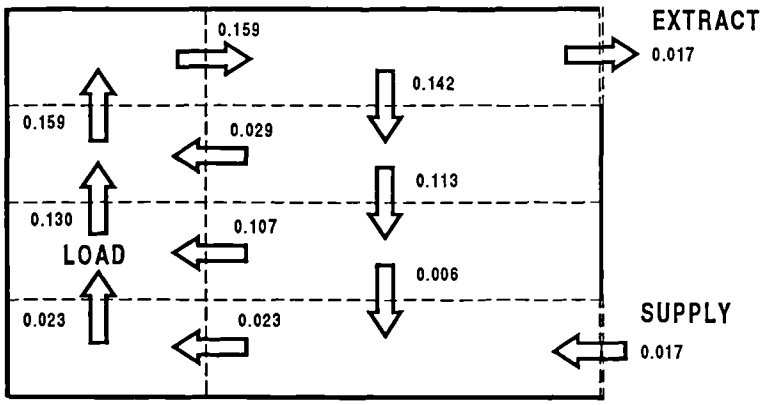


**Figure 7.10:** Integrated air flows calculated for test case DV9 from the numerical results. Note that the plume is represented on the left. The units are $kW.K^{-1}$

flow network conforming to the flow pattern suggested by the numerical results has subsequently been used to derive the parameter values. The structure of this model is shown in Figure 7.11

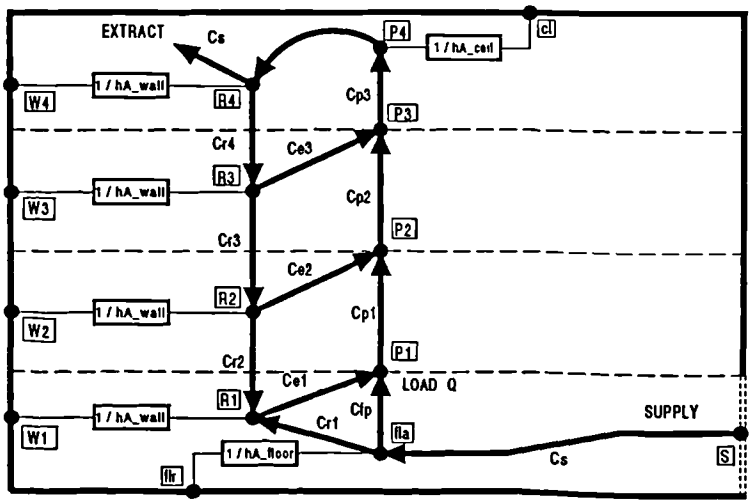


**Figure 7.11:** The model with a nodal network conforming to the air flow pattern indicated by the numerical results (Model A).

## 7.4 The Model Parameters

### 7.4.1 The approach

In the type of model considered here each air node is associated with a heat balance and mass balance equation. To use the model to predict room temperature distributions, one therefore needs to know the capacity rates and convective heat transfer coefficients which form the parameters of these equations. (The other parameters are the surface emissivities of each room surface, the selection of which is relatively straight forward and not discussed further.) The model structure described in the previous section and shown in Figure 7.11 has a total of ten air nodes including the supply node, and the air flow network includes a total of twelve capacity rate interconnections. However, the mass balance equations of the air nodes can be used to show that all these capacity rates can be expressed in terms of only four capacity rate parameters, along with the supply/extract capacity rate. The choice of which four interconnections are chosen to be the independent parameters is discussed later, but for present purposes these are taken to be the parameters representing entrainment into the plume(s): $C_{fp}$, $C_{e1}$, $C_{e2}$, $C_{e3}$. There are six convective heat transfer paths between the air nodes and surface nodes, namely those at the floor, ceiling and at the walls of the four horizontal zones. This number can potentially be reduced by assuming that some, or all, of the wall convection coefficients are the same.

There are a number of possible approaches to determining the values of the model parameters. These can be summarised as follows:

- using published correlations to find convection coefficients, and plume models to find the capacity rate parameters;
- using optimisation techniques to find the best fit between the model predictions and the experimental data;
- solving the inverted air node equations using experimental air and surface temperature measurements as boundary conditions and calculating the capacity rates and convection coefficients.

The first of these approaches is appealing, in that it allows existing rules or formulae to be readily applied. However, there is some doubt as to whether published

convection coefficient correlations could be applied given the conditions at the floor and ceiling, where buoyancy forces perpendicular to the surface are strong. There is also some difficulty in applying plume equations based on similarity considerations because of the relatively short distance over which the plumes travel before impinging on the ceiling in office size rooms. In these conditions, the transition region at the base of the plume and the impingement region at the top account for a significant extent of the plumes height. In these regions, the usual similarity equations would not apply.

An optimisation approach was tested using the model implemented in the LIGHTS program with a simple wall conduction model and a 'complex method' optimisation routine. Although results could be obtained this way, the uncertainties in the outside wall temperatures and in the radiation model are not treated in this method and must give rise to further uncertainties in the parameter values derived.

The third approach is the one adopted here. In this method, the set of equations representing the heat and mass balances at all the air nodes are effectively inverted such that the experimental air and surface temperatures become constants (inputs) in the equations and the capacity rates and convection coefficients are solved for. The heat balance and mass balance equations for each node of the model later noted as model 'B' can be written as follows:

at node fla,

$$\begin{aligned} C_s T_s + h_f A_f (T_{fl} - T_{fla}) - C_s T_{fla} &= 0 \\ C_s - C_1 - C_{fp} &= 0 \end{aligned} \tag{7.2}$$

at node R1,

$$\begin{aligned} C_1 T_{fla} + h_{w1} A_w (T_{w1} - T_{R1}) - C_2 T_{R1} &= 0 \\ C_1 - C_2 - C_{e1} &= 0 \end{aligned} \tag{7.3}$$

at node R2,

$$\begin{aligned} C_2 T_{R1} + C_3 T_{R3} + h_w A_w (T_{w2} - T_{R2}) - C_{e1} T_{R2} &= 0 \\ C_{e2} - C_2 - C_3 &= 0 \end{aligned} \tag{7.4}$$

at node R3,

$$\begin{aligned} C_4 T_{R4} + h_w A_w (T_{w3} - T_{R3}) - C_3 T_{R3} &= 0 \\ C_4 - C_3 - C_{e3} &= 0 \end{aligned} \tag{7.5}$$

at node R4,

$$\begin{aligned} C_c T_{cla} + h_w A_w (T_{w4} - T_{R4}) - C_4 T_{R4} &= 0 \\ C_c - C_4 - C_s &= 0 \end{aligned} \tag{7.6}$$

at node P1,

$$\begin{aligned} C_{fp} T_{R1} + C_{e1} T_{R1} - C_{p1} T_{p1} &= 0 \\ C_{p1} - C_{fp} - C_{e1} &= 0 \end{aligned} \tag{7.7}$$

at node P2,

$$\begin{aligned} C_{p1} T_{p1} + C_{e2} T_{R2} - C_{p2} T_{p2} + (1-R)Q &= 0 \\ C_{p2} - C_{p1} - C_{e2} &= 0 \end{aligned} \tag{7.8}$$

at node P3,

$$\begin{aligned} C_{p2} T_{p2} + C_{e3} T_{R3} - C_{p3} T_{p3} &= 0 \\ C_{p3} - C_{p2} - C_{e3} &= 0 \end{aligned} \tag{7.9}$$

and at node cla,

$$C_{p3} T_{p3} + h_c A_c (T_{cl} - T_{cla}) - C_c T_{cla} = 0 \tag{7.10}$$

The first step in determining the values of the parameters is to interpolate between the experimental temperature measurements to define equivalent temperature values at the air and surface nodes. The wall node temperatures have been arrived at by interpolating in the vertical direction between the measurements taken at four different heights, to the temperatures at the height of the wall nodes. Area weighted averages have then been taken to find a single temperature at each height equivalent to the temperatures of nodes W1–W4. The floor and ceiling node temperatures have been arrived at by simply taking the area weighted averages of the experimental measurements on these surfaces.

To find equivalent air temperatures, the single set of air temperature measurements has been used. Although these measurements were made only at one horizontal location, these temperatures are representative of the average outside the plumes. This is reasonable because, both measurements at different horizontal locations, and the numerical results, showed very little lateral variation in air temperature.

The temperature at high level($\sim$2.5 m) is known to be very close to the extract air temperature (as illustrated in Figure 4.17). In the calculation of the parameters,

the extract temperature was taken to be that of node R4, as this is the extract point in the model and the point at which the heat balance on the air stream is calculated. It seems reasonable, then, to compare this temperature with that of the measured air temperature profile at a corresponding height.

### 7.4.2 Calculating the Parameter Values

The air node heat balance and mass balance equations have been solved to find the parameters using a general purpose equation solver code known as 'EES - Engineering Equation Solver' (Klien and Alvarado 1997). This code automatically groups the equations before applying Newton's method to any sub-sets of simultaneous equations. As Newton's method is sensitive to the initial guess, and as the equation set is significantly constrained, it was necessary to start the solution procedure with good guess of the parameter values. This required first solving the entire set of equations to find the air temperatures and adjusting the capacity rates and convection coefficients manually until a workable set of guess values was obtained. It was then possible to specify each of the air temperatures in turn and calculate associated capacity rates until all the room air temperatures had been specified and all the capacity rates calculated.

It was found that the room air node equations are tightly constrained in some cases. The equations are always constrained by the need for the parameters to be positive (i.e. so that mass is conserved and the second law of thermodynamics is observed everywhere). In the case of the room air nodes the equations are further constrained because air in the model flows either up, or down, from one room air node to the next after splitting (e.g. R2 or R3). This imposes a mass balance constraint, in that the flow from a given room air node towards the next must be smaller than that from the 'upstream' node. As the flow at the upstream nodes is determined from a heat balance equation, flow at one room air node is dependent on the heat balance at an upstream node, as well as the mass balance. As the heat balances at the room air nodes are also dependent on the convection coefficients, this sometimes imposes a constraint on its value (i.e. $h_w$ can only lie within a certain range for the capacity rates to be positive everywhere). For this reason it was found necessary to specify a lower value of $h_w$ at the lowest level of the wall, at node R1. This parameter is denoted $h_{wl}$.

In principle there are enough independent equations for the floor, wall and ceiling

convection coefficients to be calculated as well as the capacity rates. However, it was found that it was not possible to use the experimental value for $T_{cla}$ and find a value of both $h_c$ and $h_w$ that were consistent with the heat balance at node R4 (see Figure 7.11). Consequently, either $h_w$ or $h_c$ had to be specified in some other way, and the other calculated. When the model is run in a 'forward' mode and the air temperatures calculated the value of $T_{cla}$ is not in agreement with that obtained from the experiments. This is probably due to a deficiency in the model structure. However, the deviations in the value of $T_{cla}$ were small.

In one case it was possible to find a value of both $h_w$ and $h_c$ that was consistent with the measured values of $T_{R4}$ and $T_{cla}$. It was found that, in this case, there was little difference to the other results if $h_w$ and $h_c$ were chosen to calculate the correct value of $T_{cla}$ or not, provided the correct overall heat balance (i.e. value of $T_{R4}$ was obtained. Hence, as $T_{cla}$ is not an output of the model, it seems acceptable in general to allow values of $h_w$ and $h_c$ that do not give the correct value of $T_{cla}$, provided overall air heat balance is maintained. In general then, either $h_w$ or $h_c$ could have been specified and the other calculated. As there is more independent information pertaining to wall convection coefficients it was decided to specify $h_w$ and calculate $h_c$. A value of $3\,\mathrm{W.m^{-2}.K^{-1}}$ has been used in the calculation of the parameters unless other constraints forced it to be slightly higher or lower.

In the previous section it was shown that it was necessary, for the Li *et al.* test cases, to direct the flow between the room air nodes R1–R4 in a downward direction so that air was recirculated from R4 down towards R1. This was, in fact, necessary to reproduce the correct relationship between the room air temperatures and the wall temperature using Li *et al.*'s test data. In general the direction of these flows is determined by thermodynamic considerations alone (i.e. so that the second law of thermodynamics is always obeyed). In particular, the direction of the flow between R1 and R2 ($C_{R2}$) is dependent on the relationship between R2 and the associated wall temperature W2. If $T_{W2}$ lies between $T_{R1}$ and $T_{R2}$ then $C_{R2}$ must be downward. If, however, $T_{R2} < T_{W2} < T_{R3}$ then $C_{R2}$ must be upward. As these conditions occur in the Loughborough test chamber data it is necessary to use two further variations on the model structure shown previously in Figure 7.11. The original model structure is noted a 'Model A', and the two further variations are noted as model B and C and are illustrated in Figures 7.12 and 7.13.

It does not seem physically unreasonable that model B should apply in the Loughborough test cases rather than model A because of the higher position of the heat

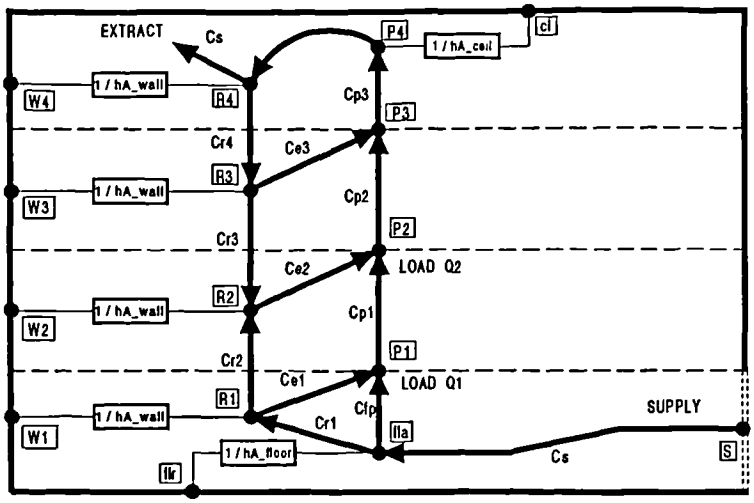


Figure 7.12: The model with a nodal network conforming to the air flow pattern indicated by the numerical results (Model B).

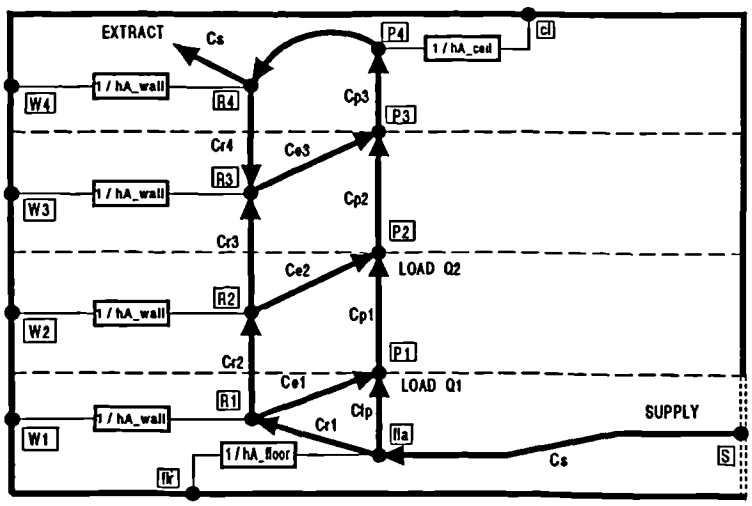


Figure 7.13: The model with a nodal network conforming to the air flow pattern indicated by the numerical results (Model C).

sources in the room. (Note also that the load has been introduced at node P2 rather than P1 in these cases to take further account of this.) In these cases recirculation might only be expected down to the bottom of the plumes in the worst cases.

A consequence of having some flow recirculated downwards from one room air

nodes to the next in the model, is that at one room air node incoming flow is from two 'upstream' nodes, rather than one. In model 'A' this occurs at node R1, in model 'B' at R2 and in model 'C' at node R2. This has implications for the solution of the equations to find the capacity rates. Specification of the node temperature and the two upstream node temperatures only allows the ratio of the capacity rates to be found. Determining the absolute value of the capacity rate requires specification of the corresponding downstream node temperature. In this case the specification of one of the plume node temperatures is required. For example, in model B (Figure 7.12) it becomes necessary to specify the plume node temperature at P2.

Although plume temperature measurements were made, it is difficult to interpolate between these measurements along the plume centre-line and the plume node temperatures. This is because it is not certain which height in the plume the nodes represent and also the nodes are bulk temperatures, rather than centre-line (maximum) temperatures. It was further found that the solution of the equations was sensitive to the value of the plume temperature specified. The value of the corresponding plume temperature had to be taken from the results of the calculation that was made with the initial guess of the parameters. It was found that the plume temperature was constrained to be within narrow limits—in a band of $\sim 1.5\,\mathrm{K}$ at most. Having found this, the values of plume temperature nodes that had to be used were consistent with the measured plume temperatures and load sizes.

The results of the parameter calculations are shown in Tables 7.1–7.3 for the Li *et al.*, displacement ventilation, and chilled ceiling test cases respectively. The model type (A–C) applicable to each calculation has been indicated in the tables.

The parameter values found from the solution of the model heat and mass balance equations have been used to implement models of some of the test cases in the LIGHTS program (Sowell 1989). These models have been implemented in two ways, with different boundary conditions. Firstly, the models were implemented using fixed inside surface temperature boundary conditions. The purpose of this was mainly to demonstrate the validity of the implementation and that the parameter values reproduce the correct relationship of the air and surface temperatures. Temperature profiles predicted in this way are shown for a number of the test cases in Figures 7.14–7.15. It can be seen that, with these boundary conditions, the air temperature profiles predicted conform to those measured. The temperature near the ceiling, given by $T_{da}$ does, however, deviate from the measured profiles. In

| *Case* | *B1* | *B2* | *B3* |
|---|---|---|---|
| Model | A | A | A |
| Load (W) | 100 | 200 | 300 |
| $C_s$ | 13.86 | 27.7 | 41.6 |
| $C_{fp}$ | 8.88 | 17.4 | 17.8 |
| $C_{e1}$ | 9.4 | 15.0 | 28.6 |
| $C_{e2}$ | 63.0 | 58.5 | 33.7 |
| $C_{e3}$ | 44.7 | 48.2 | 92.4 |
| $h_{wl}$ | 0.89 | 0.92 | 1.3 |
| $h_w$ | 5.5 | 5.5 | 6.3 |
| $h_c$ | 13.91 | 9.88 | 8.51 |
| $h_f$ | 8.60 | 7.25 | 6.06 |

**Table 7.1:** Capacity rate and convection coefficient parameters calculated for the NSIBR test cases B1–B3. The units are $W.K^{-1}$ and $W.m^{-2}.K^{-1}$ respectively.

| *Case* | *DV7* | *DV8* | *DV9* | *DV10* | *DV11* | *DV12* |
|---|---|---|---|---|---|---|
| Model | B | B | C | C | C | B |
| Load (W) | 100 | 200 | 300 | 300 | 400 | 400 |
| $C_s$ | 23.3 | 23.3 | 23.3 | 46.6 | 46.6 | 46.6 |
| $C_{fp}$ | 6.3 | 6.7 | 2.1 | 9.2 | 5.0 | 9.2 |
| $C_{e1}$ | 12.6 | 12.6 | 1.703 | 22.9 | 1.3 | 20.6 |
| $C_{e2}$ | 10.33 | 4.8 | 10.3 | 0.2 | 7.4 | 17.3 |
| $C_{e3}$ | 4.52 | 9.9 | 14.3 | 16.7 | 40.5 | 30.6 |
| $h_{wl}$ | 0.65 | 0.9 | 0.8 | 1.7 | 2.2 | 1.4 |
| $h_w$ | 3.5 | 3.0 | 1.8 | 1.7 | 5.0 | 3.0 |
| $h_c$ | 11.66 | 6.09 | 14.6 | 15.0 | 38.9 | 8.3 |
| $h_f$ | 0.8 | 1.1 | 1.3 | 1.6 | 2.3 | 2.3 |
| $h_{w4}$ | 3.5 | 3.0 | 5.0 | 7.1 | 5.0 | 3.0 |

**Table 7.2:** Capacity rate and convection coefficient parameters calculated for the displacement ventilation test cases DV7–DV12 (the units are $W.K^{-1}$ and $W.m^{-2}.K^{-1}$ respectively).

the Li *et al.* cases this temperature is slightly low, and in the other cases, slightly high. As was noted previously, this shortcoming does not seem significant as the

| *Case* | *DC10* | *DC11* | *DC12* | *DC13* | *DC14* | *DC15* | *DC16* |
|---|---|---|---|---|---|---|---|
| Model | B | C | C | B | C | B | B |
| $T_{sw}$(°C) | 16 | 16 | 17 | 14 | 14 | 17 | 17 |
| Load (W) | 1200 | 800 | 450 | 450 | 600 | 600 | 600 |
| $C_s$ | 46.6 | 46.6 | 46.6 | 46.6 | 46.6 | 46.6 | 23.3 |
| $C_{fp}$ | 9.0 | 1.4 | 13.8 | 4.6 | 8.6 | 7.4 | 2.3 |
| $C_{e1}$ | 32.7 | 23.4 | 0.6 | 1.0 | 6.8 | 20.1 | 0.9 |
| $C_{e2}$ | 15.1 | 18.1 | 26.2 | 48.3 | 22.4 | 23.6 | 24.9 |
| $C_{e3}$ | 303.9 | 7.0 | 13.3 | 120.8 | 12.1 | 18.7 | 1.9 |
| $h_{wl}$ | 0.8 | 1.3 | 0.6 | 1.2 | 1.1 | 1.4 | 1.2 |
| $h_w$ | 3.0 | 3.0 | 3.0 | 2.0 | 3.0 | 3.0 | 3.0 |
| $h_c$ | 4.4 | 5.5 | 6.8 | 4.8 | 6.6 | 6.7 | 6.8 |
| $h_f$ | 5.8 | 2.4 | 1.3 | 1.0 | 2.5 | 3.0 | 2.6 |

**Table 7.3:** Capacity rate and convection coefficient parameters calculated for the displacement ventilation and chilled ceiling test cases DC10–DC16 (the units are $W.K^{-1}$ and $W.m^{-2}.K^{-1}$ respectively, $T_{sw}$ is the chilled water flow temperature setpoint).

temperature at this point is not required as an output of the model.

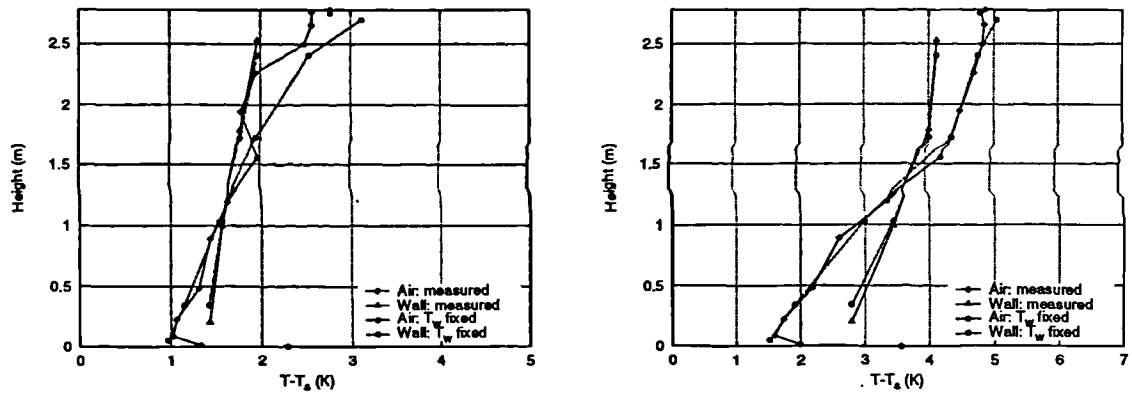


**Figure 7.14:** Results from the nodal model for cases DV8 (left) and DV12 (right) using fixed inside surface temperature boundary conditions.

The second way the models have been implemented in the LIGHTS program has involved adding six additional nodes to represent the room outer surfaces and connecting these to the internal surface nodes. The conductance of these connections was set using the appropriate fraction of the surface area ($\frac{1}{4}$ of the total for each

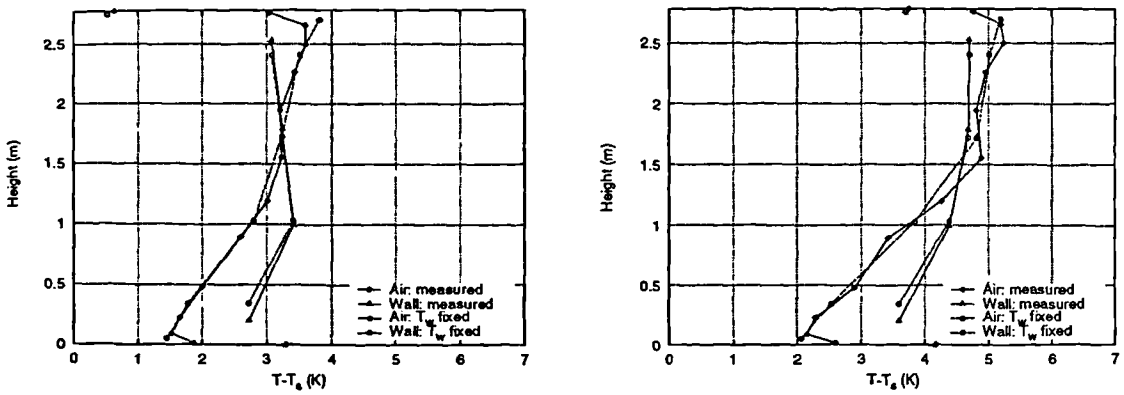


Figure 7.15: Results from the nodal model for cases DC11 (left) and DC15 (right) using fixed inside surface temperature boundary conditions.

wall node) multiplied by the conductance measured in the coheating experiment. The external surface temperature measured in each experiment were then used as the boundary conditions and the internal surface temperatures calculated. In this way the room radiant heat exchange is calculated explicitly.

This is essentially the manner in which the model is intended to be used in a simulation environment—both air and surface temperatures predicted by the model. The disadvantage of this calculation method, in terms of testing the model, is that additional uncertainties are introduced. These uncertainties are in the conducted flux due to errors in the measurement of the outside temperature (and partly in assuming the outer surfaces are isothermal) and measurement of the wall, ceiling and floor conductances. Some uncertainty also arises from the radiation model. Not only are the emissivities only approximately known (although the model is relatively insensitive to moderate changes in emissivity), but some of the view factors are approximated. It was possible to calculate the main room surface view factors reasonably accurately but only approximately for those associated with the load.

In the Li *et al.* test cases it is not essential to model the long wave radiation from the load separately, as a low emissivity heat source was used and good results (see Figure 7.8) could be obtained assuming all the load was added into the plume. The heat sources used in the Loughborough experiments had, however, a radiant output measured as 53% of the total (where the mean dry bulb was ~27°C and the mean room surface temperature ~24°C). This is a value more representative of real building loads. For this reason, and because the radiant coupling of the load and the ceiling was thought to be important, a separate node was introduced

at which only the radiant portion of the load was added. This node has attributes of area and emissivity and has associated view factors, but is not connected to the other nodes, except by radiant exchange.

The results from the model using the second calculation method, where the surface temperatures have been calculated by the model, are shown for cases DV8 and DV12 in Figure 7.16 and for cases DC11 and DC15 in Figure 7.17. Some error in the calculation of the overall heat transfer to the air stream (represented by the temperature difference at node R4) has clearly been introduced. In cases DV8 and DV12 the error is most evident in the upper part of the room. In case DC15 the errors are relatively small, but in DC11 the temperature profile is significantly shifted.

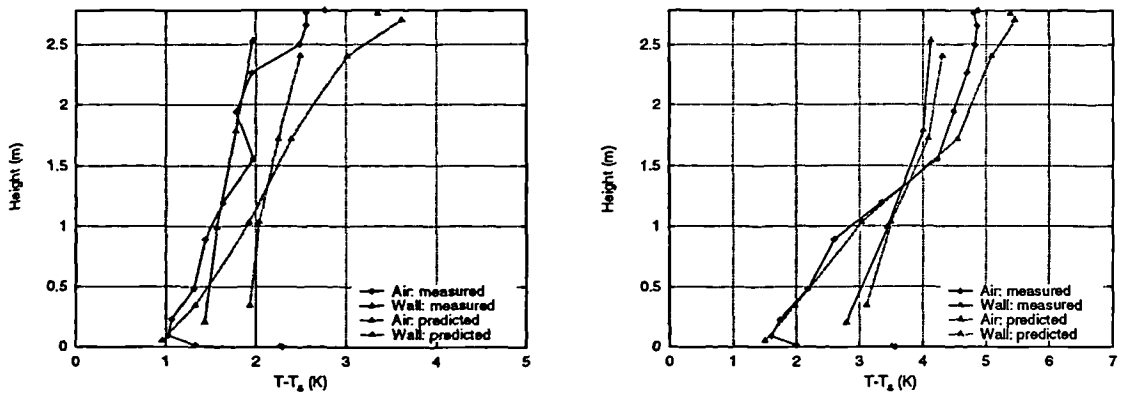


**Figure 7.16:** Results from the nodal model for cases DV8 (left) and DV12 (right) using fixed outside surface temperature boundary conditions.

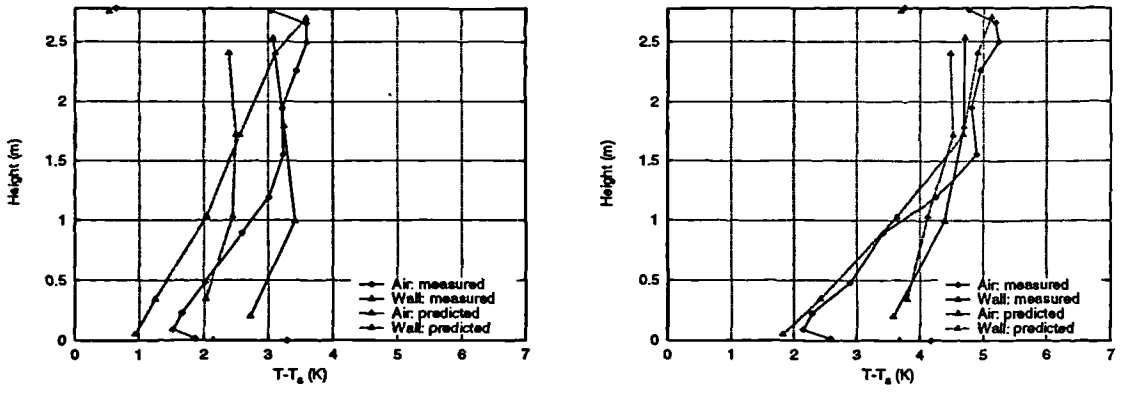


**Figure 7.17:** Results from the nodal model for cases DC11 (left) and DC15 (right) using fixed outside surface temperature boundary conditions.

The error in the calculated heat transfer to the air stream has been listed for a number of cases in Table 7.4. In making these calculations, the most obvious

uncertainty is in the conducted fluxes due to the associated uncertainty in the value of the conductances (see Table 4.5). It was previously noted that the size and direction of the conducted flux at the south wall could not be accurately determined from the inside or outside temperature measurements. For this reason, the surface temperatures at the south wall have been fixed at their measured values in these calculations. The discrepancy between the heat balance on the air, calculated by the two calculation methods, must be due to the uncertainties introduced by explicitly modeling the wall conduction and radiant heat transfer already noted. From Table 4.5 it can be seen that the largest error occurs in cases DV8. In this test, case the conducted fluxes are much more significant than the heat transferred to the room air. Consideration of the conducted fluxes calculated for case DC15 shows that the conducted fluxes are correspondingly insignificant (of order 10 W).

| *Test Case* | *Total Load (W)* | *Measured* $Q_a$ *(W)* | *Predicted* $Q_a$ (W) | *Error (%)* |
|---|---|---|---|---|
| DV8 | 200 | 58.5 | 70.2 | 20.1 |
| DV12 | 400 | 212.8 | 233.5 | 9.7 |
| DC10 | 1200 | 248.9 | 227.6 | 8.6 |
| DC11 | 800 | 164.7 | 145.2 | 11.8 |
| DC14 | 600 | 162.4 | 133.2 | 18.0 |
| DC15 | 600 | 242.2 | 228.9 | 5.5 |

**Table 7.4:** Heat transfer to the room air predicted by the nodal model where both air and surface temperatures have been calculated.

To examine the significance of the uncertainties in the temperature measurements, and the conductances, further calculations have been made for cases DV8 and DC15. In these calculations the external surface temperatures and the conductances have been perturbed to show the potential effects of errors in their measurement. In the case of the outer surface temperatures, they have been perturbed from the measured value by $\pm 0.3\,\mathrm{K}$. The wall, ceiling and floor conductances have been altered by $\pm$ their expected uncertainty as indicated in Table 4.5. The results of these calculations are shown in Figure 7.18. In the case of the calculation for case DC15 the temperature profiles associated with the upper and lower limits of the conducted fluxes lie either side of that measured. In the case of the calculation for DV8 the uncertainty in the conducted fluxes only accounts for part of the discrepancy between the measured and calculated temperatures. In this case,

either there must be greater error than expected in the temperature, conductivity or air flow rate measurements, or in the calculation of the radiant fluxes.

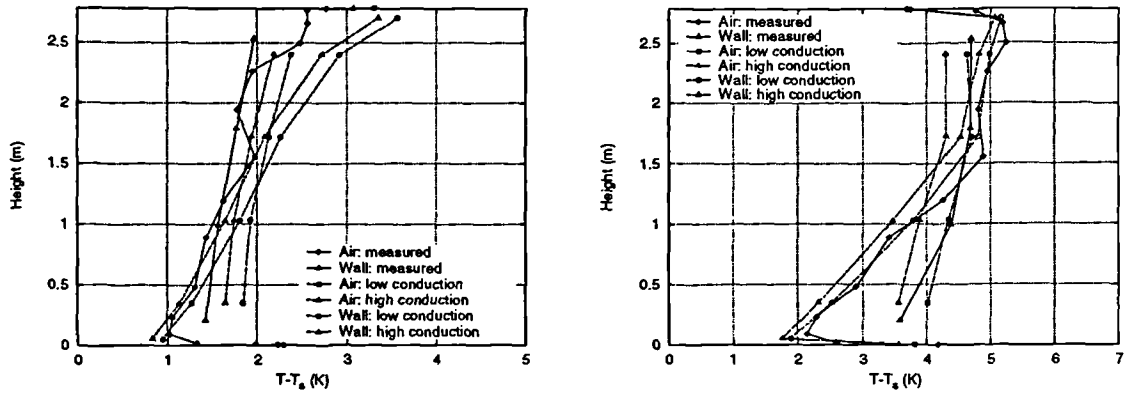


Figure 7.18: Results from the nodal model for cases DV8 (left) and DC15 (right) where the upper and lower estimates of the conducted fluxes have been calculated.

### 7.4.3 Generalisation of the Parameters

For the model to be useful in predicting the thermal loads and temperatures of rooms with displacement ventilation and chilled ceilings under a variety of conditions it is clearly necessary to be able to generalise the parameters of the model. This requires the definition of functions or rules that could be used to establish the model parameters from either other model inputs or more conventional design parameters. The convection coefficient parameters are considered first.

#### The Model Convection Coefficients

Consider the convection coefficients used in the model. It has already been noted that it was necessary to use a lower convection coefficient for the lowest section of the room walls when calculating the parameters. There is some physical basis for making such a distinction between the lowest part of the walls and the upper part. In the discussion of the numerical results and the visualisation experiment, it was noted that the velocities and the degree of mixing in the bottom part of the room (below the heat sources) were noticeably lower than those in the upper part of the room. In the bottom part of the room the flow is dominated by that from the diffuser and a return current flowing over the top of the boundary layer

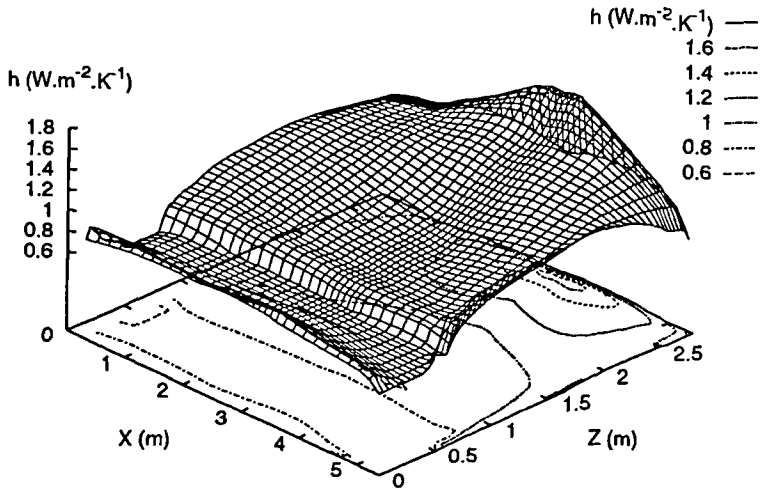


Figure 7.19: Local heat transfer coefficient calculated for the north wall from the numerical results for test case DV9 (Z is in the vertical direction).

near the floor and the flow over the walls, mainly a horizontal direction. In the upper part of the room, the flow is much more mixed with higher velocities near the walls. The convection coefficients in the upper part of the room may therefore be expected to be higher in view of the higher velocities and turbulence intensity.

This difference in values of the convective heat transfer coefficient at high and low level, is demonstrated in the predictions of the local heat transfer coefficient on the north wall from the numerical calculations for case DV9. The predicted local heat transfer coefficient is plotted in Figure 7.19. A distinct region $z < 0.7\,\mathrm{m}$ where the convection coefficient is lower ($0.6 < h < 0.8\,\mathrm{W.m^{-2}.K^{-1}}$) can be seen. In the calculations of the parameters, in nearly all the test cases, a value of convection coefficient satisfying the constraints of the model could be found using the correlation published by Hatton and Awbi (1995). Hatton and Awbi carried out natural convection experiments with heated and cooled surfaces in room size enclosures and arrived at a correlation $h_c = 1.49(\Delta T)^{0.345}\,\mathrm{W.m^{-2}.K^{-1}}$ for turbulent flows. This gives higher values than other correlations for isolated surfaces but within the quoted range for enclosures. This then, seems a reasonable basis for defining the value of the parameter $h_{wl}$ in the model.

In calculating the parameter values, the wall convection coefficient $h_w$ for the upper walls was specified and the ceiling convection coefficient calculated, as noted previously. The choice of wall convection coefficient is therefore not independent

of the choice of ceiling convection coefficient if the measured heat balance on the air stream is to be reproduced. Some other means is required to fix the value of, or define a correlation for, one of the coefficients. By varying the wall convection coefficient in the parameter calculation, it is possible to see the effect on the ceiling coefficient. It is also necessary, however, to give consideration to how well defined the relationship between the two coefficients is, when errors in the temperature measurements are taken into account. The ceiling heat transfer coefficients corresponding to given wall convection coefficients for test cases DV11, DC11 and DC14 are shown in Figure 7.20. In this figure the effect of perturbing the temperature of the upper room air node R4, by the estimated measurement error is also shown. It should also be noted that the extent of the lines plotted shows the upper and lower limits within which the wall coefficient is constrained.

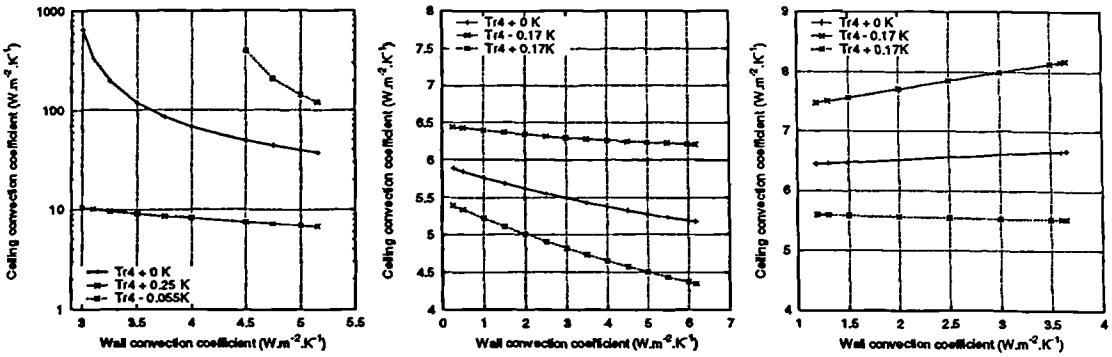


Figure 7.20: The relationships between the wall and calculated ceiling convection coefficients for test cases DV11 (left), DC11 (centre) and DC14 (right) showing the effects of measurement error.

It can be seen that the value of the ceiling heat transfer coefficient is very sensitively coupled to the value of the wall coefficient in case DV11 where there are larger errors in the temperature measurements. The ceiling coefficient is somewhat less sensitively coupled to the value of the wall coefficient cases DC11 and DC14. This is partly due to the temperature differences between the ceiling and the air nodes being much larger, and the measurement errors less significant, in these cases. From this, given the possible measurement errors, certain limits for these coefficients may be defined but some independent means of determining the values must be found.

In the case of the wall convection coefficient, a value of $3.0\,W.m^{-2}.K^{-1}$ was used in the parameter calculations. This value is the value for horizontal heat transfer at internal surfaces suggested in the CIBSE Design Guide A (1986, Table A3.6). This value seems a reasonable constant value to accept, as it lies towards the

middle of the constraint limits for cases DC11 and DC14, and gives reasonable values of ceiling coefficient for many of the test cases. It is more difficult to find independent correlations for convection coefficients representative of conditions at the ceiling.

A value of $4.3\,\mathrm{W.m^{-2}.K^{-1}}$ is given in the CIBSE Design Guide A for horizontal surfaces, upward heat flow, and in still air conditions ($v < 0.1\,\mathrm{m.s^{-1}}$). Some enhancement of the convective heat transfer at the ceiling can be expected compared to still air conditions, due to the action of the plumes impinging on the ceiling. Values of $h_c$ for small isothermal jets with similar Re impinging on flat plates are in the range 24–96 $\mathrm{W.m^{-2}.K^{-1}}$ according to Gardon and Akfirat (1965). Values for non-isothermal jets can be expected to be lower (Hollworth and Gero 1985) but published measurements in conditions closer to those found at the ceiling have not been found. The values given for still conditions, and for impinging jets, probably represent the lower and upper limits of what could be expected for the convection coefficient at the ceiling.

The numerical results are another possible source of heat transfer coefficient data although heat fluxes at the ceiling are expected to be over-predicted in the regions where the flow impinges. Effective convection coefficients can be derived from the numerical heat flux and temperature data. One approach to doing this is to consider the average flux at the ceiling given by the numerical results and the temperature difference appearing in the model. For case DV9, for example, this gives a value of $h_c$ of $19.1\,\mathrm{W.m^{-2}.K^{-1}}$, and for case DC10 a value of $12.8\,\mathrm{W.m^{-2}.K^{-1}}$.

From this it seems reasonable to expect the values of $h_c$ in the model to lie between the value of $4.3\,\mathrm{W.m^{-2}.K^{-1}}$ given by the CIBSE Guide, and the values of the order $12\,\mathrm{W.m^{-2}.K^{-1}}$ found from the numerical results. Considering the values of $h_c$ found from the parameter calculations using values of $h_w$ of $3\,\mathrm{W.m^{-2}.K^{-1}}$, there is some distinction between the values found for the displacement ventilation cases and those of the chilled ceiling cases. Nearly all the values of $h_c$ are close to the average of $5.9\,\mathrm{W.m^{-2}.K^{-1}}$ for the chilled ceiling cases. The values for the displacement ventilation cases are higher, the average being $11.7\,\mathrm{W.m^{-2}.K^{-1}}$. There is also greater variation about the mean value of $h_c$ in the displacement ventilation cases. The coefficient is probably less well defined in these cases than in the chilled ceiling cases because of the small temperature differences at the ceiling, and corresponding greater significance of the measurement errors. These values fall within the expected range. In view of the lack of good independent information concerning the value of the ceiling convection coefficient, it is proposed

that the mean values found from the parameter calculations are used as constant coefficients in the model.

The value of the floor heat transfer coefficient found in the parameter calculations, is given by a single equation $h_f = C_s(T_{fla} - T_s)/(T_{fla} - T_{fl})A_f$. This equation can be solved independently of the others, given a value for $T_{fla}$. Nearly all the values calculated in this way fall in the range 1-3 $W.m^{-2}.K^{-1}$. Some dependence of the convection coefficient on the supply capacity rate, $C_s$, might be expected. This is shown in the results of the parameter calculations for the displacement ventilation test cases where $h_f$ is in the range 0.85–1.25 $W.m^{-2}.K^{-1}$ for the cases with a supply capacity rate of 23.3 $W.K^{-1}$, and in the range 1.6–2.3 $W.m^{-2}.K^{-1}$ for the cases with the higher supply capacity rate of 46.6 $W.K^{-1}$ (see Tables 7.2–7.3). This trend is not, however, evident in the displacement ventilation and chilled ceiling parameter calculations, where case DC16 with a capacity rate of 23.3 $W.K^{-1}$ gave a relatively high value of $h_f$=2.6 $W.m^{-2}.K^{-1}$. No particular difference was expected in the value of $h_f$ between the displacement ventilation test cases and those with the chilled ceiling, as the flow conditions near the floor have been shown to be very much the same in both types of test case. The convection coefficient values calculated for both series of test cases show very similar ranges. Again, in the absence of better information, it is proposed to use the mean value of the floor convection coefficient, 2.1 $W.m^{-2}.K^{-1}$, to define a constant value of $h_f$ for use in the model.

The uncertainty in these calculated heat tranfer coefficients is largely dependent on the size of the temperature errors in relation to the temperature differences involved. In the case of the chilled ceiling test cases these temperature differences are significant at the ceiling and only moderate at the floor. For example the temperature difference $T_{fla} - T_s$ is of the order $2 \pm 0.17$ K (using the errors estimated in Appendix A) and the difference $T_{fla} - T_{fl}$ of order $1 \pm 0.3$ K. Using the expression for $h_f$ noted above, these would give values between 3.9 $W.m^{-2}.K^{-1}$ and 8.6 $W.m^{-2}.K^{-1}$.

The sensitivity of the model to variations in the value of the wall, floor, and ceiling convection coefficients has been examined by using case DC15 as a base case, and setting each of the coefficients at high and low values. The high and low values for each of the coefficients have been selected from the upper and lower limits of the coefficients found from the parameter calculations. These parameter values have been used with the model implemented in the LIGHTS program using fixed external surface temperature boundary conditions. The results are shown in

Figures 7.21 and 7.22.

The effect of changes in the value of the wall convection coefficient is to shift the lower part of the temperature profile along the temperature axis. The temperature gradients in the lower part of the room are very similar to those measured and the change in extract temperature is smaller than that at the nodes in the lower part of the room. The effect of changes in the value of the floor convection coefficient (Figure 7.22, left) are more dramatic as the air temperature at the floor is changed significantly as $h_f$ changes from 0.85 $W.m^{-2}.K^{-1}$ to 8.6 $W.m^{-2}.K^{-1}$. The temperature changes at the upper nodes of the model are still relatively small. The third test (Figure 7.22, right) shows the effect of changing $h_c$, but with the ceiling temperature fixed. As the radiant coupling is very similar with the ceiling temperature fixed, the changes in the temperature nearer the floor are very small. There is, however, a significant change in the predicted extract temperature and in the temperature of node R3. The model therefore shows more sensitivity to the value of the floor and ceiling coefficients than those of the wall. The ceiling coefficient has the most significant effect on the prediction of the overall heat balance on the air, which is unsurprising for a chilled ceiling test case.

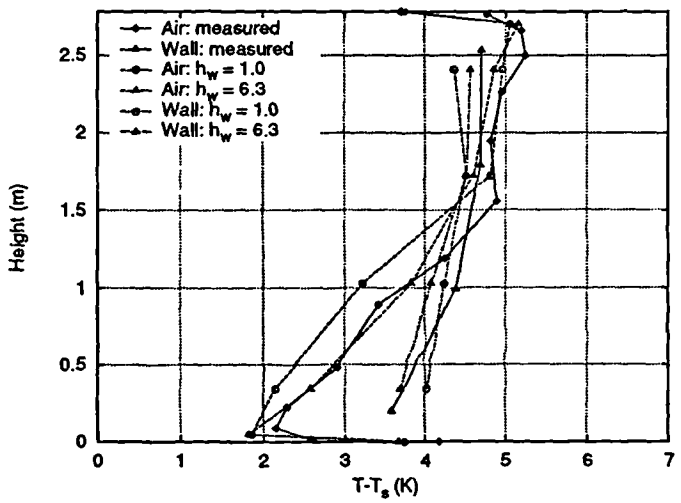


**Figure 7.21:** The response of the model to extreme values of the wall convection coefficient parameter $h_w$ (using case DC15 as a base case).

### The Model Capacity Rate Parameters

Before considering the specific capacity rate parameters, it is necessary to consider the choice between the variations of the basic model, namely models A–C. It is

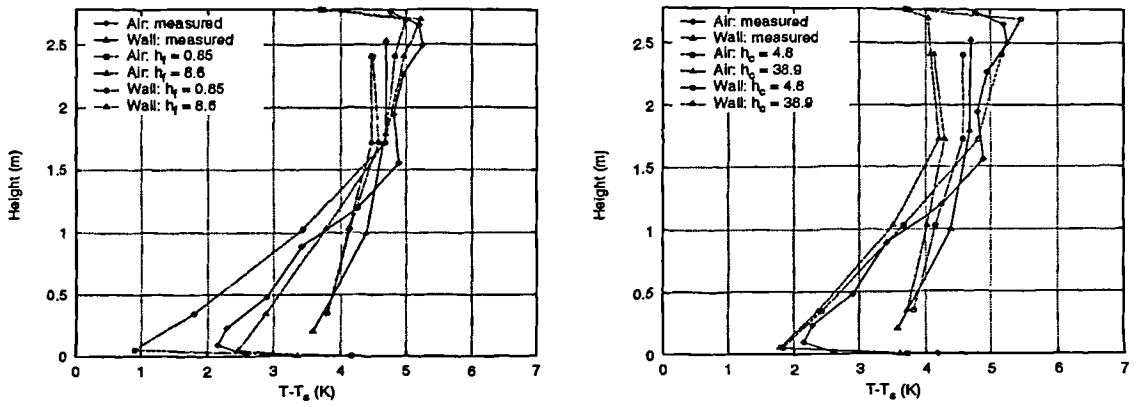


**Figure 7.22:** The response of the model to extreme values of the convection coefficient parameters for the floor $h_f$ (left), and for the ceiling $h_c$ (using case DC15 as a base case).

only Li *et al.*'s test cases, where the load was very near the floor, that required the use of model A. In this case, it seems reasonable that the recirculation in the room should descend to the lowest of the four zones of the room. The Loughborough test cases, however, require the use of both models B and C, involving recirculation only to the second and third zones above the floor respectively (see Figures 7.12 and 7.13). There seems to be no particular correlation between the operating conditions and the form of the model required. The choice between models B and C is entirely dependent on the sign of the temperature difference between the nodes R3 and W3. If $T_{r3} > T_{w3}$, model B is required to ensure the second law of thermodynamics is satisfied everywhere in the model. Correspondingly, if $T_{r3} < T_{w3}$, model C is required. Inspection of these temperature differences, however, reveals that they are very small in every test case. These temperature differences are listed in Table 7.5. It can be seen that the magnitudes of these temperature differences is smaller than the estimated error limits associated with the surface-to-air temperature measurements ($\pm 0.33\,\mathrm{K}$).

In view of the size of these temperature differences in relation to the measurement uncertainties, the choice in a particular case between the two forms of the model seems arbitrary. For the sake of simplifying the model the use of model B is proposed for all the Loughborough test cases. A revised set of model parameters has been calculated for the cases previously noted as requiring the use of model C, using model B and after reversing the temperature difference between nodes R3 and W3. The complete revised parameter values are shown in Tables 7.6 and 7.7. Having made this simplification, the choice between models A and B can be made

| *Test Case* | $T_{r3} - T_{w3}$ (K) | *Test Case* | $T_{r3} - T_{w3}$ (K) |
|---|---|---|---|
| DV7 | 0.064 | DC10 | 0.308 |
| DV8 | 0.102 | DC11 | -0.02 |
| DV9 | -0.114 | DC12 | -0.02 |
| DV10 | -0.231 | DC13 | 0.043 |
| DC11 | -0.237 | DC14 | -0.104 |
| DC12 | 0.355 | DC15 | 0.164 |
| | | DC16 | 0.039 |

**Table 7.5:** Temperature differences at nodes R3 and W3 in each test case (negative temperature differences indicate the use of model C rather than B).

simply on the basis of the height of the heat sources—model B representing rooms with loads at desk top height. Model C may be applicable still in situations where the wall surface temperatures are driven high, relative to the air temperatures. Such situations might include those where the loads were positioned at high level, or where hot walls or glazing surfaces were present.

In the process of considering trends in the model parameters alternative methods of parameterising the model were considered. It has been noted that there are four independent capacity rate parameters. These have been initially chosen as the capacity rates representing flow into the plume, namely $C_{fp}$, $C_{e1}$, $C_{e2}$ and $C_{e3}$. This method of parameterising the model has the advantage that the parameters can be thought of a representing the entrainment processes and are always in the same direction, but has the disadvantage that the parameters are dimensionalised. A similar method might be to specify the capacity rates between the room air nodes, namely $C_{R1}$, $C_{R2}$, $C_{R3}$, $C_{R4}$. These parameters have the disadvantage that they represent flows that are not always in the same direction in each form of the model. Either of these sets of parameters may be non-dimensionalised by dividing each by the supply capacity rate, $C_s$.

A system of parameters that is non-dimensional and also has the advantage of being bounded in the range 0–1.0 can be found from considering the splits in the flow network and defining parameters as ratios of one of the branch capacity rate to the upstream capacity rate. For example the parameter $S_1$ could be defined as $C_{fp}/C_s$. The disadvantage of this set of parameters is that they would not

| *Case* | *DV7* | *DV8* | *DV9* | *DV10* | *DV11* | *DV12* |
|---|---|---|---|---|---|---|
| Model | B | B | B | B | B | B |
| Load (W) | 100 | 200 | 300 | 300 | 400 | 400 |
| $C_s$ | 23.3 | 23.3 | 23.315 | 46.63 | 46.63 | 46.6 |
| $C_{fp}$ | 6.3 | 6.7 | 2.069 | 9.172 | 1.211 | 9.2 |
| $C_{e1}$ | 12.6 | 12.6 | 5.334 | 1.41 | 0.969 | 20.6 |
| $C_{e2}$ | 10.33 | 4.8 | 17.6 | 44.03 | 47.81 | 17.3 |
| $C_{e3}$ | 4.52 | 9.9 | 1.065 | 3.062 | 3.9 | 30.6 |
| $h_{wl}$ | 0.65 | 0.9 | 0.75 | 1.7 | 2.4 | 1.4 |
| $h_w$ | 3.5 | 3.0 | 1.2 | 2.9 | 5.0 | 3.0 |
| $h_c$ | 11.66 | 6.097 | 11.91 | 30.53 | 56.67 | 8.3 |
| $h_f$ | 0.8 | 1.1 | 1.3 | 1.6 | 2.3 | 2.3 |
| $h_{w4}$ | - | - | 5.0 | 8 | - | - |

**Table 7.6:** Capacity rate and convection coefficient parameters calculated for the displacement ventilation test cases DV7–DV12 using model form B only. The units are $W.K^{-1}$ and $W.m^{-2}.K^{-1}$ respectively.

be defined in exactly the same way in each form of the model, and also they are less easy to relate directly to the physical flows. Both these sets of parameters have been calculated for each case and are given in Tables 7.8–7.11. The split ratio parameters are defined as $S_1 = C_{fp}/C_s$, $S_2 = C_{e1}/C_{R1}$, $S_3 = C_{e3}/C_{R4}$, $S_4 = C_{R4}/C_{p3}$.

Considering each of the sets of capacity rate parameters it is apparent that some of the parameters do not show any particular variations with the usual design parameters such as load size, air change rate, or ceiling temperature. However, some of the parameters have values confined within definite limits. The trends in the capacity rate parameters can be summarised as follows.

- Parameters $S_1$ and $C_{R1}$ fall within relatively narrow limits. $S_1$ for example, falls in the range 0.03–0.29. This can also be shown by considering the ratio $C_{R1}/C_s$ which is listed in Tables 7.8 and 7.9. The limiting of the value of both these parameters shows that $C_{fp}$ is always a limited fraction of the supply capacity rate.

- Parameter $C_{R3}$ falls within a relatively narrow range of 0.48–10.2 $W.K^{-1}$ and

| *Case* | *DC10* | *DC11* | *DC12* | *DC13* | *DC14* | *DC15* | *DC16* |
|---|---|---|---|---|---|---|---|
| Model | B | B | B | B | B | B | B |
| $T_sw$ | 16.0 | 16 | 17 | 14.0 | 14 | 17.0 | 17.0 |
| Load (W) | 1200 | 800 | 450 | 450 | 600 | 600 | 600 |
| $C_s$ | 46.6 | 46.63 | 46.63 | 46.6 | 46.63 | 46.6 | 23.3 |
| $C_{fp}$ | 9.0 | 1.35 | 8.36 | 4.6 | 8.57 | 7.4 | 2.3 |
| $C_{e1}$ | 32.7 | 21.83 | 4.95 | 1.0 | 5.37 | 20.1 | 0.9 |
| $C_{e2}$ | 15.1 | 26.16 | 34.57 | 48.3 | 34.59 | 23.6 | 24.9 |
| $C_{e3}$ | 303.9 | 11.70 | 18.12 | 120.8 | 46.05 | 18.7 | 1.9 |
| $h_{wl}$ | 0.8 | 1.3 | 0.7 | 1.2 | 1.1 | 1.4 | 1.2 |
| $h_w$ | 3.0 | 3.0 | 3.0 | 2.0 | 3.0 | 3.0 | 3.0 |
| $h_c$ | 4.4 | 5.5 | 6.8 | 4.8 | 6.1 | 6.7 | 6.8 |
| $h_f$ | 5.8 | 2.4 | 1.3 | 1.0 | 2.5 | 3.0 | 2.6 |

**Table 7.7:** Capacity rate and convection coefficient parameters calculated for the displacement ventilation and chilled ceiling test cases DC10–DC16 using model form B only. The units are $W.K^{-1}$ and $W.m^{-2}.K^{-1}$ respectively, $T_{sw}$ is the chilled water flow temperature setpoint.

| *Case* | *DV7* | *DV8* | *DV9* | *DV10* | *DV11* | *DV12* |
|---|---|---|---|---|---|---|
| Model | B | B | B | B | B | B |
| Load (W) | 100 | 200 | 300 | 300 | 400 | 400 |
| $C_s$ | 23.3 | 23.3 | 23.315 | 46.63 | 46.63 | 46.6 |
| $C_{R4}$ | 10.39 | 10.60 | 2.75 | 11.04 | 7.26 | 31.11 |
| $C_{R3}$ | 5.87 | 0.65 | 1.69 | 7.98 | 3.36 | 0.48 |
| $C_{R2}$ | 4.46 | 4.10 | 15.91 | 36.05 | 44.45 | 16.85 |
| $C_{R1}$ | 17.06 | 16.65 | 21.25 | 37.46 | 45.42 | 37.43 |
| $C_{R1}/C_s$ | 0.73 | 0.71 | 0.91 | 0.80 | 0.97 | 0.80 |
| $C_{e1}/C_{e2}$ | 1.22 | 2.64 | 0.30 | 0.03 | 0.02 | 1.19 |
| $C_{e1}+C_{e2}$ | 22.93 | 17.30 | 22.93 | 45.44 | 48.78 | 37.91 |

**Table 7.8:** Alternative capacity rate parameters calculated for the displacement ventilation test cases DV7–DV12 (the units are $W.K^{-1}$).

is always of similar magnitude to parameter $C_{fp}$.

| *Case* | *DC10* | *DC11* | *DC12* | *DC13* | *DC14* | *DC15* | *DC16* |
|---|---|---|---|---|---|---|---|
| Model | B | B | B | B | B | B | B |
| $T_s w$ | 16.0 | 16 | 17 | 14.0 | 14 | 17.0 | 17.0 |
| Load (W) | 1200 | 800 | 450 | 450 | 600 | 600 | 600 |
| $C_s$ | 46.6 | 46.63 | 46.63 | 46.6 | 46.63 | 46.6 | 23.3 |
| $C_{R4}$ | 314.09 | 14.41 | 19.38 | 128.14 | 47.95 | 23.13 | 6.78 |
| $C_{R3}$ | 10.21 | 2.71 | 1.26 | 7.34 | 1.90 | 4.44 | 4.86 |
| $C_{R2}$ | 4.93 | 23.45 | 33.32 | 40.98 | 32.69 | 19.13 | 20.04 |
| $C_{R1}$ | 37.64 | 45.28 | 38.27 | 42.02 | 38.06 | 39.22 | 20.99 |
| $C_{R1}/Cs$ | 0.81 | 0.97 | 0.82 | 0.90 | 0.82 | 0.84 | 0.90 |
| $C_{e1}/C_{e2}$ | 2.16 | 0.83 | 0.14 | 0.02 | 0.16 | 0.85 | 0.04 |
| $C_{e1} + C_{e2}$ | 47.84 | 47.99 | 39.52 | 49.36 | 39.96 | 43.66 | 25.85 |

**Table 7.9:** Alternative capacity rate parameters calculated for the displacement ventilation test cases DV7–DV12 (the units are $W.K^{-1}$).

| *Case* | *DV7* | *DV8* | *DV9* | *DV10* | *DV11* | *DV12* |
|---|---|---|---|---|---|---|
| Model | B | B | B | B | B | B |
| Load (W) | 100 | 200 | 300 | 300 | 400 | 400 |
| $S_1$ | 0.27 | 0.29 | 0.09 | 0.20 | 0.03 | 0.20 |
| $S_2$ | 0.74 | 0.75 | 0.25 | 0.04 | 0.02 | 0.55 |
| $S_3$ | 0.44 | 0.94 | 0.39 | 0.28 | 0.54 | 0.98 |
| $S_4$ | 0.31 | 0.31 | 0.11 | 0.19 | 0.13 | 0.40 |

**Table 7.10:** Alternative non-dimensional capacity rate parameters calculated for the displacement ventilation test cases DV7–DV12.

- The sum of parameters $C_{e1}$ and $C_{e2}$ is always very close to the supply capacity rate. This summation has been indicated in the bottom row of Tables 7.8 and 7.9.

- Parameter $C_{e3}$, which represents the entrainment at the top of the plume and degree of mixing in the upper part of the room is relatively small in the displacement ventilation cases and becomes large (up to 6.5 times the supply capacity rate) when the loads are large and/or the ceiling temperature is lower.

| *Case* | *DC10* | *DC11* | *DC12* | *DC13* | *DC14* | *DC15* | *DC16* |
|---|---|---|---|---|---|---|---|
| Model | B | B | B | B | B | B | B |
| $T_{sw}$ | 16.0 | 16 | 17 | 14.0 | 14 | 17.0 | 17.0 |
| Load (W) | 1200 | 800 | 450 | 450 | 600 | 600 | 600 |
| $S_1$ | 0.19 | 0.03 | 0.18 | 0.10 | 0.18 | 0.16 | 0.10 |
| $S_2$ | 0.87 | 0.48 | 0.13 | 0.02 | 0.14 | 0.51 | 0.05 |
| $S_3$ | 0.97 | 0.81 | 0.94 | 0.94 | 0.96 | 0.81 | 0.28 |
| $S_4$ | 0.87 | 0.24 | 0.29 | 0.73 | 0.51 | 0.33 | 0.23 |

**Table 7.11:** Alternative non-dimensional capacity rate parameters calculated for the displacement ventilation test cases DV7–DV12.

The small value of the parameter $C_{fp}$ and the nearly constant value of $C_{e1} + C_{e2}$ could be expected. The effect of these parameters is mainly to control the temperature gradient in the lower part of the room. The experimental results showed that the non-dimensionalised temperature gradients in the lower part of the room are very similar for test cases with the same supply capacity rate. The temperature gradients found in the experiments fall, therefore, into a relatively narrow range. Hence, the parameters controlling the prediction of the temperature gradient in the lower part of the room might be expected to fall into a limited range.

From these observations of the parameter variations, some rules can be defined that help in the definition of the parameter values. Firstly, as $C_{fp}$ varies little, its value might be set from the mean value of parameter $S_1$, namely 0.15. It also seems reasonable to set $C_{e1} + C_{e2} = C_s$. If this is done, continuity restraints dictate that $C_{R3} = C_{fp}$, which is constant with the observations of the parameter $C_{R3}$ noted above. Having established these rules it remains necessary to find the ratio $C_{e1}/C_{e2}$ and the value of $C_{e3}$. The only notable trend concerning the value of $C_{e3}$ is that for all the displacement ventilation test cases, except DV12, its value lies towards the bottom of its range, such that $C_{e3}/C_s \sim 0.1$. For the displacement ventilation and chilled ceiling test cases there is a much wider variation of $C_{e3}$.

The ratio $C_{e1}/C_{e2}$ has been listed in the penultimate rows of Tables 7.8 and 7.9, from which it can be seen that this ratio has a relatively wide range of 0.03–2.64. To examine the effect of the choice of this ratio, and of the value of parameter $C_{e3}$, the sensitivity of the model has been tested by predicting the air and wall tem-

peratures with a range of parameter values, using case DC15 as a base case. The results of these calculations is shown in Figure 7.23. The results illustrate that increasing the ratio $C_{e1}/C_{e2}$ results in an approximately proportional increase in the air and surface temperatures $T_{R2}$ and $T_{W2}$ and, consequently the temperature gradient predicted in the occupied zone of the room. Increasing the value of parameter $C_{e3}$ results in an increase in the temperatures $T_{R3}$ and $T_{W3}$. The increase in $T_{R3}$ is notably non-linear. Increasing $C_{e3}$ from 3 to 6 has a much smaller effect on $T_{R3}$ than the increase from 0.1 to 1.0.

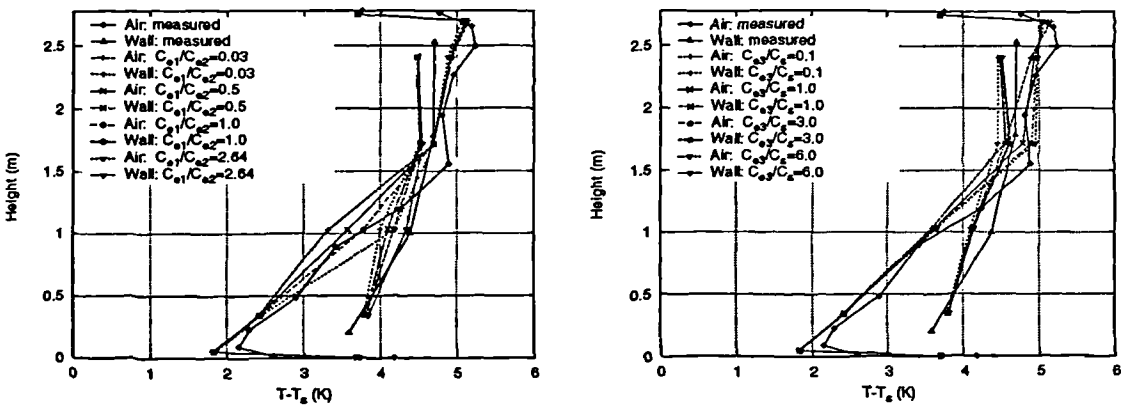


**Figure 7.23:** The response of the model to variations in the ratio of parameters $C_{e1}/C_{e2}$ (left), and in the value of parameter $C_{e3}$ (right). Case DC15 is used as a base case.

One notable result of varying the parameters $C_{e1}/C_{e2}$ and $C_{e3}$ is that there is only a very small change in the overall heat balance on the air. Also, as the temperature $T_{R3}$ is not expected to be used as an output of the model, finding a definitive mechanism to establish the value of $C_{e3}$ is not essential. The parameter ratio $C_{e1}/C_{e2}$ clearly has a strong bearing on the predicted temperature gradient in the occupied zone and the value of $T_{R2}$. The prediction of temperature $T_{R2}$ is of some importance, as it is representative of the temperature in the occupied part of the room. Unfortunately, the data collected and the parameter values calculated do not show how the parameter ratio $C_{e1}/C_{e2}$ can be readily established. For the purposes of testing the model further, and demonstrating how it could be used, this ratio has been set at 1.0.

To summarise, the rules found that can be used to establish each of the model parameters are shown in Table 7.12. It may be noted that the choice between forms A and B of the model is dependent on whether the load is positioned at low or high level respectively.

| *Parameter* | *Value* |
|---|---|
| $h_f$ | 2.1 W.m$^{-2}$.K$^{-1}$ (mean of calculated parameter values) |
| $h_c$ | 5.9 W.m$^{-2}$.K$^{-1}$ (mean of calculated parameter values) |
| $h_w$ | 3.0 W.m$^{-2}$.K$^{-1}$ (CIBSE Design Guide A) |
| $h_{wl}$ | $1.49(\Delta T)^{0.345}$ (Hatton and Awbi 1995) |
| $C_{fp}$ | $0.15C_s$ |
| $C_{e1}, C_{e2}$ | $C_{e1} + C_{e2} = C_s$ in general, and $C_{e1}/C_{e2} = 1$ |
| $C_{e3}$ | $0.1C_s$ for displacement ventilation cases |
| | $1.0C_s$ (or more) for high loads/chilled ceiling cases |

**Table 7.12:** Summary of the rules found for pre-determining the model parameters.

## 7.5 Testing of the Model

The nodal model has been tested in the following ways:

- by making comparisons between the air heat balance predicted with the generalised parameters and that predicted using the parameters calculated for that specific case and for an equivalent mixed ventilation system (This has been done using fixed outside surface temperatures);
- by making comparisons between the value predicted by the model with generalised parameters of temperature $T_{R2}$ and that predicted for a mixed system and the measured value;
- by making a qualitative study of the models response to design parameters such as supply air temperature, internal load, ceiling temperature, and supply air flow rate.

For the first of these tests, predictions have been made using parameter values given by the rules summarised in Table 7.12 for the cases previously listed in Table 7.4. Calculations have been made using the outside experimental surface temperature data as boundary conditions. The results are summarised in Table 7.13. The errors in the prediction of the overall heat transfer to the air, should be compared to those where the calculated parameters for each case have been used (see Table 7.4). The magnitude of the errors differ little from the calculations with the specifically calculated parameter values. In some cases the error is

slightly larger, in others slightly less. The predicted value of $Q_a$ is most different in case DC10. It is in this case that the generalised parameters differ most from the ones calculated from the experimental data.

| *Test Case* | *Total Load* (W) | *Measured* $Q_a$ (W) | *Predicted* $Q_a$ (W) | *Mixed System* $Q_a$ (W) | *Error* (%) |
|---|---|---|---|---|---|
| DV8 | 200 | 58.5 | 70.8 | 51.6 | 21.0 |
| DV12 | 400 | 212.8 | 229.5 | 196.3 | 7.8 |
| DC10 | 1200 | 248.9 | 193.1 | 198.8 | -22.4 |
| DC11 | 800 | 164.7 | 142.1 | 141.2 | -13.7 |
| DC14 | 600 | 162.4 | 139.1 | 140.3 | -14.3 |
| DC15 | 600 | 242.2 | 235.3 | 222.1 | -2.8 |

**Table 7.13:** Heat transfer to the room air predicted by the nodal model using the generalised parameter values. Values from an equivalent fully mixed air distribution system are also listed. Error is defined as $100 \times (Q_{a(meas.)} - Q_{a(pred.)})/Q_{a(meas.)}$.

Air heat balances have also been calculated from a model of the room with a fully mixed air distribution system and listed in Table 7.13. In these cases, the same load and radiant heat transfer model have been used. Air was introduced at the same temperature and flow rate as in the displacement ventilation and chilled ceiling model. The same external boundary conditions have been used. In the displacement ventilation cases DV8 and DV12 the results of the two types of model are rather different. In the case of the displacement ventilation and chilled ceiling test cases the results are very similar. This suggests that there my be little difference in heat transfer to the air stream when using either a conventional or mixed, or displacement ventilation system, with a chilled ceiling.

Another factor of interest in considering the relative performance of mixed and displacement ventilation systems, is the relationship between the supply temperature and the room comfort temperature. The occupied zone air temperature in a mixed ventilation system can be expected to be the same as the extract temperature. In the case of displacement ventilation systems the air temperature at 1.1 m is representative of that in the occupied zone. In the model here this is very close to the temperature $T_{R2}$. Predictions of these temperatures, using the generalised parameters in the model, have been listed in Table 7.14. In most cases the predicted temperatures $T_{R2}$ are reasonably close to that measured. In case DC10 the prediction is poor, as was the prediction of the air heat balance, for the

reasons noted above.

| *Test Case* | *Measured* $T_{R2}$ (°C) | *Predicted* $T_{R2}$ (°C) | *Mixed System* $T_{R2}$ (°C) |
|---|---|---|---|
| DV8 | 22.10 | 22.50 | 22.78 |
| DV12 | 21.37 | 21.59 | 22.59 |
| DC10 | 24.33 | 22.81 | 23.56 |
| DC11 | 21.85 | 21.93 | 20.57 |
| DC14 | 18.28 | 17.76 | 18.58 |
| DC15 | 19.08 | 19.00 | 20.01 |

**Table 7.14:** Comparisons of the measured and predicted room air temperature $T_{R2}$, along with values for the equivalent mixed air distribution system.

To test the ability of the model to reproduce some of the characteristics of displacement ventilation and chilled ceiling systems a hypothetical test zone has been used. This zone was of the same geometry as the Loughborough test chamber but all the walls were given conductance of $0.3\,W.m^{-2}.K^{-1}$. A base test case was devised in which the outside temperatures were 25°C, the ceiling temperature was 20°C, the air supply temperature was 19°C and flow rate equivalent to $3.0\,ac.h^{-1}$. The load was set at 600 W for the base case. A single parameter was varied in turn about the value in the base case. The response of the model to changes in air flow rate, ceiling temperature, air supply temperature and load have been calculated in this way. The results are shown in Figure 7.24.

Although these parametric tests do not enable any quantitative comparisons with the experimental data, they illustrate the way in which the model responds qualitatively. From the results shown in Figure 7.24 the following characteristics can be seen.

- As the supply air temperature is increased and approaches the external temperature the heat transferred to the air stream reduces.
- As the ceiling temperature is reduced, so the proportion of the load transferred to the air stream reduces and the comfort temperature becomes closer to the supply air temperature.
- As the air flow rate is increased, so the air temperatures become closer to that of the air supply.

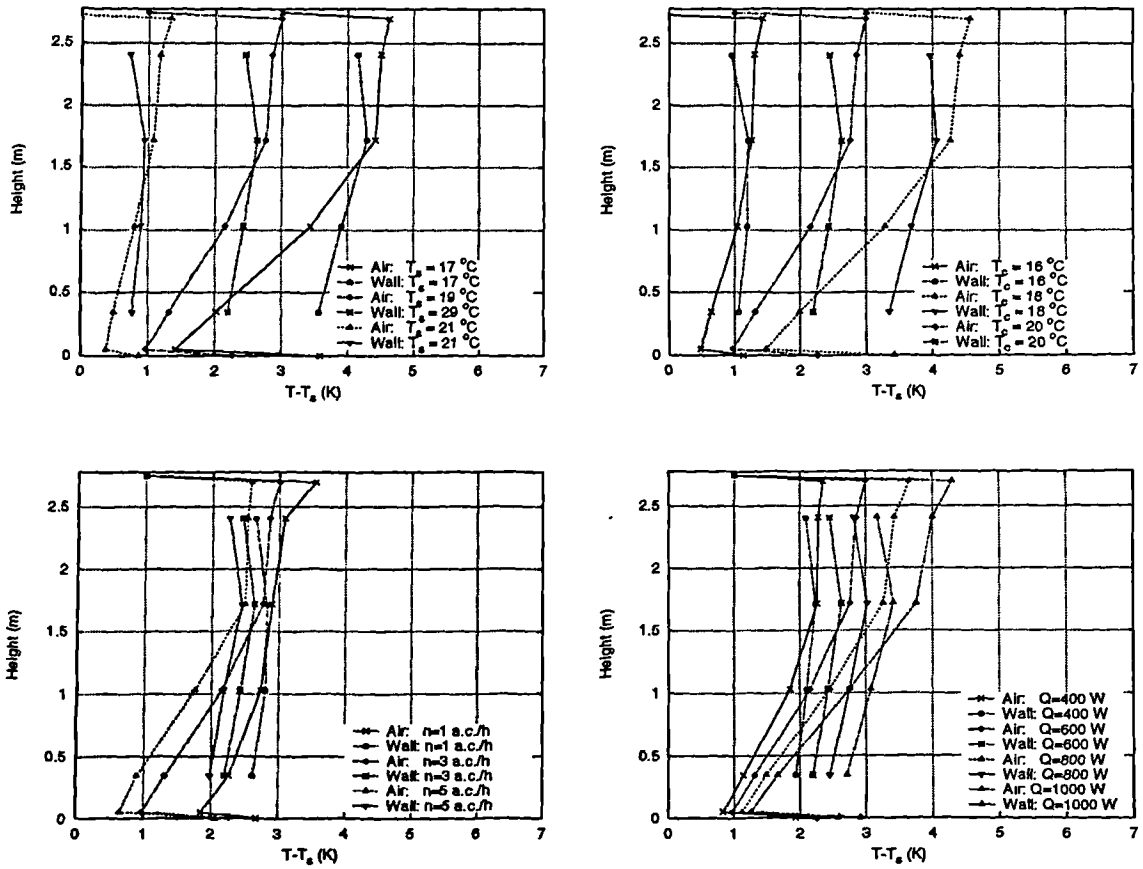


Figure 7.24: The response of a hypothetical model zone to changes in the design parameters. The parameters varied are supply air temperature (top left), ceiling temperature (top right), supply flow rate (bottom left) and load (bottom right).

- As the internal load is increased, so the heat transferred to the air stream increases.

## 7.6 Conclusions

A nodal model has been developed to represent room heat transfer in displacement ventilation and chilled ceiling systems. A single air flow network has been found sufficient to enable both displacement ventilation systems, and systems with chilled ceilings to be represented. The following conclusions concerning the structure, parameters and performance of the model can be made.

1. The structure of the model includes air nodes representing different regions of the room air and air flowing in the plume(s). This is divided into four horizontal zones. This structure allows the air and surface temperature gradients to be calculated. The outputs of the model are the heat balances on the air, ceiling and the conducted fluxes. Any of the node air temperatures may form an output of the model, but the air temperature in the occupied zone at node R2 is of most interest.

2. By separately representing the air movement in the plume(s) and the rest of the room, the model is able to correctly represent the relationship between the internal load and the air and surface temperatures found in the occupied part of the room. The performance in this respect is better than that of the simpler 'plug flow' models.

3. It has been shown that the bulk air flows represented by the air flow network in the nodal model are similar to those found in the numerical results. It seems of particular importance to represent the effects of recirculation in the upper part of the room.

4. A method has been demonstrated whereby capacity rate parameter values can be calculated by solving the heat and mass balance equations of the nodal model using the experimental temperatures as inputs. The parameters calculated in this way were used to correctly reproduce the air temperature measurements using fixed surface temperature boundary conditions in the model. When using external surface temperatures as boundary conditions and calculating the conducted fluxes, error in calculating the air heat balance was introduced. This is due mostly to the uncertainties in the experimental measurements and wall conductances.

5. It is possible to define convection coefficient parameters for the model using a combination of published correlations and calculated parameter values. Although there is some uncertainty in the calculated convection coefficients, the values fall within the expected range.

6. Analysis of the calculated capacity rate parameters has enabled some rules to be defined to enable their value to be pre-determined. Further work is required to better define the ratio of the parameters $C_{e1}/C_{e2}$.

7. It has been possible to make reasonable predictions of the room air temperatures and heat balances using the generalised parameter values. There was very little difference between the results obtained with the specifically

calculated parameters and those obtained with the generalised parameter values.

8. Preliminary comparisons of the nodal models ability to predict the heat balance on the air stream and the room air temperatures in the occupied zone, compared to predictions for a fully mixed system, indicate over-prediction in some cases, and under prediction in others. Where the conducted fluxes are less significant the agreement with measured values is good.

9. The model has been shown able to reproduce the expected performance characteristics in response to changes in the design parameters.

# Chapter 8

# Conclusions

## 8.1 Conclusions

The overall aim of this work has been to develop a thermal model of displacement ventilation and chilled ceiling systems suitable for use in building system simulation. The approach to this task has been to study the thermal characteristics of such systems, both experimentally and by making numerical calculations of the air flow and heat transfer under different operating conditions. This information has been used in the development of the nodal model, both to devise a suitable intra-zone air flow network and to find the model parameter values. A number of the experimental and numerical findings have also been of interest in themselves.

Test chamber experiments have been conducted with a displacement ventilation and chilled ceiling system operating under a range of conditions. Comprehensive air and surface temperature measurements have been made as well as a limited number of air speed measurements. The significant findings of the experimental work can be summarised as follows.

1. In displacement ventilation, with and without a chilled ceiling, the air supply is heated as it flows over the floor surface. In the absence of significant conductive heat flow this convective flux is balanced at the floor by long wave radiation from the ceiling and the heat sources in the room. In the case of displacement ventilation and chilled ceiling systems, this heating effect is reduced at lower ceiling temperatures. In these cases, the radiation

from the load appears more significant and it was found that even at low ceiling temperatures the supply flow was still heated by the floor.

2. The variation of temperature with height in the lower part of the room was found to be nearly linear, with and without a chilled ceiling. It is most likely that the air in this part of the room is heated by convective fluxes at the walls. When non-dimensionalised temperature profiles were considered, it was found that this temperature gradient was constant at a given supply flow rate and different internal loads.

3. The characteristics of displacement ventilation and chilled ceiling systems were found to be rather different to those of pure displacement ventilation systems in the upper part of the room. At higher loads, and where the chilled ceiling temperatures were lower, there was evidence of greater mixing of the air in the upper part of the room. It was found that the extent of mixing increased with the number of heat sources as well as the load size. This suggests that it is the total flow in by the plumes, and not just the convective load, that determines the extent of mixing.

4. Higher total convective loads are associated with the use of chilled ceilings. Previous data (Külpmann 1993) has shown that chilled ceiling systems produce lower temperature gradients in the upper part of the room. This has brought concerns regarding poorer air quality in the case of displacement ventilation combined with chilled ceilings. A wide range of loads and ceiling temperatures has been tested. Experiments with higher loads and different ceiling temperatures suggest that it is the total flow in the plumes, determined by the number of heat sources as well as the convective power, that has the most significant effect in increasing the degree of recirculation. The presence of the cold ceiling surface has a secondary effect in reducing the temperature gradient and inducing recirculation.

5. In the displacement ventilation and chilled ceiling experiments, the temperature profile showed a change in gradient at a consistent height of 1.2 m. This is the height of the base of the plumes (the top of the heat sources) and suggests that plume flow was large enough, in relation to supply flow, for air to be recirculated to near the base of the plumes in nearly all cases.

Numerical calculations have been made using a steady state method to calculate conjugate heat transfer in the case of the displacement ventilation test chamber experiments carried out by Li *et al.* and as part of this work. A fully transient

calculation method has been used in the calculation of flow and heat transfer of the displacement ventilation and chilled ceiling experiments, where fixed surface temperature boundary conditions have been used. The principal conclusions of these numerical calculations can be summarised as follows.

6. In all of the calculations the air flow pattern was found to be rather different in the lower part of the room. Below the heat sources and the top of the supply diffuser, the air movement is dominated by the flow from the supply diffuser, which moves in a boundary layer across the floor. In all the calculations, some form of counter-flowing stream moving over this boundary layer was predicted. These counter-flowing streams are either drawn into the bases of the plumes or entrained into the incoming flow near the top of the inlet. Where experimental measurements of air speeds in this region are available, good agreement with the calculations is found.

7. In the displacement ventilation cases, the flow in the upper part of the room is dominated by the plume. Recirculating flows in these cases were found to take the form of a thin wall jet flowing across the ceiling and boundary layers, diminishing in thickness, flowing down the walls. Under these conditions the flow surrounding the plume is of very low velocity, such that stable stratification of the flow is sustained.

8. It is possible to calculate the room heat transfer in the displacement ventilation cases using a conjugate heat transfer procedure in which the wall conductive fluxes were calculated explicitly, and balanced with the convective and radiant fluxes at the internal surfaces of the room. Using this procedure, it was possible to take account of the heat lost from the room by conduction. Errors in the predicted heat balance on the room air can be attributed to uncertainties in the boundary conditions as well as the predictions of the convective fluxes. In each case, the importance of taking into consideration the coupling of the flow and the surface radiation was demonstrated.

9. A rather different situation was shown to exist in the flow in the upper part of the room in the displacement ventilation and chilled ceiling cases. In these cases, the convective loads were higher (a maximum of 71 $W.m^{-2}$) and four heat sources were modeled. A fully transient calculation procedure was necessary and predicted periodic fluctuations in the flow. These fluctuations consisted mainly of lateral motion of the plumes.

10. Analysis of the motion of the plumes showed a complex interaction between the plumes and the surrounding recirculating flows. A high degree of mixing of the air was indicated, and these recirculating flows were large enough to induce some swirling motion in the plumes. The predicted time averaged air speeds showed good agreement with the experimentally measured air speeds.

11. The numerical calculations predicted steady periodic oscillations in the plume velocities and in the room air temperatures. The amplitude of these oscillations was predicted to be largest near the ceiling. Analysis of the experimental temperature data showed oscillations of a similar nature. These transient fluctuations in the experimental data could not have been expected without the insight given by the numerical calculations.

It has been possible to use the experimental measurements of temperatures and heat fluxes and make use of some insight into the bulk airflow patterns from the numerical results in the development of the nodal model of the system. The model consists of a network of ten air nodes, together with surfaces nodes on the floor, ceiling and walls. The room is divided into four horizontal zones, with room air and wall surface nodes at each level to allow temperature gradients to be represented. The air nodes are connected in a network that separately represents the bulk air flow in the plume(s) and the surrounding recirculating flow. The significant conclusions regarding the nodal model can be summarised as follows.

12. It was found necessary to represent the room air and the plume (or aggregate of the plumes) separately in order to correctly predict the room air temperatures and wall surface temperatures in the lower part of the room. Simpler flow networks, with all the air nodes in series, were not able to reproduce the correct wall surface temperatures or model the coupling of the load to the room air in a realistic way. It was also found necessary to treat recirculation of air in the air flow network. The air flow network of the nodal model has air flow paths that are similar to those predicted by the numerical calculations.

13. A method has been demonstrated whereby capacity rate parameter values can be calculated by solving the heat and mass balance equations of the nodal model using the measured temperatures as inputs. By analysing the capacity rate parameters calculated in this way, a number of rules by which these parameters can be pre-determined were found. Convection coefficient

parameters for the model were defined by using a combination of the calculated values and published correlations.

14. The nodal model has been implemented in the LIGHTS program to operate in a steady state mode. The model was tested with two types of boundary conditions. With fixed inside surface temperature boundary conditions, the model was able to reproduce the correct relationship between the air and surface temperatures. With external surface temperature boundary conditions, some error was introduced into the prediction of the air heat balance and room temperatures. This error can be attributed to the uncertainties in the boundary conditions and the value of the wall conductances.

15. Using the generalised parameters it was possible to make reasonable predictions of the room temperatures and to demonstrate that the model reproduces the correct characteristics in response to changes in the system design parameters

The intra-zone air flow has a significant impact on the room heat transfer in displacement ventilation and chilled ceiling systems. The approach used in this work to arrive at a workable air flow network for a nodal model, and to arrive at the capacity rate parameters, could conceivably be used to develop models of other systems where the intra- zone air flow is important.

## 8.2 Recommendations for Further Work

The development of the nodal model has reached a stage where it can be readily used for building system simulation. However, it is acknowledged that the model could benefit from further work, firstly, to establish more generally applicable correlations for some of the parameters, and secondly, to make the model applicable to a wider range of operating conditions. In particular, it would be beneficial to gather further experimental data under a wider range of operating conditions. Determination of further sets of capacity rate parameters should enable the effect of the parameter ratio $C_{e1}/C_{e2}$ to be better understood and correlated more effectively with the usual design parameters.

The experiments conducted in this work used only one type of heat source. These heat sources were intended to be representative of a combination of office equipment and occupants. Some effect of the height of the heat sources was noted in

the experiments, and so it would be useful to investigate the effect heat source geometry on the temperature profiles. The different proportions of radiant and convective output could also be usefully investigated.

The experiments and numerical models used to date have not treated the thermal effect of artificial lighting. To evaluate the effect of such loads, further experiments with different types of artificial lighting would be beneficial. In particular, it would be of interest to study how the gains produced by such lighting were absorbed by the ceiling and air streams, and whether convective gains from lighting at high level had any effect on room air temperature profiles. Similarly, it would be interesting to investigate the effects of solar gains in rooms with displacement ventilation and chilled ceilings and to see how the absorption of such gains was different from all-air type systems—for example, the effect of sun patches

Surprisingly little published information was found relating to the convective heat transfer conditions at the floor and ceiling. At the ceiling of rooms with displacement ventilation and chilled ceilings, convective fluxes are expected to be enhanced (compared to other surfaces in the room) due to the action of the plumes impinging on the ceiling surface. Several workers have considered convective heat transfer conditions where both single and arrays of jets impinge on flat surfaces, but not the case of plumes. Jet impingement is of considerable interest to the aerospace industry and this has obviously spurred research in this area. As plume impingement is also of relevance to natural ventilation conditions, perhaps a fundamental study of this phenomena is overdue. A number of interesting experimental techniques have been developed in studying jet impingement, such as the use of thermal imaging and liquid crystal substrates to measure surface temperatures at the point of impingement, and it may be possible to adapt some of these techniques to study plume impingement.

Similarly, there is a need for study of convective heat transfer conditions in situations similar to that occurring at the floor of rooms with displacement ventilation. The flow in these situations has been identified as similar to that of a gravity current. In these circumstances, the boundary layer does not grow in thickness, as entrainment is severely inhibited by buoyancy forces. As the convective heat transfer at the floor has such a significant effect on the thermal environment in the occupied zone of rooms with displacement ventilation, it seems worthwhile to make further study of such phenomena. It is also conceivable that such conditions could be usefully studied by numerical models that allow detailed representation of conditions at wall surfaces—such as with a low Reynolds number $k$–$\varepsilon$ turbulence

model.

Numerical models have been used successfully in this work to give some insight into the unsteady nature of the flow in rooms with displacement ventilation and chilled ceilings. As such transient calculations are computationally expensive to perform, it has only been possible to study two test cases. The calculations for these two test cases have shown that the period of the fluctuations reduces with increasing convective power of the load. In order to understand better the nature of these fluctuations it would be useful to make further transient calculations under a wider range of load conditions.

In the work reported here, a method of calculating the conjugate heat transfer in rooms with displacement ventilation has been demonstrated. Although the accuracy of the calculations was diminished by the uncertainties in the boundary temperatures and conductance data, the numerical method offers an effective way of predicting conditions in rooms with this type of system with realistic boundary conditions. It is also acknowledged that there is some uncertainty about the ability of the wall function treatment to accurately predict convective heat fluxes. One approach to improve the prediction of these fluxes would have been to adopt a low Reynolds number form of $k$–$\varepsilon$ turbulence model. This would, however, involve considerable computational cost due to the much denser grid and slower convergence rate. An alternative approach would have been to use alternative wall functions that are more applicable to the mixed convection conditions found in these flows. One possibility would be to use the set of wall functions developed by Yaun and Moser (Yuan et al. 1993, Yuan 1995) which are applicable to natural convection conditions with room size vertical surfaces. Some progress was made in implementing these wall functions but time did not allow this work to be completed.

It was originally intended that numerical data, produced by making conjugate heat transfer calculations with different boundary conditions, be used in the derivation of the nodal model parameters. Such calculations might be made to study the effect of different room geometry and a wider range of external conditions. Although time has not allowed such calculations to be performed, it is clear that this could be done in a straight forward manner. In order to use such data, surface temperatures equivalent to the surface node temperatures in the model would be derived by taking area weighted averages of the cell surface temperatures in the numerical model over the appropriate portions of the room internal surfaces. Air temperature profile data would be gathered by taking the air temperatures

predicted numerically at a position in the room equivalent to that used in the experiments. This air temperature data would then be interpolated to find temperatures equivalent to that of the room air nodes in the model. This set of node temperatures would then be used, in the same way as the experimental data, to find a set of nodal model parameters by solution of the nodal heat and mass balance equations.

The motivation for and original purpose of, developing a simplified model of displacement ventilation and chilled ceiling systems was to enable annual building system simulation of such systems. The model has been developed to such a stage that this can be attempted. The logical path to implement the model in a simulation environment would be to use the version of the LIGHTS program adapted for use with HVACSIM+ (Sowell 1991, Clark and May 1985). This form of LIGHTS could also be easily adapted for use in with TRNSYS (Klein et al. 1976). In the longer term it would be desirable to implement the model in a code more suited to annual energy simulation such as ENERGY+. A prototype system simulation has already been tested within HVACSIM+ using an earlier development of the nodal model. Details of this prototype simulation, where the room model was coupled to

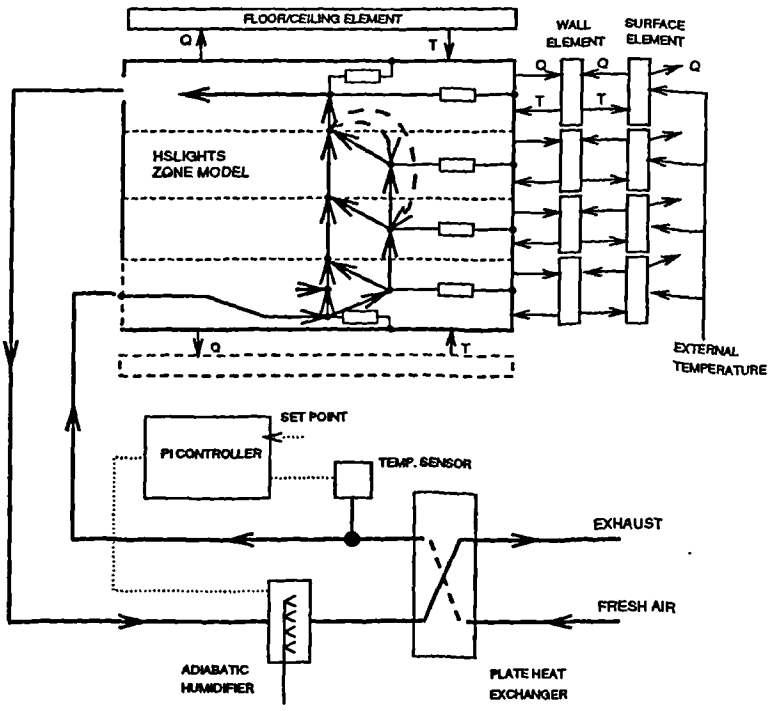


**Figure 8.1:** Configuration of the nodal model and a prototype evaporative cooling system implemented in the HVACSIM+ simulation environment. Published previously in Rees and Haves (1995).

the room model was coupled to a simple indirect evaporative cooling system, are given in Rees and Haves (1995). In this simulation the nodal model was coupled to separate models of the room walls, ceiling and floor, which were in turn coupled to separate model elements representing the wall outer surfaces. The arrangement of the model and the other elements of this simulation are shown in Figure 8.1.

There is considerable scope for study of systems using displacement ventilation and chilled ceilings through carrying out annual building simulation. Displacement ventilation and chilled ceiling systems have the thermodynamic advantage of being able to use higher supply air and chilled water temperatures than conventional systems—typically 14°C instead of 6°C for chilled water and 20°C instead of 14°C for the air supply. There is consequently much greater potential for making use of heat sinks with correspondingly higher temperatures. This also makes it possible for such systems to work in conjunction with other low energy technologies. Such technologies include evaporative cooling (on the air and water side), desiccant cooling, absorption chilling plant and ground coupled air cooling. Models of elements of these other types of low energy system have been developed by other participants in Annex 28 of the International Energy Agency and could be used to develop simulations of a number of these systems.

# Appendix A

# Instrument Calibration and Testing

## A.1 Calibration of the Interface Cards

The process of calibrating the temperature and heat flux measurement system was carried out in several stages. All signals from the thermocouples and heat flux meters pass through the signal processing/multiplexing and A/D interface cards and so the performance of the measurement system is strongly dependent on the performance of these components. The first stage in the calibration of the system was to check and calibrate these components using the elementary calibration procedures suggested by the card manufacturers before connecting any thermocouples.

The DAS-08 Analogue-to-Digital interface card used here has a fixed gain and a nominal input range of $\pm 5$ V. Potentiometers are provided on the card for periodic calibration through minor adjustments to the gain and offset. Full scale digital output for the card is 4095 so that an input of $-5$ V should correspond to 0 digital output, and 0 V should correspond to 2047.5 (2047/2048). This was checked and adjusted using a precision DC voltage source and a digital voltmeter while monitoring the digital output through software. It was found that the zero voltage reading was repeatable to within 2/3 bits (each bit is equivalent to 0.07 K in the final system). It was also found that the calibration of the A/D card was dependent on the actual computer used. This was probably due to variations in the

| *Card* | *Channels* | *A-to-D channel* | *Nominal Gain* | *Measured Gain* |
|---|---|---|---|---|
| card A | 0–15 | 0 | 800 | 816 |
| | 16–31 | 1 | 800 | 824 |
| card B | 0–15 | 2 | 800 | 814 |
| | 16–31 | 3 | 800 | 815 |
| card C | 0–15 | 4 | 800 | 818 |
| | 16–31 | 5 | 800 | 812 |

**Table A.1:** Measured gains of the signal processing/multiplexer interface cards.

computer's internal power supply voltage, which is used in generating the reference voltage in the card. The same computer was used throughout the calibration and experimental procedures.

Each of the signal processing/multiplexing interface cards is divided into groups of 16 input channels with a single multiplexing chip and amplifier serving each group. The gain of this amplifier can be pre-set through D.I.P switches but there is no means of trimming the gain. There is however, a potentiometer for adjustment of offset. The offset was adjusted by linking out the terminal in the first channel of each group and monitoring the digital output read through the A/D card. The gain of each group of 16 channels was measured by applying $\pm 6.0\,\mathrm{mV}$ (full scale should have been $\pm 6.25\,\mathrm{mV}$) to the first channel of each group and monitoring the output range. The gain of each group was found to be high, with some variation from group to group, as can be seen in Table A.1. This variation in gain was compensated for by using the measured values (rather than the nominal 800) in the configuration file used by the library software during the cold junction compensation procedure.

The thermistor used to measure the cold junction temperature on each card has a nominal output of $24.4\,\mathrm{mV.K^{-1}}$ and so its signal is therefore large enough to be passed through to the A/D card on its own channel without further amplification. The gain applied to this measurement is therefore only dependent on the adjustment of the gain on the A/D card. The offset on this measurement can, however, be further adjusted on the signal processing/multiplexer card. The suggested method of doing this is to convert the output to a voltage and then temperature (using the above conversion factor) while measuring the air temperature next to

the thermistor with a thermometer and adjust the offset until the readings are in agreement. This procedure was followed and the initial readings found to be offset by ~1.5 K. With the thermistor channel adjusted and thermocouple input channels linked out (i.e. simulating zero temperature difference between hot and cold thermocouple junctions) one would expect that the thermocouple temperature measurement taken using the cold junction compensation procedure would be the same as the thermocouple temperature. This was found not to be the case. This could be for a number of reasons.

i) Non-linearity in the temperature/resistance characteristic of the thermistor;

ii) inadequacy of the voltage-to-temperature conversion made in the library software;

iii) offset introduced artificially by current flowing through the shorted input terminals.

It was also found that the readings from adjacent channels within each group of 16 varied by an unacceptable amount. The conclusion of these initial tests was that it would be necessary to individually calibrate thermocouple/input channel combinations in order to approach the required accuracy.

## A.2 Initial Calibration of the Thermocouples

Calibration corrections to the raw thermocouple data have been applied using a linear correlation between the raw data and temperature for each thermocouple/input channel combination. The temperature-voltage characteristic of the type T thermocouple is known to be non-linear over its full working range of -300–800°C however, the temperature range used here of 10–30°C is small enough that a linear approximation should give acceptably accurate results. The method initially used to derive the coefficients of the linear equations used for the correlation was to take readings from the thermocouples immersed in a water bath at two known temperatures. The cold junction compensation method was used in deriving these thermocouple temperatures.

This process was carried out for groups of eight surface thermocouples at a time. Each group was immersed (inside a plastic bag) in a constant temperature bath

which incorporated an electric stirrer. The water bath was then operated at ~12°C and then at ~ 30°C after being left to stabilise at each stage. Measurements of the water bath temperature were made with a mercury in glass thermometer (0.2°C sub-divided scale). Thermocouple readings averaged over 30 second intervals were logged and a set of readings at each temperature used to calculate the constants in the line equation $T = A.T_{in} + C$, where $T_{in}$ is the raw thermocouple reading. The same procedure was used for the room air thermocouples except that sixteen were processed at once.

The calibration coefficients derived by this method were checked by immediately applying the calibration correction to a further set of thermocouple readings taken at an intermediate tank temperature. The raw readings were found to vary by up to ±0.75 K. After applying the calibration corrections this was typically reduced to ±0.6 K. A notable finding was that the 'A' coefficients (i.e. the gains) varied by only a few percent above or below 1.0 from group to group. The 'C' coefficient (i.e. the offset) varied much more widely, even within each group of 16 channels using the same A/D channel. When the thermocouples were swapped randomly to other channels (within a group of 8) the spread in readings increased only slightly, from 0.09 K to 0.1 K. This suggests that there was more variability in the offset between input channels than there was in gain or between different thermocouples (of the same pattern at least). The calibration data derived using this procedure was used in the first series of experiments where the cold junction compensation method of measurement was employed.

## A.3 In-situ Calibration of the Thermocouples

The later series of experiments and the co-heating experiment were conducted using calibration data from measurements made with all the thermocouples and extension wires installed in the test chamber. The objective in carrying out the calibration in this way was to make all the thermocouple measurements at the same time and thus when the signal processing/multiplexing cards were exposed to steady thermal conditions. (The reasons why this proved to be necessary are discussed in Section A.6.1). It was also undesirable and impractical to remove the surface thermocouples to a water bath for re-calibration once they had been installed.

Using this method it was still possible to control the temperature of all the air

temperature thermocouples using the water bath after temporarily removing them from their stands (but still using the complete extension leads). The surface temperature thermocouples were calibrated by making independent measurements of surface temperature at each thermocouple site. These measurements were taken with a hand held digital thermometer using a type 'K' thermocouple surface probe and a second thermocouple in an ice bath as a reference. (This combination of thermocouples and digital thermometer was previously calibrated against the mercury/glass thermometer used in the water bath.)

The procedure for collecting the data involved recording all thermocouple temperatures at 30 second intervals. The air thermocouples in the water bath were kept at a constant temperature during the calibration procedure. Measurements were made at each surface thermocouple site in turn using the digital thermometer and surface probe. Each measurement was made over a 30 second interval and the elapsed time at which each measurement was made recorded. This procedure took approximately one hour to complete. The water bath temperature was checked at the end. Measurements could then be compared from the hand held instrument

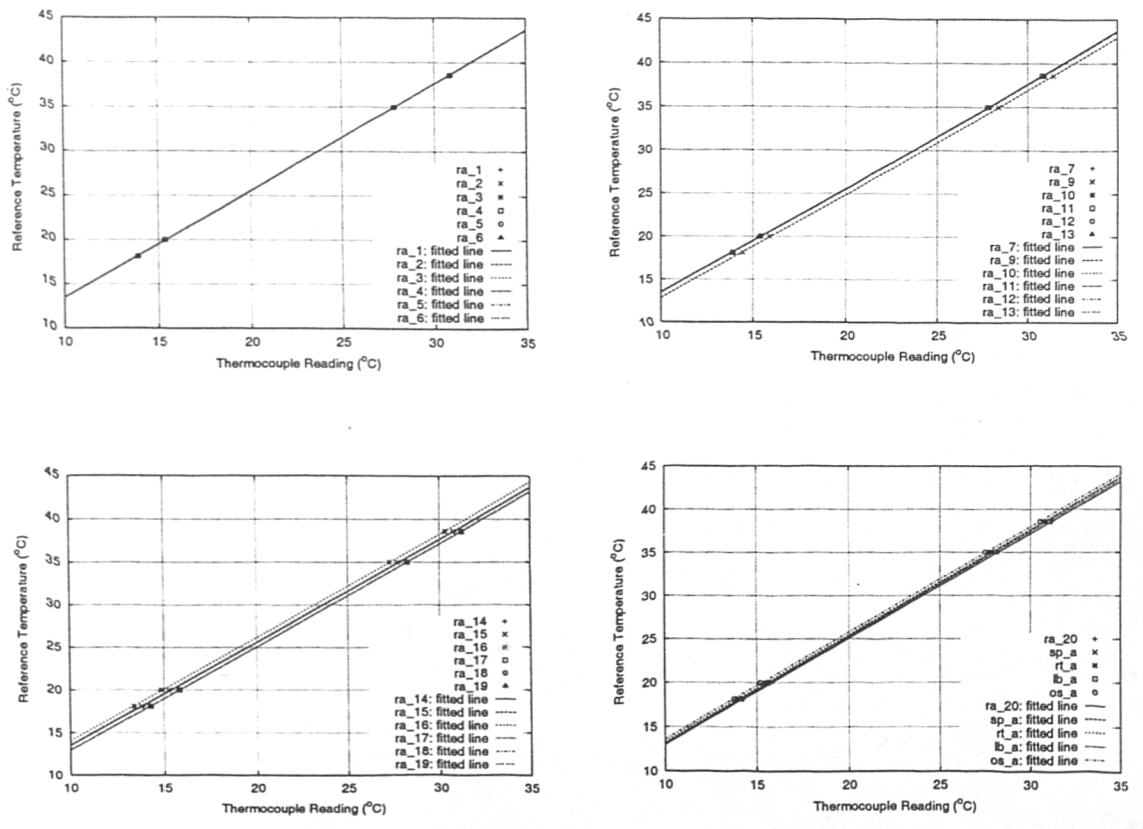


**Figure A.1:** Air thermocouple calibration data and the corresponding fitted straight lines used with the ice point system.

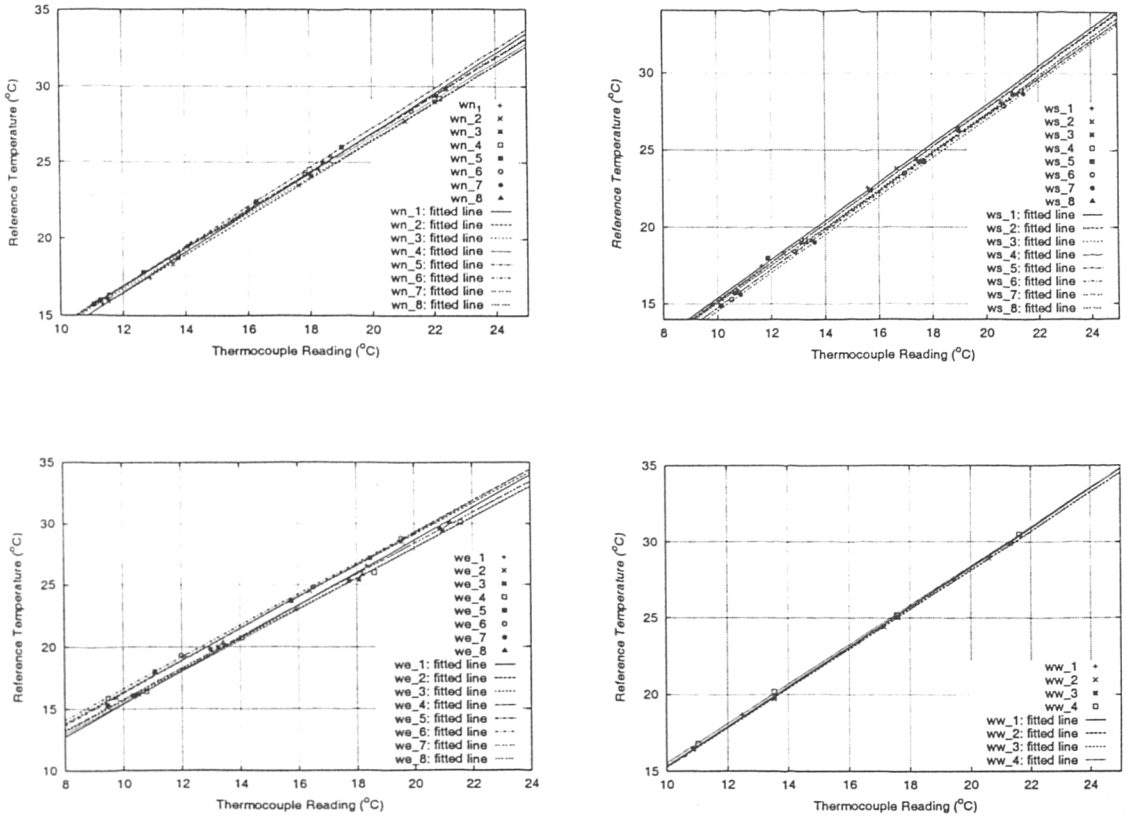


**Figure A.2:** Surface thermocouple calibration data and the corresponding fitted straight lines used with the ice point system.

with the thermocouple reading from the data logger file taken at the same time. This in-situ calibration procedure was firstly used to improve the relative accuracy in the second series of experiments where cold junction compensation was used.

Calibration measurements for the ice point based system were also made using this in-situ calibration procedure taking four sets of measurements in the test chamber over the 10–30°C range. Calibration corrections were derived from this data by applying a least-squares fit of a straight line. A graph showing the calibration data and the fitted straight lines for the air temperature thermocouples is shown in Figure A.1 and for the surface temperature thermocouples in Figure A.2.

## A.4 Calibration of the Heat Flux Meters

The heat flux meters were both calibrated by the manufacturer to have an output of $49.0\mu V.W^{-1}.m^2$. The heat flux meter measurements have been calibrated

by using the manufacturers calibration data and by making electrical calibration measurements for each input channel used, and deriving a linear calibration correction for each. The channels of the signal processing/multiplexing channels have a full scale of ±6.25 mV which gives a resolution of 0.15W.m$^{-2}$ per bit.

A precision DC voltage source was used to apply ±6.0 mV to each channel and a voltage measurement recorded to file. The gain and offset corrections could then be calculated from each pair of measurements. These calibration measurements were made at the start of the second series of experiments and again at the very end of the experimental work—some three months apart. The calibration data from these two dates is shown in Table A.2. Over this period the gain has drifted down slightly and the offset drifted up by similar amounts for both channels. The later set of calibration figures have been used for the heat flux measurements reported here as the measurements were taken much closer to the later date than the first.

## A.5 Calibration of the Air Speed Measurement System

Each sensor of the Dantec 54N10 system had been calibrated by the manufacturer in a low velocity wind tunnel. The calibration data is provided in the form of a velocity reading error at a high and low calibration velocity. This data was used to post-correct the air speed measurements using a linear calibration correction for each sensor. The general accuracy of the air speed sensors is quoted as ±0.01 m.s$^{-1}$ ±5% in the 0.05–1.0 m.s$^{-1}$ range used here. The temperature sensors

| *Flux Meter* | *Time* | *Gain Coefficient* | *Offset Coefficient* |
|---|---|---|---|
| A | start | 1.236 | -0.013 |
| | finish | 1.230 | 0.0 |
| B | start | 1.236 | 0.021 |
| | finish | 1.232 | 0.033 |

**Table A.2:** Measured gain and offset corrections for the signal processing/multiplexer channels used for the heat flux meters.

of the system have a quoted accuracy of only ±0.5 K (and are less accurate at very low velocities) and so were not used as a primary source of temperature data.

## A.6 Testing of the Temperature Measurement System

A number of tests were made on the temperature measurement system before, during, and after the experimental measurements were made. The purpose of these tests was to check the correct operation of the measurement system and make an assessment of its accuracy. These tests and the results of the calibration process are reported and discussed in this section.

### A.6.1 Testing of The Cold Junction Compensation Based System

Following the first series of experiments the calibration of the thermocouples—made using groups of thermocouples in the water bath—was checked. This was done by cross checking measurements from the first group of air thermocouples with those from the remaining air thermocouples placed in the water bath together. This showed that the first group of thermocouples—that were originally calibrated together—gave measurements that were closely grouped together, but they were offset relative to other groups by up to approximately one degree (i.e. the different groups appeared to have drifted apart). This was true even for two groups using the same A/D card channel. This latter fact suggested that this was not just an electrical problem.

One explanation for this behaviour was that the cold junction compensation procedure using the thermistor mounted on the interface cards was not compensating properly for the changes in room temperature. If this was the case, it would mean that the calibration corrections would be dependent on the temperature that the interface cards were exposed to. To check this possibility, a number of simple tests were made with the air thermocouples in the water bath held at a stable temperature while changing the room temperature by several degrees over a number of hours. During the test the thermocouple readings (made using the cold junction correction procedure) were logged and the tank and room air temperatures moni-

tored using mercury/glass thermometers. The results of one of these tests is shown in figure A.3.

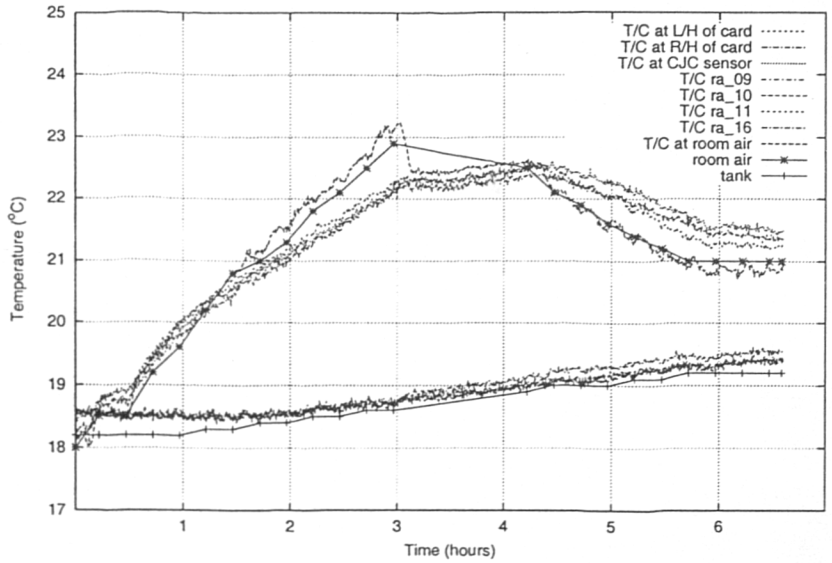


**Figure A.3:** Variation of thermocouple readings with lab temperature using the cold junction compensation method.

The graph shows that as room temperature rises, measurements from the thermocouples in the water bath fall relative to the thermometer readings by up to 0.4 K. The thermocouple readings do however, appear to move to the same degree with a similar offset on each channel. Some dynamic effects can also be seen. Firstly, readings from the thermocouple in the enclosure next to the thermistor can be seen to lag behind the thermometer readings of air temperature. This is particularly evident when the room temperature begins to fall and a greater temperature differential appears over the length of the card.

The reasons for this failure of the cold junction compensation procedure may have been some combination of, a) sensitivity of the signal processing circuitry to temperature, b) non linear behaviour of the cold junction compensation thermistor (a linear characteristic is assumed in the library software), c) uneven temperature distribution along the interface card. The main implication of this problem was that the initial calibration data were inconsistent. The temperature of the room in which the calibration measurements were made varied by several degrees during the period in which the measurements were made so that effectively each group of thermocouples was calibrated to a different reference. Measurements of temperature *differences* are the main concern in these experiments and so comparisons between thermocouple measurements within the same calibration group are still

valid, but between different groups are not (for example differences between air measurements in one group and wall surface temperatures in another). As the temperatures of the room in which the calibration measurements were made were not recorded there was no means of back-correcting the data from the initial series of experiments.

This finding obviously reduces the usefulness of the data from the first series of experiments. In order to derive a useful consistent set of calibration data it would thus seem necessary to try and calibrate all the thermocouples at the same time. This was attempted by using the in-situ calibration procedure described in Section A.3 before carrying out the second series of experiments.

Earlier tests had showed that variations in the calibration of different input channels were mainly in the form of different amounts of offset. The initial calibration procedure should still have resulted in valid values for the correction to each channel/thermocouples gain. In view of this, the data from the in-situ calibration procedure were used only to establish a consistent set of figures for the offset on each channel. This was done using a single set of calibration measurements and comparing the measurements made with the initial calibration data and the in-situ independent measurements of surface and water bath temperature. The calibration corrections for offset were then modified accordingly. Following this procedure should have ensured that all the thermocouples were calibrated to the same reference.

Using the cold junction compensation system with the revised calibration data, the absolute measurement of temperature from the thermocouples will still drift slightly during any experiment, depending on the laboratory temperature, but all measurements will have drifted by a similar amount. Measurements of temperature differences will therefore still be valid—provided they are between measurements made at the same time. The dynamic effects due to changes in room temperature are thought to have been minimised in the test chamber experiments as the lab temperature (although not controlled) changed at a very slow rate—no more than a few tenths of a degree per hour.

### A.6.2 The Ice Point based System

In view of the problems found with using the cold junction compensation method of taking thermocouples measurements, it was thought that greater accuracy might be obtained by using the ice point method. This was done for the final series of experiments and the co-heating experiment. In the co-heating experiment, it was potentially necessary to use differences between temperature measurements taken at significantly different times (because of the long phase lag between inside and outside heat fluxes at heavyweight walls) and this would require a measurement system with a stable calibration reference.

Further improvements were made to the signal processing/multiplexer card installation with a view to improving the stability and homogeneity of the thermal environment around the cards. The measures taken were:

- The power supply unit (being a source of heat) was removed from the desktop enclosure.
- A low voltage fan was added to the desktop enclosure in place of the power supply fan.
- The air flow through the wall mounted enclosure was improved.
- Insulation was added to the top of the desktop enclosure.
- Aluminium foil was fixed to the inside of each enclosure to equalise the long wave radiation distribution.

Calibration measurements for the ice point based system were made using the in-situ calibration procedure as noted in Section A.3. To check the accuracy and repeatability of the ice point based thermocouple measurement system a second set of calibration measurements were made approximately three weeks after the experiments had been completed. Data were collected at four temperatures for the air thermocouples submerged in the water bath and for the surface thermocouples on the north wall, using the in-situ calibration procedure described in Section A.3. A set of error data was generated by taking the difference between the temperature logged by the thermocouple system (i.e. as determined by the straight line fit to the original calibration data) and that recorded on the mercury in glass thermometer or surface probe and digital thermometer. This data were then used to calculate a

mean error and standard deviation for these air and surface thermocouple groups and is been shown in histogram form in Figure A.4.

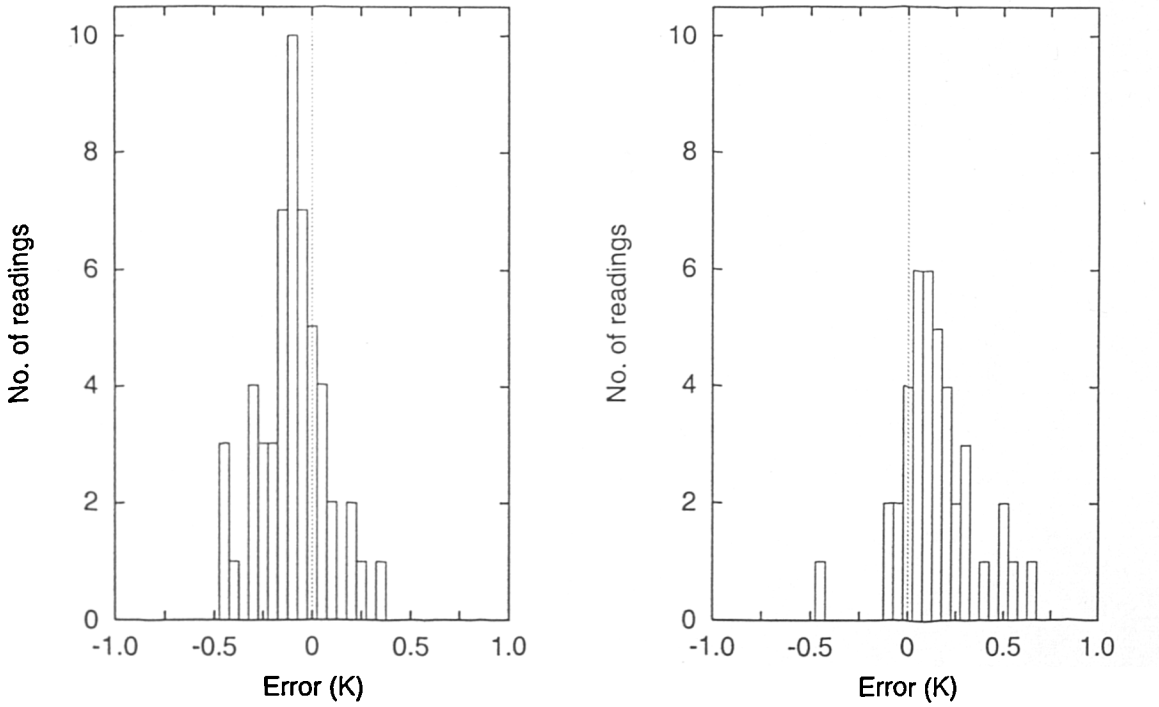


**Figure A.4:** Thermocouple repeatability test results in histogram form for air thermocouples (left) and surface thermocouples(right).

The average error recorded for the air thermocouples was -0.07 K with a standard deviation of 0.168 K. The average error recorded for the surface thermocouples was 0.122 K with a standard deviation of 0.197 K. The slightly poorer performance of the surface temperature thermocouples is probably a reflection of the poorer accuracy in the calibration of the surface thermocouples rather than poorer repeatability in the instrumentation itself. It seems from these tests that there is no particular drift in the measurements with time or room temperature as there was with the cold junction compensation system.

A number of overall errors are of relevance to the analysis of the experimental data. Firstly in the analysis of the air temperature profiles it is the relative error between air thermocouples that is of significance. It seems reasonable to take the typical error to be two standard deviations, $\pm$ 0.17 K in this case. Secondly, use is made of differences between the surface temperature measurements in calculating radiant and conducted heat fluxes. In this case the error may be typically two standard deviations of the surface thermocouple error, $\pm$ 0.2 K. Use is also made

of differences between surface and air thermocouples in calculating convective heat fluxes and convection coefficients. In this case the measurements may typically be offset by the sum of the mean errors, this error being either increased or decreased by the sum of the standard deviations, giving a maximum of 0.494 K and a minimum of -0.173 K, or ±0.33 K.

Quantifying the temperature measurement errors in the case of the cold junction compensation systems is more difficult. It could be expected that the standard deviation of thermocouples calibrated together would by only slightly worse than that of the ice point system. In the case of the initial calibration method (tests noted as CJC1) different groups of air and wall thermocouples would be offset due to the effects of varying room temperature at calibration. This effect was previous noted as being of order 0.4 K. In these cases the air-to-air temperature error is taken to be ±0.2 K (although the absolute error for air temperature must be more like ±0.4), the surface-to-surface temperature error to be ±0.5 K, and the surface-to-air temperature error to be ±0.5 K.

Where the cold junction compensation system was used along with the in-situ calibration procedure the relative errors were improved. In this case (tests noted as CJC2) the air-to-air temperature error is taken to be ±0.2 K, the surface-to-surface temperature error to be ±0.3 K, and the surface-to-air temperature error to be ±0.4 K. Here again the absolute error of the temperature measurements must be increased by approximately 0.4 K due to the drift evident in the cold junction compensation procedure. The errors in temperature measurement for the different measurement systems are summarised in Table A.3.

| *Measurement* | *Cold Junction Compensation 1* | *Cold Junction Compensation 2* | *Ice Point* |
|---|---|---|---|
| Air (Absolute) | ±0.4 | ±0.4 | ±0.17 |
| Air-to-air | ±0.2 | ±0.2 | ±0.17 |
| Surface-to-Surface | ±0.5 | ±0.3 | ±0.2 |
| Surface-to-air | ±0.5 | ±0.4 | ±0.33 |

**Table A.3:** Summary of the estimated thermocouple temperature measurement errors.

# References


Allard, F. and Inard, C. (1992). Natural and mixed convection in rooms:prediction of thermal stratification and heat transfer by zonal models., *Proc. of ASHRAE conf. Room Air Convection and Ventilation Effectiveness,Tokyo, Japan.*, pp. 335–342.

Appleby, P. (1988). A ceiling for cooling, *Building Services, The CIBSE Journal* **10**(7): 57–59.

Arai, Y., Togari, S. and Miura, K. (1994). Unsteady-state thermal analysis of a large space with vertical temperature distribution, *Transactions of the American Society of Heating Refrigeration and Air Conditioning Engineers.*

Baines, W. and Turner, J. (1969). Turbulent bouyant convection from a source in a confined region., *Journal of Fluid Mechanics* **37**: 51–80.

Baker, A. (1983). *Finite Element Computational Fluid Dynamics.*, Hemisphere.

Bakhmeteff, B. (1936). *The Mechanics of Turbulent Flow*, Princeton University Press.

Baughn, J. and Shimizu, S. (1989). Heat transfer measurements from a surface with uniform heat flux and an impinging jet., *ASME journal of Heat Transfer* **111**: 1096–1098.

Behne, M. (1993). The influence of the arrangement of cooling ceilings on thermal comfort, *Proc. of 'Indoor Air '93', Helsinki, Finland.*, Vol. 5, pp. 413–418.

Bergstrom, D., Stubley, G. and Strong, A. (1993). Numerical prediction of countergradient thermal transport in a turbulent plume, *ASHRAE Transactions* **99**(1): 422–429.

BLAST (1986). *BLAST (Building Loads and System Thermodynamics)*, BLAST Support Office, University of Illinois at Urbana-Champaign.

Bream, N. and Slatte, J. (1992). Displacement ventilation in industry – a design principle for improved air quality, *Buildings and Environment* **27**(4): 447–453.

Brown, T. G. (1992). Trends in office layout and space planning, *Proceedings of workshop on innovative cooling systems, Solihull, UK. International Energy Agency Future Buildings Forum.*, pp. F1–F7.

Brunk, M. (1993). Cooling ceilings — an opportunity to reduce energy costs by way of radiant cooling., *Transactions of the American Society of Heating Refrigeration and Air Conditioning Engineers.*

Busweiler, U. (1993). Air conditioning with a combination of radiant cooling, displacement ventilation, and desicant cooling., *Transactions of the American Society of Heating Refrigeration and Air Conditioning Engineers* **99**(2): 503–510.

CFDS (1996a). *CFX-FLOW3D Release 4.1 User Guide*, AEA Technology, Computational Fluid Dynamics Services, Harwell, Didcot, Oxfordshire.

CFDS (1996b). *CFX-RAD3D Release 4.1 User Guide*, AEA Technology, Computational Fluid Dynamics Services, Harwell, Didcot, Oxfordshire.

Chen, Q. and Chao, T. (1996). Predicition of buoyant plume and displacement ventilation with different turbulence models., *Procedings of ROOMVENT-96*, pp. 787–792.

Chen, Q. and Moser, A. (1991). Simulation of a multiple-nozzle diffuser, *Procedings of 12th AIVC Conference, Ottawa, Sept. 24–27*, Vol. 2, pp. 1–13.

Christoffersen, L. and Modsen, T. (1992). Determination of the boundary layer level in a large displacement ventilated factory building, *Proc. of 'ROOMVENT-92', Aalborg, Denmark.*, Vol. 2, pp. 207–213.

CIBSE (1986). *CIBSE Design Guide Volume A*, The Chartered Institute of Building Services Engineers., London.

Clark, D. and May, W. (1985). *HVACSIM+ Building System and Equipment Simulation Program - Users Guide*, National Bureau of Standards.

Cooper, P. and Linden, P. (1992). Multiple sources of buoyancy in a naturally ventilated enclosure, *proc. of 11th Australasian Fluid Mechanics conference, Hobart, Australia*, p. 4.

Courant, R., Isaacson, E. and Rees, M. (1952). On the solution of non-linear hyperbolic differential equations by finite differences, *Communications in Pure and Applied Mathmatics* 5: 243.

Crow, S. and Champagne, F. (1971). Orderly jet structure in jet turbulence, *Journal of Fluid Mechanics* 48: 547–549.

Dalicieux, P. and Bouia, H. (1993). *Présentation d'une meélisation simplifiée des mouvements d'air à l'intérieur d'une pièce d'habitation.*, Electricite de France report HE 12 W 3269, 29 p.

Daly, B. and Harlow, F. (1970). Transport equations in turbulence, *Physics of Fluids* **13**: 2634.

Dascalaki, E., Santamouris, M., Balaras, C. and Asimokopoulos (1994). Natural convection heat transfer coefficients from vertical and horizontal surfaces for building applications, *Energy and Buildings* (20): 243–249.

Davidson, L. and Olsson, E. (1989). Ventilation by displacement: calculation of the flow in a three-dimensional room., *proc. of 10th AIVC Conference, Dipoli, Finland.*, pp. 367–391.

Davis, D. G. (1994). A model performance, *Building Services, The CIBSE Journal* **16**(6): 29–30.

De Moor, M. and Berckmans, D. (1994). Building a grey box model to model the energy and mass transfer in an imperfectly mixed fluid by using experimental data, *Proceedings of 'System Simulation in Buildings – 94', Liege, Belgium. December.*

Dickson, D. (1994). A testing time for chilled ceilings, *Building Services, The CIBSE Journal* **16**(6): 31–32.

Djilali, N., Gartshore, I. and Salcudean, M. (1989). Calculation of convective heat transfer in recirculating turbulent flow using various near wall turbulence models, *Numerical Heat Transfer, Part A* **16**: 189–212.

DOE-2 (1982). *DOE-2 Engineers Manual, part 1–2, version 2.1A*, Building Energy Simulation Group, Lawrence Berkeley Laboratory., Berkeley, C.A.

FACET (1991). *APACHE User manual*, FACET Ltd., St Albans, UK.

Fanger, P., Ipsen, B., Langkilde, G., Olesen, N. and Christensen, N.K. ans Tanabe, S. (1985). Comfort limits for asymetric thermal radiation, *Energy and Buildings.*

Feustel, H. and Stetiu, C. (1995). Hydronic radiant cooling – preliminary assessment., *Energy and Buildings* **22**: 193–205.

Fitzner, K. (1989). Forderprofil einer warmequelle bei verschiedenen temperaturgradienten und der einfluss auf die raumstromung bei quelluftung., *Klima-Kälte-Heizung.* **10**: 476–481.

Fletcher, C. (1988). *Computational Techniques for Fluid Dynamics - Volume II*, Springer-Verlag, Berlin.

Gardon, R. and Akfirat, J. (1965). The role of turbulence in determining the heat-transfer characteristics of impinging jets., *International Journal of Heat and Mass Transfer* **8**: 1261–1272.

Gutmark, E. and Ho, C. (1983). On the preferred modes and spreading rates of jets, *Physics of Fluids* **26**: 2932–2938.

Haves, P., Rees, S. and Harrington, L. (1995). Modelling and simulation of low energy cooling systems, *Proc. of 'TSINGHUA-HVAC-95',2nd. Int. Symp. on HVAC, Beijing, China, Sept. 25–27*, Vol. 1, pp. 29–38.

Heiselberg, P. and Sandberg, M. (1990). Convection from a slender cylinder in a ventilated room., *Proc. of 'ROOMVENT-90', Oslo, Norway.*

Hensen, J. and Huygen, B. (1996). Energy simulation of displacement ventilation in offices, *Proc. of CIBSE National Conference*, pp. 1–8.

Hollworth, B. and Gero, L. (1985). Entrainment effects on impingement heat transfer: Part II—local heat transfer measurements., *Journal of Heat Transfer* **107**: 910–915.

Howarth, A. (1983). *Temperature Distribution and Air movements in Rooms with Convective Heat Source.*, PhD thesis, University of Manchester Institute of Science and Technology.

I.S.O. (n.d.). *ISO Standard 7730: Moderate thermal environents—determination of the PMV and PPD indices and specification of the conditions for thermal comfort.*, International Standards Organisation, Geneva.

Inard, C. and Buty, D. (1991). Simulation of thermal coupling between a radiator and a room with zonal models, *Proc. of Building Simulation '91*, pp. 113–117.

Jackman, P. (1990). *Displacement Ventilation, Technical Memorandum 2/90*, BSRIA, Bracknell, Berkshire.

Jackman, P. J. (1991). Displacement ventilation, *Proc. of CIBSE national conference, Canterbury*, pp. 364–380.

Jacobsen, T. V. and Neilsen, P. V. (1993). Numerical modelling of thermal environment in a displacement-ventilated room, *Proc. of 'Indoor Air '93', Helsinki, Finland.*, Vol. 5, pp. 301–306.

Jayatilleke (1969). The influence of Prandtl number and surface roughness on the resistance of the laminar sublayer to momentum and heat transfer, *Progress in Heat and Mass Transfer* **1**: 269–289.

Jones, P. and Whittle, G. (1992). Computational fluid dynamics for building air flow prediction - current status and capabilities, *Building and Environment* **27**(3): 321–338.

Kegel, B. and Schulz, U. (1989). Displacement ventilation for office buildings, *Proc. of 10th AIVC Conference, Dipoli, Finland.*, pp. 393–411.

Kilkis, B. (1993). Radiant ceiling cooling with solar energy: Fundamentals, modeling, and a case design.,, *Transactions of the American Society of Heating Refrigeration and Air Conditioning Engineers* **99**(2): 521–533.

Klein, S. A., Beckman, W. A. and Duffie, J. A. (1976). TRNSYS - a transient simulation program, *Transactions of the American Society of Heating Refrigeration and Air Conditioning Engineers.*

Klien, S. and Alvarado, F. (1997). *EES Engineering Equation Solver: User Guide.*, F-Chart Software, Wisconsin.

Kofoed, P. and Nielson, P. V. (1990). Thermal plumes in ventilated rooms - measurements in stratified surroundings and analysis by use of an extrapolation method., *Proc. of 'ROOMVENT-90', Oslo, Norway.*

Krühne, H. (1993). Effect of cooled ceilings in rooms with displacement ventilation on the air quality, *Proc. of 'Indoor Air '93', Helsinki, Finland.*, Vol. 5, pp. 395–400.

Külpmann, R. (1993). Thermal comfort and air quality in rooms with cooled ceilings - results of scientific investigations., *Transactions of the American Society of Heating Refrigeration and Air Conditioning Engineers* **99**(2): 488–502.

Laine, T. (1993). Cool ceiling system: for better control of office building indoor climate, *Proc. of 'Indoor Air '93', Helsinki, Finland.*, Vol. 5, pp. 423–430.

Launder, B. and Spalding, D. (1974). The numerical computation of turbulent flow, *Computer Methods in Applied Mechanics and Engineering* **3**: 269–289.

Lebrun, J. (1970). *Exigences physiologiques et modalités physiques de la climatisation par source satique concentrée.*, PhD thesis, University of Liège.

Lebrun, J. and Ngendakumana, P. (1987). Air circulation induced by heating emitters and corresponding heat exchanges along the walls: Test-room results and modelling, *Proc. of 'ROOMVENT-87', Stockholm, Sweden.*, p. 15.

Leschziner, M. (1980). Practical evaluation of three finite difference schemes for the computation of steady state recirculating flows, *Computational Methods in Applied Mechanics and Engineering* **23**: 293–312.

Li, Y. (1995). Personal communication.

Li, Y. and Fuchs, L. (1991). A two band radiation model for calculating room wall surface temperature, *Recent Advances in Heat Transfer, Sunden, B. and Zukauskas, A. (eds)* **Elsevier Science Publishers**: 388–400.

Li, Y., Fuchs, L. and Sandberg, M. (1993a). Numerical prediction of airflow and heat-radiation in a room with displacement ventilation, *Energy and Buildings* **20**: 27–43.

Li, Y., Sandberg, M. and Fuchs, L. (1993b). Effects of thermal radiation of airflow with displacement ventilation: an experimental investigation, *Energy and Buildings* **19**: 263–274.

Li, Y., Sandberg, M. and Fuchs, L. (1993c). Vertical temperature profiles in rooms ventilated by displacement: Full-scale measurement and nodal modelling., *Indoor Air* (2): 225–243.

Linden, P., Lane-Serff, G. and Smeed, D. (1990). Emptying filling boxes: the fluid mechanics of natural ventilation, *Journal of Fluid Mechanics* **212**: 309–335.

Lockwood, F. and Shah, N. (1980). A new radiation solution method for incorporation in general combustion prediction procedures, *Procedings of the Eighteenth Symposium (International) on Combustion, The Combustion Institute*, pp. 1405–1412.

Lytle, D. and Webb, B. (1994). Air jet impingement heat transfer at low nozzle–plate spacings., *International Journal of Heat and Mass Transfer* **37**(12): 1687–1697.

Malalasekera, W. and James, E. (1993). Thermal radiation in a room: Numerical evaluation, *Building Services Engineering Research and Technology* 4(14): 159–168.

Manzoni, D. and Guitton, P. (1997). Validation of displacement ventilation simplified models., *Proc. of BUILDING SIMULATION-97*, pp. 233–239.

Manzoni, D. and Rongère, F. (1996). Simplified models of displacement ventilation systems., *Proc. of ROOMVENT '96*, pp. 478–448.

Mathisen, H. (1989). Case studies of displacement ventilation in public halls, *Transactions of the American Society of Heating Refrigeration and Air Conditioning Engineers* **95**(2): 1018–1027.

Mathisen, H. M. (1988). Air motion in the vicinity of air-supply devices for displacement ventilation., *Proc. of 9th AIVC Conference, Gent, Belgium.*, pp. 105–123.

Mathisen, H. M. (1990). Displacement ventilation - the influence of the characteristics of the supply air terminal device on the airflow pattern, *Proc. of 'ROOMVENT-90', Oslo, Norway.*

McGuirk, J. and Whittle, G. (1991). Calculation of buoyant air movement in buildings—proposals for a numerical benchmark test case, *Procedings of Computational Fluid Dynamics - Tool or Toy?, Institution of Mechanical Engineers, London, 26 November*, pp. 13–32.

Meierhans, R. (1993). Slab cooling and earth coupling, *Transactions of the American Society of Heating Refrigeration and Air Conditioning Engineers* **99**(2): 511–518.

Meirzwinksi, S. (1992). Testing and modeling of thermal plumes in rooms, *Proc. of ASHRAE conf. Room Air Convection and Ventilation Effectiveness, Tokyo, Japan.*, pp. 281–292.

Melikov, A. and Langkilde, G. (1990). Displacement ventilation - airflow in the near zone, *Proc. of 'ROOMVENT-90', Oslo, Norway.*

Melikov, A., Langkilde, G. and Derbiszewski, B. (1990). Airflow characteristics in the occupied zone of rooms with displacement ventilation, *Transactions of the American Society of Heating Refrigeration and Air Conditioning Engineers* 96(1): 555–563.

Milkov, A. and Nielson, J. (1989). Local discomfort due to draft and vertical temperature difference in rooms with displacement ventilation, *Transactions of the American Society of Heating Refrigeration and Air Conditioning Engineers* 95(2): 1050–1057.

Morton, B., Taylor, G. and Turner, J. (1956). Turbulent gravitational convection from maintained and instantaneous sources., *Proc. of the Royal Society, London.* **234**: 1–23.

Mundt, E. (1990). Convection flows above common heat sources in rooms with displacement ventilation, *Proc. of 'ROOMVENT-90', Oslo, Norway.*

Mundt, E. (1996). *The performance of displacement ventilation systems—experimental and theoretical studies.*, PhD thesis, Royal Institute of Technology, Stockholm.

Nielsen, P. (1994). Stratified flow in a room with displacement ventilation and wall-mounted air terminal devices, *Transactions of the American Society of Heating Refrigeration and Air Conditioning Engineers.*

Nielsen, P., Hoff, L. and Pedersen, L. (1988). Displacement ventilation by different types of diffuser., *Proc. of 9th AIVC Conference, Gent, Belgium.*, pp. 13–29.

Niu, J. (1994). *Modelling of Cooled-Ceiling Air-Conditioning Systems.*, PhD thesis, Delft University of Technology.

Niu, J. and van der Kooi, J. (1992). A dynamic cooling-load program for cooled ceiling systems., *Proc. of CLIMA 2000, London 1992.*

Niu, J. and van der Kooi, J. (1993). Numerical investigations of thermal comfort and indoor contaminant distributions in a room with cooled ceiling systems, *Proc. of 'Indoor Air '93', Helsinki, Finland.*, Vol. 5, pp. 331–336.

Palonen, J., Ukkonen, M., Helenius, T. and Majanen, A. (1990). Displacement ventilation in a lecture hall, a case study., *Proc. of 'ROOMVENT-90', Oslo, Norway.*

Papadimitriou, C. (1985). *The Prediction of Turbulent Stably-Stratified Buoyant Flows*, PhD thesis, Dept. of Mechanical Engineering, Imperial College, London.

Patankar, S. (1980). *Numerical Heat Transfer and Fluid Flow*, Hemisphere, New York.

Patankar, S. and Spalding, D. (1972). A calculation procedure for heat, mass and momentum transfer in three-dimensional parabolic flows, *International Journal of Heat and Mass Transfer* **15**: 1787–1806.

Popiolek, Z. (1987). *Testing and modelling of buoyant convection flows in consideration of ventilation processes forming. Dsc.Thesis.*, TU Gliwice. Zeszyty Naukowe Inzynierii Srodowiska (in Polish), New York.

Popiolek, Z. and Meirzwinksi, S. (1983). Convective flow above a human body as a factor to air motion control in ventilated room., *Proc. of 2nd Int. Congr. on Building Energy Management.Iowa, U.S.A.*, pp. 6.23–6.30.

Popiolek, Z. and Meirzwinksi, S. (1984). Buoyant plume calculation by means of an integral method., *K.T.H Stokholm, Inst. Uppvarmn och Ventil.*

Raithby, G. (1976). A critical evaluation of upstream differencing applied to problems involving fluid flow, *Computational Methods in Applied Mechanics and Engineering* **9**: 75–103.

Rees, S. and Haves, P. (1995). A model of a displacement ventilation system suitable for system simulation, *Proc. of 'Building Simulation–95', Madison, Wisconsin, August 14–18*, Vol. 1, pp. 199–205.

Renz, U. and Terhaag, U. (1990). Predictions of air flow pattern in a room ventilated by an air jet. the effect of turbulence model and wall function formulation, *Proc. of 'ROOMVENT-90', Oslo, Norway.*

Rhie, C. and Chow, W. (1982). A numerical study of the turbulent flow past an isolated airfoil with trailing edge separation, *AIAA Journal* **21**(11): 1525–1532.

Roache, P. (1982). *Computational Fluid Dynamics*, Hermosa Publishers, Alberquerque.

Sandberg, M. (1994). Measurement techniques in room air flow, *Proc. of 'ROOMVENT-94', Krakow, Poland.*, Vol. 1, pp. 60–92.

Sandberg, M. and Blomqvist, C. (1989). Displacement ventilation in office rooms, *Transactions of the American Society of Heating Refrigeration and Air Conditioning Engineers* **95**(2): 1041–1049.

Sandberg, M. and Holmberg, S. (1990). Spread of supply air from low-velocity air terminals, *Proc. of 'ROOMVENT-90', Oslo, Norway.*

Sandberg, M. and S.Lindstrom (1990). Stratified flow in ventilated rooms - a model study, *Proc. of 'ROOMVENT-90', Oslo, Norway.*

Schaelin, A. and Kofoed, P. (1994). Numerical simulation of thermal plumes in rooms, *Procedings of ROOMVENT-94*, Vol. 4, pp. 137–157.

Shah, N. (1979). *New Method of Computation of Radiant Heat Transfer in Combustion Chambers*, PhD thesis, Dept. of Mechanical Engineering, Imperial College, London.

Shankar, V., Davidson, L. and Olsson, E. (1994). Displacement ventilation: Calculation of the flow in vertical plumes, *Procedings of ROOMVENT-94*, Vol. 4, pp. 59–74.

Silvana, S., Cardoso, S. and Woods, A. (1993). Mixing by a turbulent plume in a confined stratified region, *Journal of Fluid Mechanics* **250**: 277–305.

Skåret, E. (1987). Displacement ventilation, *Proc. of 'ROOMVENT-87', Stockholm, Sweden.*, Vol. 4a.

Skistad, H. (1994). *Displacement Ventilation*, Research Studies Press.

Sowell, E. (1991). *A general zone model for HVACSIM+: Users manual*, Department of Engineering Science, report No. 1889/91, University of Oxford.

Sowell, E. and O'Brien, P. (1972). Efficient computation of radiant-interchange configuration factors within the enclosure, *Tran. of A.S.M.E., Journal of Heat Transfer* **94**(3): 326–328.

Sowell, E. F. (1989). *LIGHTS User's Guide*, Department of Computer Science, California State University. CA, USA.

Spalding, D. (1972). A novel finite difference formulation for differential expressions involving both first and second derivatives, *International Journal of Numerical Methods in Engineering* **4**: 551–559.

Stahl, M. and Keller, G. (1992). A new development in air conditioning, *Transactions of the American Society of Heating Refrigeration and Air Conditioning Engineers* **98**(1): 49–57.

Svensson, A. (1989). Nordic experiences of displacement ventilation, *Transactions of the American Society of Heating Refrigeration and Air Conditioning Engineers* **95**(2): 1013–1017.

Takla, A. (1992). Impacts of the Montreal protocol on mechanical cooling systems of buildings, *Proceedings of workshop on innovative cooling systems, Solihull, UK. International Energy Agency Future Buildings Forum.*, pp. A1–A7.

TAS (n.d.). *TAS Users Manual*, Environmental Design Solutions Ltd., Stoney Stratford, Bucks, UK.

Thompson, J., Warsi, Z. and Mastin, C. (1982). Boundary-fitted coordinate systems for numerical solution of partial differential equations, *Journal of Computational Physics* **47**: 1–108.

Togari, S., Arai, Y. and Miura, K. (1993). A simplified model for predicting vertical temperature distribution in a large space, *Transactions of the American Society of Heating Refrigeration and Air Conditioning Engineers* **99**(1): 84–99.

Turner, J. (1979). *Buoyancy Effects in Fluids*, Cambridge Universtity Press., Cambridge.

Turner, J. (1986). Turbulent entrainment: the development of the entrainment assumption and its application to geophysical flows., *Journal of Fluid Mechanics* **173**: 431–471.

Udagawa, M. (1993). Simulation of panel cooling systems with laminar subsystem model, *Transactions of the American Society of Heating Refrigeration and Air Conditioning Engineers* **99**(2): 534–547.

Van Doormaal, J. and Raithby, G. (1984). Enhancements of the simple method for predicting incompressible fluid flows, *Numerical Heat Transfer* **7**: 147–163.

Wyatt, T. and Bunn, R. (1991). The future for cooling ceilings, *Building Services, The CIBSE Journal* **13**(11): 33–36.

Yuan, X. (1995). *Wall Functions for Numerical Simulation of Natural Convection along vertical surfaces*, PhD thesis, Laboratorium für Energiesysteme, ETH Zürich.

Yuan, X., Moser, A. and Suter, P. (1993). Wall functions for numerical simulation of turbulent natural convection along vertical plates, *International Journal of Heat and Mass Transfer* **36**(18): 4477–4485.